Università degli Studi di Napoli
Federico II

Doctorate Thesis

Dipartimento di
Ingegneria
Industriale

Development and validation of simulation models for the energy performance assessment of innovative solar technologies and energy storage systems

Ph.D. candidate:

Giovanni Barone

Supervisors:

Prof. Adolfo Palombo

Prof. Annamaria Buonomano

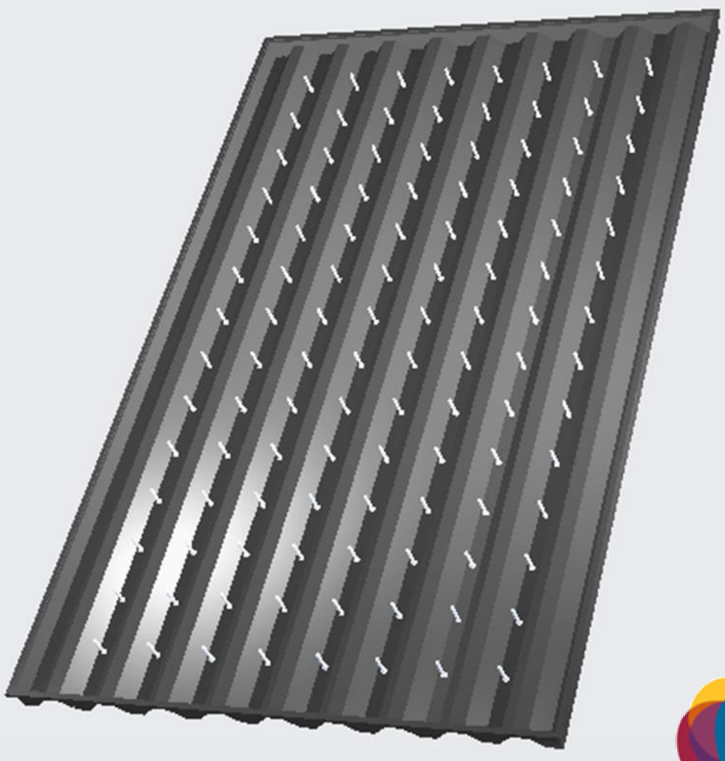

UNIVERSITY OF NAPLES FEDERICO II

SCHOOL OF DOCTORATE IN INDUSTRIAL ENGINEERING

RESEARCH DOCTORATE IN INDUSTRIAL ENGINEERING

XXXII CYCLE

DOCTORATE THESIS

Development and validation of simulation models for the energy performance assessment of innovative solar technologies and energy storage systems

SUPERVISORS
PROF. ADOLFO PALOMBO
PROF. ANNAMARIA BUONOMANO

Ph.D. CANDIDATE
GIOVANNI BARONE

DOCTORATE COORDINATOR
PROF. MICHELE GRASSI

March 2020

To my family

"if we knew what it was we were doing, it would not be called research, would it?"

Albert Einstein

Acknowledgments

In the beginning, I would like to say thanks to my supervisor Prof. Adolfo Palombo for his guide. He inspired and motivated me with his extensive knowledge. By stimulating my curiosity and interest in research, he improved me not only as a student but also as a person. He taught me the culture of work and sacrifices. I couldn't have wished for a mentor better than him.

Secondly, but not in order of importance, I am pleased to say thank you to Prof. Annamaria Buonomano. I owe her all the things that I know about coding. She continuously supported my research with her valuable support, her rare kindness, brightness, and high competency. I will never stop to say thank to her for how she is with her students.

Apart from my "home" supervisors, I want to express my gratitude to Prof. Soteris Kalogirou. He has been my foreign supervisor. By providing his wise support during my period abroad, he gave to me the opportunity to increase knowledge in his research field. During this period, I discovered a great person beyond the great scientist. It has been an honour to be led by him and collaborate with him.

Thanks to Dr. Vittorio Palmieri, Dr. Francesco Vitobello and the entire staff of TVP solar company. They hosted and provided me all the instruments and support to accomplish my research in their company. Thanks to their extreme expertise, they offered to me a big chance to enhance knowledge about solar thermal systems.

I would also remember my travelling companion, Mr. Cesare Forzano, for the time we spent together. I'm glad for having shared these years with him and for the continuous help and support that we exchanged each other. Thanks to Dr. Maria Vicidomini for her friendship and for having shared the office and the time with me.

In the end, I am grateful to my relatives and friends who continuously endured me. I would be nothing without my parents. I thank them for their help: they made me the man who I'm and I'm grateful for all the efforts that they have done for me. They gave me enough moral support, encouragement, and motivation to accomplish my personal goals. Thanks to my brothers Domenico and Mariano, and my aunt Anna. They are my life and they are always with me despite the short time that we have spent together in the last years.

Alle persone che mi amano ed hanno amato,

a quelle che mi hanno scelto e che hanno creduto in me,

ai no che aiutano a crescere.

Ivan Barone,

Naples, March 2020

Abstract

This study aims to investigate the thermal behaviour of innovative solar technologies and energy storage systems. It focuses on solar systems able to produce thermal and/or electric energy to cover energy needs in the building sector (i.e. heating, cooling, dwelling hot water, electricity, etc.). The thesis includes the experimental and numerical investigation of several innovative technologies.

At first, two innovative solar thermal collectors with a vacuum space (adopted for insulating the absorber plate and avoiding convective heat losses), are presented. Here, both the design and the mathematical simulation model (developed in MatLab environment) of the two novel evacuated flat-plate solar thermal collector prototype are introduced. The first solar thermal collector is characterized by a very low initial cost, whereas the second one is characterized by high-vacuum space (i.e. 10^{-8} mbar) for dwelling hot water storage purposes.

The study is then focused on an innovative low-cost air-based photovoltaic/thermal collector prototype, for which a novel dynamic simulation model is suitably developed in order to investigate its energy performance and economic feasibility under different operating conditions. The prototype is tested under different operating conditions and the experimental data are used to validate the developed simulation model. A suitable case study in which the photovoltaic/thermal collectors are coupled to an air-to-air heat pump for space heating of a sample building, is also presented.

Thus, with the aim of investigating the passive effects of the integration into the building envelope of the above-mentioned solar technologies, the experimental validation of an in-house building simulation model, called DETECt, is presented. Here, with the use of a comparative analysis between numerical results and measurements obtained on a real test room, the experimental validation of the dynamic simulation model is presented.

Finally, the integration of air open-loop photovoltaic thermal systems on the façade of a high-rise buildings is analysed, with a special focus on their active and passive effects. The system energy performance and its impact on the building heating and cooling demands and electrical production are assessed through a dynamic simulation model suitably modified and linked into DETECt. In addition, with the aim of analysing the potentiality of electricity storage system, a novel energy management system for buildings connected in a micro-grid, by considering electric vehicles as active components of such energy scheme is also investigated.

Contents

List of Figures

List of Tables

Abbreviations

Acronyms

BEPS	building energy performance simulation
BESTEST	building energy simulation test
BIPV/T	building integrated photovoltaic/thermal system
BIPV	building integrated photovoltaic system
CDD	cooling degree days
CFD	computational fluid dynamics
COP	coefficient of performance
DER	distributed energy resources
DHW	domestic hot water
DPB	discounted pay-back
EPBD	energy performance building directive
EV	electric vehicles
EVB	electric vehicle battery
FEM	fine element method
FPCs	flat-plate solar thermal collectors
HDD	heating degree days
HP	heat pump
HVAC	heating, ventilation, and air conditioning system
IEA	international energy agency
IRR	internal rate of return
ISR	incident solar radiation *NOCT* nominal operating cell temperature
NPV	net present value
NZEB	net-zero energy building
nZEB	nearly-zero energy building
OECD	organization for economic co-operation and development
PCM	phase change material
PES	primary energy savings
PI	profit index
PLR	part load ratio
PMV	predicted mean vote
PPD	predicted percentage of dissatisfied
PV	photovoltaic panel
PV/T	photovoltaic/thermal collector
RC	resistance capacitance
REF	reference system
RES	renewable energy systems
SC	solar collector
SPB	simple pay-back
V2B	vehicle-to-building
V2B^2	building-to-vehicle-to-building
V2G	vehicle-to-grid
ZEB	zero Energy Building

Nomenclature

Symbols

A	surface (m^2)
a	interest rate (-)
C	thermal capacitance (J/K)
Cap	battery energy capacity (kWh)
C_b	bond conductance (W/(m·K))
C_d	channel coefficient (-)
CO_2	carbon dioxide
c_p	specific heat (J/(kg·K))
D	diameter (mm)
d	distance (m)
D_{eq}	equivalent diameter (mm)
e	average error (%)
E	energy (kWh)
EC	yearly energy consumption (kWh/y)
EcS	yearly economic Savings (k€/y)
EER	energy efficiency ratio (-)
ES	yearly energy savings (kWh/y)
f	load factor (-)
F'	collector efficiency factor (-)
FGE	feed to grid electricity (kWh)
f_{grid}	grid matching index (-)
f_{load}	load matching index (-)
f_{PLR}	part load ratio (-)
F_R	heat removal factor (-)
h	convective heat transfer coefficient (W/(m^2·K))
I	solar irradiation (W/m^2)
IC	Investment cost (k€)
I_{cl}	clothing insulation (clo)
IRR	internal rate of return (%)
j	hourly purchase price (€/kWh)
k	thermal conductance (W/(m·K))
L	length (m)
M	molecular weight (kg/mol)
M	maintenance cost (k€/y)
$\dot{m}$	mass flow rate (kg/s)
N	number of collectors in parallel (-)
Nu	Nusselt number (-)
Obj	objective function
OC	operative cost (k€/y)
p	pressure (Pa)
P	power (W)
PGE	purchase grid electricity (kWh)
PI	profit index (-)
Pr	Prandtl number (-)
Q	thermal power
R	resistance ((m^2·K)/W)
Ra	Rayleigh number (-)
R_{gas}	gas constant (J/(mol·K))
s	side
T	temperature (K)
t	time (s)
U	heat loss coefficient (W/(m^2·K))
V	volume (m^3)
v	velocity (m/s)
W	width (m)
w	wind speed (m/s)
x	x-coordinate (m)

Greek symbols

α	absorbance (-)
β	tilted angle of the solar collector (°C)
γ	coefficient (-)
Δ	variation (-)
δ	thickness (mm)
ε	emittance (-)
η	efficiency (-)
θ	angle refracted beam (°)
κ	incident angle modifier (-)
λ	thermal conductivity (W/(m·K))
μ	dynamic viscosity (Pa·s)
υ	kinematic viscosity (m^2/s)
ξ	air inlet number (-)
$\rho(..)$	Pearson correlation coefficient (-)
ρ	density (kg/m^3)
σ	Stefan-Boltzmann constant (W/(m^2·K^4))
τ	transmittance (-)

Subscripts/Superscripts

air	air
amb	ambient
appliances	lighting and equipment
B	building
b	bottom
bck	back
bond	bond
c	collector
cavity	cavity
ch	channel
cond	conductive
conv	convective
cooling	cooling
duct	duct
e	edge
el	electical
eq	equivalent
ev	evaporator
EV	electric vehicle
ext	external
fan	fans
field	total gross area of PVs
g	glass cover
gas	gas into the gap spacing
grid	grid
HC	heating and cooling system
heating	heating
House	house
HP	heat pump
i	inner
in	inlet
ins	insulation
inv	inverter
L	overall
loss	loss
m	generic building element
mod	module
N	nominal
n	node of a generic building element
NSP	national single price
Office	office
out	outlet
p	absorber plate
pillars	pillars
pipes	riser pipes
pp	people
pro	proposed case
PV	photovoltaic
r	components of the incident solar radiation
rad	radiative
ref	reference case
roof	refer to roof mounted
s	sensible
sky	sky
sp	specific
t	top
th	thermal
tot	total
u	useful
v	venilation
V	volumetric flow rate (m^3/h)
wall	refer to wall mounted
wf	working fluid

CHAPTER
1

1. Introduction

As commonly known, thermal energy and electricity are conventionally produced by using fossil fuels (e.g. petroleum, coal, natural gas, etc.). However, the burning of these fuels leads to gas emissions which are the primary cause of air pollution and global climate change. In this framework, the growing concerns about environmental pollution, caused by a sensible increase of World energy consumption, have led the research community toward the development of sustainable energy policies. Therefore, to avoid pollution by fossil fuel combustion, a viable strategy is the adoption of renewable energy-based technologies. These kinds of systems are commonly accepted by human society for their high environmental-friendly attitude. Among all the available renewable energy, the most promising one is solar energy [1]. It is freely available, allowing users to harvest thermal power and/or electricity.

According to the IEA statistics for energy balance, the use of energy in buildings accounts for more than one-third of total energy end-use [2]. In OECD countries the building sector is responsible for approximately 40% of total final energy consumption, being an important source of pollution. Buildings can play a crucial role to tackle climate change and energy consumptions through the adoption of energy-efficient strategies incorporated into design, construction, and operation of new and retrofitted buildings. A significant amount of energy consumed in buildings is used to cover heating and domestic hot water demands. During the time, these needs were mainly covered by intensive exploitation of fossil fuels. However, many drawbacks regarding environmental impact and reduction in quality of life led to the development of environmental-friendly technologies based on renewable energy [3]. Among all the available renewable energy sources (RES), solar energy is the one that properly matches energy demands of buildings [4], and solar-based technologies in their active or passive forms, can deliver the entire set of needs.

Solar energy can be exploited for satisfying energy needs required for space heating and cooling, domestic hot water production, and electricity. Technologies based on solar RES, such as photovoltaic panels (PV), solar thermal collectors (STCs), and photovoltaic thermal collectors (PV/T), can be easily integrated into the shell of a new building, by substituting conventional building materials with no additional surface area. Also, as an on-site energy production option, it is to be highly preferred, among others, and particularly effective in the case of building renovations [5]. Their utilization provides the ability to reduce significantly or nullify the share of non-renewable energy sources consumed in buildings, as long as sufficient surfaces for integration are available [6].

In this regard, the adoption of these technologies facilitates the achievement of net/nearly zero energy building (NZEB/nZEB) goals. This concept has attracted the interest of the research community, building stakeholders, and policymakers supporting the shift towards a low-carbon economy [4]. An nZEB is considered as a building with very high energy performance which requires a very low amount of energy, to be covered to a very significant extent, or even completely, using RES, produced on-site or nearby [4]. Therefore, appropriate nZEB designs or renovations must combine high efficiency active and passive technologies (e.g. natural ventilation, daylighting) with renewable energy production, providing an opportunity for cost-effective measures, aiming at converting the building stock from an energy consumer to an energy producer.

1.1. Subject this study

The subject of this thesis is the energy performance assessment of innovative solar technologies and energy storage systems. This research is conducted with the twofold aim to investigate innovative technologies by adopting a dynamic simulation approach and provide useful design criteria. As previously discussed, solar-based technologies are suitable for matching energy demands of buildings, however, different problems occur in the design and application of these technologies. Furthermore, despite several approaches adopted by many researchers in order to understand the physical effects and mechanisms of these systems, deep investigations need to be carried out and different solutions must be provided for some specific issues.

In this thesis, the most promising innovative technologies and energy efficiency strategies are investigated as follows: i) solar vacuum thermal collector; ii) stand-alone photovoltaic/thermal collectors; iii) building integrated photovoltaic/thermal system (BIPV/T system); iv) electricity storage and electricity fluxes optimization by means of electric vehicles and vehicle to building strategy. For each investigated technology a deep experimental campaign is carried out. Then, with the aim of assessing the system performance under different operating conditions, suitable dynamic simulation models are purposely developed. By means of the gathered data during the experimental campaigns, the developed mathematical models are validated.

Initially, stand-alone devices (i.e. solar thermal collector and photovoltaic thermal collector) are analysed. Then, with the aim of assessing the passive effect of the integration of these technologies into the building envelope, a previously developed building energy performance simulation tool, called DETECt, is adopted. Specifically, its reliability is investigated by means of a suitable experimental campaign carried out on a real test cell. Finally, the integration of an air-based PV/T system into the building envelope of a high-rise building is investigated. In addition, the exploitation of electricity production is optimized by means of the vehicle to building strategy and electric storage system. Interesting results by the energy, economic and environmental point of view are achieved and discussed hereinafter, with the aim to provide useful design criteria.

1.2. Aim of this study

Summarising, the new goals of this thesis are:

- develop new mathematical models able to assess the energy performance of innovative solar-based devices and new energy efficiency strategies;
- experimentally validate the developed mathematical models by means of real data gathered during suitable experimental tests;
- investigate heat and electricity performance offered by the integration of these technologies into the building envelope;
- optimize the design of the developed prototypes by utilizing the developed mathematical models;
- provide punctual design guidelines and criteria for the exploitation of these technologies.

CHAPTER
2

2. Literature review

In this chapter, the literature review of the innovative investigated technologies is presented. Specifically, the main findings of the recent scientific literature are here reported with the twofold aim of analysing what has been done and highlighting the lack of knowledge.

2.1. Solar thermal collector system

Many typologies of solar thermal systems are available on the market, however flat-plate solar thermal collectors (FPCs) are the most common type [7], due to its numerous advantages (e.g. simple construction, low cost, safe operation, etc.). The available literature on FPCs, highlights the presence of many studies focused on the development and enhancement of the working fluid’s outlet temperature and system’s thermal efficiency.

Different designs and materials were investigated on this topic, as described by Ali Sakhaei et al. [8]. From this review article, it is clearly noted that the most critical parameters that affect the performance of the FPCs are referring mostly to the thickness of the various materials as the glass cover, the absorber plate, the riser pipes and the gap spacing between the absorber plate and insulation.

In addition, other important parameters are the optical properties of the materials [9] that characterize the heat exchange between the above-listed components and the ambient. Several ways to enhance the thermal efficiency of FPCs are described in literature as well and different glass cover thicknesses are adopted. Ramadhani et al. [10] investigated the effect of the thickness of the glass cover on the performance of FPCs. They have tested experimentally the thermal efficiency of the FPC with glasses with low-iron oxide content and thickness of 4, 5 and 6 mm. It is concluded that, the adoption of a thickness of 4 mm can improve the thermal efficiency about 7.6% compared to the thickness of 5 and 6 mm. However, if the 4 mm glass cover is used, the risk of breaking the glass is higher than the one with 5 and 6 mm. Another critical feature of the glass cover is its emissivity, typical values range from 0.79 to 0.89 [11]. Giovannetti et al. [12] improved the optical properties of the glass cover by applying highly transmitting and spectrally selective coatings. They analysed two different FPCs (single and double glass cover). Such a solution can provide a significant increase of the performance of FPCs (i.e. 60% higher than that of a typical FPC single-glazed available on the market). Boudaden et al. [13] investigated the optical characteristics of titanium dioxide and silicon dioxide dielectric materials in order to create a non-reflective coatings for solar thermal applications. Based on the spectroscopic results, it is shown that the non-reflective coatings could be successfully used in solar thermal applications as they can offer low absorbance, low reflectivity, and high solar transmittance (about 87% for double coating, and 70 % for triple coat).

The absorption of the absorber plate is also a critical parameter. Kalogirou et al. [14] evaluated the application and performance of various colour dyes in the absorber plate of FPC. From both the theoretical and the experimental analysis, the coloured collectors (85% absorbance and 10% emissivity) showed lower performance than standard black-dye collectors (95% absorbance and 10% emissivity).

Regarding the riser pipes, Garcia et al.[15] used steel wire inserts to assess the heat transfer through pipes. Tests were conducted for laminar, transient and turbulent flow, whereas the heat transfer fluids used were water and propylene glycol. It is shown that it is possible to affirm that the use of wire inserts in the tubes led to an increase in the heat transfer rate of up to 200%. The same authors [15] utilized steel wire inserts into the riser pipes of a typical solar thermal collector. Tests were conducted for mass flow rate ranges from 0.011 to 0.047 kg/s and an increase of the thermal efficiency between 14 and 31% was detected. From these two works, it is clear that the increase of the performance of the solar thermal collector is directly related to the mass flow rate of the working fluid, but for very high flow rates of the working fluid, the increase in the heat transfer rate is not significant. Jaisankar et al. [16] conducted experiments by adding helix strips into the copper tubes of a FPC to determine the heat transfer characteristics and pressure drop. In this experimental procedure, Jaisankar et al. used copper metallic strips with different rotational ratios, while the Reynolds number ranged from 3000 to 23000. Based on the results from the experimental procedure, it was found that with the increase of the twisting ratio, turbulence was increased, resulting in an increase of the heat transfer rate between the pipe walls and the heat transfer fluid, as well as the pressure drop across the pipes which also increases the pumping power required. In addition, it has been shown that the use of helical strips within the tubes of the FPC can reduce the active surface of the collector from 8 to 24% for stable collector performance.

Comparing to the typical FPC, the evacuated flat-plate collector works better during cloudy days and in weather zones characterized by cold climate [17]. This is due to two reasons: i) evacuated FPCs can collect the diffuse radiation; ii) vacuum chamber between the absorber plate and the glass cover provide a very low heat loss coefficient. Souliotis et al. [18] developed a novel integrated collector storage solar water heater. Such a collector is composed by two concentric cylinders and, between them, an anulus in which the vacuum is made. Several experimental tests were carried out considering different pressure levels into the anulus and various experimental correlations were obtained for thermal loss coefficients as function of the vacuum pressure. Moss et al. [19, 20] developed and presented two water-based evacuated FPCs characterized by a significant low internal pressure (0.5 Pa). By means of a deep experimental investigation, remarkable results in terms of heat loss coefficient reduction (i.e. from 7.4 to 3.6 W/(m^2·K)) and a corresponding improved efficiency (i.e. from 36 to 56%) were achieved. Juanicó [21] stated that the adoption of a transient model is necessary for a vacuum system, in order to take into account the thermal mass effects on the FPC performance. Such approach is required for taking into account the dynamical response of the system.

In this regard, Saleh [22] developed a dynamic simulation model capable to simulate a whole solar thermal system. Such approach was needed for taking into account the thermal behaviour of the hot water storage tank. The model is based on one-dimensional thermal network and it is able to evaluate the transient processes occurring. A similar approach was considered by Zhou et. al. [23] who have developed a transient model in order to assess the enhancement provided by the adoption of PCM between the absorber plate and the back-insulation layer. In fact, if the authors had adopted a quasi-steady state approach, the advantages offered by PCM layer into the FPC (i.e. heat released and stored by PCM during time) would not have been considered. Therefore, from the works [22, 23] it seems clearly that the adoption of transient dynamic simulation model is required in case of systems with components with a thermal mass which is not negligible.

A different approach was considered by Dara et al. [24], since they have developed a quasi-steady state model for assessing the performance of FPC collector. By means of such a code, they investigated the top loss heat transfer coefficient by varying the absorber plate emittance and air gap spacing between the absorber plate and the cover plate, separately. They considered a gap spacing variation ranging from 9.0 to 50 mm and an emissivity of the absorber plate ranging from 0.5 to 0.95. Finally, they assessed an increase of the efficiency from 0.646 to 0.680 by increasing the gap spacing (with a consequential decrease of the top heat loss heat transfer from 8.2 to 6.3 W/(m^2·K), equal to -23%). In addition, by decreasing the emissivity of the absorber plate, an increase on the thermal efficiency is achievable (from 0.65 to 0.69). Such results are obtained by adopting a parametric analysis in which the effectiveness of a single variable on the thermal efficiency is assessed.

2.2. Photovoltaics/thermal collector

Another promising solar-based technology is the photovoltaic solar thermal collector system (PV/T system). Despite space constraints for the installation of these devices, considerable effects of temperature on the PV efficiency opened up a new front of research, where both technologies (i.e. photovoltaic cells and thermal absorbers) are combined into a single hybrid device. This device is able to harness thermal energy, simultaneously increasing the PV electrical efficiency.

This hybrid technology, which converts solar energy to electricity and heat, is known as photovoltaic/thermal (PV/T) collector and has been studied extensively since the 1970s. Research led to the development of a wide range of PV/T technologies starting from the first PV/T prototype, conceived by Wolf and proposed as economic and space saving technique of energy production [25]. Both electrical and thermal energy production can be harvested from a single PV/T device. In particular, PV cells convert photon energy to electricity whereas solar thermal energy is recovered through a heat extraction system and transferred to the user through a suitable working fluid [26]. Wolf examined the possibility to replace the absorber of a traditional solar thermal collector with a PV panel for electricity production[25]. Balancing the energy demands of a single-family house was considered as a suitable application for the PV/T collectors, which caused a decrease of the system's overall energy performance (ranging from 10 to 20%, compared to PV panels and solar thermal collectors fields). This result was considered promising at the time, thus a number of studies regarding the development and improvement of the PV/T technology have been carried out.

The available literature on PV/T collectors highlights the presence of many studies focused on the development and enhancement of the PV/T system configuration and overall energy conversion efficiency. From this point of view different designs, system materials, and working fluids were investigated, as reviewed by Abdelrazik et al. [27].

Regarding the collector layout, a number of attempts on increasing the system overall energy efficiency have been carried out. Several authors analysed the use of a glass cover, installed above the PV module of the PV/T collector, to improve the system energy performance, as reviewed by Al-Waeli et al. [28]. A comprehensive review written by Babu et. al [29] highlighted the slight decrease of the electrical efficiency of glazed PV/T collectors (around 10.6%) with respect to unglazed systems (about 11.0%). On the other hand, as reported by Slimani et al. [30], the glass cover increases the PV/T collector overall energy performance at the expense of the capital cost increase, as discussed by Kabir et al. [31].

Additional layout options were proposed in the literature to optimize the PV/T systems performance. In particular, the enhancement of the heat transfer to the air flowing through the channel of PV/T collectors has been investigated by several authors in the recent years. Tonui and Tripanagnostopoulos [32] conducted an experimental investigation to analyse the effect of metal sheet and fins installed in the air channels. This modification decreased the PV operating temperature by 4 and 10°C with respect to a PV/T collector without this metal sheet and fins. This concept also appears in the study of Jin et al. [33], where an air-based PV/T system with internal multiple rectangular channels was compared to a typical system without this equipment. The analysis was conducted by taking into account five different air flow rates and two solar irradiances. Results showed an increase in the cooling effect and in the system's thermal efficiency (almost 30% with respect to the reference system). Franklin and Chandrasekar [34] studied the effects of adding staves (vertical thin metal sheets) in the trailing portion of the air channel of a PV/T system. A prototype was experimentally tested in Tamilnadu (India) and compared to two reference systems (a standard PV and a PV/T without staves). An increase of 5 and 2.5 °C was observed on the outlet air temperature under high and low speed conditions, respectively, while a reduction of the PV operating temperature was recorded. The use of longitudinal fins inside the air channel of an air-cooled PV/T was recently investigated by Fan et al. [35], achieving a significant increase of the air outlet temperature (with respect to the channel without fins). Ali et al. [36] added staggered plate segments inside a parallel plate heat exchanger of a PV/T collector to enhance the heat transfer, whereas Hussain et al. [37] proposed the installation of a hexagonal honeycomb heat exchanger into the air passage located under the PV module, which increased the recovered thermal energy up to 60%. An experimental study was conducted on water-cooled PV/T collectors by Yuan et al. [38] in order to compare the energy performance of a simple PV panel, a commercial water-based PV/T system and a PV/T collector equipped with a micro-channel heat pipe array. The micro-channels increased the electrical efficiency between 10 and 11.2%, being much lower in case of the PV panel (ranging between 7.0 and 8.6%) and of the commercial PV/T device (ranging between 7.7 and 9.6%).

A different PV/T layout concept was proposed by Wu et al. [39], which unlike the traditional collectors, presented a water-cooled prototype with the heat exchanger placed above the PV panel.

This arrangement was designed for increasing thermal efficiency by sacrificing the electrical one. Results showed that by considering a water flowrate of 0.003 kg/s, a 4% increase of thermal efficiency (with respect to a standard PV/T system) was achieved. Conversely, a 0.8% decrease of the electrical efficiency was detected due to the heat exchanger shielding effect on the PV cells.

Concerning the system materials, a novelty is represented by the use of a phase change material (PCM) layer placed on the back of a PV/T collector. Such an option was investigated by Chauhan et al. [40], which compared a water-cooled PCM-based PV/T system to a standard one. A 33% growth of thermal energy storage capacity and an increase of the useful time period from 75 to 100% was detected for the PCM-based PV/T collector with respect to the traditional one. The possibility of replacing the standard thermal insulation panel on the back of a PV/T system with a PCM layer was also investigated by Yang et al. [41]. They compared the PCM-PV/T system with a traditional PV/T collector, observing a decrease of the PV back temperature with a consequent increase of the electrical efficiency from 6.98% (for the standard configuration) to 8.16% (for the proposed one).

Air and water are typically adopted as working fluids into PV/T collectors for their wide availability and naught cost. As an alternative to these conventional working fluids, other promising ones have been recently investigated. Al-Shamani et. al [42] compared two PV/T collectors cooled with water and a nanofluid (based on silicon dioxide, $SiO2$), observing an enhancement in terms of PV operating temperatures. Specifically, the temperature of the PV/T absorber plate dropped from 65 to 45°C with the $SiO2$ nanofluid, and from 65 to 50°C with water.

Nevertheless, despite the better performance obtained with the use of innovative working fluids, air- and water-based PV/T systems are more often adopted, mostly for their lower initial and operating costs [43]. From this point of view, several tests were performed by Tripanagnostopoulos et al. [44] with the aim of comparing air to water as working fluids. The analysis was conducted on PV/T collectors made by polycrystalline and amorphous silicon PV cells. A better performance was achieved by using water, obtaining an increase of the electrical efficiency of about 3% with respect to the air cooling option.

The use and spread of PV/T systems are also linked to the prediction of their energy and economic performance on a yearly basis. To this aim, simulation tools are nowadays crucial as they are able to provide reliable prediction of the energy performance and economic convenience of modern PV/T collectors, as well as to aid the design process of the system. From this point of view several studies are available in the literature. A well-known mathematical model was developed by Florschuetz [45], who proposed an extension of the Hottel-Whillier-Bliss correlation, commonly used for the flat plate solar collectors, to be applied for air- and water-based PV/T systems. Florschuetz described the steady state efficiency as a function of the average value of the heat removal factor and the heat loss coefficient, proposing several major modifications, such as to use a linear relationship between the cell efficiency and its operating temperature, by taking into account a reduction of optical efficiency caused by the PV operation. This simple approach was extended and integrated with many steady-state simulation models, as reviewed by Das et al. [46]. As an example, the quasi-steady state approach was adopted by Herrando et al. [47], that modelled the performance of an energy system based on novel water-cooled PV/T collectors. The model, developed in EES environment, was used to conduct an economic analysis for assessing the feasibility of the PV/T prototype to balance the energy needs of a single-family house located in three different weather zones. Finally, concerning the calculation of the PV cells operating temperature to be used in the Hottel-Whillier-Bliss approach, several novel equations for the calculation of the effective PV temperature (which in a PV/T system also depends on the operating conditions) were proposed by Tripanagnostopoulos [48]. Recently, a modification of the formula for the temperature of the PV module for a water-based PV/T systems has been proposed by Bigorajski and Chwieduk [49].

It is noteworthy to observe that steady state and quasi-steady state approaches appears today rather unsuitable for accurately assessing the energy performance of PV/T collectors. In fact, the operation of these solar devices is intrinsically dynamic and the above mentioned methods could be lacking to fully assess the effective behaviour of PV/T systems. Therefore, several tools were developed for the dynamic analysis of these solar systems. A dynamic simulation model for assessing the performance of water-based PV/T collectors in response to boundary condition changes was developed by Chow [50]. The tool was based on a suitable resistance-capacitance thermal network composed of seven nodes (one for each system component) and solved with the finite difference method. A similar approach was adopted by Rejeb et al. [51], who presented a transient mathematical model for analysing the thermal behaviour of a water-based PV/T collector. The mathematical model, based on the energy balance of six main components (a transparent cover, a PV module, a plate absorber, a tube, water in the tube and insulation), was validated against experimental results available in the literature. This tool is able to assess the effects of meteorological, design and optical parameters on the performance of the PV/T system. Results showed that for the Tunisian climate conditions the best electrical performance, pay-back period and economic convenience was achieved by unglazed PV/T collectors. Kuo et al. [52] presented a detailed method for the water-based PV/T collector optimization by means of the TRNSYS software. In particular, the PV/T system performance was simulated by varying six critical parameters affecting the system performance: plate material; azimuth; panel angle; a number of tubes; mass flow rate; and volume to surface ratio of the hot water storage tank. The best set of these parameters was used to build the prototype subsequently tested. A remarkable increase of electrical and thermal efficiencies was detected (12.7 and 34.1%, respectively) with respect to the standard PV/T system. A computational fluid dynamics (CFD) approach was considered by Thinsurat et al. [53] for developing a detailed simulation model able to assess both thermal and electrical power generation of PV/T collectors. By this tool, authors analysed the system feasibility for domestic hot water (DHW) production applications. A suitable integration with a thermochemical sorption system for seasonal energy storage was also analysed. Results showed that through the proposed integrated system (featured by 7.76 m^2 of PV/T collectors) it was possible to balance the DHW demand of a single-house in the weather zone of Newcastle.

Over the past 20 years, the issues related to the integration of PV/T collectors in the building envelope has been gradually investigated [54]. The building integration of these devices has opened up to the investigation of different thermodynamic and aesthetic issues of solar building roof/façades [55]. In this framework, the design of a novel building integrated photovoltaic/thermal (BIPV/T) solar collector was presented by Anderson et al. [56]. Here, for a suitable PV/T system, integrated into the roof of a sample building, a simulation model (based on a modified Hottel-Whillier-Bliss approach) for the system performance assessment was developed and experimentally validated, Yang and Athienitis [57] presented a numerical and experimental study for an air-based BIPV/T system. A simulation model was developed in order to analyse the energy performance and optimize the design of a PV/T system based on multiple air inlets, causing in a 5% increase of the thermal efficiency. With the aim of assessing the building passive effects of BIPV/T systems, Athienitis et al. [58] presented an in-house developed dynamic simulation model (based on the thermal network method) for the assessment of both passive and active effects due to the integration of air-based BIPV/T collectors into the vertical façade of a high-rise building. Recently, Tomar et al. [59] developed a detailed analytical model with the aim of estimating the electrical and thermal efficiency of four BIPV/T systems and of understanding their implications on the building energy behaviour. To this purpose, four different PV/T configurations integrated on four prototype test cells were tested and their overall performance was compared for identifying the most suitable PV/T configuration for the climatic condition of the Northern of India.

Innovative applications of this technology concern the coupling of PV/T collectors to other devices in order to improve their energy performance [60]. From this point of view an example was proposed by Zhang et al. [61]. Here, a water-based PV/T solar field was coupled through a suitable heat exchanger to the evaporator of a gas engine driven heat pump for space heating. An increase in the coefficient of performance, from 2.9 to 3.7, was achieved with respect to a heat pump equipped with a traditional evaporator. Finally, it is worth noting that although the PV/T technology is relatively new, its applications (particularly those conceived for the building sector and the mitigation of the associated emissions) have gained significant attention by the research community and stakeholders, as reviewed by Chauhan et al. [40].

2.3. Building energy performance simulation model

Thus, after the introduction of solar and photovoltaics thermal collectors, the idea is to investigate how it is possible to integrate such devices into the building. With the aim of assessing the environmental and energy-related impacts, the adoption of a suitable building energy performance simulation (BEPS) tool is more and more crucial.

The sustainable energy transition of the building sector is driven by the proper implementation of energy efficiency actions. In this regard, the use of BEPS tools is essential for predicting all the possible benefits achievable through innovative solutions and techniques conceived for energy saving purposes [62, 63]. Given the growing concern about the energy efficiency in buildings, several tools have been developed with the aim of assessing the energy performance of single buildings as well as of providing global and city-scale planning and setting guidance for the use of policy-makers and stakeholders [64]. Concerning the individual building analysis, the available tools have been mostly developed and used with the aim to:

- support an energy efficient building design or redesign, construction or refurbishment, and operation [65-67];
- deal with all the most important phenomena occurring in the building [68-70];
- address the effectiveness of applied energy efficiency techniques or renewable energy sources [5, 71] while promoting their implementation for the building energy diagnosis [72, 73].

Building simulation models mostly differ in temporal and spatial resolution and modelling approaches. An overview of theory and assumptions is presented in reference [74]. Here, authors compare the capabilities of the major building energy simulation tools [75], whereas selection criteria, based on energy's user needs, are discussed in reference [76]. Reviews of BEPS tools are proposed by several authors, concerning the analysis of the integration of renewable energy [77, 78], the simulation of district-level energy systems [79, 80], and the performance of low-energy buildings [76, 81].

Although BEPS tools have been in use throughout the building energy community since decades, their adoption has been boosted by the recent advances in computational methods and computer calculation power [82], which provide opportunities for the enhancement of simulation tools and for the development of new ones, especially developed for simulating innovative building energy efficient technologies [83]. In fact, despite of the availability of commercial BEPS codes (often characterized by high level of flexibility and complete user interfaces/data libraries), the development of up to date tools and novel in-house simulation models have become more and more common for research aims and, more in general, for aiding the implementation of new unreleased energy efficiency measures (e.g. [84-88]). In this regard, the use of BEPS codes in the building design process is highly recommended especially for the design of the next generation of buildings requiring different innovative features/materials and energy efficient measures (e.g. phase change materials, thermally activated systems, passive strategies, integrated renewable technologies, etc.). In case of new and/or not commercialized technologies and materials, for which no experimental data are available yet [89], the development of suitable simulation models is often required and recommended. This is particularly true for the design of the next generation of buildings (as NZEBs) to be carried out through suitable computer-based energy analyses [71, 90-92]. New BEPS tools are also developed with the purpose to evaluate the occupants' comfort, and to stimulate models robustness and fidelity also toward the implementation of innovative control strategies [74, 89].

Despite of such progress and effort, building energy simulation is still nowadays a complicated process that requires and involves modelling and analytical skills [93]. The use and development of BEPS tools and the analysis of the obtained results can be considered as a challenge for building designers and practitioners, sometimes undecided about the choice of the BEPS tool to be adopted as well as by the reliability of the related calculation results [89]. In this regard, since these tools are developed to predict the thermal performance of new buildings or to recommend energy retrofit packages for refurbishment, validation procedures (sometimes improperly substituted by calibration ones) are necessary to reduce simulation uncertainties [94, 95]. In fact, the validation of a novel in-house developed BEPS tool is mandatory to ensure unfailing and accurate energy analyses and to prevent untrustworthy results.

To ensure the reliability of a BEPS code, standard validation processes are frequently used [89] to validate new models, examples are reported in references [91, 95-97]. The use of validation procedures has been recently emphasized by the Energy Performance Building Directive (EPBD) issued by the European Union, which also underlines the need of new certified tools for decision-makers and practitioners to be developed with the aim to support integrated building design applications while ensuring the compliance with higher energy efficiency standards.

The available literature includes several general criteria and standard procedures for the validation of novel BEPS tools [98, 99]. These procedures consist of comprehensive and integrated suites of building energy analysis tool tests, involving empirical, analytical, and comparative approaches [100-102]. Here, the differences depend on the method in which the calculated outputs (i.e. by a subroutine, algorithm, software, etc.) are compared to the data considered as reference ones [98, 103]. Specifically, simulation results relative to a building tool or component to be validated can be compared to i) measured data, obtained by a real building, a test cell, or laboratory experiments, in case of the empirical validation, ii) results from accepted numerical methods or standard analytical solutions (i.e. simulation of the heat transfer mechanisms under certain boundary conditions), in case of the analytical verification procedure, iii) results obtained by the current state-of-the-art codes (considered as reference tools and more reliable than the code under exam), in case of the comparative test procedure [101]. More details regarding the advantages and disadvantages of such procedures are reported in [100, 102].

Despite of the progresses in validation methods for building energy simulation tools, the validation process is still time consuming and rather difficult to be accomplished [104]. Although empirical validation procedures, based on real metering and auditing data, are considered as very reliable procedures [105], they are often used for the validation of tools and mathematical models developed for simulating specific phenomena. In this regard, the literature shows several examples of such a procedure applied to the validation of models relative to thermally activated building systems [106-108], daylighting or HVAC interactions with respect to window or solar gain [109, 110], double skin facades or ventilated cavity [111-114], activities of occupants and their interaction with the building loads [115], etc.. It is worth noticing that though experimental validations of single mathematical models for the simulation of the energy performance of a specific new building's technology, component or material, can be often easily carried out, the experimental validation of whole BEPS tools is mostly unfeasible. This is the case of dynamic building simulation tools including innovative and integrated energy and building envelope solutions which would require extensive testing procedures, costly and time consuming [71, 116]. For this reason, very often new and validated subroutines (developed for simulating specific innovative technologies) are added to commercial BEPS tools [89] for conducting whole building energy simulation analyses. Nevertheless, the correct experimental validation of whole BEPS tools integrating novel technologies would require the construction of full-scale buildings, rather expensive and often impracticable. For these reasons, experimental validation procedures through suitable test cells or scale building models are becoming more and more frequent [117]. For novel thermal models few empirical validations works are available in the literature, as reported in references [106, 118, 119]. Here, suitable test cells are often used for analyzing the accuracy of the related results, whereas idealized test cells are built for suitably taking into account the effects of specific building features to be studied [100]. In case of unavailability or unfeasibility of a suitable experimental set-up, the comparative approach (also known as code-to-code validation) is considered. Here, the results obtained by the simulation model under exam are compared to those obtained by different comparative tests cases, necessary to evaluate the reliability of the building simulation model under different operating conditions. From this point of view, the IEA commissioned a number of projects for developing proper validation methodologies for building energy models [100, 120-122]. Among these, the Building Energy Simulation Test (BESTEST) [101, 102, 123] and the ANSI/ASHRAE Standard 140 [124] suites aim of increasing confidence in the use of BEPS tools, by producing standardized test procedures for validating, diagnosing, and improving the current generation of software.

2.4. Building integrated photovoltaic thermal system

Among the above-mentioned devices, the hybrid solution, i.e. PV/T, is a promising technology for the simultaneous generation of electricity and useful heat. As already mentioned in section 2.2, this arrangement, that has attracted an increasing attention since 1970s, aims at increasing the electrical efficiency by extracting waste heat during photovoltaic operation [125]. Depending on the operating fluid, PV/T systems are divided in two types: air-based and liquid-based. Liquid based devices are more efficient than air cooled PV/T ones and their efficiencies are often comparable to those of conventional solar thermal collectors. On the other hand, if compared to liquid models, air based PV/T devices show lower installation and maintenance costs, and reduced risk of leakage and freezing [126]. Innovative systems and products have been assembled and industrialized in the last decades, while theoretical models have been developed, mainly by academics, for the evaluation of their energy performances [127]. A survey about recent advancements and trends in PV/T technologies, research and development is available in [28].

A remarkable research effort has been focused on the Building Integration PV/T (BIPV/T) systems, where solar modules are suitably connected and mounted on or into the building envelope to serve as a material (cover or structure), to produce useful electrical and thermal energy, and to increase aesthetic [128]. These systems may become a standard building component, to be taken into consideration during the design stage of new buildings or in case of building renovations, where the implementation of energy efficient measures and renewable technologies is crucial to reach the current building energy efficiency standards adopted worldwide. Currently, BIPV/T systems are considered as a promising and effective measure to promote net and nearly ZEBs through enhanced on-site solar energy utilization, especially in case of grid-connected systems [4].

In the last few decades, as a function of the BIPV/T fluid used to cool the PV (e.g. air, water, refrigerants) and of the typology of receivers (e.g. flat plate, concentrating), different BIPV/T systems have been developed. Although the research and industrial attention on this technology, few surveys investigating different aspects of the building integration of PV/T have been published. In particular, recent research works focused on techniques capable to make PV/T collectors more viable for the building heating load are analysed in [129]. Here, a particular attention is paid on the examination of theoretical and experimental analyses on BIPV/T systems for heating applications. A review on electrical performance (e.g. energy generation amounts, nominal power, efficiency, etc.) and on simulation and numerical studies relative to BIPV/T systems is reported in [130]. A comprehensive survey about advantages and limitations of air and water based BIPV/T systems, with a special focus on the installation methods, applications, and system performance as well as economic and social aspects, is reported in [131]. Another interesting comprehensive review article of BIPV/T including research and development issues, application, and current status of BIPV/T technologies is presented in [132]. Here, author also discuss the recent experimental and numerical methods developed for studying BIPV/T systems and their impact of BIPV/T on the building performance [132].

In the following section, recent development of BIPV/T system with a focus on the technology of interest for this work, i.e. air based flat-plate open loop active BIPV/T, is discussed with the twofold aim to identify the lack of knowledge and to introduce this study. Interested readers are highly encouraged to refer to the available reviews before presented about PV/T [28, 125, 127, 129, 130] and BIPV/T [131, 132] systems.

The air based BIPV/T technology, despite its poor thermo-physical properties, is generally preferred for building applications due to its cost-effectiveness if compared to the liquid based technology, i.e. lower installation and maintenance costs [131]. In air BIPV/T systems, an air cavity is created between the upper PV modules and the lower insulation layer, mounted on the building roof / façade, replacing expensive materials. Through the air gap, outdoor air flows (naturally ventilated or fan-driven) cooling the PV modules, with a resulting enhancement of the PV electrical efficiency. The heated outlet air may be recovered for multipurpose aims, as space heating among others. The utilization of both electricity and useful heat is obtained through open loop active air PV/T systems, whereas in passive devices the outlet air is exhausted to the environment and only electricity production is achieved [132].

To increase the performance of air based BIPV/T systems, in terms of useful thermal and electrical energy, different improvements, here discussed, have been recently proposed in literature [128]. In particular, to enhance the useful thermal energy production, obtained by boosting the heat transfer, different configurations have been proposed.

A first cost-effective solution to augment the heat transfer in air based PV/T systems is reported in [133]. Such novel configuration consisted on the use of a suspended thin flat metallic sheet or fins, placed at the middle, or at the back wall, of an air duct. An experimental investigation on the performance of an innovative air PV/T device, with a double pass configuration and vertical fins in the lower channel (air flows from the upper channel to the lower one), is presented in [134]. The heat transfer rate and the PV efficiency resulted to be enhanced by the implementation of fins arranged perpendicularly to the direction of the air flow.

The inclination of the air channel has been proved to have a remarkable impact on the air circulation in the cavity gap, where natural or forced convection influences the heat extraction from the PV panels. The characteristics of the air flow in an inclined heated cavity model, under steady conditions, were experimentally assessed in [135]. Here, authors found out that the convection in tilted channels takes benefits of low natural force of buoyancy, being less performing than vertical channels. In this regard, two mathematical relationships for assessing the convective heat transfer coefficients for the top and bottom surface of the PV panels (in an air open loop BIPV/T system) were recently estimated as a function of the tilt angle (from 30 to 45°) of the system [136]. From the analyses of measured data, no significant difference in Nusselt numbers was found out, suggesting that buoyancy effects are almost constant in the investigated roof slopes [136].

Comparative studies about different BIPV/T system configurations have been conducted by several authors. As an example, three open-loop air BIPV/T roof system layouts for heating purposes, consisting of an unglazed roof BIPV/T system, also connected to vertical glazed solar air collectors, and of a glazed roof BIPV/T system, were theoretical and experimental analysed in [137]. Authors found out that through the unglazed BIPV/T system configuration with extra short string of vertical solar air heater showed the best electrical and thermal performance, also for sloped roofs in cold climates [137]. The performance of a roof mounted BIPV/T system with four different configurations consisting of series and parallel combinations are proposed in [138]. In the investigated cold climates, the combination of all rows connected in series, with constant air mass flow rate, resulted to be the best configuration among the proposed (reaching an overall thermal efficiency of more than 50%), with a sensible reduction of the heating peak demand [138]. A comparative analysis of roof mounted air BIPV/T system, based on an opaque solar cell tile array and on a semi-transparent PV/T array, was conducted with the aim to calculate the indoor air temperature [139]. Simulation results showed that a higher extraction of heat from PV cells (i.e. the outlet air temperature was about 24% higher) is obtained in case of semi-transparent PV/T collectors (mostly due to their lower packing factor), with a consequent lower internal room temperature compared to the opaque tile array roof system. Another comparative study carried out to assess how an air BIPV/T system influences the building energy profile and load is reported in [140]. Here, three different BIPV and BIPV/T applications, consisting of a wall BIPV with no ventilation, an air gap BIPV/T system, and an air gap BIPV/T with indoor air flow operation, were compared. The last configuration, due to the outdoor air circulated to the indoor, resulted to be the more effective in reducing the heating load (about 27% lower), and capable to prevent the decreasing of the PV efficiency [140]. A case study on a double pass semi-transparent PV/T system integrated in the building façade for space heating purposes was presented in [141]. The proposed configuration resulted to be more efficient than conventional opaque PV double pass systems, resulting in higher thermal and electrical productions. Its energy performance was evaluated through a numerical model suitably developed by the authors, predicting an increase of the indoor air temperature by 5-6 °C in winter days.

The influence of the channel depth, length, air distribution duct diameter, and air mass flow rate per unit collector area on the whole system performance has been investigated by different authors, as discussed in [129]. For instance, an PV/T air collector linked to the air distribution system of a residential building and the air mass flow rate was tested by varying the required temperature increase [142]. The smaller collector depth resulted to be more efficient in terms of good performance for large temperature difference. On the other hand, in such study it was also noted that the design is also very sensitive to the ratio of mass flow rate and collector area. An interesting concept of modular PV/T system is presented in [143]. Here, PV/T modules were integrated onto the vertical exterior wallboards, assembled to replace roof systems removing its drawbacks (e.g. reduce system cost, overcome roof leak due to snow, etc.). In particular, a two months test was carried out on a modular wallboard integrating PV/T panels, tilted at 80°; such layout was also compared to other configurations obtained by varying the PV protective material. Authors found out, according to the literature, that a glass cover produces the enhancement of the thermal efficiency from 22 to 29%, whereas the electrical efficiency (about 11-12%) was not affected by the typology of protective material [143]. Marginal differences on the PV efficiency of a novel configuration of multi-functional roof-integrated PV/T system were obtained by analysing the air gap ventilation mode [144]. In particular, no significant differences were detected between the electrical yields of the two operating modes [144]. A study on the energy performance assessment of a photovoltaic solar wall, with different operating conditions for the ventilated PV façade, is presented in [145].

Recently, the strategic placement of PV/T modules has been proven to be crucial to enhance the heat extraction from PV modules. To this aim, the use of modular solar walls with broken lines (i.e. openings) among PV/T modules is a feasible and interesting solution for helping to prevent excessive heat, as demonstrated for example by the SolarWall® technology (Conserval Engineering Inc.). Such concept, known as multiple inlet approach, aims to enhance the performance of air based BIPV/T collectors, and has gained much attention in the last years [146]. In particular, the optimization of a single inlet prototype of an open loop air based BIPV/T system is proposed in [57]. Here, the design of the BIPV/T system was improved with the multiple inlets concept, and other means of heat transfer enhancement, studied through simulations. Simulation results showed that the use of two inlets may still lead to marginal electrical efficiency rise, increasing the thermal efficiency by about 5%. Moreover, the addition of a solar air heater system with a smooth air channel enhanced the thermal efficiency up to 8%, reaching 10% with a wire mesh packed air cavity. The decrease of the peak PV temperature (of about 1.5 °C) was also observed (though the marginal increase in PV efficiency), whereas a temperature decrease from 5 to 10 °C is expected in case of larger installations (5-6 meter) [57]. The developed and experimented model related to four inlets was also applied to a BIPV/T roof of an existing solar house, showing an increase of thermal efficiency of about 7% [57]. Different configurations of such BIPV/T system were investigated in case of opaque and semi-transparent mono-crystalline silicon PV panels [147]. Here, experimental results demonstrated that the semi-transparent configuration with two inlets enhances the thermal efficiency by 7.6% if compared to the opaque system. Authors also found out that no significant costs are added in case of the two-inlet BIPV/T design. These air based glazed BIPV/T systems with multiple inlets, obtained through a modular plug and play solution for building façade and roof applications, were also compared to non-building integrated unglazed thermal collectors (as reported in [146]), showing very similar thermal efficiency [148]. The results of a numerical investigation carried out to compare the performance of single and multiple-inlet BIPV/T systems is presented in [149]. Here, electrical and thermal performance, and PV temperature distributions were compared by taking into account a cold winter and a hot summer day, as well as different wind conditions. Such study includes a detailed flow distribution model, developed by using pressure drop and flow correlations, wind tunnel pressure measurements, and a modified energy balance model for the multiple inlet system. The authors found out that, through a multiple inlet BIPV/T system, the increase of the electrical efficiency is still marginal (about 1%), whereas the thermal efficiency increases by about 24%. Finally, a multiple inlet configuration was also taken into account during the experimental investigation of the influence of the underneath cavity on buoyant-forced cooling of a BIPV/T located on inclined roofs [150]. The building prototype consists of an insulated polystyrene chain structure, experimented in a solar simulator positioned in an atmospheric wind tunnel to naturally ventilate the cavity. The observed PV temperatures resulted to be significantly lower in the configuration with three openings, compared to the single one. As reported by the authors, experimental tests were also done to be later used for the development of tools capable to predict the PV degradation probability as a function of the climate, in order to quickly obtain aging test conditions and enhance the durability of the PV modules [150].

By means of simulation models, specific phenomena of PV/T collectors, regardless of the working fluid and configuration, are commonly simulated by assuming as one-dimensional the heat transfer and by taking into account thermal network models discretized through the finite difference scheme [132], whereas other methods include the modified Hottel-Whiller approach and the use of computational fluid dynamics [130]. The thermal network approach, especially in case of air type PV/T, has been recently adopted by several authors, focusing on the assessment of the system performance (e.g. [137, 151]) and on the flow and heat transfer [152, 153], calculated under variable working and design conditions. The overall energy performance of BIPV/T systems, focusing on the whole building-plant, is generally carried out by using commercial software, e.g. TRNSYS, EnergyPlus and ESP-r [154]. The use of whole building simulation analyses is also used for the assessment of the economic feasibility of the BIPV/T system, examples are recently reported in [155, 156]. By means of such tools, to the best knowledge of the authors, several studies concerning the analysis of the air based BIPV/T system integrated with other energy systems (such as heat pumps, heat storage, heat recovery ventilator and absorption and adsorption chillers) are available in literature (e.g.[157, 158]). Nevertheless, although the incredible research effort on the analysis of BIPV/T systems, the available literature still found that the behaviour of the coupled system needs to be further investigated, being crucial for the promotion of this technology [154]. An example of a novel analysis developed for a non-cold climate is reported in [158]. Here, a typical air open loop façade BIPV/T system for the Mediterranean climate (i.e. Greece) and its energy saving potentials were investigated by means of TRNSYS [158], showing that diverse BIPV/T (e.g. aspect ratio, flow rate, etc.) design versions must be adapted to different climatic conditions and building orientations.

Although the BIPV/T technology has been largely investigated, there is still a lack of analysis concerning the impact of the building integration on both the active and passive effects, and, therefore, on the building energy performance [4, 132]. As reported in the above mentioned surveys, further BIPV/T system research is necessary to provide methods for carrying out comprehensive building performance analyses, with the aim to increase the attractiveness of such system [132]. In fact, in most of the numerical investigations available in literature, many important aspects linked to the integration of PV/T devices into or onto building envelope (e.g. variation of the visible and light transmittance, thermal transmittance, impact of the solar radiation on the building energy needs, etc.) are neglected. Therefore, researchers are encouraged to focus on the analysis of passive effects due to the building integration of PV/T devices on the overall building performance [154]. To this aim, the use of suitable numerical and predictive models is also crucial [159].

To assess the BIPV/T system active and passive behaviours, with the aim to optimize the system design and operation, the development of simulation tools is recommended [4, 154]. Suitable numerical models are more and more developed aiming at modelling and simulating the energy performance of novel system configurations or system operation strategies, which cannot be analysed through commercial software; by such tools the analysis of the effects due to some critical design and operation parameters on the BIPV/T system performance may not be always possible. Therefore, especially in case of novel system configurations and/or specific flow and heat transfer conditions, novel in-house mathematical models have been recently developed [57, 149, 160]. In such studies, authors suitably developed simulation models based on the energy balance approach and on the thermal network analogy, committing a particular attention to the simulation of a specific phenomenon or aspect, e.g. flow distributions, multiple inlet PV/T performance, heat transfer coefficient between air the wire mesh. As highlighted by the available literature, in many in-house developed models, the main focus is on a specific characteristic of the BIPV/T system, whereas the building thermal modelling is simplified, and its thermal behaviour is often neglected. Moreover, many commercial simulation tools for BIPV/T analysis are based on static calculation methods and on the decoupled modelling approach. Here, the back temperature of collector calculated is calculated by neglecting the wall/roof thermal capacity and it is imposed as a boundary condition of the building envelope integrating the PV/T. These widely accepted simplifications are not suitable for low or null insulation between the PV and the wall/roof and for heavyweight building envelopes (typical of hot climates and thermal cooling applications), where the thermal modelling of the building becomes curial for its energy requirements calculation, as also pointed out in [160].

None of the study available in literature focus on the investigation of the performance of a façade BIPV/T system for high rise buildings, obtained by taking into consideration both passive and active effects on the building overall energy consumptions. Such concept is suitable for this kind of buildings in which a large amount of surface is available. In particular, this thesis presents a new in-house developed simulation model for the dynamic analysis of air based open-loop BIPV/T systems, with a particular emphasis on the building thermal behaviour. By means of the code, the performance of an air BIPV/T system for high rise building façade, to be considered in case of retrofits or new designs, is investigated.

2.5. Building to vehicle to building

The concept of net or Nearly Zero Energy Buildings (ZEB) has brought to the forefront by the EPBD (Energy Performance of Buildings Directive) [161], considered as a promising approach to minimize the building sector energy consumptions (about 30–40% of the world primary energy consumptions in regions belonging to the Organisation for Economic Co-operation and Development (OECD) [162]) and carbon dioxide emissions, while increasing the penetration of technologies based on Renewable Energy Sources (RES) in buildings [4]. A net or nearly zero energy building is a high energy performance building [163] that requires a very low amount of energy, obtained through the efficient design [5, 164-166], to be covered to a very significant extent, or even completely, through RES [167].

The common basic design rule of ZEBs is to address demand first, and then supply [168]. Despite of the available energy carriers (electricity, natural gas, hot/cold fluids by thermal networks for district heating/cooling, biomass and other fuels), a key-feature of a ZEB is the ability to locally produce on-site energy vectors. In fact, a ZEB should be designed to match its own load by on-site generation (exploiting local RES on-site) and exporting or importing energy with utility grids, working in synergy with them. In this regard, the two-way grid concept is crucial to increase the share of electrical renewable energy within the grids [169].

In this regard, a wide dissemination of distributed generation may compromise power stability and quality in grid structures, mainly at local distribution grid level [169]. Nowadays, developing novel methodologies to minimize the energy consumption of a building, while suitably integrating RES into the power grid (main electricity source) seems to be a crucial issue which will greatly contribute to a more sustainable community [170]. For this reason, shifting the building energy sources away from the electricity grid toward on-site RES is a key concept for a sustainable building sector and ZEBs. In this regard, among available RES (solar panels, wind turbines, etc.), the use of solar based technologies, e.g. solar photovoltaics (PV), to supply the energy demand of buildings is crucial, as investigated by many authors [171, 172].

In the available literature, the ZEB target is mostly considered at the building scale, so the effort toward its definition [163], the development of standards and calculation methods [71, 173], together with the development of tools for the early design of ZEB [174] and of relevant case studies [175] are basically focused on single buildings considered as independent energy users. On the contrary, by expanding the energy framework toward a larger scale, it becomes crucial to consider the location of the buildings and their operation with respect to human activities as highly impacting on the energy efficiency of buildings and mobility energy consumptions. Similarly to ZEB, the mobility energy consumption, although widely investigated in literature, is mostly considered as a single energy entity [176, 177]. Very few papers, available in literature, focused on the analysis of ZEB in a urban / district concept. An example is reported in references [178] and [179], where authors analyze the potentialities of an integrated approach, by linking transportation and building energy consumptions, developing a tool for assessing the consumption in residential buildings and for daily mobility.

The transport sector is the most dependent on oil (about 95 %) in which road vehicles account for about 35% of the global energy use for transport [2]. The daily mobility represents a significant contributor to the total final energy demand at a city and neighbourhood level [178]. Such demand is being driven by the spatial distribution of human activities [180], especially by the home-to-work commuting, thus, it is often linked to the building consumption for spatial planning policies [181].

One of the promising solution to reduce the dependence on fossil fuel by the transportation sector, decreasing the greenhouse gas emission, is the shift toward the electrification of automobile powertrains [182]. This will reduce the local emissions resulting in an improvement in air quality and higher energy efficiency compared to internal combustion engine vehicles [183]. Nevertheless, a potential issue linked to the massive adoption of Electric Vehicles (EVs) is the simultaneous charge due to a high number of vehicles, which can lead to a considerable increase of the peak load of the electricity demand [184]. This issue highlights the need of suitable energy policies to improve grid stability [185].

Nowadays, the car industry is allocating remarkable investments in the development of EVs, and their energy demands will be increasingly covered by distributed energy resources (DER) located in our cities [186]. A review on EV technologies, their connectivity and impacts on grid as well as standards required for their efficient and profitable operation with DER is presented in reference [187]. EVs can be considered as fundamental parts of a smart grid, being capable of providing valuable services to power systems (by acting as energy sources), other than just consuming power (by acting as energy sinks). In this regard, several papers available in literature analyse different aspects of the integration of EVs in the power grid, focusing on services, optimization and control aspects [188], computational scheduling methods for the intelligent integration with power systems [189], issues related to driving patterns and charging behaviour [190], as well as forecasting methods [191] to promote the smart managing of the EV charging operation [192] and its use as mobile storage units via Vehicle-to-Grid (V2G) technologies [193]. It is worth noting that the implementation of smart charging strategies for EVs batteries can minimise the cost linked to the upgrade of grid capacity while enhancing the operation of grid systems, by providing a large responsive storage system constituted by EVs batteries [194].

As distributed electrical storage systems, EVs play a crucial role in the management of the energy fluxes in buildings. In fact, by means of intelligent bidirectional chargers, an EV may be powered by renewable energy sources installed on-site and may be a viable energy source to supply the power demand of a building [195], in addition to RES. EVs may potentially become one of the main energy contributors of buildings to the achievement of the NZEB goal at a large scale [178, 196]. This concept, known as Vehicle-To-Home (bidirectional V2H technology), allows one to achieve the integration of EVs with RES (e.g. PV, wind turbines), toward a more efficient and sustainable energy paradigm [197]. A V2H system allows the EV battery to store eventual excess of energy generation from renewables, to be subsequently used when the main source of power generation system is not capable to meet the building energy demand. This leads to a number of advantages, namely: matching supply and demand, minimizing the infrastructure of power transmission and improving the power grid stability [197]. The basic idea behind the V2H technology is the possibility to use electric vehicles as storages, exchanging power to and from the grid when parked and plugged in. The major challenge and potential of V2H systems are grid losses and balance of the intermittence of the generation and the load [198].

V2H technology has been studied from different points of view, such as: i) development of simulation models [199], ii) challenges and prospects to use vehicles to home and vehicles to grid systems [197], iii) case study analysis on the grid interaction [200]; iv) economic [201] and environmental aspects; v) optimization analysis of V2H system for NZEBs [195]. Nevertheless, few studies on V2H system available in literature focus on the energy management at a building level [202-204]. Many authors focused their study on a specific aspect of EV technology and its coupling with buildings, such as the EV battery performance with different charging/discharging strategies [184, 205, 206], driver behaviour [207, 208] and models for the evaluation of energy and economic impact [207, 209, 210]. The design of an energy management system to enhance the integration of EVs into building is presented in reference [209]. Here, authors formulated an objective function for minimizing the total power demanded by the system and the total power injected back to the grid, by modelling the scheduling of the EV with a stochastic method (to simulate trips, charging and discharging phases) [209]. An operation decision model for electric vehicle to building integration is presented in [207]. Here, authors carried out a simplified analysis based on hourly electric and thermal energy demands data of a medium office building interconnected with an EV charging station.

Simulations, carried out for a sample summer day, aimed to minimize the operation costs of both building and charging station (economic saving of about 23%) [207]. The same model is used to evaluate the impacts of driver behaviours and building categories on the economic performance of electric vehicles integrated in buildings [207]. An optimal control model is developed in reference [210] with the aim to study the economic feasibility and the benefits of the grid interaction of smart charging and the control of space heating loads of several residential buildings (each one connected to a single EV), with on-site photovoltaics.

Only few papers analyse the energy demand of vehicles as building-related energy use, including the EV in the energy buildings' energy balance. Specifically, the first study investigates the role of electric vehicles and solar energy sources as potential featured in a net zero energy building (NZEB), by means of dynamic simulations [195]. Results show that the V2H system is capable to reduce the electricity required from the grid by up to 68% [195]. A second study, based on the development of a mixed-integer linear optimization model, addresses the energy management problem of housing and personal mobility with EV [196]. Here, the optimization model is applied to a novel house concept integrating photovoltaic panels and district heating/ground source heat pump. Simulations results demonstrate that the V2H technology is capable to enhance the annual imported/exported energy, as well as energy matching indexes [196]. Finally, the investigation of strategies aimed at limiting the impact of both heat pumps and EVs on the electrical demand of future dwellings integrating PV is presented in [211].

The analysis of the literature highlights a great research effort toward the study of the EV operation within the grid, whereas only few studies focus on the V2H concept, such as on the EVs integration within the energy balance of the building integrating RES. Since the share of electric, and autonomous, vehicles is expected to increase in the near future along with the level of automatization of buildings [211], the need of intelligent energy management schemes to control the energy exchange between all the key users (i.e. EVs, buildings, RES), will be crucial. Consequently, an accurate prediction of building electric loads, EV consumption and PV generation is necessary, together with the possibility to optimize the size of electrical storages, aiming at improve the economic feasibility of the whole system [196]. Such research gaps, highlighted by the literature, must be also applied to a larger building scale, as EVs represents the next step of distributed energy systems. In this regard, the ZEB concept applied to a neighbourhood or to a city refers to scenarios where transportation, buildings and electric grid, powered by RES are analysed with an integrated approach [212].

2.6. Conclusions

In this chapter, a deep scientific literature review of the five topics, on which this thesis is based, is introduced. Here, the main researches and the main subjects treated in recent scientific literature are highlighted. By considering the analysed papers, the methodology adopted in this thesis was suitably developed and it can be summarized in the flow chart reported in Fig. 2.1:

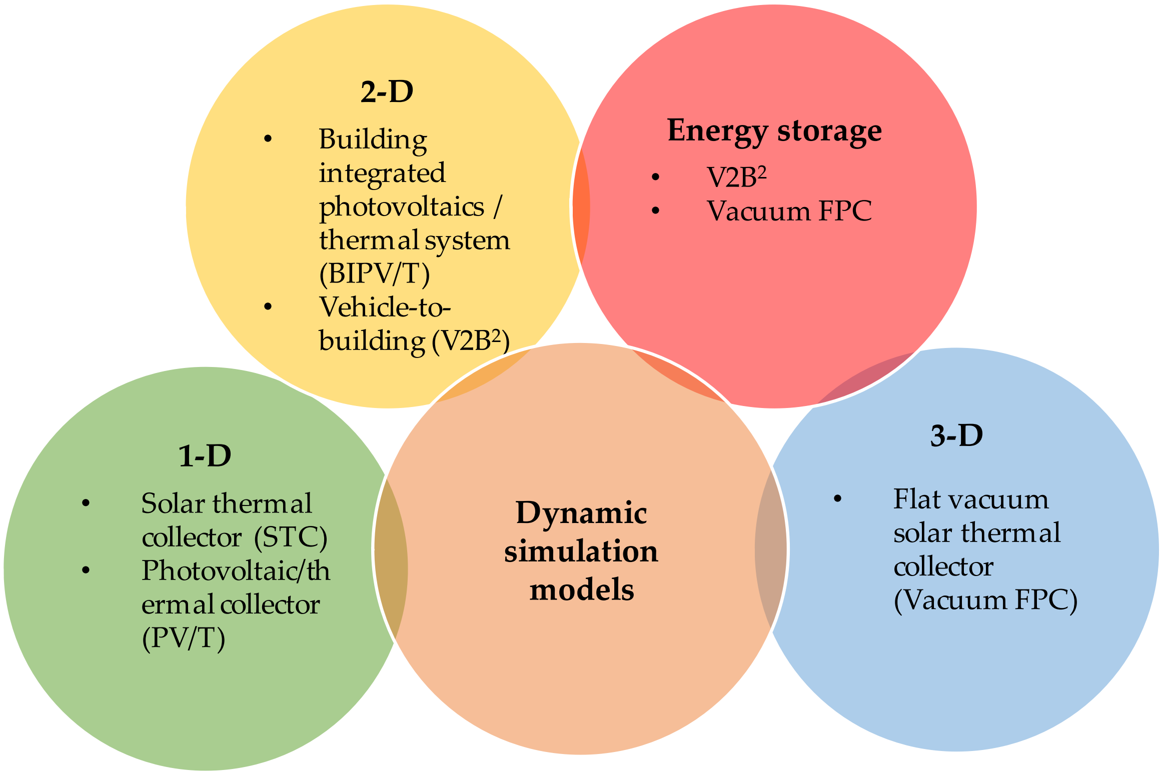

Fig. 2.1. Methodology adopted.

In this chapter, a deep scientific literature review of the five topics, on which this thesis is based, is introduced. In this chapter, the main researches and the main subjects treated in recent scientific literature are highlighted. At the end of this analysis, significant lacks of knowledge were detected and they can be summarised as follow:

- there are no available studies involving the simultaneous optimization of the main parameters affecting the performance of flat plate solar thermal collector systems;
- there are no flat plate vacuum solar thermal collector systems able to store thermal energy without the adoption of suitable hot water storage tank;
- there are no studies focusing on the design of low-cost PV/T prototype suitable coincided for be integrated into the building envelope;

- there are no criteria and guidelines involving the coupling of photovoltaic/thermal collector with air-to-air heat pump;
- a lack of knowledge regarding the assessment of both active and passive effects provided by building integration photovoltaics thermal system in high-rise building is detected;
- very few studies on V2H system available in literature focus on the energy management at a building level.

CHAPTER

3

3. Solar thermal collectors

As it can be derived from the literature review reported in chapter 2, the performance of a solar thermal collector is affected by several parameters. With the aim of optimizing such technologies, the adoption of parametric analysis is not enough. Therefore, with a simple parametric analysis it is not possible to carry out a comprehensive analysis and discover the correlations among the parameters characterizing the performance of the collector. For such a reason, a sensitivity analysis is needed. The sensitivity analysis can be adopted for determining the effect of the parameters on results [213]. With this kind of investigation, it is possible to obtain a rank of the most influencing parameters and decide which of the selected parameters need to be improved. A structural analysis is also considered for the design of both glass cover and absorber plate thicknesses. In addition, two novel evacuated flat-plate solar thermal collector prototype are introduced. The first solar thermal collector is characterized by a very low initial cost whereas the second one (called Tank_v.2) is characterized by high-vacuum space (i.e. 10^{-8} mbar) for dwelling hot water storage purposes.

3.1. Aim of the work and content of the chapter

The literature review shows that despite a wide number of papers focusing on the investigation of different parameters characterizing FPCs, there are no available works involving on the simultaneously optimization of the main parameters affecting the performance of FPC systems. In this chapter, a mathematical model written in MatLab environment is developed with the aim to assess the energy performance of FPC systems. The code adopts a quasi-steady approach and it is based on Hottel-Whillier-Bliss equations adjusted for assessing the features of the FPC collector technology. Then, in order to optimize a typical FPC, a sensitivity analysis on the main effective parameters is also presented. This analysis is based on the developed code that is implemented in a suitable tool available in MatLab Simulink. Such sensitivity analysis is conducted with the twofold aim to identify the main parameters and to find out which of them have the greatest influence on two considered objective functions (i.e. maximize the working fluid outlet temperature, maximize the thermal efficiency). Finally, a comparison between the optimized FPCs against a typical one is also presented in order to show the potential of the proposed method.

3.2. Method and model description

In this section, the considered method is described in detail. Firstly, the investigated solar thermal collector with the main features is described, and secondly the developed mathematical model for assessing the performance of the investigated FPC is presented. Finally, at the last part of this section, a sensitivity analysis is presented, which is carried out based on the described code, in order to identify the most effective parameters for the performance of the investigated FPC.

3.2.1. Solar thermal collector description

For this work, a typical FPC available on the market is investigated. A schematic representation of the collector can be seen in the sketch depicted in Fig. 3.1.

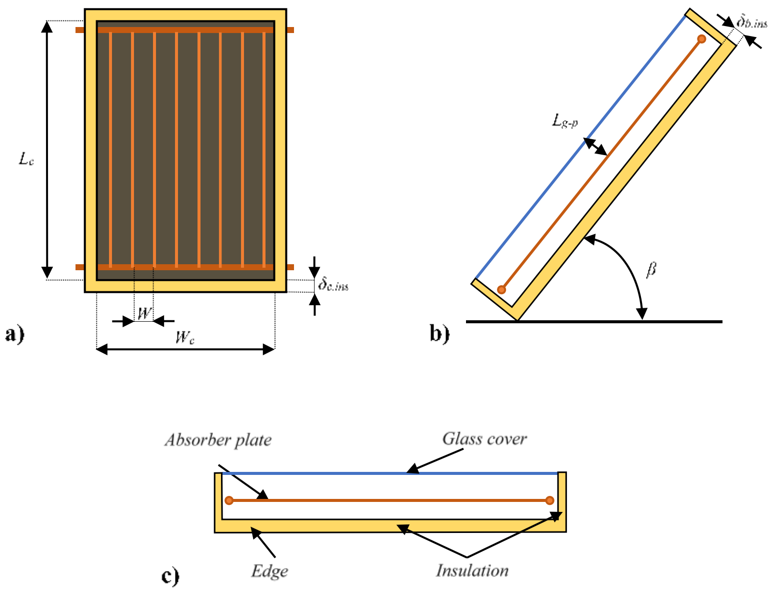

Fig. 3.1. Solar thermal collector details: a) top view b) side view c) cross-section view.

The device consists of a glass cover, a copper absorber plate, a set of copper riser pipes, a glass wool insulation layer, and steel sheet edge cover (Fig. 3.1a). The glass cover has a length (L_c) of 2.0 m, a width (W_c) of 1.1 m, a thickness (δ_g) of 8.0 mm, and a gross area (A_c) of 2.2 m^2. The copper absorber plate has the same dimension of the glass cover except from the thickness (δ_p) that is 0.5 mm. A number of (N_{pipes}) 8 copper riser pipes, with an inner diameter (D_i) of 13.4 mm, an outer diameter (D) of 15 mm and a thickness (δ_{pipes}) of 0.8 mm, are welded on the absorber plate. An air gap spacing ($L_{g\text{-p}}$) of 50 mm is made between the glass cover and the absorber plate, as it is clearly visible in Fig. 3.1b. A glass wool insulation layer with a thickness ($\delta_{e,ins}$) of 30 mm wrapped the edges whereas the same material with a different thickness ($\delta_{b,ins}$), of 50 mm, is adopted to insulate the bottom of the collector as well. A sheet metal (δ_b) of 0.5 mm is composing the edge cover. The main geometrical and thermophysical features of the system are reported in Table 3.1.

Table 3.1. Features of typical flat-plate solar thermal collector.

Symbol	Value	Unit	Design parameter
L_c	2.0	m	Length of the glass cover
W_c	1.1	m	Width of the glass cover
δ_g	8.0	mm	Thickness of the glass cover
A_c	2.2	m^2	Gross area of solar thermal collector
κ	16	-	Glass extinction coefficient
ε_g	0.84	-	Emissivity of the glass cover
α_g	0.062	-	Absorbance of the glass cover
τ_g	0.859	-	Transmittance of the glass cover
k_g	0.80	W/(m·K)	Thermal conductivity of the glass cover
L_p	2.0	m	Length of the absorber plate
W_p	1.1	m	Width of the absorber plate
A_p	2.2	m^2	Area of the absorber plate
δ_p	0.5	mm	Thickness of the absorber plate
ε_p	0.84	-	Emissivity of the absorber plate
α_p	0.90	-	Absorbance of the absorber plate
k_p	385	W/(m·K)	Thermal conductivity of the absorber plate
N_{pipes}	8	-	Number of riser pipes
Di	13.4	mm	Inner diameter of riser pipes
D	15.0	mm	Outer diameter of riser pipes
δ_{pipes}	0.8	mm	Thickness of riser pipes
k_{pipes}	385	W/(m·K)	Thermal conductivity of the absorber plate
$L_{g\text{-p}}$	50	mm	Air gap spacing between the glass cover and absorber plate
$\delta_{e,ins}$	30	mm	Thickness of the insulation wrapped the edge
$\delta_{b,ins}$	50	mm	Thickness of the insulation wrapped the bottom
k_{ins}	0.035	W/(m·K)	Thermal conductivity of the insulation
δ_b	0.5	mm	Thickness of the bottom
k_b	180	W/(m·K)	Thermal conductivity of the bottom

3.2.2. Mathematical model

The mathematical code developed to investigate the performance of the FPC is based on Hottel-Whillier-Bliss equations [214], suitable adjusted for assessing the features of the FPC collector technology. With the aim of physically modelling the FPC, a few simplifying assumptions were considered as follows:

1. The collector is in a steady state.
2. The collector is of the header and riser type fixed on a sheet with parallel tubes.
3. The headers cover only a small area of the collector and can be neglected.
4. Heaters provide uniform flow to the riser tubes.
5. Flow through the back insulation is one dimensional.
6. The sky is considered as a blackbody for the long-wavelength radiation at an equivalent sky temperature.
7. Temperature gradients around tubes are neglected.
8. Properties of materials are independent of temperature.
9. No solar energy is absorbed by the cover.
10. Heat flow through the cover is one dimensional.
11. Temperature drop through the cover is negligible.
12. Cover is opaque to infrared radiation.
13. Same ambient temperature exists at the front and back of the collector.
14. Dust effects on the cover are negligible.
15. There is no shading of the absorber plate.
16. Emissivity of the glass cover is considered the same for both the front and back surface.

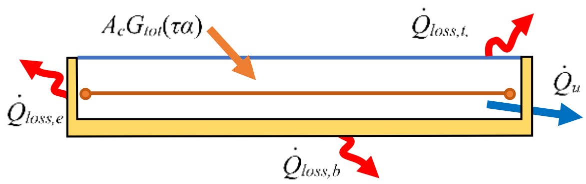

Fig. 3.2. Energy fluxes.

The code is able to calculate the energy fluxes, the thermal efficiency, the temperature of each component (i.e. glass cover, absorber plate, insulation and edge), and the working fluid outlet temperature within the riser pipes. For sake of clarity, a sketch of the investigated FPC with the thermal powers exchanged with the environment are depicted in Fig. 3.2.

The useful energy (Q_u) supplied to the working fluid flowing along the riser pipes is calculated as follow:

$$Q_u = A_c F_r \left[G_{tot} (\tau\alpha) - U_L \left(T_{wf,in} - T_{amb} \right) \right] \tag{3.1}$$

where A_c is the collector area, F_r is the heat removal factor, G_{tot} is the incident solar radiation per collector area, ($\tau\alpha$) is the transmittance-absorptance product, U_L is the overall heat loss coefficient based on the collector area, $T_{wf,in}$ is the inlet working fluid temperature, and T_{amb} is the ambient temperature.

The calculation of thermal efficiency (η_{th}) is based on the ratio between the useful energy collected and the incident energy on the solar collector surface.

$$\eta_{th} = \frac{Q_u}{G_{tot} A_c} = F_r \left[\left(\tau_g \alpha_p \right) - \frac{U_L \left(T_{wf,in} - T_{amb} \right)}{G_{tot}} \right] \tag{3.2}$$

where τ_g is the transmittance of the glass cover and, α_p is the absorbance of the absorber plate. Note that, the transmittance of the glass cover is calculated by means of the following equations:

$$\tau_g = \frac{\tau_\alpha}{2} \left[\frac{(1 - r_\perp)}{1 - (r_\perp r_\alpha)} + \frac{(1 - r_\parallel)}{1 - (r_\parallel r_\alpha)} \right] \tag{3.3}$$

where τ_α = exp[-$\kappa\delta_g/(\theta_2)$], κ is the extinction coefficient of the glass cover, θ_2 the angle refracted beam, $r_\perp$ and $r_{//}$ are the perpendicular and parallel components of the incident solar radiation, derived by Fresnel's equations [1].

In order to calculate the useful heat and the thermal efficiency, the heat removal factor (F_r) is calculated as following:

$$F_r = \frac{\dot{m} c_p}{A_c U_L} = \left[1 - \exp\left(- \frac{U_L F' A_c}{\dot{m} c_p} \right) \right] \tag{3.4}$$

where $\dot{m}$ is the mass flow rate of the working fluid flowing along the riser pipes, c_p is the specific heat of the working fluid, and F' is the collector efficiency factor.

The fin efficiency factor is a characteristic parameter of a solar thermal collector and it is function of the geometry of the collector, the thermophysical properties of the material composing the collector (e.g. thermal conductance of the welded bond) and the working fluid. It is calculated by eq.(3.5) as following:

$$F' = \frac{1/U_L}{W\left[\left(U_L \left(D + (W - D) F \right) \right)^{-1} + (C_b)^{-1} + \left(\pi D_i h_{wf} \right)^{-1} \right]} \tag{3.5}$$

where W is the distance between the riser pipes, D is the outer diameter of the riser pipes, F is the collector efficiency factor, C_b is the bond conductance, D_i is the inner diameter of the riser pipes, and h_{wf} is the convective heat transfer coefficient between the working fluid and the riser pipes.

The bound conductance is evaluated as follow:

$$C_b = \frac{k_{bond} W_{bond}}{\delta_{bond}} \tag{3.6}$$

where k_{bond} is thermal conductivity of the welded bond, W_{bond} is the width of the welded bond, and δ_{bond} is the thickness of the welded bond.

In addition, by referring to eq.(3.5) the collector efficiency factor can be calculated as following

$$F = \frac{\tanh\left(m \cdot (W - D)/2\right)}{m \cdot (W - D)/2} \tag{3.7}$$

where k_p is the thermal conductivity of the absorber plate and, δ_p is the thickness of the absorber plate. Note that, the fin efficiency is a constant parameter for a given collector.

Heat losses

As depicted in Fig. 3.1, the heat losses through the FPC are essentially three:

- $Q_{loss,t}$ heat loss through the glass cover.
- $Q_{loss,e}$ heat loss through the edge.
- $Q_{loss,b}$ heat loss through the bottom.

The model calculates these thermal losses, by means of the following equation:

$$Q_{loss} = A_c U_L \left(T_p - T_{amb}\right) \tag{3.8}$$

where U_L is the overall heat loss coefficient based on collector area and, T_p is the temperature of the absorber plate. The overall heat loss coefficient can be expressed as:

$$U_L = U_t + U_b + U_e \tag{3.9}$$

where U_t is the heat loss coefficient of the top surface of the collector, U_b is the heat loss coefficient of the bottom surface of the collector and, U_e is the heat loss coefficient of edge surface.

In order to assess the above-defined heat loss coefficients, the developed model considers different calculation procedure based on the thermal network depicted in Fig. 3.3.

The heat loss coefficient of the top surface of the collector, is calculated as following:

$$U_L = U_t + U_b + U_e \tag{3.10}$$

where $h_{c,amb-g}$ is the convective heat transfer coefficient between the ambient and the glass cover, $h_{r,sky-g}$ is the linearized radiative heat transfer coefficient between the sky and the glass cover, $h_{c,g-p}$ is the convective heat transfer coefficient between the glass cover and the absorber plate and, $h_{r,g-p}$ is the linearized radiative heat transfer coefficient between the glass cover and the absorber plate.

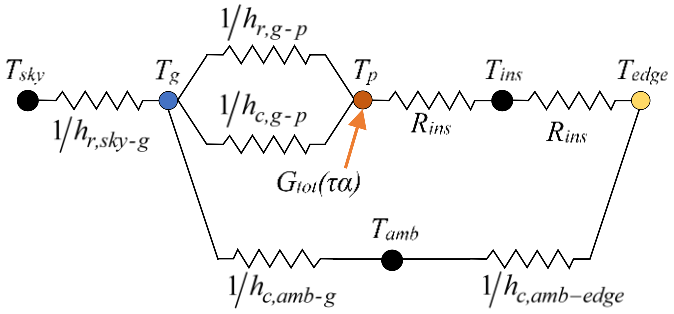

Fig. 3.3. Thermal network.

As mentioned before, the radiative heat transfer coefficients ($h_{r,sky\text{-}g}$ and $h_{r,g\text{-}p}$) are linearized and can be calculated by means of eqs.(3.11)-(3.12):

$$h_{r,sky-g} = \varepsilon_g \sigma \left(T_{sky} + T_g\right)\left(T_{sky}^2 + T_g^2\right) \tag{3.11}$$

$$h_{r,g-p} = \frac{\sigma\left(T_g + T_p\right)\left(T_g^2 + T_p^2\right)}{1/\varepsilon_g + 1/\varepsilon_p - 1} \tag{3.12}$$

where ε_g is the emissivity of the glass cover, σ is the Stefan-Boltzmann constant, T_{sky} is temperature of the sky, T_g is the temperature of the glass cover and, ε_p is the emissivity of the absorber plate. Note that, in the developed model the emissivity of the glass cover is considered the same for both the faces. Note also that, the sky temperature is considered equal to $0.0552 \cdot T_{amb}^{1.5}$ for clear sky condition [215] or equal to T_{amb} for cloudy sky [216].

Regarding the convective heat transfer coefficient between the glass cover and the ambient, the Mitchell's correlation [217] is taken into account:

$$h_{c,g-amb} \frac{8.6 \cdot w_{wind}^{0.6}}{L_c^{0.4}} \tag{3.13}$$

where w_{wind} is the wind speed and, L_c is the length of the collector.

The natural convection between the glass cover and the absorber plate is assessed as following:

$$h_{c,p-g} = \frac{Nu \cdot k_{gas}}{L_{g-p}} \tag{3.14}$$

where k_{gas} is the conductance of the air inside the air-gap spacing considered at a medium temperature between the glass cover and the absorber plate, $L_{g\text{-}p}$ is the distance between absorber plate and the glass cover and Nu is the Nusselt's number calculated by means of Holland's equation [218], as follows:

$$Nu = 1 + 1.44\left[1 - \frac{1708}{Ra \cdot \cos(\beta)}\right]^{+}\left[1 - \frac{1708\left[\sin(1.8\beta)\right]^{1.6}}{Ra \cdot \cos(\beta)}\right] + \left[\left(\frac{Ra \cdot \cos(\beta)}{5830}\right)^{0.333} - 1\right]^{+} \tag{3.15}$$

where Ra is the Rayleigh number, and β is the tilted angle of the collector.

In case of vacuum inside the gap spacing, the model considers another equation that is able to characterize the heat loss through the vacuum space. In eq.(5.10), the term $h_{c,g\text{-}p}$ is void and replaced with the following:

$$h_{vacuum} = h_{gas} + h_{pillars} \tag{3.16}$$

where h_{gas} is the heat transfer coefficient due to the residual gas into the gap spacing and $h_{pillars}$ is the conductive heat transfer coefficient through the pillars. Note that, such pillars are needed for keeping the vacuum and prevent the implosion of the evacuated FPC. These heat transfer coefficients are calculated as following:

$$h_{gas} = \left[\frac{\upsilon_p \cdot \upsilon_g}{\upsilon_p + \upsilon_g\left(1 - \upsilon_g\right)}\right] \cdot \left[\frac{\gamma_{gas} + 1}{\gamma_{gas} - 1}\right] \cdot \left[\frac{R_{gas}}{4\pi M\left(T_p + T_g\right)}\right]^{\frac{1}{2}} \cdot p_{gas} \tag{3.17}$$

$$h_{pillars} = \frac{2 \cdot k_{glass} \cdot r}{d^2} \tag{3.18}$$

where υ_p and υ_g are the accommodation coefficients for the absorber plate and the glass cover, γ_{gas} is the heat capacity ratio of the residual gas into the gap spacing, R is the gas constant, M is the molecular weight of the residual gas and, p_{gas} is the pressure inside the gap spacing.

The heat loss coefficient of the bottom surface of the collector, is calculated as following:

$$U_b = \left(2 \cdot R_{b,ins} + \frac{1}{h_{c,edge-amb}}\right)^{-1} \tag{3.19}$$

where $R_{b,ins}$ is the conductive resistance of the bottom edge, $h_{c,edge\text{-}amb}$ is the convective heat transfer coefficient between the bottom edge and the ambient. The conductive resistance is calculated as following:

$$R_{b,ins} = \frac{\delta_{b,ins}}{2k_{ins}} \tag{3.20}$$

where $\delta_{b,ins}$ is the thickness of the insulation wrapped the bottom edge and k_{ins} is the thermal conductivity of the insulation. Note that, in eq.(5-19), due to the small thickness and the high thermal conductivity of the edge, the resistance of the steel edge is neglected.

The heat loss coefficient of the side edge is calculated as following:

$$U_e = \left(2 \cdot R_{e,ins} + \frac{1}{h_{c,edge-amb}} \right)^{-1} \tag{3.21}$$

where $R_{e,ins}$ is the conductive resistance of the side edge. Such a resistance is calculated as:

$$R_{e,ins} = \frac{\delta_{e,ins}}{2k_{ins}} \tag{3.22}$$

where $\delta_{e,ins}$ is the thickness of the insulation wrapped the side edge.

3.3. Sensitivity analysis methodology

The main issue during the optimization of a typical FPC are due to several factors that need to be considered, such as the number of parameters to be estimated, the solution method or to the optimization method to find the parameter values. To assure that the feature parameters correspond to the best set of values, a sensitivity analysis must be performed [213]. In this section, a sensitivity analysis is presented. The methodology of the carried-out analysis is reported Fig. 3.4.

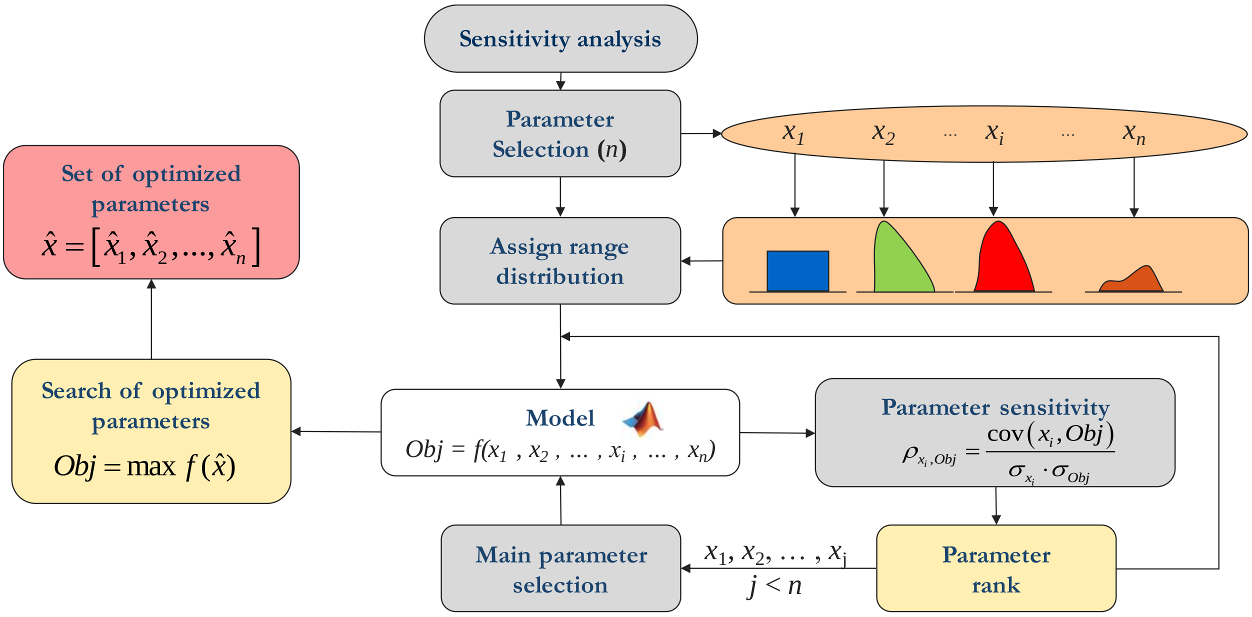

Fig. 3.4. Sensitivity analysis: methodology.

This is based on the above-described mathematical model suitable implemented in a tool in MatLab Simulink called “Sensitivity Analysis Tool”. The considered approach is based on the global sensitivity analysis in which a significant representative set of samples is used with the aim of exploring the whole of the design space.

Two different objective functions are taken into account: i) maximizing the thermal efficiency; ii) maximizing the working fluid outlet temperature. During the sensitivity analysis, all the considered parameters are altered simultaneously, allowing for the simultaneous assessment of the relative contribution of each individual parameter on the two considered objective function, as well as the interactions between the parameters. The first step is the initialization of parameters because the optimal solution depends mostly on initial guesses of parameters. Among all the features characterizing the FPC performance, twelve effective parameters are selected and summarized in Table 3.2. In addition, the variables assumed to be constant are shown in Table 3.3 according to the ISO 9806:2017 [219]. By adopting the values shown in Table 3.2, the sensitivity analysis continues with the definition of samples. The sampling procedure is based on the Sobol sequence. It is a quasi-random sequence that is able of producing multiple set of parameters that cover the considered multidimensional space. Each sample can be expressed as following:

$$\overline{x} = [x_1, x_2, ..., x_{12}] \tag{3.23}$$

where $\overline{x}$ is a generic set of parameters, and x_1, x_2, ..., x_{12} are the single parameters composing the generic sample.

Table 3.2. Sensitivity analysis: investigated parameters and initial values.

Parameter	Symbol	Minimum	Maximum	Initial	Unit	Step size
back insulation thickness	$\delta_{b,ins}$	2.0	6.0	5.0	cm	D
edge insulation thickness	$\delta_{e,ins}$	2.0	6.0	3.0	cm	D
gas used	-	atm. air, vacuum		atm. air	-	D
glass cover emissivity	ε_g	0.06	0.98	0.84	-	C
glass cover thickness	δ_g	4.0	8.0	4.0	mm	D
glass extinction coefficient	κ	4.0	32	16	m^{-1}	D
mass flow	$\dot{m}$	0.010	0.090	0.033	kg/s	D
number of riser pipes	N_{pipes}	7	11	8	-	C
plate - glass cover gap	$L_{g\text{-}p}$	4.0	8.0	5.0	cm	D
plate absorbance	α_p	0.50	0.99	0.90	-	C
plate emissivity	ε_p	0.06	0.98	0.84	-	C
plate thermal conductivity	k_p	60	385	385	W/(m·K)	D

D = discretized C = continuous

Table 3.3. Input variables.

Parameter	Symbol	Value	Unit
fluid input temperature	$T_{wf,in}$	45	°C
ambient air temperature	T_{amb}	20	°C
incident solar radiation	G_{tot}	1000	W/m^2
wind velocity	w_{wind}	3.0	m/s
collector slope	β	45	°
radiation incident angle	θ	0	°
sky condition		Clear sky	
insulation thermal conductivity	k_{ins}	0.035	W/(m·K)
glass refractive index	–	1.526	–
bond thermal conductivity	k_b	195	W/(m·K)
bond with back	b_b	1	mm
bond thickness	s_b	1	mm

Then, in order to find the correlation between each input variable and the considered objective function, a statistical analysis based on Pearson correlation coefficient [220] is considered. Such correlation (ρ) indicates the linear correlation between each parameter (x_1, x_2, …, x_{12}) and the objective function and it is calculated as following:

$$\rho_{x_i,Obj} = \frac{\mathrm{cov}\left(x_i, Obj\right)}{\sigma_{x_i} \cdot \sigma_{Obj}} \tag{3.24}$$

where *Obj* is the objective function, cov is the covariance, σ_{xi} is the standard deviation of the i-th x variable, and σ_{Obj} is the standard deviation of the objective function. Note that, ρ is an a-dimensional number that ranges between -1 and +1. It represents how strong the correlation between the x_i variable and *Obj* is: when ρ is equal to zero no correlation is detected, when the correlation coefficient is 1, there is a strong positive correlation (the higher the x_i, the higher the *Obj*), whereas when the value is -1 there is a strong negative correlation (the higher the x_i, the lower the *Obj*).

Finally, after the sensitivity analysis completion, it is possible to carry out the optimization by selecting the main effective variables ($\hat{x}$) with the strongest correlations to the considered *Obj*. At this stage it is possible to assess the best set of parameters capable of maximize the objective function:

$$Obj = \max\ f(\hat{x}) \tag{3.25}$$

3.4. Structural analysis results

Thus, with the aim of assessing the vacuum level that the solar thermal collector is able to stand, a structural analysis is conducted. By adopting Ansys R18.1 software, the optimum thickness of both glass cover and absorber plat is assessed.

In Fig. 3.5, the considered mesh grid for the entire solar thermal collector is depicted.

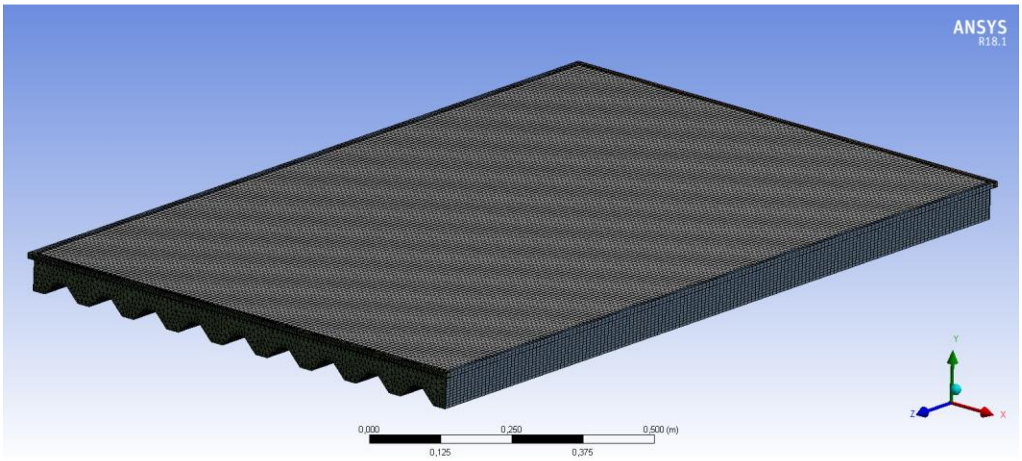

Fig. 3.5. Mesh for structural analysis: adaptive size with a characteristic size of $1.764 \cdot 10^{-4}$ mm.

Specifically, an adaptive geometry with a maximum characteristic size of $1.764 \cdot 10^{-4}$ mm is considered. Such size is selected as trade-off between the required computational time for a single simulation and results reliability. In the following figures (Fig. 3.6 - Fig. 3.7) the main findings of the structural analysis for both the absorber plate and the glass cover, are shown. These results are referring to a glass thickness of 8.0 mm and an absorber plate thickness of 0.5 mm.

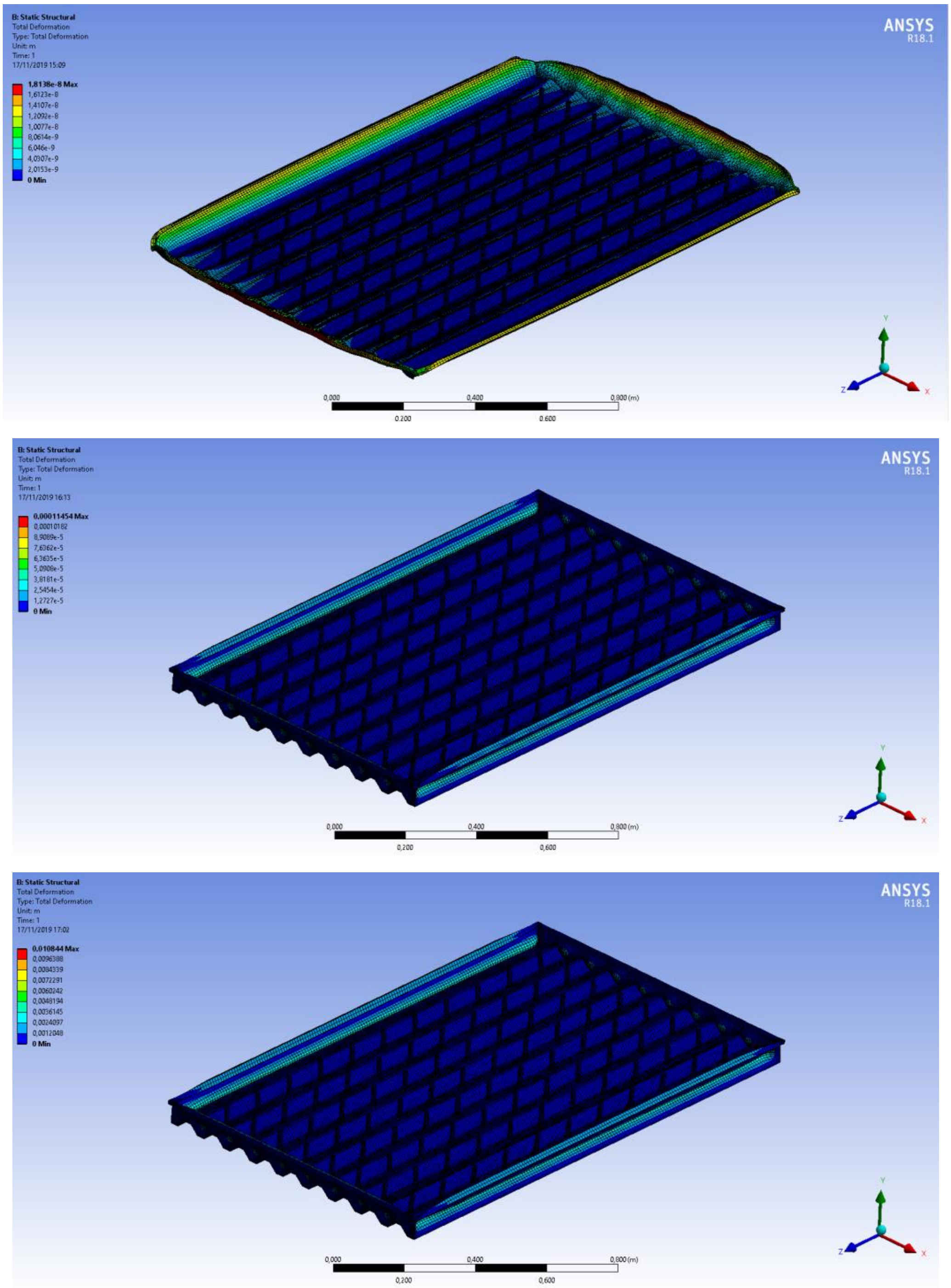

Fig. 3.6. Total deformation for the absorber plate and the edge (for low, medium, and high-vacuum).

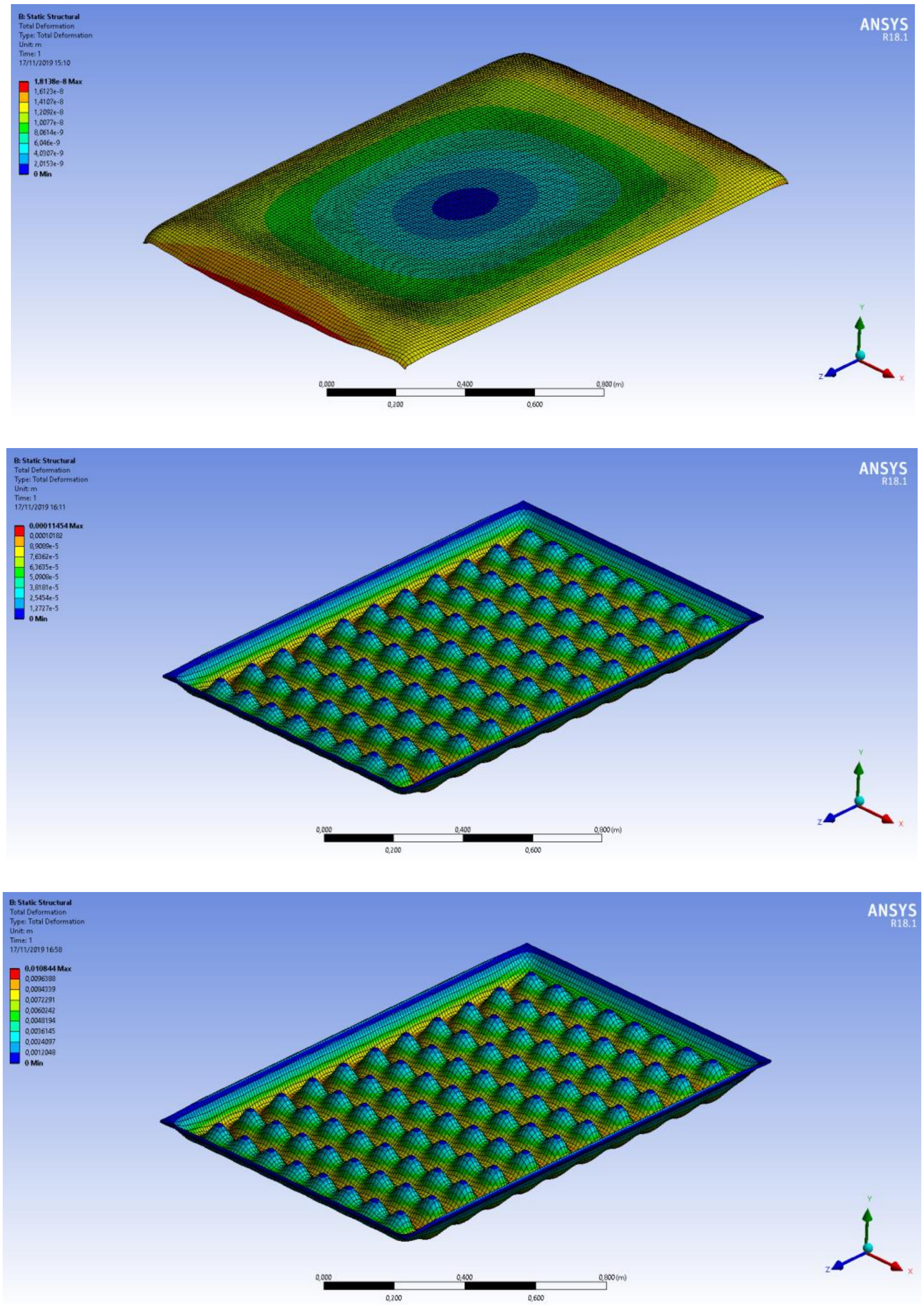

Fig. 3.7. Total deformation for the glass cover (for low, medium, and high-vacuum).

In Table 3.4, for each vacuum level, the mechanical stress (σ_{max}) and the corresponding deformation (ε_{max}) are reported. Here, it is possible to evaluate the vacuum quality level allowed by the selected thickness (i.e. 8.00 mm for the glass cover and 0.50 mm for the absorber plate).

For the selected design structure, it is possible to stand a medium vacuum (10^{-3} mbar) by admitting a deformation of 1.1 10^{-3} mm.

Table 3.4. Mechanical stress and deformation for each vacuum level.

Vacuum quality	**Pressure** [mbar]	σ_{max} [MPa]	ε_{max} [mm]
Low	10^{2}	$6.7 \cdot 10^{-6}$	$8.3 \cdot 10^{-6}$
	10^{1}	$2.3 \cdot 10^{-5}$	$2.1 \cdot 10^{-5}$
Medium	10^{0}	$8.2 \cdot 10^{-4}$	$5.7 \cdot 10^{-4}$
	10^{-1}	$5.4 \cdot 10^{-3}$	$4.3 \cdot 10^{-3}$
	10^{-2}	$4.2 \cdot 10^{-2}$	$1.8 \cdot 10^{-2}$
High	10^{-3}	$6.8 \cdot 10^{-1}$	$1.1 \cdot 10^{-1}$
	10^{-4}	$0.8 \cdot 10^{0}$	$0.3 \cdot 10^{0}$
	10^{-5}	$1.5 \cdot 10^{2}$	$1.7 \cdot 10^{1}$
	10^{-6}	$7.2 \cdot 10^{3}$	$1.0 \cdot 10^{2}$

*Boundary conditions T_{amb} = 20°C, G_{tot} = 800 W/m² $T_{max,absorber}$ ≈ 240°C

3.5. Sensitivity and optimization results

In order to show the potential of the developed model, a typical FPC is considered as a reference case. The model will be first applied on the typical FPC described previously in Section 2.1. By considering the initial values characterizing the reference FPC, a sensitivity analysis on the twelve selected parameters (list in Table 3.2) will be presented. The effectiveness of each parameter on the two considered objective functions will be described. This will be followed by an optimization on the main six parameters (detected at the end of the sensitivity analysis) that show the stronger correlation with the considered objective functions. Next, two different optimized FPC will be presented and compared with the reference one.

Sensitivity analysis results

The assessment of the weight of each parameter on the thermal efficiency and the working fluid outlet temperature is performed by considering as initial values the ones summarized in Table 3.2. A number of 577 samples are taken into account, and for each set of parameters, $\overline{X}$, the thermal efficiency and the working fluid outlet temperature are assessed.

In Fig. 3.8, the correlation between the absorbance of the absorber plate and the thermal efficiency of the solar thermal collector is shown.

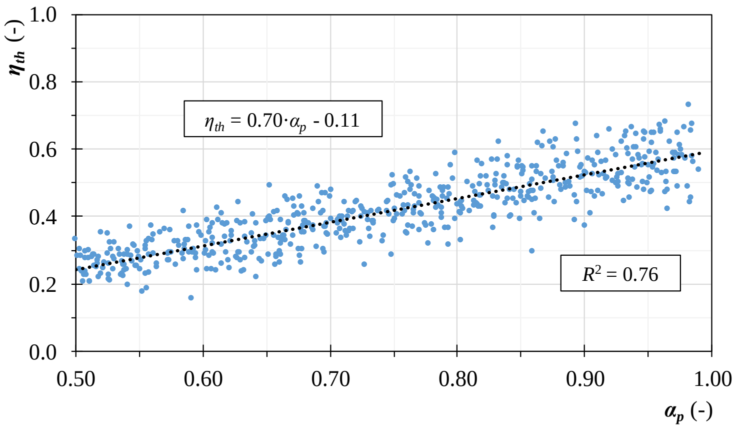

Fig. 3.8. Correlation between the absorbance of the plate and the thermal efficiency.

As can be seen, the higher the absorbance of the absorber plate, the higher the thermal efficiency of the FPC. This result is not obvious without the sensitivity analysis, because the considered sensitivity analysis takes into account the simultaneous variations of all the considered parameters allowing the assessment of the relative contribution of each individual parameter on the objective functions. Thus, such analysis is able to discover hidden correlations between different parameters. In fact, such hidden correlations cannot be assessed with a simple parametric analysis. However, the trend of the thermal efficiency with the absorbance plate can be expressed with a linear equation (η_{th} = $0.70 \cdot \alpha_p - 0.11$, depicted in the Fig. 3.8) with a coefficient of determination equal to 0.76. Note that, among all the investigated parameters, the absorbance of the absorber plate is the most effective one that affect the thermal efficiency, with a Pearson correlation coefficient, $\rho(\alpha_p, \eta_{th})$, equal to 0.87.

In Fig. 3.9 the correlation between the emissivity of the glass cover and the thermal efficiency is shown. By comparing Fig. 3.8 and Fig. 3.9, a different trend for the emissivity of the glass cover is detected. Here, the higher the emissivity of the glass cover, the lower the thermal efficiency.

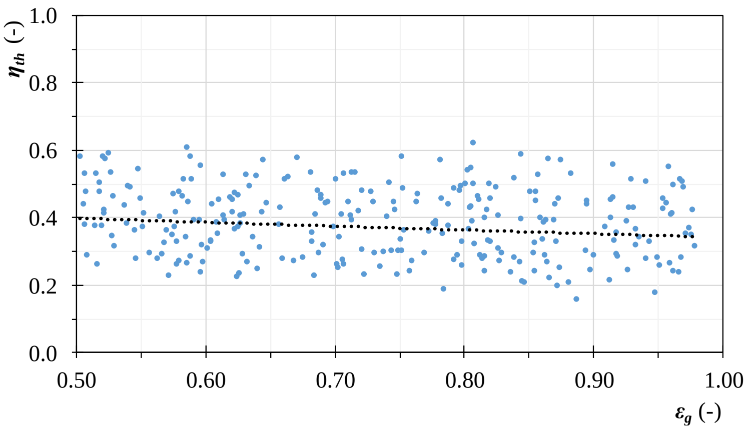

Fig. 3.9. Correlation between the emissivity of the glass cover and the thermal efficiency.

In Fig. 3.10, the correlation between the mass flow rate of the working fluid and the working fluid outlet temperature is shown.

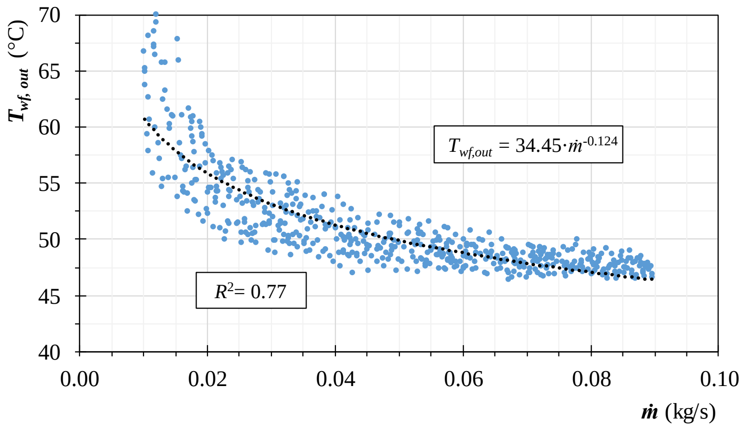

Fig. 3.10. Correlation between the working fluid mass flow rate and working fluid outlet temperature.

In this case, the higher the mass flow rate the lower the working fluid outlet temperature. An exponential correlation between this parameter and the considered objective function is calculated ($T_{wf,out}$ = 34.45·$\dot{m}^{-0.124}$) with a coefficient of determination equal to 0.77. By means of the sensitivity analysis, the mass flow rate has a Pearson correlation coefficient, $\rho(\dot{m}, T_{wf,out})$, equal to -0.76. By referring to Fig. 3.8, Fig. 3.9, and Fig. 3.10, same analyses could be conducted for the remaining parameters (listed in Table 3.2), but for sake of brevity only the most representative ones are shown. Specifically, for all the considered parameters, the correlation between them and the considered objective functions can be assessed by means of Fig. 3.11 and Fig. 3.12.

In these figures, the tornado plots of the all the investigated parameters for the two analyzed objective function are shown.

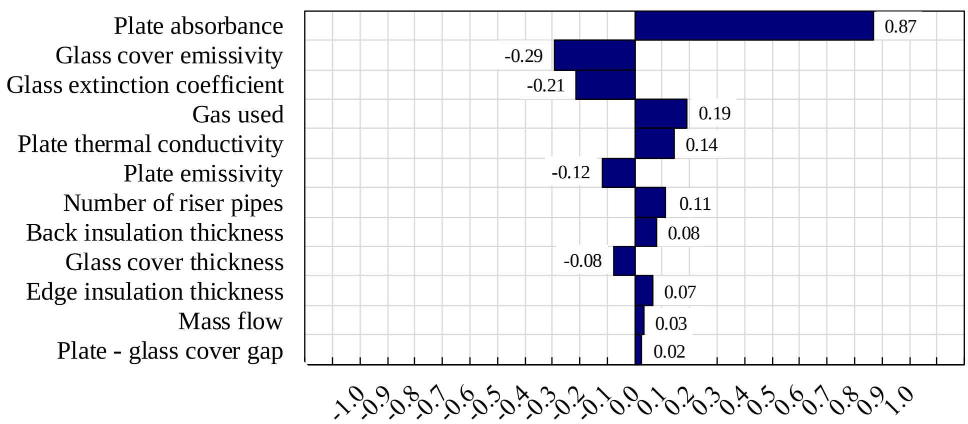

Fig. 3.11. Tornado diagram for the solar collector performance.

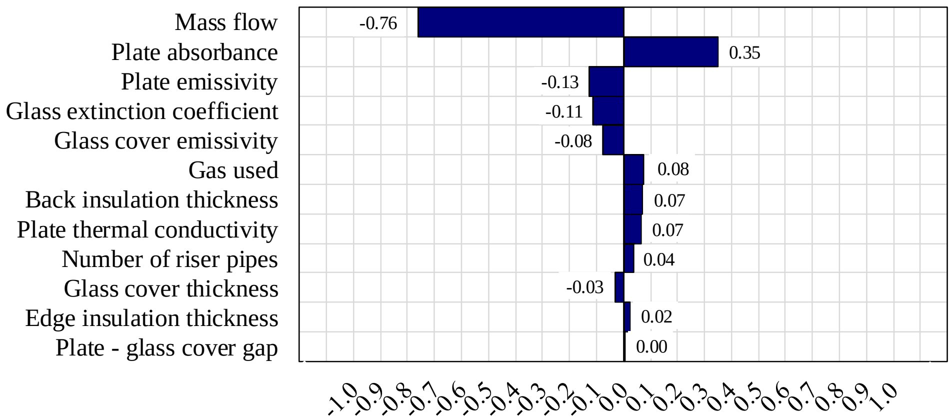

Fig. 3.12. Tornado diagram for the working fluid outlet temperature.

In these figures, it is possible to assess the rank of the effect of the twelve parameters on the thermal efficiency and the working fluid outlet temperature, respectively. In addition, it is also possible to evaluate the Pearson correlation coefficient of each parameter. The parameters located to the right of the vertical axis have a positive effect on the considered objective function. In this case, the objective function increases with the increase of the value of the parameter. For example, regarding Fig. 3.11, this happen for the parameter "Plate thermal conductivity" which has a Pearson correlation coefficient, $\rho(k_p, \eta_{th})$, of 0.14. Vice versa, the parameters located to the left of the vertical axis have a negative effect on the considered objective function. In this case, the objective function decreases with the increase of the value of the parameter.

As can be observed in Fig. 3.11, the parameters with the higher effect on the efficiency of the solar collector are: the absorbance of the absorber plate, glass cover emissivity, glass cover extinction coefficient and, gas used into the gap spacing. Specifically, the first and the fourth parameters have a strong positive effect on the thermal efficiency whereas the other two mentioned parameters have a strong negative one.

From Fig. 3.12, it can be seen that the parameters with the higher effect on the working fluid temperature are: the mass flow rate, the absorbance of the absorber, the emissivity of the absorber plate and, the glass cover extinction coefficient. Additionally, it is shown that the first, third and fourth parameters have a strong negative effect on the working fluid temperature whereas the second one has a strong positive effect.

<u>Optimization analysis results</u>

Referring to the tornado plots shown in Fig. 3.11 and Fig. 3.12, six parameters (the first four for the efficiency and the other, not in common, two for the working fluid outlet temperature) are selected and summarized below in Table 3.5.

Table 3.5. Parameters selected for the optimization process.

Parameter	**Symbol**	**Minimum**	**Maximum**	**Unit**
Gas used	-	atmospheric air, vacuum		-
Glass extinction coefficient	κ	4	32	m^{-1}
Glass cover emissivity	ε_g	0.06	0.98	-
Mass flow rate	$\dot{m}$	0.010	0.090	kg/s
Plate absorbance	α_p	0.50	0.99	-
Plate emissivity	ε_p	0.06	0.98	-

The goal of the optimization analysis is to find out the set of parameters ($\hat{x}$), that are able to maximize the two considered objective functions, defined as follow:

i) maximize the thermal efficiency, max (η_{th}) = f ($\hat{x}_{th}$) (Optimized (1));

ii) maximize the working fluid outlet temperature, max($T_{wf,\,out}$) = f ($\hat{x}_T$) (Optimized (2)).

In order to evaluate the sets of parameters that maximize the thermal efficiency ($\hat{x}_{th}$) and the working fluid outlet temperature ($\hat{x}_T$), many attempts were considered during the optimization procedure. Such attempts are shown in Fig. 3.13 and Fig. 3.14: fifty-one and fifty-three iterations been needed for obtaining the required sets (for thermal efficiency and the working fluid outlet temperature, respectively). Note that, between each iteration many sets of variables are evaluated.

In Fig. 3.13 is clearly visible that after nineteen iterations and four steps, the code is able to detect the set of parameters that maximize the thermal efficiency, however the remaining thirty-two iterations have been needed in order to check and compare the best set with the other available. More complicated has been the detection of the set of variable able to maximize the working fluid outlet temperature. As can be observed from Fig. 3.14, thirty-eight iterations and seven steps has been needed. The other fifteen iterations have been needed in order to check and compare the best set with the other available, as done for the thermal efficiency.

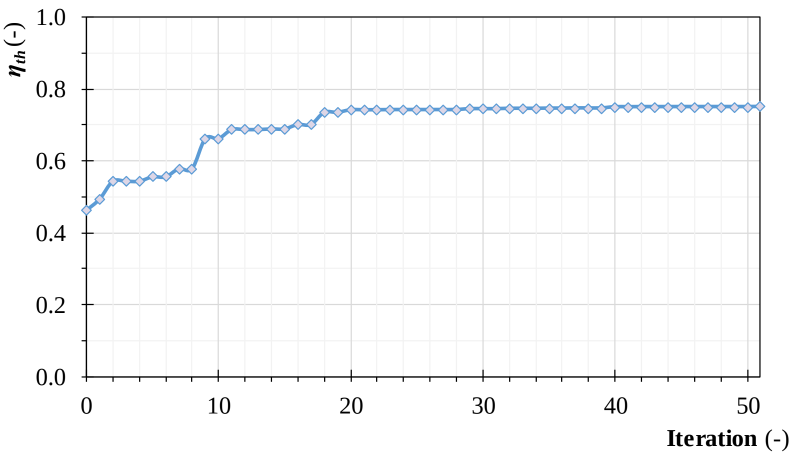

Fig. 3.13. Optimization processes: number of iterations vs. thermal efficiency.

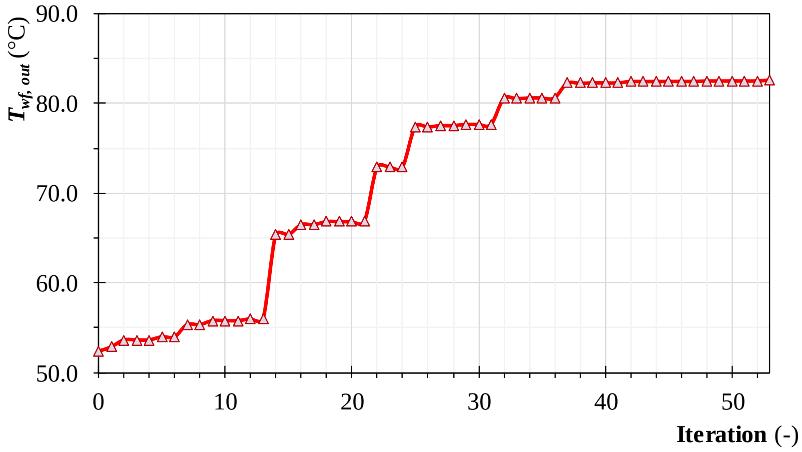

Fig. 3.14. Optimization processes: number of iterations vs. working fluid outlet temperature.

FPCs: typical vs. optimized

In the following Table 3.6, the calculated sets of variables are shown.

Table 3.6. Features of traditional vs. optimized FPCs.

Parameter (symbol)	**Unit**	**Typical**	**Optimized (1)** ($\hat{x}_{th}$)	**Optimized (2)** ($\hat{x}_T$)	$\rho(x_i, \eta_{th})$	$\rho(x_i, \eta_{th})$
gas used (-)	-	atmospheric air	Vacuum		0.19	0.08
glass extinction coefficient (κ)	m^{-1}	16.0	4.0	4.0	-0.21	-0.11
glass cover emissivity (ε_g)	-	0.8400	0.0607	0.0602	-0.29	-0.08
mass flow rate ($\dot{m}$)	kg/s	0.0330	0.0897	0.0100	0.03	-0.76
plate absorbance (α_p)	-	0.9000	0.9494	0.9499	0.87	0.35
plate emissivity (ε_p)	-	0.850	0.0609	0.0609	-.0.12	-0.13

As expected, the optimized FPCs are characterized by vacuum with gas used into the gap spacing. Note that, the gap spacing for the vacuum solution, is considered at a pressure of 0.01 Pa. In addition, it is possible to see that the parameter that changes more from the first to the second optimized FPC is the mass flow rate: a mass flow rate of 0.0897 kg/s is required for maximizing the thermal efficiency whereas 0.0100 kg/s is needed for maximizing the working fluid outlet temperature. Such a high variation is in accordance to Fig. 3.11 and Fig. 3.12. In fact, the mass flow rate is the only parameter that has a positive correlation for thermal efficiency ($\rho(\dot{m}, \eta_{th})$ equal to 0.03) and negative one for the working fluid outlet temperature($\rho(\dot{m}, T_{wf,out})$ equal to -0.76). The other five parameters considered in the optimization have the same effectiveness with different weight on the two objective functions (see last two columns of Table 3.6).

The different values of the glass extinction factor, 16.0 m^{-1} for the typical FPC and 4.0 m^{-1} led to the calculation of different optical features, as reported in Table 3.7. Such results are calculated by eq.(3.3). Due to enhancement of glass cover extinction coefficient (from 16.0 m^{-1} for the typical collector to 4.0 m-1 for the optimized ones) an increase of the transmittance of the glass cover from 0.859 to 0.902, around 5% is achieved.

Table 3.7. Optical features traditional vs. optimized STC.

Parameter	Unit	Typical	Optimized (1) - (2)
τ_g	-	0.859	0.902
α_g	-	0.062	0.016
ρ_g	-	0.079	0.082

Furthermore, another enhancement for the glass cover was achieved by the decrease of the emissivity of the glass cover, from 0.850 to 0.0609. Such improvements led to the decrease of the thermal loss related to the top and, consequentially, to the overall thermal loss, as shown in Table 3.8.

Remarkable decreases in term of heat loss coefficient of the top surface and overall heat loss coefficient are achieved:

i) heat loss coefficient of the top surface from 5.947 W/(m²·K) for the typical FPC to 0.227 and 0.243 W/(m²·K) for the first and second optimized FPC (around 96.16 and 95.9%.
ii) overall heat loss coefficient from 7.678 W/(m²·K) for the typical FPC to 1.958 and 1.974 W/(m²·K) for the first and second optimized FPC (around 74.49 and 74.29%).

Table 3.8. Thermal features of traditional vs. optimized STC.

Parameter	Unit	Typical	Optimized (1)	Optimized (2)
$T_{wl,\ out}$	°C	52.4	49.4	82.6
T_{glass}	°C	28.6	20.3	20.7
F_r	-	0.829	0.959	0.918
U_L	W/(m²·K)	7.678	1.958	1.974
U_t	W/(m²·K)	5.947	0.227	0.243
U_b	W/(m²·K)	0.663	0.663	0.663
U_e	W/(m²·K)	1.068	1.068	1.068
η	-	0.463	0.749	0.718
$\eta_0 = F_r(\tau\alpha)_n$	-	0.622	0.797	0.763
$a_1 = F_r U_L$	W/(m²·K)	6.367	1.878	1.813
$T_{stagnation}$	°C	116	444	440

Of course, this reduction of the overall heat loss coefficient is not only due to the decrease of the emissivity of the glass cover, but to the combination of this with the adoption of vacuum into the gap spacing. In fact, by adopting the vacuum, the absorber plate is more insulated and the heat loss from the top are significantly reduced. It should be noted that the average temperature of the glass cover is also reduced from 28.6°C for the typical FPC to 20.3 and 20.7°C for the first and second optimized FPC.

Regarding the working fluid outlet temperature, by comparing the typical with the first optimized FPC, the temperature is slightly reduced from 52.4 to 49.4°C (around -5.7%). Such a result is acceptable if it is considered that the aim of the first optimization is to maximize the thermal efficiency of the FPC, since an increase of thermal efficiency from 0.463 to 0.749 is achieved (61.7%). For the second optimization, in which the goal is the maximization of the working fluid outlet temperature, a sensible increase of the working fluid outlet temperature, from 52.4 to 82.6°C (around 57.6%) is achieved.

Note that, due to the quite similar behaviour (in terms of Pearson correlation) of the six optimized parameters, the effects of the enhanced parameters, on the thermal efficiency, are quite similar for both the optimized FPCs. In fact, for the second optimized FPC, the thermal efficiency is increased from 0.463 of the typical FPC to 0.718. Such a thermal efficiency is comparable to that of the first optimized FPC (0.749). In fact, they differ only by 0.031 (around 4.1%). By comparing the two optimized FPCs, it is clearly visible that their thermal efficiencies are comparable whereas the working fluid outlet temperature are considerably different. For such a reason, the best optimized FPC is the second one. The characteristic curves of the three investigated FPCs are shown in Fig. 3.15.

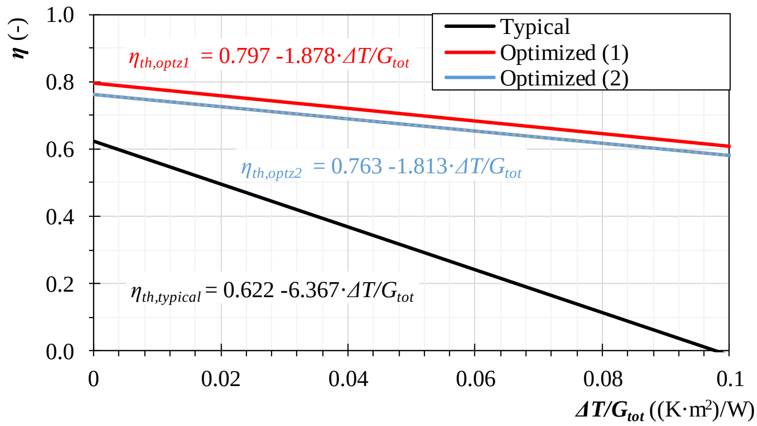

Fig. 3.15. Thermal efficiency curves for the traditional vs. optimized FPC.

Here it is possible to see the trends of the characteristic curves of the investigated FPCs. The three FPCs show substantial differences in terms of optical and thermal losses. The optical losses can be assessed by considering the $F_r(\tau\alpha)_n$ parameter: the higher $F_r(\tau\alpha)_n$ the lower the optical losses. As expected, the highest optical losses are detected for the typical (non-optimized) FPC whereas the lowest are observed for the first optimized FPC. Furthermore, the same happens for the thermal losses: the highest thermal losses (as already seen in Table 3.8) are detected for the typical collector whereas the lowest one are observed to the fist optimized FPC.

3.6. High vacuum solar thermal collector: Tank_v.2

This section focuses on the design of an innovative high-vacuum solar thermal collector produced by TVP solar company, for which a novel dynamic simulation model is suitably developed in order to investigate its energy performance under different operating conditions. The main novelty of this solar thermal collector is the capability of storing hot water with no need for any additional storage tank. In fact, thanks to the high-vacuum space between the glass cover and the absorber plate, the convective thermal losses are almost nullified. In this way, it is possible to store hot water into the solar thermal collector without the use of a hot water storage tank. The prototype is tested under different operating conditions and the experimental data are used to validate the presented simulation model.

3.6.1. Prototype description

The novel high-vacuum solar thermal collector prototype consists of eight steel pipes of 95.0 mm diameter, and 1860 mm length, suitably painted with a solar coating utilized for increasing their absorbance. These pipes are suitably welded in order to shape a serpentine working as absorber. A volume of 130 l is available for storing hot water. A vacuum space of 110 mm between the glass cover and the absorber plate is considered. Here, a high vacuum (almost 10^{-8} mbar) is made for insulating the absorber and avoiding the convective thermal losses. In order to stand the vacuum and avoid a collapse of the glass cover on the absorber plate, 189 pillars (e.g. 9 rows of 21 pillars) of 110 mm length and 5.2 mm diameter are welded on the edge. The cross-section of the solar thermal collector is shown in Fig. 3.16 whereas the front is depicted in Fig. 3.17.

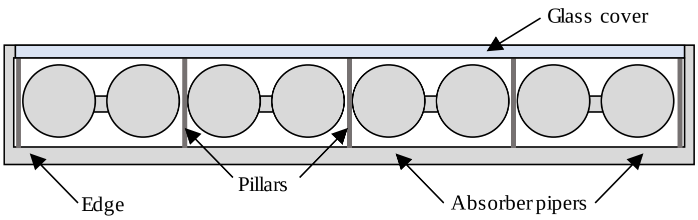

Fig. 3.16. Cross section with glass and edge nodes.

Fig. 3.17. Front face high-vacuum solar thermal collector (left), prospective rendering view (right).

3.6.2. Mathematical model

The dynamic simulation model of the innovative high-vacuum solar thermal collector is based on a finite volume approach for the numerical solution of the three-dimensional heat conduction. A set of suitable equations is obtained for each node of the adopted thermal resistance-capacitance (RC) network, including conductive, radiative and convective heat transfer occurring within and through the high-vacuum solar thermal collector. This set of equations was implemented in a suitable tool developed in MatLab environment. A sketch of the considered discretization system and the relative RC thermal network are shown in Fig. 3.18 and Fig. 3.19, respectively. Note that, for the sake of brevity, the thermal network is depicted for only one absorber pipe. Note also that, the thermal behaviour of each absorber pipe is affected by the adjacent ones, which is considered in the developed model.

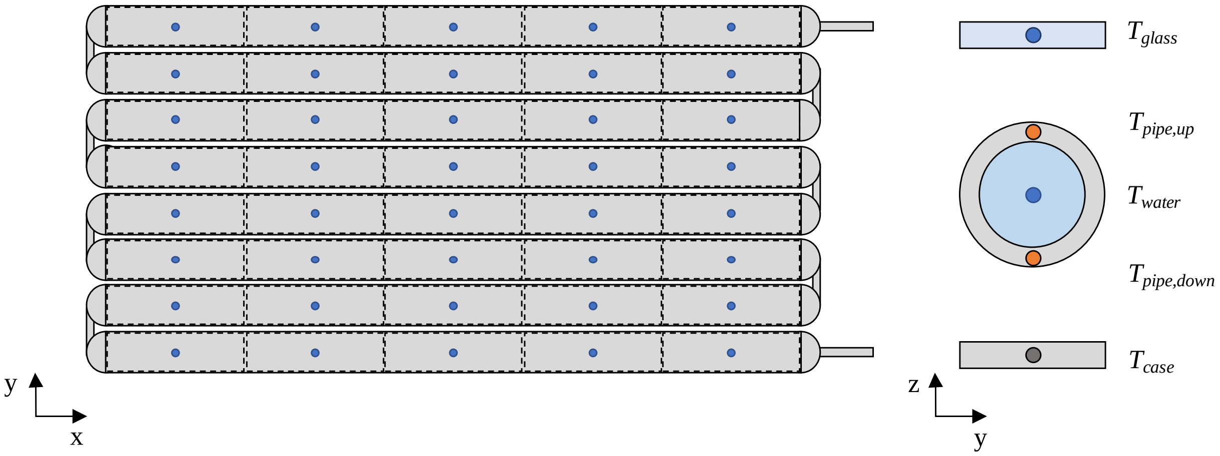

Fig. 3.18. Discretization: top view (left), cross section view (right).

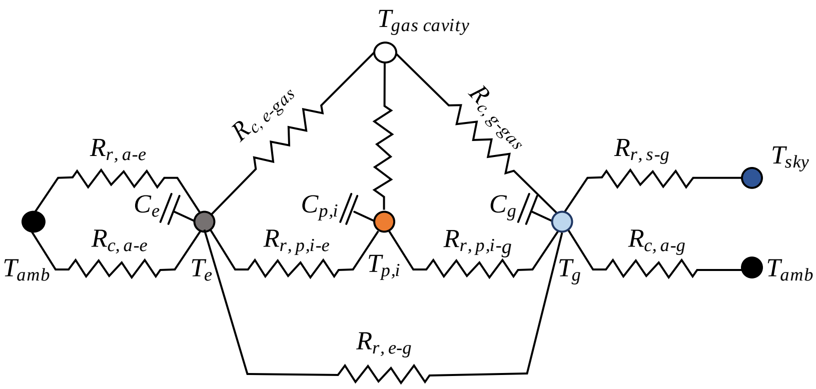

Fig. 3.19. RC thermal network.

To calculate the water temperature gradient along the absorber pipes, both the absorber and the water volume are discretised in capacitive nodes to model their thermal inertia. A two-dimensional Cartesian coordinate (x-y) system is considered. Differently from the absorber pipes and water volume, the glass cover and the edge are discretized in only one capacitive node (see the two-dimensional Cartesian coordinate (y-z) in Fig. 3.18).

The glass cover temperature is calculated as:

$$C_g\left(\frac{dT_g}{d\theta}\right)=\alpha_g A_g G_{tot}+\varepsilon_g\sigma A_g\left(T_{sky}^4-T_g^4\right)+A_g h_{c,\,a-g}\left(T_{amb}-T_g\right)+\ldots$$
$$\ldots+\sum_{i=1}^{N}\left(\frac{\sigma\left(T_{p,i}^4-T_g^4\right)}{\frac{1-\varepsilon_g}{A_g\varepsilon_g}+\frac{1-\varepsilon_g}{A_g F_{g-p,i}}+\frac{1-\varepsilon_p}{A_{p,i}\varepsilon_p}}\right)+\frac{\sigma\left(T_c^4-T_g^4\right)}{\frac{1-\varepsilon_g}{A_g\varepsilon_g}+\frac{1-\varepsilon_g}{A_g F_{g-e}}+\frac{1-\varepsilon_c}{A_c\varepsilon_c}} \tag{3.26}$$

where C_g is the thermal capacity of the glass cover, T_g is the glass cover temperature, $d\theta$ is the infinitesimal delta time, α_g is the absorbance of the glass cover, A_g is the surface of the glass cover, G_{tot} is the global irradiance, ε_g is the emissivity of the glass cover, σ is the Stefan-Boltzmann constant, T_{sky}, is the sky temperature, $h_{c,\,a\text{-}g}$ is the convective heat transfer coefficient between the glass cover and the ambient air, T_{amb} is the ambient air temperature, i is the *i-th* node in which the absorber is discretized, N is the number of the absorber pipe nodes, $T_{p,i}$ is the *i-th* absorber pipe node temperature, $F_{g\text{-}p,i}$ is the view factor between the glass cover and the *i-th* absorber pipe node, $A_{p,i}$ is the surface of the *i-th* absorber pipe, ε_p is the emissivity of the absorber, T_c is the case temperature, $F_{g\text{-}e}$ is the view factor between the glass cover and the case, ε_c is the emissivity of the case. Note that, in eq.(3.26) the convective heat transfer between the glass cover and the air in the gas cavity is intentionally neglected because of the high-vacuum level (i.e. 10^{-8} mbar).

Considering the *i-th* absorber pipe node, its temperature is calculated as:

$$C_{p,i}\left(\frac{dT_{p,i}}{d\theta}\right)=\left(\tau_g\alpha_p\right)A_{p,i}G_{tot}+U_w A_{p,i}\left(T_{w,i}-T_{p,i}\right)+\frac{\sigma\left(T_g^4-T_{p,i}^4\right)}{\frac{1-\varepsilon_p}{A_{p,i}\varepsilon_p}+\frac{1-\varepsilon_p}{A_{p,i}F_{p,i-g}}+\frac{1-\varepsilon_g}{A_g\varepsilon_g}}+\ldots$$
$$\ldots+\frac{\sigma\left(T_c^4-T_{p,i}^4\right)}{\frac{1-\varepsilon_p}{A_{p,i}\varepsilon_p}+\frac{1-\varepsilon_p}{A_{p,i}F_{p,i-c}}+\frac{1-\varepsilon_c}{A_c\varepsilon_c}}+\sum_{j=1}^{K}\frac{A_{p,i}\sigma\left(T_{p,j}^4-T_{p,i}^4\right)}{\frac{2}{\varepsilon_p}-1} \tag{3.27}$$

where $C_{p,i}$ is the thermal capacity of the i-th absorber pipe node, τ_g is the transmittance coefficient of the glass cover, α_p is the absorbance of the absorber pipes, U_w is the global transmittance between the i-th water volume and the i-th pipe node, $T_{w,i}$ is the i-th water volume temperature, $F_{p,i\text{-}g}$ is the view factor between the glass cover and the absorber pipe node, $F_{p,i\text{-}c}$ is the view factor between the case and the absorber pipe node, j is the *j-th* adjacent absorber pipe node, and K is the number of adjacent absorber pipe nodes.

Regarding the edge, the temperature is assessed as follows:

$$C_c\left(\frac{dT_c}{d\theta}\right)=\left(\tau_g\alpha_c\right)A_cG_{tot}+h_{c,\,a-e}A_e\left(T_{amb}-T_c\right)+\ldots$$

$$\ldots+\sum_{i=1}^{N}\left(\frac{\sigma\left(T_{p,i}^4-T_c^4\right)}{\frac{1-\varepsilon_c}{A_e\varepsilon_c}+\frac{1-\varepsilon_c}{A_cF_{c-p,i}}+\frac{1-\varepsilon_p}{A_{p,i}\varepsilon_p}}\right)+\frac{\sigma\left(T_g^4-T_c^4\right)}{\frac{1-\varepsilon_c}{A_c\varepsilon_c}+\frac{1-\varepsilon_c}{A_cF_{c-g}}+\frac{1-\varepsilon_g}{A_g\varepsilon_g}} \tag{3.28}$$

where C_c is the thermal capacity of the case, α_c is the absorbance of the case, A_c is the surface of the case, $h_{c,\,a\text{-}e}$ is the convective heat transfer coefficient between the case and the ambient air, and $F_{c\text{-}g}$, is the view factor between the glass cover and the case.

Considering the *i-th* water volume node, its temperature is calculated as:

$$C_w\left(\frac{dT_{w,i}}{d\theta}\right)=U_wA_p\left(T_{p,i}-T_{w,i}\right)+\sum_{j=i-1}^{i+1}\dot{m}_wc_{p,w}\left(T_{w,j}-T_{w,i}\right) \tag{3.29}$$

where C_w is the thermal capacity of the water volume, $\dot{m}_w$ is the water mass flow rate, $c_{p,w}$ is the specific heat of water, and $T_{w,j}$ is j-th water volume of the adjacent water volumes to the i-th water volume.

3.6.3. Experimental analysis

A suitable experimental setup is built and tested in August 2019 in the weather zone of Avellino (Italy). This period of the year has been selected as a suitable one for testing this technology. In fact, in August, the weather zone of Avellino is characterized by high solar irradiation (e.g. with a peak valeu about 900 W/m^2) and quite low ambient air temperature during the night time. This occurrence is needed for assessing the effectiveness of the vacuum insulation and the relative water drop temperature. In Fig. 3.20 the test bench is shown.

Fig. 3.20. Test bench.

Here, with the aim of measuring the boundary conditions that affect the performance of the high-vacuum solar thermal collector, the following instruments are utilized:

i) an anemometer (AM-4222; speed range: 0.4 - 30.0 m/s; temperature range: 0 - 50°C; accuracy: ± 1%) for measuring the wind speed;

ii) a pyranometer (Kipp and Zonen CM11) for assessing the incident solor radiation;

iii) a termoygrometer for evaluating both the temperature and relative humidity of the ambient air.

In Fig. 3.21 the placement of the adopted instruments for testing the high-vacuum solar thermal collector is reported. Specifically, four PT100 thermocouples, two T-Type thermocouples, one flow transmitter, and one manometer are connected through a compact Rio. With reference to Fig. 3.21, the following measurements are obtained:

i) water flow temperature at the outlet ($T_{water\ outlet}$) and inlet ($T_{water\ inlet}$) of the high-vacuum solar thermal collector, points a and b;

ii) water flow temperature in the middle of the first ($T_{f\ right}$) and last ($T_{f\ left}$) pipe of the high-vacuum solar thermal collector, points c and d;

iii) glass cover temperature (T_{glass}), point e;

iv) case temperature (T_{case}), point f;

v) mass flow rate (*flow transmitter*) at the inlet of the hig-vacuum solar thermal collector;

vi) water pressure (P) at the outlet of the high-vacuum solar thermal collector.

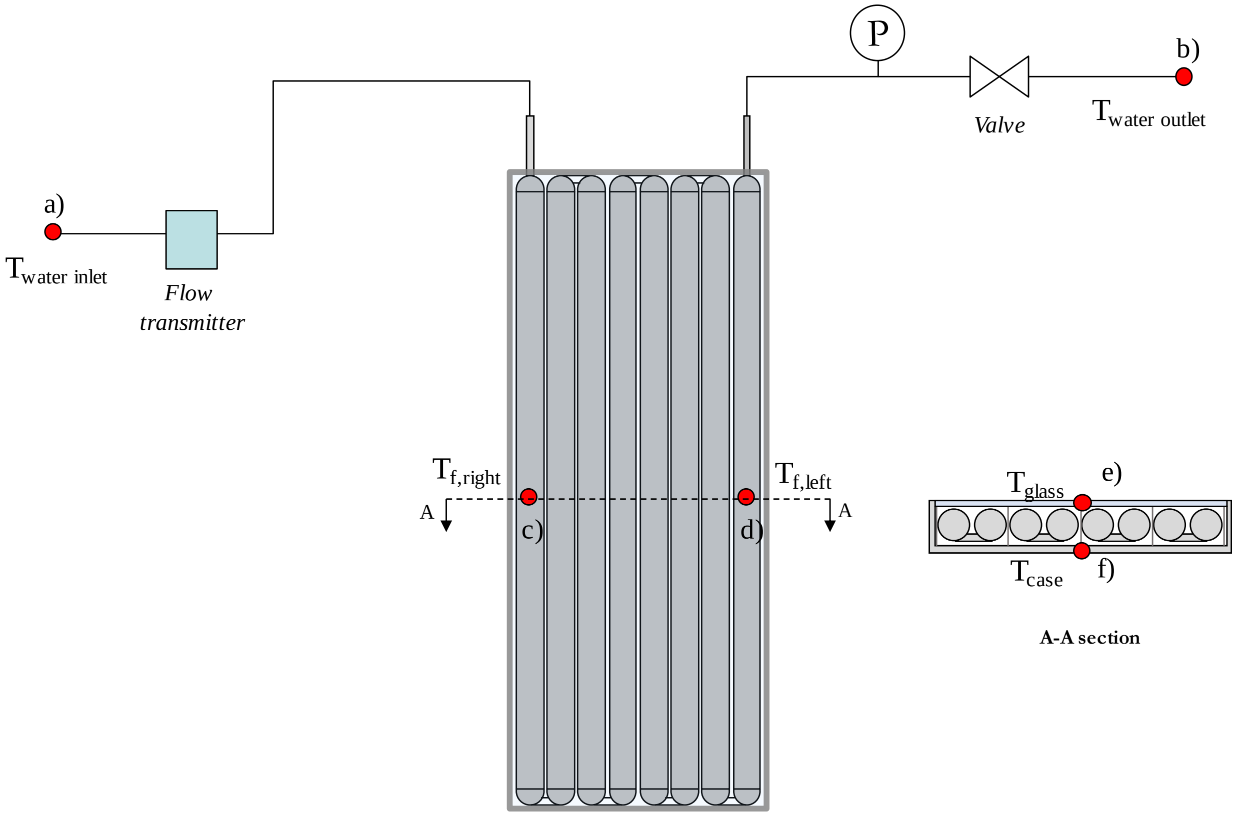

Fig. 3.21. Experimental setup: instruments arrangement.

3.6.4. Experimental validation

The results of the conducted experimental analyses and the relative experimental validation, for the aforementioned configurations, are reported in this section. The developed dynamic simulation model is validated against the experimental data. The validation process consists of comparing the measured parameters against the calculated ones, relative to the: i) water flow temperature at the middle of the first absorber pipe ($T_{f\ right}$); ii) water flow temperature at the middle of the last absorber pipe ($T_{f\ right}$); iii) glass cover temperature (T_{glass}); iv) case temperature (T_{case}). In order to assess these parameters, the simulation model requires as input data the: i) ambient air temperature (T_{amb}); ii) incident solar radiation (G_{tot}); and iii) wind velocity (w_{wind}). During the experiments, in order to assess the insulation magnitude provided by the high vacuum, the solar thermal collector was experimentally assessed with a volume full of water (i.e. 130 l) and no mass flow rate from and to the outside was adopted. Such a circumstance was selected for assessing the temperature drop during the night. The validation procedure is carried out for a week. Nevertheless, for the sake of brevity, one significant day is here discussed and shown hereinafter. The experimental measurements with the relative gathered data are summarised in Fig. 3.22. In addition, boundary conditions are reported in Fig. 3.23.

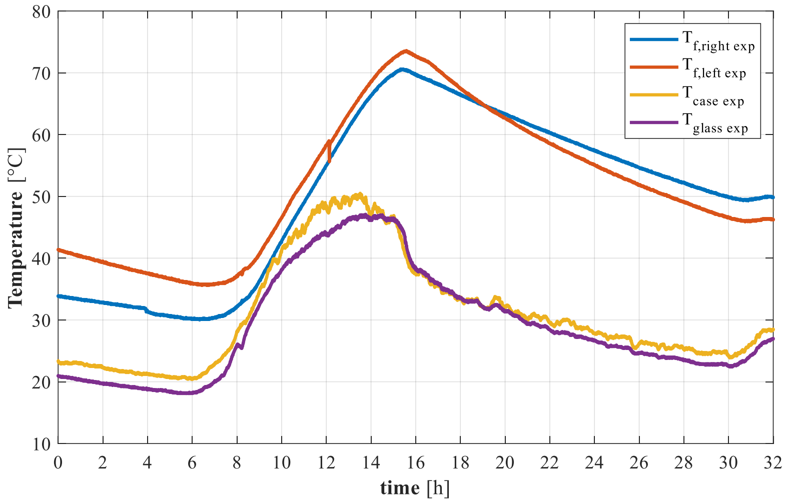

Fig. 3.22. Experimental data.

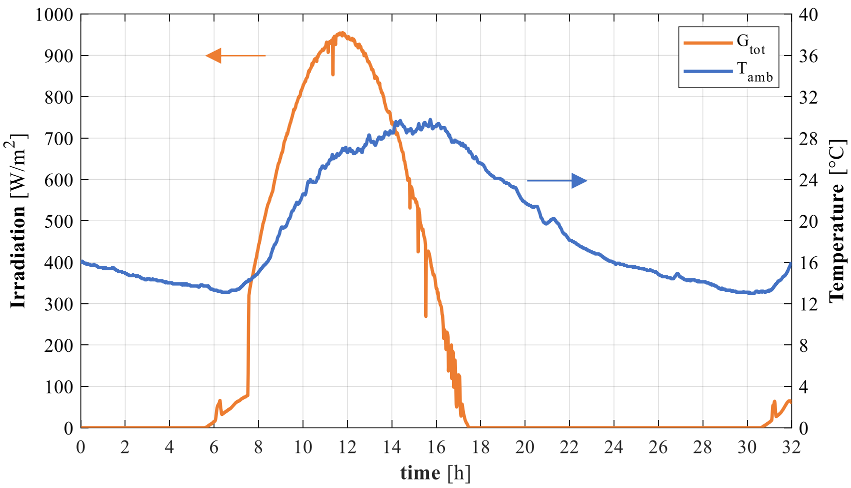

Fig. 3.23. Boundary conditions.

Here it is possible to detect a maximum water temperature around 74°C (15th hour). Note that, this result is achieved at a time of the day that does not correspond to the one in which the maximum solar radiation is observed (i.e. around 12th hour with maximum solar radiation of 951 W/m^2). This occurs because of the high-vacuum system and the capability of storing hot water by strongly limiting the convective heat losses. Furthermore, the trend of the temperature changes around 16th hour. Here, the heat losses are higher than the collected heat. By analysing Fig. 3.22, a temperature drops around 1.6°C/h (from 64°C recorded at 20th hour to 48°C detected at 30th hour) is achieved. Such a result is achieved by combining two technologies: i) high-vacuum level; ii) solar coating. In fact, as above described, thanks to the high-vacuum adoption, during the night the only thermal losses are the one due to the radiative heat exchange between the absorber pipes and the sky. These thermal losses are reduced by adopting a suitable solar coating characterized by an emissivity of 0.25 and an absorbance of 0.95.

In Fig. 3.24, the comparison between the simulated and the experimental data of the working fluid temperature at the middle of the first ($T_{f\ right}$) and last ($T_{f\ left}$) pipe are shown.

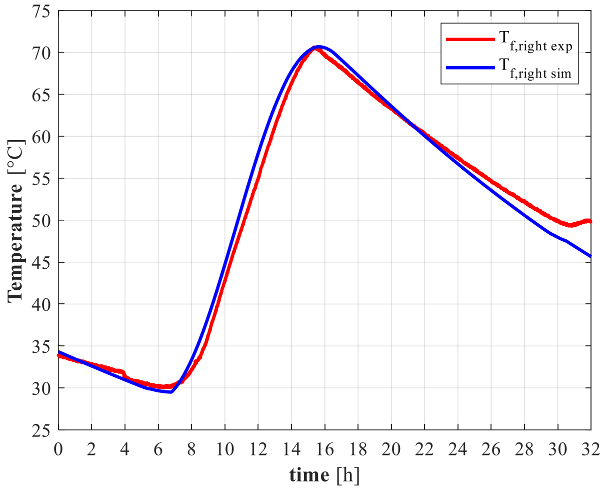

Fig. 3.24. Working fluid temperatures comparisons (right and left): experimental vs. simulated.

Here, a very good match between simulated and experimentally measured is achieved for both the working fluid temperatures. Specifically, $T_{f\ right\ exp}$ is well fitted by $T_{f\ right\ exp}$ whereas a higher discrepancy for the $T_{f\ left}$ is observed. This circumstance is due to the different location between the test bench (i.e. the place in which the boundary conditions are recorded, see Fig. 3.20) and the experimental setup (i.e. located in the opposite side of the building, see Fig. 3.21).

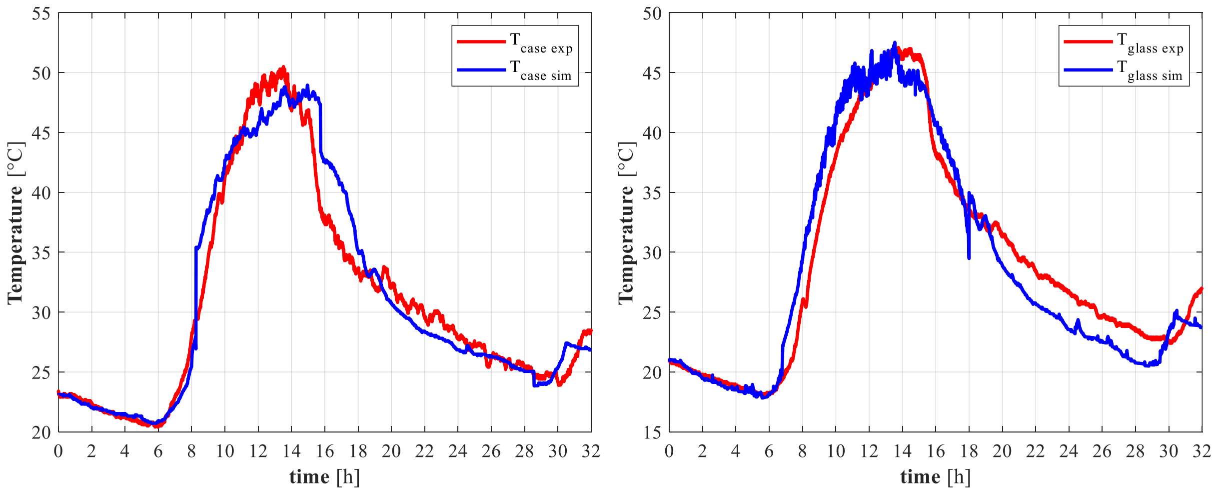

Fig. 3.25. Case (left) and glass cover (right) temperature comparisons: experimental vs. simulated.

In fact, these two systems are located in two different places. Specifically, the test bench takes place on the roof wherase the experimental setup reported in Fig. 3.21 is located on the ground, where during the afternoon, a building shadow reduces the incident solar radiation on the high-vacuum solar thermal collector so the simulated temperature are quite higher than the measured one.

In Fig. 3.25, the comparison between the simulated and the experimental data of both the case (T_{case}) and the glass cover (T_{glass}) temperatures are shown.

A very good agreement is observed between simulated and measured results for both the case and glass cover temperatures. Specifically, acceptable errors are achieved for all the investigated parameters.

In Fig. 3.26 the comparison between all the experimental and simulated temperatures is reported.

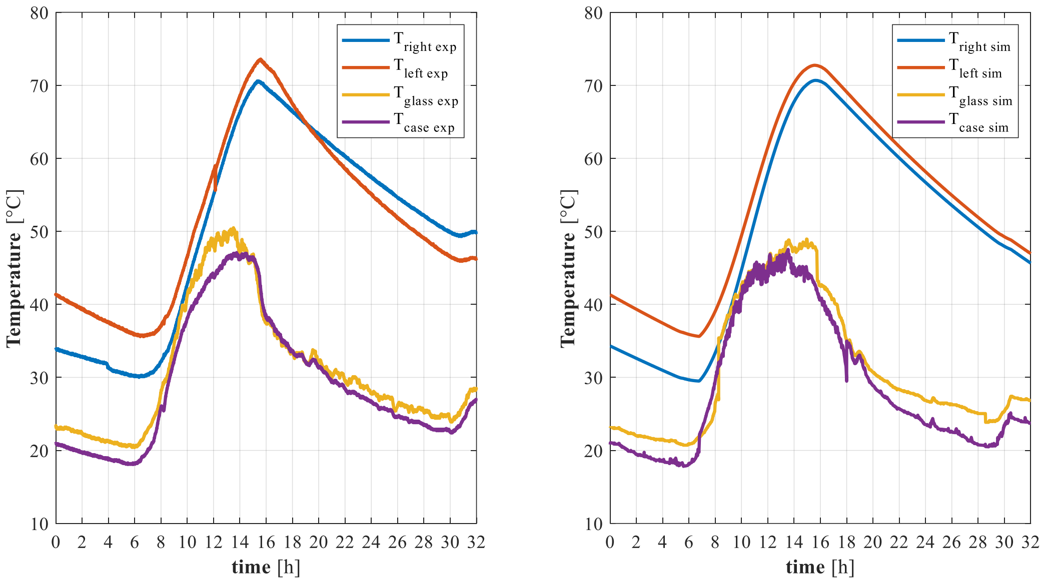

Fig. 3.26. Experimental (left) and simulated (right) temperatures comparisons.

By analysing the experimental working fluid temperature trends ($T_{right\ exp}$ and $T_{left\ exp}$), an intersection of the two temperatures is detected around 19th hour. Such circumstance is due to a malfunction of the pressure valve at the outlet of the high-vacuum thermal collector. Here, a mixing between the cold water (coming from the outer pipes) and the water inside the left side of the solar thermal collector occurs. In this way, a sensible reduction of the $T_{left\ exp}$ occurs. In fact, by comparing the simulated working fluid temperature trends ($T_{right\ sim}$ and $T_{left\ sim}$), with the experimental ones ($T_{right\ exp}$ and $T_{left\ exp}$), it is possible to assert that if the pressure valve works without any malfunction, the two considered tempeartures drop with the same gradient (without any intersection, as reported in Fig. 3.26, right). In Fig. 3.27 the validation results for the entire experimental period are reported.

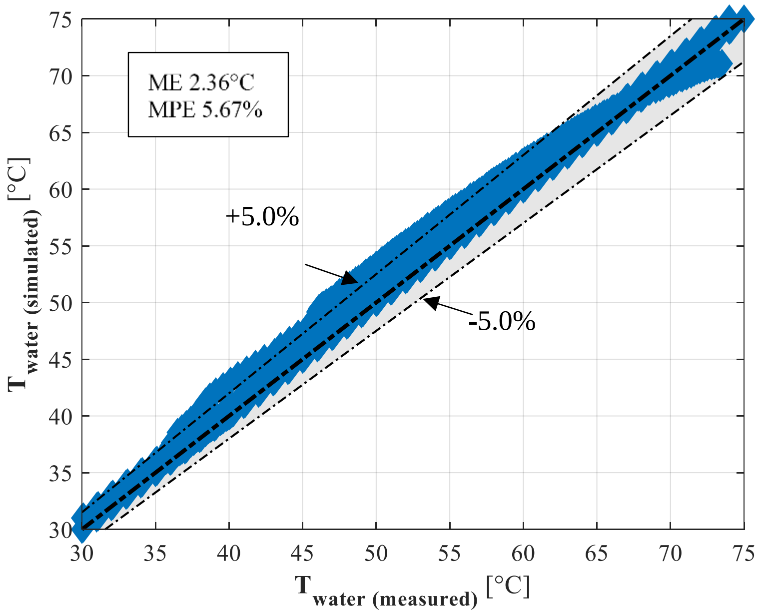

Fig. 3.27. Water air temperature: simulated vs. experimental results (for the entire experimental period).

Specifically, both the mean error and the mean percentage error are assessed according to the following equations:

$$\mathrm{ME} = \frac{1}{Z} \cdot \sum_{z} \left| T_{sim,z} - T_{mea,z} \right|$$
$$\mathrm{MPE} = \frac{1}{Z} \cdot \sum_{z} \frac{\left| T_{sim,z} - T_{mea,z} \right|}{T_{sim,z}} \cdot 100 \tag{3.30}$$

By observing this figure, it can be detected a mean error about 2.36°C and a mean percentage error of 5.67%.

3.7. Conclusions

As it is shown, the performance of a flat-plate solar thermal collector depends on many parameters e.g. material, geometrical features, optical properties, mass flow rate etc. In this chapter a mathematical model based on Hottel-Whillier-Bliss equations is presented. Such a model is able to assess the performance of standard flat-plate solar thermal collector technology. A sensitivity analysis is also carried out with the twofold aim of identifying the main parameters and to find out which of them have the greatest influence on the performance of the investigated technology. The sensitivity analysis is based on twelve parameters and 577 samples were generated with the Sobol sequence. Based on the results provided by the sensitivity analysis, an optimization was conducted. The aim of the presented optimization was to maximize two objective functions: i) thermal efficiency, ii) working fluid outlet temperature. Two optimized flat-plate solar thermal collectors characterized by a high vacuum (0.01 Pa) into the gap spacing were assessed. Two rankings in which the effects of the twelve parameters on thermal efficiency and working fluid outlet temperature are presented. Characteristic curves for the three investigated flat-plate solar thermal collector were assessed and shown as well. In addition, a structural analysis is also conducted with the aim of characterizing both the glass cover and absorber plate thicknesses.

The main findings of this study are summarized in the following list:

- The main six parameters that show a strong correlation with the efficiency and the working fluid outlet temperature were detected: i) plate absorbance, ii) glass cover emissivity, iii) glass extinction coefficient, iv) mass flow rate, v) plate emissivity and vi) gas used.
- Thermal efficiency increases from 0.463 (typical) to 0.718 (optimized).
- Working fluid outlet temperature increases from 52.4 (typical) to 82.6°C (optimized).

The second part of the chapter is dedicated to an innovative high-vacuum solar thermal collector. Such a system is adopted for both collect and store thermal energy. In fact, by means of suitable vacuum space, the convective thermal losses are avoided. In this way, it is possible to store thermal energy without the adoption of a hot water storage tank. In this chapter, a 3-D dynamic simulation model able to assess the energy performance of such a system is introduced. Here, the model is validated by comparing the experimental data with the simulated one. A very good agreement between the simulated and experimental data is achieved.

CHAPTER
4

4. Photovoltaics/thermal collectors

Currently, the commercially available PV/T systems often refer to devices that are still more expensive than alternative cheaper and easier technologies. In the future this issue could be solved by low-cost PV/T collectors.From this point of view, an innovative and low-cost air-based PV/T prototype is described in the present work. For such an innovative device, a dynamic energy performance simulation model is developed and experimentally validated. The model, based on the Hottel-Willier-Bliss approach, is implemented in a MatLab tool. The performance of a combined system obtained by coupling a PV/T prototype to an air-to-air heat pump for space heating is also assessed. The developed tool allows for complete energy and economic analyses of the building and the heating, ventilation and air conditioning (HVAC) system. The potential of the innovative system and the features of the developed simulation tool are analysed through a case study analysis. It refers to the simulation of the energy performance of an array of PV/T collectors mounted on the tilted roof of a two-floor building, which includes a commercial open-space located on the first floor and a single-family house at the second floor. With the aim of providing data about the optimal design and operation of the proposed system as a function of the climate, simulations are performed for different weather zones.

4.1. Aim of the work and content of the chapter

In the literature there are no studies focused on the design of a similar PV/T prototype, the experimental assessment, the system modelling, and the investigation of its performance on an HVAC system application. The main novelties of the present work are:

- new low-cost PV/T collector prototype: design and construction;
- innovative experimental setup including the new PV/T collector prototype;
- experimental analysis of the new PV/T collector prototype under different boundary conditions (hourly weather data, water temperatures, etc.);
- new dynamic simulation model of the new PV/T collector prototype. Suitable performance maps of an air-to-air heat pump coupled to the new PV/T prototype. MatLab tool for the dynamic energy and economic performance analysis of the innovative system;
- novel case study to assess the energy, economic and environmental impact performance of the innovative PV/T-HVAC system for eight different European weather zones.

4.2. Methods and model description

The PV/T prototype is fabricated and tested at Renewable Energy Laboratory of University of Patras (Greece). A suitable experimental setup is used to assess the energy performance of the novel prototype as a function of the tilt angle of the system and the air flow rates. Furthermore, in order to calculate the energy performance of the prototype under different weather conditions, a suitable dynamic simulation model is developed and validated against experimental data. The considered approach is summarised with the help of a synoptic block diagram depicted in Fig. 4.1.

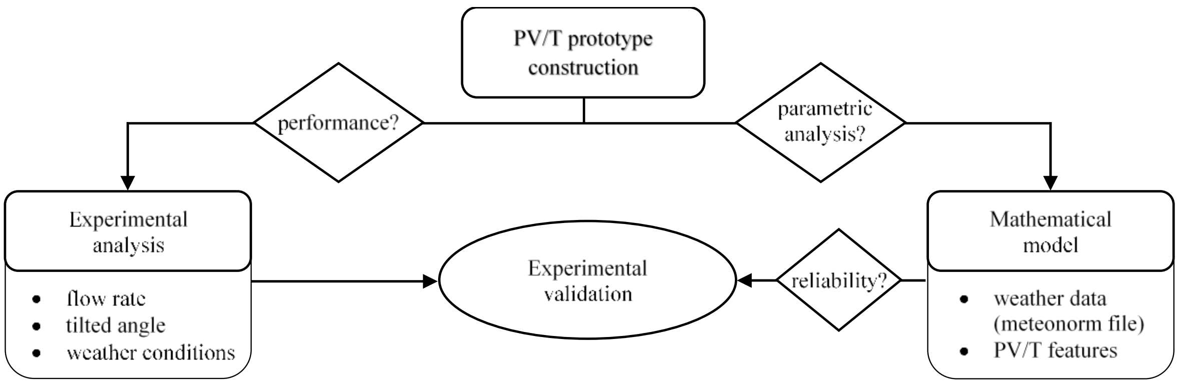

Fig. 4.1. Synoptic block diagram.

4.2.1. Prototype features

The novel PV/T prototype consists of a commercial polycrystalline silicon PV module coupled to a low-cost air-based heat extraction system. Seven hexagonal air ducts are built with two overlapped galvanized corrugated steel sheets typically used for roofing (Fig. 4.2).

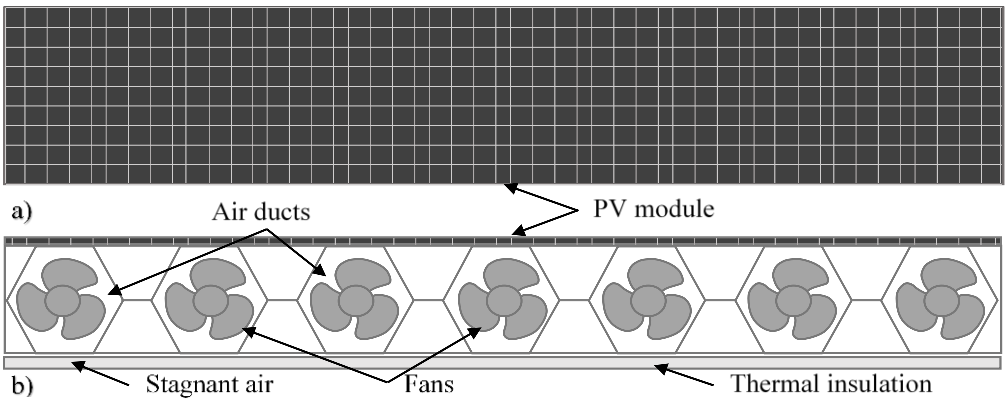

Fig. 4.2. a) PV panel top view b) PV/T collector cross-sectional view.

Table 4.1. Main features of PV/T prototype.

Symbol	Value	Unit	Description
l_{PV}	1.64	m	PV module length
w_{PV}	0.99	m	PV module width
t_{PV}	40.0	mm	PV module thickness
A_{PV}	1.62	m²	PV module gross area
ε_{PV}	0.87	-	emissivity of PV module
□α	0.905	-	absorption coefficient of prototype
t_{ins}	90.0	mm	insulation thickness
ε_{ins}	0.23	-	emissivity of insulation panel
c_{ins}	1340	J/(kg·K)	specific heat capacity of insulation
k_{ins}	0.035	W/(m·K)	thermal conductivity of insulation
t_{duct}	1.28	m	duct length
w_{duct}	67.0	mm	duct width (horizontal)
ξ_{duct}	0.05	mm	duct roughness
s_{duct}	46.0	mm	duct width (oblique)
t_{duct}	22.0	mm	duct thickness
A_{duct}	65.7	cm²	Cross-section area
d_{duct}	80.0	mm	distance between ducts
c_{duct}	470	J/(kg·K)	specific heat capacity steel sheet
d_{duct}	52.0	W/(m·K)	thermal conductivity of steel sheet

The steel sheets are painted black to maximize the system radiative heat transfer (Fig. 4.3a). The air input and the air duct fans are located at the bottom of the solar collector (Fig. 4.3a). The heat extraction system is fixed to the back of the PV module with four aluminium rectangular profiles supports (Fig. 4.3b). Geometrical and thermophysical features of the system are reported in Table 4.1.

The back surface of the heat extraction system is thermally insulated with an extruded polystyrene sheet with a thickness of 30.0 mm (Fig. 4.3c). A reflective coating is placed behind the insulation layer in order to reduce radiation losses to the environment (Fig. 4.3d). Thus, an aluminized Mylar™ sheet is attached on the insulation behind the metallic sheets with commercial glue for polyester materials, as shown in (Fig. 4.3d).

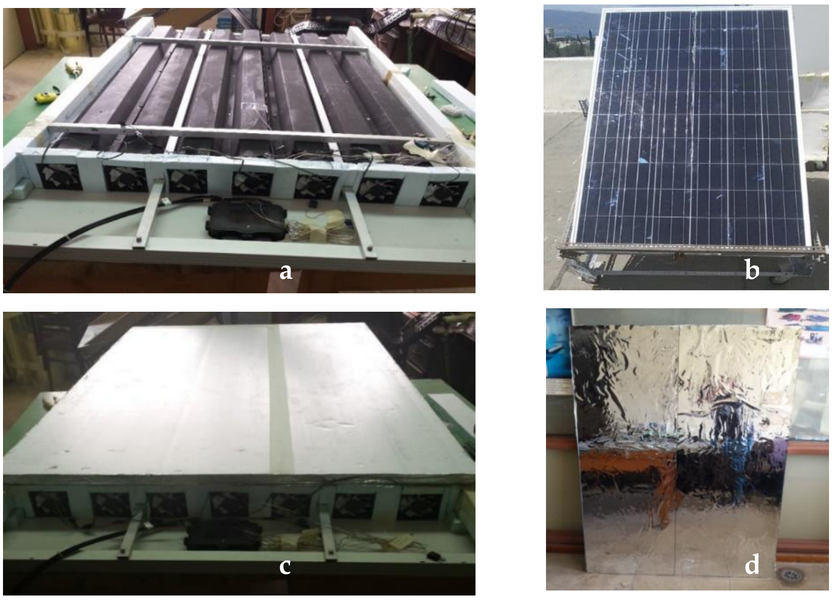

Fig. 4.3. a) Details of the heat extraction system b) PV/T prototype c) Extruded polystyrene sheet insulation d) Reflective coating of the back of the panel.

4.2.2. Mathematical modelling

The performance of the novel PV/T prototype is investigated both numerically and experimentally and the numerical solution results are compared with experimental data for validation purposes. The developed mathematical model is based on Hottel-Whillier-Bliss equations, used to calculate temperatures of the PV cells and the outlet air of the heat extraction system [45]. The main assumptions of the developed mathematical model are:

- steady state conditions;
- negligible temperature gradients around ducts;
- thermal and radiative properties of materials invariable with temperature;
- negligible entry regions effects ($x_{duct}/D_{eq} \approx 4.4 \cdot Re^{1/6}$) and fully developed turbulent flow;
- negligible temperature drops through the cover;
- the sky is considered as a blackbody for the long-wavelength radiation and an equivalent sky temperature is modelled;
- the front and back of the PV/T collector face the ambient air at the same temperature;
- negligible dust and shading effects on the panel;
- constant air speed into the ducts.

<u>Photovoltaic/thermal model</u>

The thermal performance of the PV/T collector is affected by different system design parameters and operating conditions. The PV/T prototype is assumed to be represented as a flat-plate collector with a single unglazed sheet composed of the PV panel working as an absorber. In terms of energy balance on the PV module node, the PV operating temperature (T_{PV}) is calculated as:

$$T_{PV} = \frac{G_{tot}\left(\tau\alpha\right)_{PV}}{\left(h_{out,PV-out} + h_{rad,PV-out}\right)} - \frac{h_{out}T_{amb} + h_{rad}T_{sky}}{\left(h_{out,PV-out} + h_{rad,PV-out}\right)} - \frac{\left(P_{el} + Q_u + Q_{loss}\right)}{A_{PV}\left(h_{out,PV-out} + h_{rad,PV-out}\right)} \tag{4.1}$$

where G_{tot} is the total incident solar radiation, $(\tau\alpha)_{PV}$ is the product between the solar transmittance and the absorbance of the PV panel, $h_{out,PV\text{-}out}$ is the convective heat transfer coefficient between the PV cells and the outdoor air, $h_{rad,PV\text{-}out}$ is the linearized radiative heat transfer coefficient between the PV panel and the sky $\left(h_{rad,PV-out} = \varepsilon_{PV}\sigma\left(T_{PV} + T_{sky}\right)\left(T_{PV}^2 + T_{Sky}^2\right)\right)$, T_{amb} is the ambient temperature, T_{Sky} is the effective sky temperature, P_{el} is the gross electrical power production of the PV/T collector, Q_u is the useful collected heat, and Q_{loss} is the heat loss from the PV/T system to the ambient.

The useful heat Q_u absorbed by the PV/T panel and transferred to the heat transfer fluid is calculated as [45]:

$$\dot{Q}_u = A_{PV}F_R\left[G_{tot}\left[(\tau\alpha)_{PV} - \eta_{PV}\right] - \sum_k U_k\left(T_k - T_{amb}\right)\right] \tag{4.2}$$

where F_R is the heat removal factor representing the ratio between the actual and the useful energy gain of the collector [221], η_{PV} is the electrical efficiency of the PV panel, U_k is the heat loss coefficient between the k-th PV/T component (front of the PV panel and the back of the system) and the ambient (the heat loss related to the edge surface is neglected due to its small surface), and T_k is the average temperature of the k-th PV/T component. Both convective and radiative heat exchanges are taken into account. Therefore, the overall PV/T collector heat loss coefficient can be calculated as

$$U_{PV} = \left(\frac{1}{\frac{C}{T_{PV}}\left[\frac{T_{PV} - T_{amb}}{1+f}\right]^{0.430(1\,+\,100/T_{PV})}} + \frac{1}{h_{out}}\right)^{-1} + \frac{h_{rad}}{\varepsilon_{PV}\left[\left(\varepsilon_{PV} + 5.91\cdot 10^{-3}\cdot h_{out}\right)^{-1} + \frac{1+f-0.967\varepsilon_{PV}}{\varepsilon_{PV}}\right]} \tag{4.3}$$

$$U_{back} = \left(\frac{t_{ins}}{k_{ins}} + \frac{t_{air}}{k_{air}} + \frac{1}{h_{out}}\right)^{-1} \tag{4.4}$$

where f and C are two mathematical operator functions of $h_{out,PV\text{-}out}$, $h_{rad,\,PV\text{-}out}$, ε_{PV} and the tilt angle of the PV/T collector [222], k_{air} and t_{air} are the thermal conductivity and the thickness of the stagnant air between the galvanized steel sheet and the insulation layer, respectively (Fig. 4.2).
Considering eq.(4.2), the heat removal factor is calculated as [223]:

$$F_R = \frac{\dot{m} \cdot c_p}{A_{PV} U_L} \left[1 - \exp\left(-\frac{A_{PV} U_L F'}{\dot{m} \cdot c_p} \right) \right] \tag{4.5}$$

where $\dot{m}$ is the mass air flow rate, c_p is the specific heat of the flowing air, $D_{eq,out}$ and $D_{eq,in}$ are the hydraulic diameter for the inner and outlet duct surface, C_b is bond conductance; and F' is the fin efficiency factor defined as:

$$F' = \frac{(U_L)^{-1}}{d_{duct} \left[U_L \left(D_{eq,out} + \left(d_{duct} - D_{eq,out} \right) F \right) \right]^{-1} + (C_b)^{-1} + \left(\pi D_{eq,in} h_{air} \right)^{-1}} \tag{4.6}$$

The electrical (η_{PV}), thermal efficiency (η_{th}), and the global efficiency are calculated as [224]:

$$\eta_{th} = F_R \left[(\tau\alpha)_{PV/T} - \frac{U_L \left(T_{in} - T_{amb} \right)}{G_{tot}} \right] \tag{4.7}$$

$$\eta_{PV} = \eta_0 \left[1 - \beta \left(T_{PV} - T_{NOCT} \right) \right] \tag{4.8}$$

$$\eta_{tot} = \frac{\dot{Q}_u + P_{el}}{G_{tot} A_{PV}} \tag{4.9}$$

where η_0 is the nominal electrical efficiency at the nominal operating cell temperature (T_{NOCT}), β is a temperature coefficient, and P_{el} is the gross electricity production. Once the thermal and electrical efficiencies are assessed, in order to compute the thermal and electricity gain of the PV/T system, the outlet air temperature of the PV/T system (T_{out}) is calculated as:

$$T_{out} = T_{in} + \frac{\dot{Q}_u}{\dot{m}\, c_p} \tag{4.10}$$

<u>Energy, economic and environmental model</u>

The energy and economic feasibility of the built PV/T system are carried out by means of a suitable thermo-economic model, described below. The developed code is capable of assessing the electricity and the thermal energy produced by the PV/T. The gross electricity production (P_{el}) of the prototype is obtained by:

$$P_{el} = \eta_{el} G_{tot,in} A_{PV} \tag{4.11}$$

where $G_{tot,in}$ is the net incident solar radiation converted into electricity. In the case of a PV/T collectors field, the amount of produced electricity is calculated as:

$$P_{el,field} = \sum_{j=1}^{\Omega} P_{el,j} \tag{4.12}$$

where Ω is the number of the PV/T collectors composing the solar field. The electricity production of the PV/T system can be directly used to supply the compressor electric motor of a heat pump (HP) for building space heating, whereas the air heated by the PV/T collectors can be used to supply the HP evaporator (increasing its performance) [58, 225, 226]. This way, the electricity powering the fans of the heat extraction system is provided from the PV [92]. The electric power necessary for the fans can be calculated as:

$$P_{el\ fans} = \frac{\dot{V} \cdot \Delta p}{\eta_{fans}} \tag{4.13}$$

where $\dot{V}$ is the volumetric air flow rate, Δp is the pressure drop along the ducts and η_{fans} is the fan efficiency. For the sake of clarity, the sketch of the considered innovative system layout is depicted in Fig. 4.4.

The amount of the air flow rate circulating into the PV/T solar field is calculated as:

$$\dot{m}_{field} = \sum_{j=1}^{N} \dot{m}_{air,j} \tag{4.14}$$

where N is the number of collectors connected in parallel.

The mass and energy balance necessary to assess the temperature of the supplied air to the HP evaporator ($T_{HP/PVT}$) are:

$$\dot{m}_{HP} = \dot{m}_{ext} + \dot{m}_{field} \tag{4.15}$$

$$T_{HP/PVT} = \frac{\dot{m}_{field} T_{out\ field} + \left(\dot{m}_{HP} - \dot{m}_{field}\right) T_{amb}}{\dot{m}_{HP}} \tag{4.16}$$

where $\dot{m}_{field}$ is the mass air flow rate from the solar field, $\dot{m}_{HP}$ is the air flow rate required by the HP evaporator, $\dot{m}_{ext}$ is the ambient air flow rate, $T_{out\ field}$ is the outlet air temperature from the solar field, and $T_{HP/PVT}$ is the temperature of the mixed air (due to heated ($\dot{m}_{field}$) and outdoor ($\dot{m}_{ext}$) air).

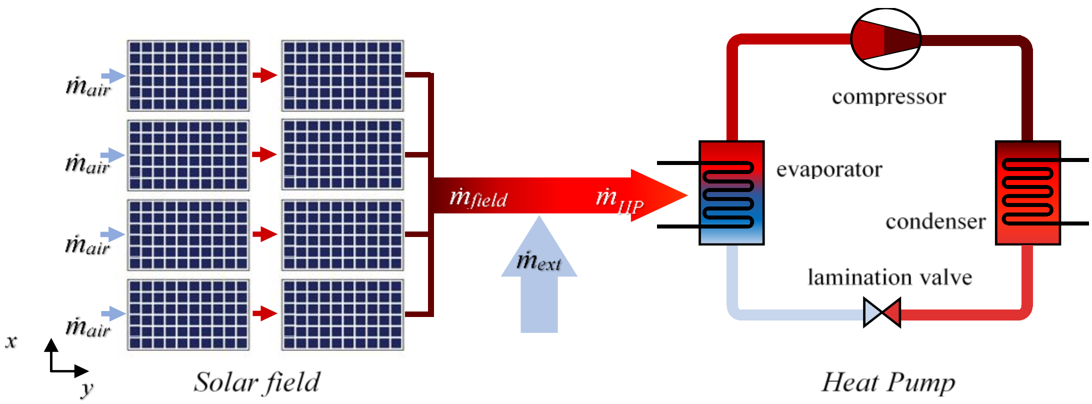

Fig. 4.4. Sketch of the considered innovative system layout: PV/T collectors + HP.

In the developed simulation model, the performance of the HP is modelled in terms of hourly coefficient of performance (COP), analytically calculated, considering the UNI/TS 11300 [227] (Italian release of ISO EN 13790). The $COP_{HP/PVT}$ of the innovative system configuration is evaluated by varying $T_{HP/PVT}$ and it is calculated as [228]:

$$COP_{HP/PVT} = \frac{COP_N}{COP_{max}} \cdot \frac{\vartheta_c + \Delta\vartheta_c}{(\vartheta_c + \Delta\vartheta_c) - (T_{HP/PVT} - \Delta\vartheta_f)} \cdot \frac{4 \cdot f_{PLR}}{0.1 + 3.6 \cdot f_{PLR}} \left[1 - 0.25 \cdot (1 - 4 \cdot f_{PLR})\right] \tag{4.17}$$

where COP_N and COP_{max} are the coefficients of performance at nominal and maximum conditions, θ_c is the heat source temperature, θ_c is the gradient temperature between the heat source and the fluid refrigerator in the HP condenser, θ_f is the gradient temperature between the cold source and the fluid refrigerator in the HP evaporator, and f_{PLR} is the part load ratio (*PLR*, ratio between the actual power to the nominal one). The electricity saving (ΔE_{el}) due to the exploitation at the HP evaporator of the air heated by the PV/T collectors is calculated as:

$$\Delta E_{el} = \sum_N Q_h \left(\frac{1}{COP_{HP,ref}} - \frac{1}{COP_{HP/PVT}} \right) \tag{4.18}$$

where Q_h is the building heating demand. Another considered parameter is the primary energy savings (*PES*), calculated as:

$$PES = \frac{\Delta PE}{PE_{ref}} = \frac{\left(E_{el,requirement} + E_{el,to\ grid}\right)_{ref} - \left(E_{el,\ from\ grid}\right)_{pro}}{\left(E_{el,requirement} + E_{el,to\ grid}\right)_{ref}} \tag{4.19}$$

where ΔPE is the yearly PES, PE_{ref} is the primary energy required by the reference system, $E_{el,requirement}$ is the electricity demand for the whole building (heating, cooling and appliances), $E_{el,\ to\ grid}$ is the electricity sold to the national grid and $E_{el,\ from\ grid}$ is the electricity purchased from the grid. In order to assess the profitability and environmental impact of the innovative system, the economic savings are computed for two different scenarios: i) standard electricity purchase/selling condition, ΔCE; and ii) ideal electricity net metering (all the monthly produced electricity supplied to the grid is delivered to the building when required, $\Delta CE'$. These economic outcomes are assessed as:

$$\begin{aligned} \Delta CE &= \left(E_{el,\ from\ grid} \cdot j_{buy.kWe}\right)_{ref} - \left(E_{el,\ from\ grid} \cdot j_{buy.kWe} + E_{el,to\ grid} \cdot j_{sell.kWe}\right)_{pro} \\ \Delta CE' &= \left(\Delta E_{el} + E_{el,\ field}\right) j_{kWh_e} \end{aligned} \tag{4.20}$$

where $j_{buy,kWe}$ is the electricity unitary cost and $j_{sell,kWe}$ is the electricity unitary selling price.

According to the investigated economic scenarios, the simple pay-back period (*SPB)* and the avoided CO_2 (ΔCO_2) emissions are calculated by:

$$SPB = \frac{A_{PV}\, j_{PV/T}}{\Delta CE} \quad \text{and} \quad SPB' = \frac{A_{PV}\, j_{PV/T}}{\Delta CE'} \tag{4.21}$$

$$\Delta CO_2 = \left(E_{el,\ field} + \Delta E_{el}\right) f_{CO_2} \tag{4.22}$$

where $j_{PV/T}$ is the capital cost per square meter of the innovative prototype, and f_{CO2} is the carbon dioxide emission conversion factor.

4.2.3. Experimental analysis

A suitable experimental setup is built and tested from May to June 2017 in Patras (Greece). The particular period is selected as the most representative according to the monthly distribution of solar irradiance observed in the Greek Peloponnesian region [229]. Specifically, the annual solar irradiance based on climatological data ranges between 1600 and 1700 kWh/m^{2}y. The monthly distribution of solar irradiance on the horizontal surface for the city of Patras is reported in Table 4.2 [230]. The highest irradiance occurs in June (about 7.2 kWh/m^{2}day), whereas the average of the hot season corresponds to the month of May (about 6.0 kWh/m^{2}day). Therefore, these two months, in which the experimental tests are conducted, can be considered as well representative of the summer climate conditions of the considered weather zone.

Table 4.2. Monthly distribution of solar irradiance for the weather zone of Patras [230].

Month	Jan.	Feb.	Mar.	Apr.	May	June	July	Aug.	Sep.	Oct.	Nov.	Dec.
kWh/(m^2·day)	2.14	2.75	3.93	4.92	5.99	7.21	7.10	6.27	4.83	3.38	2.11	1.71

In order to test the prototype performance, different experimental analyses are carried out and several parameters are experimentally assessed. Specifically, 11 T-Type thermocouples connected through a selector to a thermometer (model Mastech ms8229; range of utilization: -270 - 370°C; accuracy ±1.0°C or ±0.75%) are used. With reference to Fig. 4.5 (showing the placement of the thermocouples), several temperature measurements are obtained at the:

i) outlet (T_{out}) and inlet (T_{in}) air flow in the PV/T panel, points *b* and *g*;

ii) top of the PV module front face ($T_{PV\ top,front}$) and back face ($T_{PV\ top,bck}$);

iii) bottom of PV module front face ($T_{PV\ bot,front}$) and back face ($T_{PV\ bot,bck}$), points *d* and *e*;

iv) top of the air duct interior face: up-side ($T_{sheet\ 1,front}$) and down-side ($T_{sheet\ 1,bck}$), points *a*, *b*;

v) bottom of the air duct interior face: up-side ($T_{sheet\ 2,front}$) and down-side ($T_{sheet\ 2,bck}$), points *f*, *h*;

vi) back of the insulation layer (T_{ins}), point *i*.

Using two anemometers (AM-4222; speed range: 0.4 - 30.0 m/s; temperature range: 0 - 50°C; accuracy: ± 1%), the air flow rate ($\dot{m}_{air}$) in the PV/T system and the wind speed are measured. The incident solar radiation (G_{tot}) is measured using a Kipp and Zonen CM11 pyranometer (sensitivity: 10 ◎W/(W/m^2)), tilted at the same angle with the investigated PV/T prototype. Finally, the outdoor air temperature is measured with a T-type thermocouple. In order to assess the PV panel electricity output, four rheostats with a maximum dissipation of 0.25 W at 70°C are connected to two multimeters used for voltage and current measurement. Using these instruments, I-V curves are obtained for different outdoor conditions.

The results of the conducted experimental analyses, for the aforementioned configurations, are presented below. Specifically, the prototype characteristic curves relative to electrical (I-V and P-V curves) and thermal (η_{th} - $\Delta T/G$ curves) performances are shown for several operating conditions.

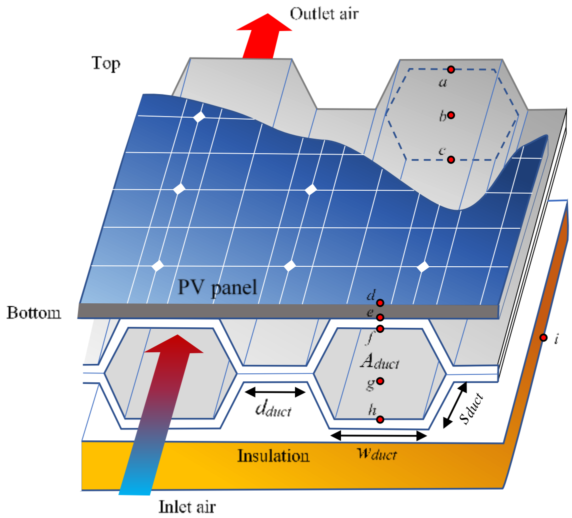

Fig. 4.5. 3-D sketch of the PV/T solar collector and thermocouples arrangement.

Electricity energy performance analysis

Since the PV module in the tested PV/T prototype is a commercial panel, the electrical efficiency is affected by the PV cells operating temperature. In order to assess the PV maximum power point (MPP), four rheostats have been used. Several tests are performed to obtain the I-V and P-V curves, which are necessary to assess the PV module performance. Considering the PV panel without the heat extraction system, the I-V and P-V curves are obtained for different PV temperatures and incident solar radiation values and are shown in Fig. 4.6. The electrical efficiency as a function of the PV temperature is also assessed from the same dataset, as shown in Fig. 4.7.

The electrical efficiency decreases from 16.4 to 14.8% as the PV temperature increases. A good agreement between the trend line related to the experimental measurements (featured by equation $\eta_{el} = - 0.0005 \cdot T_{PV} + 0.1765$; $R^2 = 0.92$) and that referred to the theoretical calculation is observed. For PV temperatures between 35 and 58°C (corresponding to the typical operating conditions), the electrical efficiency estimated by the dynamic simulation model through eq. (4.8) agrees with the experimental results.

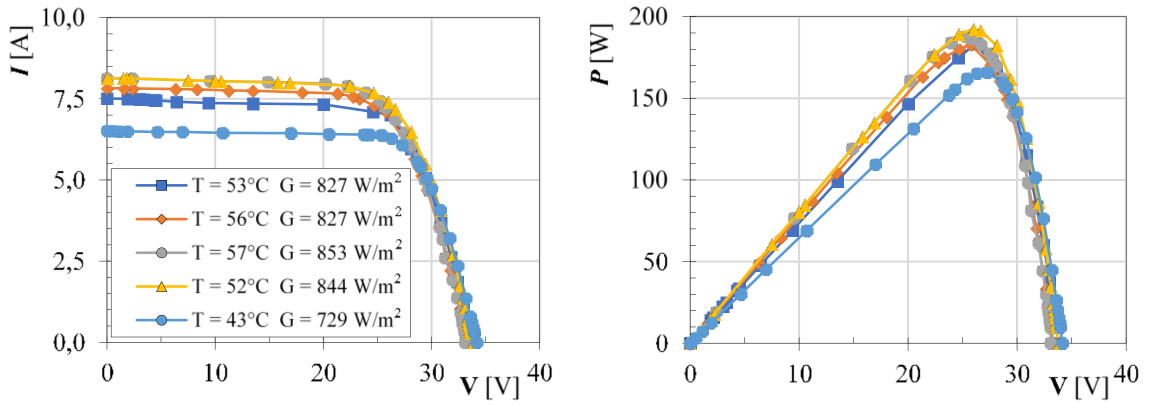

Fig. 4.6. I-V and P-V curves for PV/T prototype.

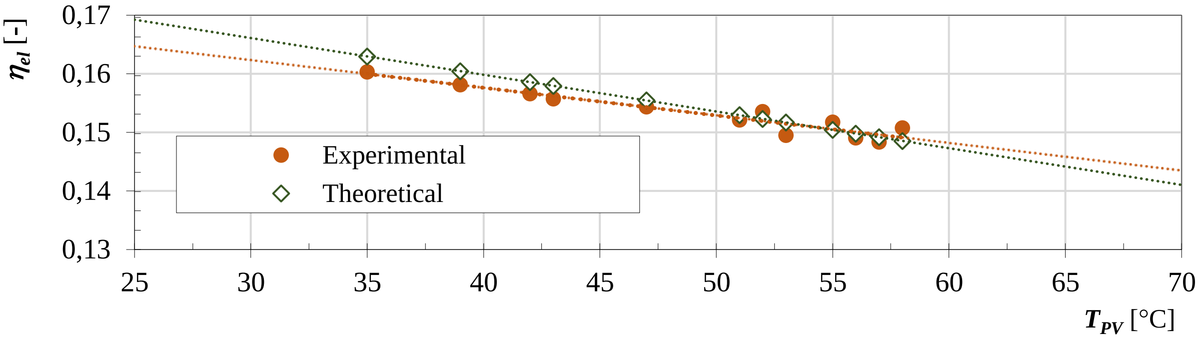

Fig. 4.7. Electrical efficiency as a function of the PV temperature.

Thermal energy performance analysis

The prototype performance is assessed under different boundary conditions and the system energy performance is investigated by taking into account:

- two air flow rates: 153.7 and 368.9 m³/h (corresponding to 0.0523 and 0.123 kg/s);
- three prototype tilt angles: 30, 45 and 60°;
- different weather conditions: sunny/cloudy and windy/no-windy days.

For each tilt angle, the stagnation conditions (with no air flow in the ducts) are also investigated. All measurements are made while the prototype is tracking the sun. A first analysis is performed by varying the collector tilt angle and the air flow rate. Fig. 4.8a shows the measured thermal efficiencies for a flow rate of 153.7 m³/h. The best result is achieved for a tilt angle of 30°, whilst the worst one for 60° (according to solar path in the investigated latitude and for the considered season of the year). Fig. 4.8b shows the results relative to the air flow rate of 368.9 m³/h.

A similar experimental analysis is performed to assess the thermal efficiency of the PV/T prototype for the same air flow rates and fixed tilt angle at the optimal value (30°). The obtained results are depicted in Fig. 4.8c. In this case, the best thermal energy efficiency is achieved for a flow rate of 368.9 m³/h ranging from 25.8 to 31.5%. In Fig. 4.8d, the influence of the wind on the PV/T thermal efficiency is also investigated: no-wind and windy day (average wind speed of 2.57 m/s). In case of no-wind condition an increase of the prototype operating temperature, with a consequent higher η_{th} (Fig. 4.8d) and lower η_{el}, are achieved.

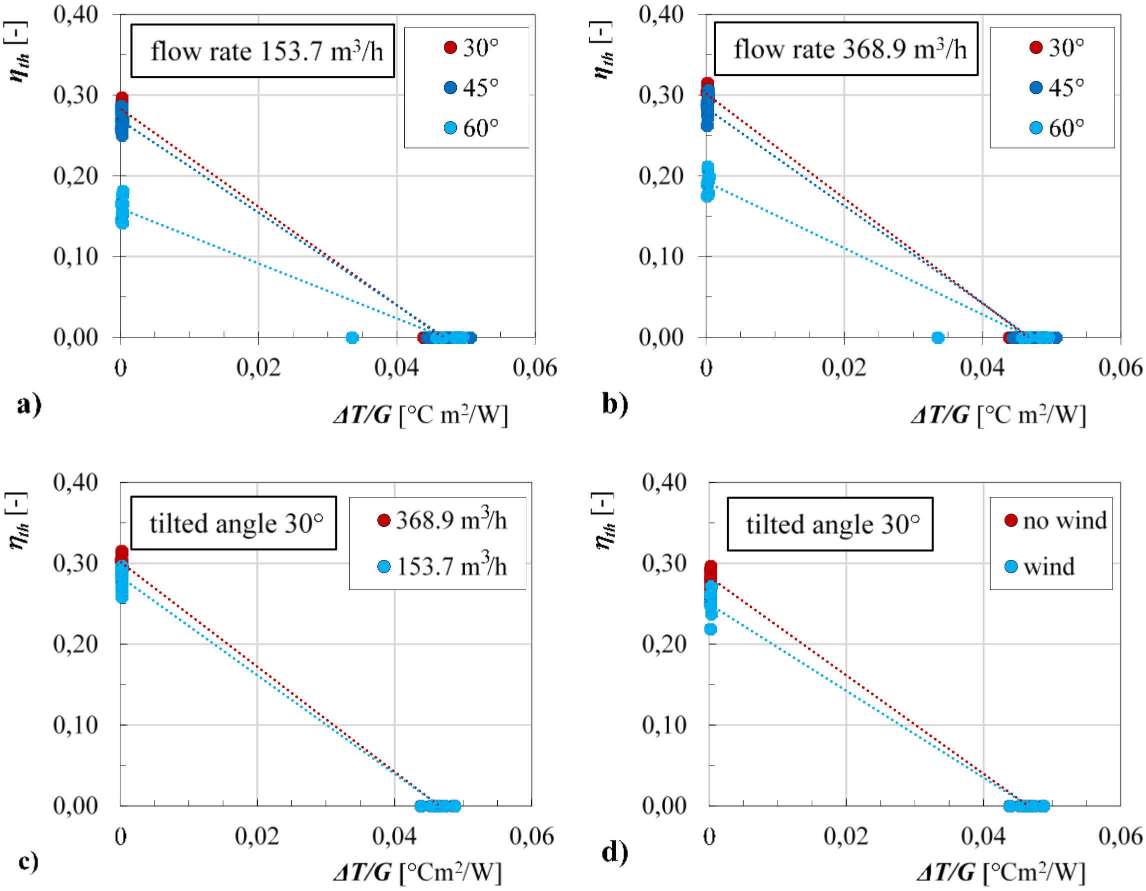

Fig. 4.8. PV/T prototype thermal efficiency with an air flow rate of: a) 153.7 m3/h; b) 368.9 m3/h c) fixed tilted angle 30° d) air flow rate of 368.9 m3/h in case of no wind and windy day.

4.2.4. Experimental validation

The developed dynamic simulation model is validated against the experimental data. The validation process consists of comparing the measured parameters against the calculated ones, relative to the: i) outlet air temperature (T_{out}); ii) PV panel temperature (T_{PV}); and iii) duct temperature (T_{sheet}). In order to assess these parameters, the simulation model requires as input data the: i) air flow rate ($\dot{m}_{air}$); ii) inlet air temperature (T_{in}); iii) ambient air temperature (T_{amb}); iv) incident solar radiation (G_{tot}); and v) wind velocity (w_{wind}). The validation procedure is carried out for all the investigated tilt angles and air flow rates. Nevertheless, for the sake of brevity, only few significant results are discussed and shown hereinafter (similar outcomes are obtained for the remaining working conditions). The reported validation results are summarised in Fig. 4.9 for different air flow rates, tilted angles and weather conditions. Here, during the experimental tests, wavy trends for the investigated temperature were detected. Such trends can be explained because of the high variability of the boundary conditions (e.g. wind, solar radiation).

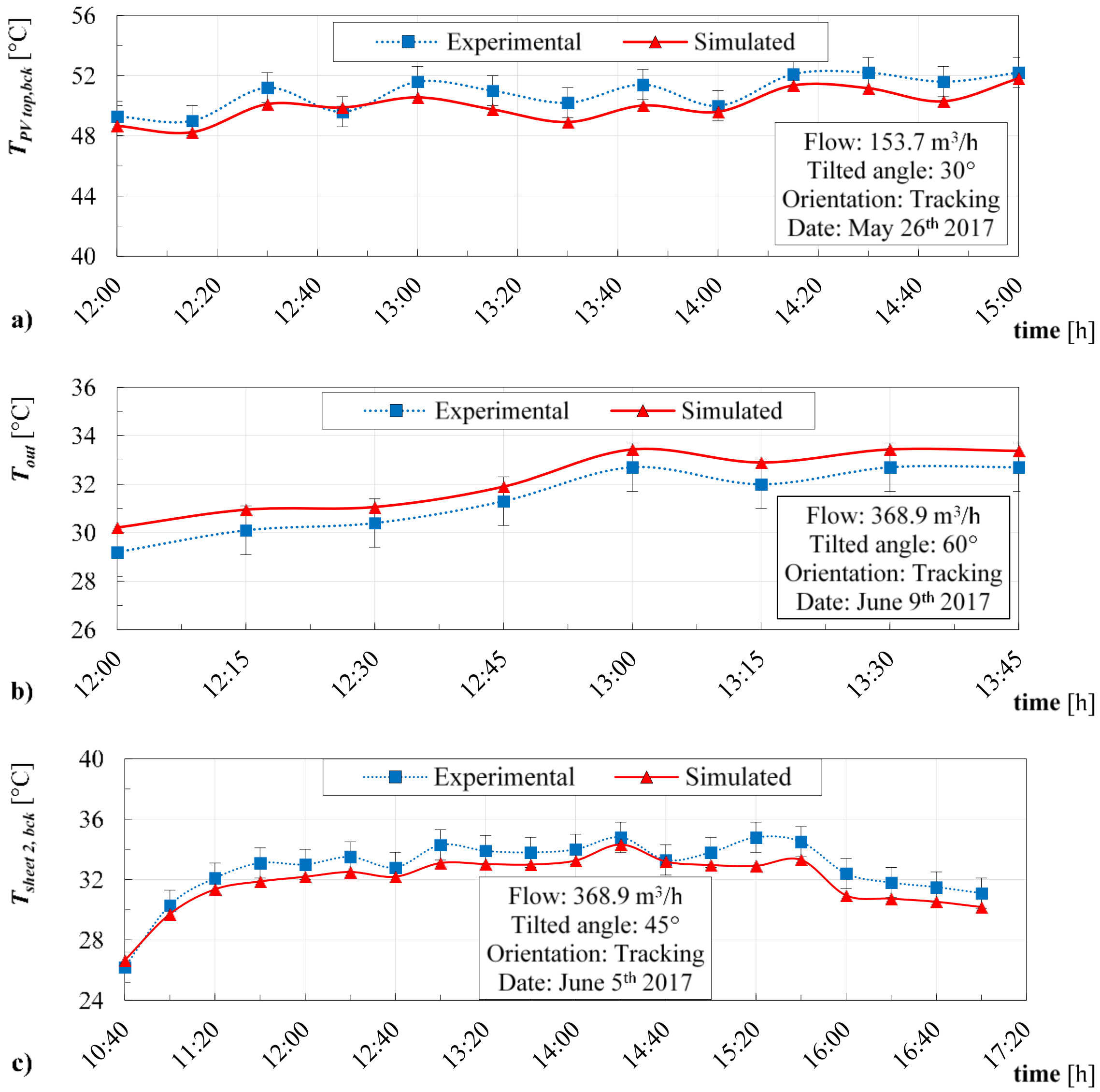

Fig. 4.9. Experimental and simulated, for: a) PV panel temperature b) outlet air temperature c) duct temperature.

An agreement is observed between simulated and measured results for the PV front face average temperature, the outlet air temperature and the duct interior face temperature. Acceptable errors are achieved for all the investigated parameters. The mean percentage errors range from 0.57 to 2.7% for $T_{PV,top,bck}$, from 1.9 to 3.5% for T_{out}, and from 0.22 to 4.2% for $T_{sheet\ 2,bck}$.

4.2.5. Case study

A case study analysis has been conducted in order to show the potential of the proposed system and of the developed simulation tool. The proposed case study analysis refers to an array of PV/T collectors mounted on the tilted roof of a two-floor building, in which a commercial open-space is located on the first floor and a single-family house on the second floor (each of 100 m^2 of floor area). The longitudinal building axis is East–West oriented. The PV/T array consists of 36 PV/T modules (6 rows × 6 columns), with a total gross area of 58.4 m^2. The cost of the single hybrid PV/T system ($j_{PV/T}$) has been estimated equal to 230 € The modelled solar field is South oriented with a tilt angle of 30° (roof slope). The sketch of the building is shown in Fig. 4.10.

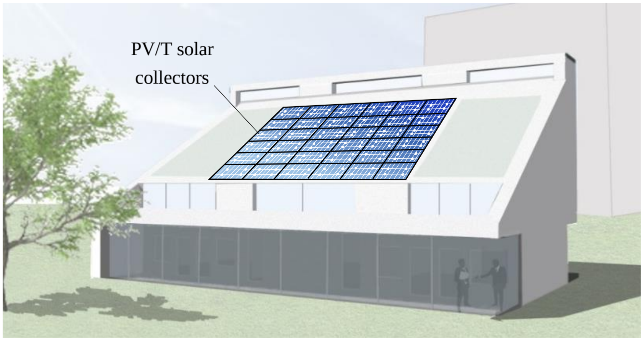

Fig. 4.10. Simulated building.

The building heating and cooling loads and the electricity needs for each floor are calculated by means of an in-house dynamic simulation code called DETECt [231, 232]. The heating and cooling set points are 20 and 25°C, respectively. A single thermal zone is considered for each building floor. Here, internal walls are considered as capacitive and perimeter wall layers include hollow bricks and thermal insulation. All the accounted details for the building envelope are reported in Table 4.3.

Table 4.3. Main features of the building envelope.

Parameter	Value	Unit	Description
t_{wall}	30.0	cm	thicknesses of building external walls
t_{ceil}	25.0	cm	thicknesses of floor/ceiling
U_{wall}	1.32	W/(m²·K)	U-value of the building external walls
U_{ceil}	1.10	W/(m²·K)	U-value of the floor/ceiling
λ_{bricks}	0.33	W/(m·K)	thermal conductivity of the hollow bricks
$\lambda_{ins,wall}$	0.05	W/(m·K)	thermal conductivity of thermal insulation
ρ_{bricks}	1600	kg/m³	density of the hollow bricks
$\rho_{ins,wall}$	13.0	kg/m³	density of thermal insulation
c_{bricks}	1200	J/(kg·K)	specific heat of hollow bricks
$c_{ins,wall}$	1100	J/(kg·K)	specific heat of the thermal insulation
$\alpha_{ext\ wall}$	0.3	-	absorbance of the external wall

A ventilation rate equal to 1.0 Vol/h and a crowding index of 0.12 person/m^2 are considered for the commercial space, whereas a ventilation rate equal to 0.5 Vol/h and a crowding index of 0.03 person/m^2 are taken into account for the house space. The considered interior thermal load for people is 115 W/p at 20°C and 90 W/p at 25°C. The users electricity needs for appliances (including equipment and lighting) follow the schedules reported in Fig. 4.11.

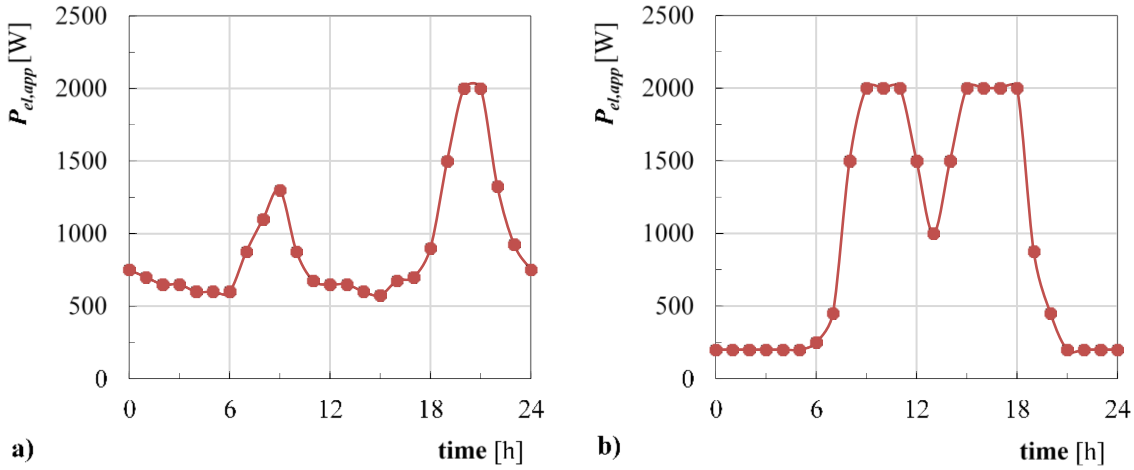

Fig. 4.11. Daily electricity demand profile for light and appliances for the house (a) and the commercial space (b).

For comparison purposes, two different HVAC system configurations are modelled and simulated:

i) an *innovative system configuration* (*HP/PVT*). The outlet air from PV/T collectors (Fig. 4.10) is supplied to the evaporator of the air-to-water HP serving the commercial space, with the aim of increasing its *COP* (calculated as a function of the occurring temperature and load conditions);

ii) a *reference case layout* (HP). Two conventional air-to-water HPs/chillers provide heating and cooling to the commercial and the residential spaces. The building roof depicted in Fig. 4.10 is to be considered without PV/T collectors.

During the summer months for both the commercial space and house, the same chillers are taken into account for both the traditional and innovative system layouts. In addition, the considered HP for the house heating is supplied by outdoor air in case of both reference and innovative system layouts. The HVAC system is switched on from 9:00 to 18:00 for the commercial space, whereas from 16.00 to 22.00 for the house. Yearly simulations start at 0:00 of January 1st and end at 24:00 of December 31st.

Meteonorm hourly data files are used for taking into account all the occurring weather conditions (outdoor air temperature, solar radiation, wind velocity, etc.) 53. The modelled building-plant system is simulated in 8 different European weather zones, featuring cold, temperate, and hot climates. Table 4.4 shows the calculated heating degree days (*HDD*), tilted incident solar radiation ($ISR_{tilted30°}$), and the minimum and maximum yearly outdoor air temperatures of each simulated weather zone.

Table 4.4. Simulated weather zones and related climatic indexes.

City	Country	HDD [K·d]	$ISR_{tilted30°}$ [kWh/(m²·y)]	T_{min} [°C]	T_{max} [°C]
Prague	(CZ)	3853	1600	-15.0	30.5
Freiburg	(DE)	3110	1724	-10.8	33.3
Milan	(IT)	2733	1828	-7.40	32.1
Bolzano	(IT)	2641	1871	-8.80	31.8
Nice	(FR)	1491	2122	1.30	30.2
Naples	(IT)	1479	2139	-1.00	34.3
Athens	(GR)	1060	2100	1.80	37.5
Limassol	(CY)	840	2108	2.90	35.9

For each weather zone, the size of each HP/chiller (one for each space, i.e. residential and commercial) is calculated as a function of the weather conditions. Energy, economic and environmental indexes are reported in Table 4.5. Note that for the calculation of the SPB, for the first investigated scenario (i.e. standard electricity purchase/selling condition, see Section 2.2.2) a 50% capital investment incentive is applied.

Table 4.5. Efficiency for conventional electricity production, carbon dioxide conversion factors and energy tariffs.

Parameter	Unit	CZ	DE	IT	FR	GR	CY
PE conversion factor	[kWh_e/kWh_p]	0.324	0.389	0.460	0.502	0.368	0.389
CO_2 conversion factor	[kg_{CO2}/kWh_e]	0.950	0.624	0.483	0.283	1.149	0.408
Feed-in tariff	[€/kWh_e]	0.079	0.100	0.039	0.029	0.073	0.100
Purchase tariff	[€/kWh_e]	0.188	0.239	0.189	0.168	0.136	0.136

4.3. Results and discussion

This section includes the description of the solar field and HP design. In addition, details about the obtained hourly, monthly and yearly simulation results are provided. For the sake of brevity, discussed hourly and monthly results (Sections 4.3.2 and 4.3.3) are relative to the weather zone of Naples only, whereas the yearly analysis (Section 4.3.4) includes the discussion of the results obtained for all the 8 investigated weather zones.

4.3.1. Solar field and heat pump design

In order to assess the optimal layout of the PV/T array to be coupled to the air-to-water HP for the space heating of the commercial zone, the analysis of the temperature gradient affecting the PV panels performance is carried out. Then, according to the array layout (number of series and parallel panels), the total air flow rate flowing through the PV/T field channels is assessed (being 0.123 kg/s that of a singular PV/T module).

Considering PV/T panels connected in series, the electricity produced by each panel and the corresponding temperature is shown in Fig. 4.12a, whereas the thermal power production and the temperature of the air flowing into each PV/T module is shown in Fig. 4.12b. These results are achieved for an average solar radiation incident on the PV/T collector array of 705 W/m^2 and a mean outdoor air temperature of 18.2°C. The temperature of the air flowing into the panels follows and approaches those of the PV modules (ranging between 29 and 40°C). The air stream cools the PV panels by increasing their electrical efficiency and electricity production only for the initial six/ten PV/T panels in series. In fact, by further increasing the panels in series, the PV and flowing air temperatures tend asymptotically to about 41 and 36°C, respectively. As a result, the cooling effect obtained through the flowing air gradually becomes negligible. For this reason, for cooling purposes an array of maximum 6 PV/T collectors in series should be selected. Furthermore, the idea of coupling PV/T collectors to an air-to-water HP consists of suppling both the obtained thermal energy and electricity to the HP. Therefore, to balance almost all the building electricity demand (HPs/chillers, equipment, etc.), an array of 36 PV/T collectors (6 sets of 6 panels connected in series) is taken into account.

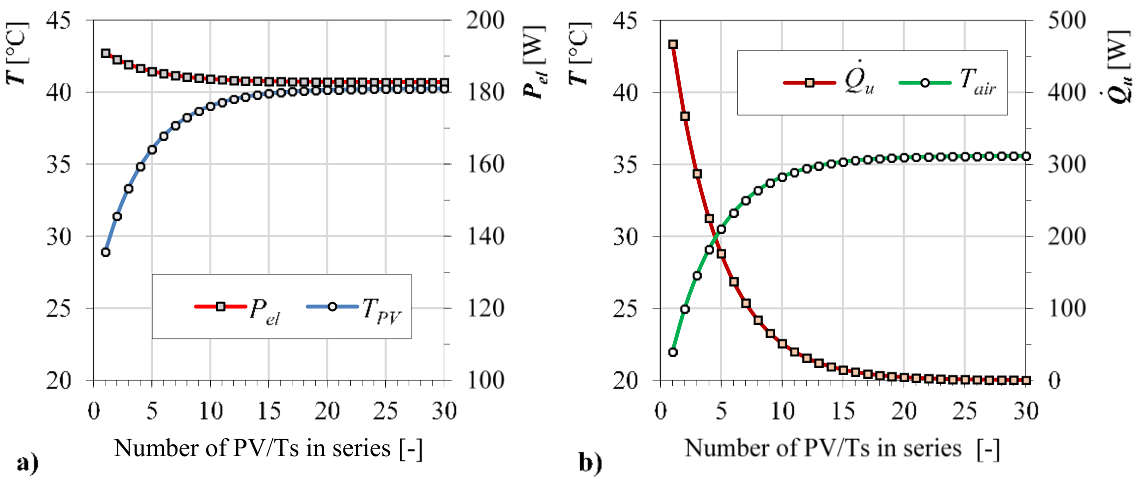

Fig. 4.12. a) Electric power and PV temperature; b) Thermal power and outlet air temperature.

The performance of the innovative system layout (Fig. 4.4) is assessed by varying the related boundary conditions. From the electricity production point of view, in order to avoid an oversized solar field, $\dot{m}_{field}$ has to be lower than $\dot{m}_{HP}$. To meet this requirement and to simultaneously reach the total air flow rate needed by the HP evaporator, $\dot{m}_{field}$ is mixed to outdoor air. In this case study, 59%

of the air flow rate demanded by the HP ($\dot{m}_{HP}$ = 1.26 kg/s) comes from the PV/T array ($\dot{m}_{field}$ = 0.738 kg/s). In Table 4.6, the variation of the outlet air temperature of the PV/T array (T_{out}) and the mixed air temperature to be supplied to the HP evaporator ($T_{HP/PVT}$, obtained by mixing 59% of the required air flow rate at T_{out} and the remaining 41% at T_{amb}) are assessed by varying the outdoor air temperature (T_{amb}, from 0 to 18°C) and the solar radiation (*G*, from 100 to 1000 W/m^2).

Table 4.6. Air temperature growth for different solar radiation and outdoor air temperatures ($\dot{m}_{field}$ = 0.738 kg/s and $\dot{m}_{HP}$ = 1.26 kg/s).

T_{amb}	G = 100 W/m²		G = 300 W/m²		G = 600 W/m²		G = 900 W/m²		G = 1000 W/m²	
	T_{out}	$T_{HP/PVT}$	T_{out}	$T_{HP/PVT}$	T_{out}	$T_{HP/PVT}$	T_{out}	$T_{HP/PVT}$	T_{out}	$T_{HP/PVT}$
[°C]										
0	2.27	1.33	6.80	3.98	13.6	7.95	20.3	11.9	22.6	13.2
1	3.27	2.33	7.79	4.98	14.6	8.95	21.3	12.9	23.5	14.2
2	4.27	3.33	8.79	5.98	15.6	9.94	22.3	13.9	24.5	15.2
3	5.26	4.33	9.79	6.98	16.5	10.9	23.3	14.9	25.5	16.2
4	6.26	5.33	10.8	7.97	17.5	11.9	24.3	15.9	26.5	17.2
5	7.26	6.33	11.8	8.97	18.5	12.9	25.2	16.9	27.5	18.2
6	8.26	7.32	12.8	9.97	19.5	13.9	26.2	17.8	28.4	19.2
7	9.26	8.32	13.8	11.0	20.5	14.9	27.2	18.8	29.4	20.1
8	10.3	9.32	14.8	12.0	21.5	15.9	28.2	19.8	30.4	21.1
9	11.3	10.3	15.8	13.0	22.5	16.9	29.2	20.8	31.4	22.1
10	12.3	11.3	16.8	14.0	23.5	17.9	30.2	21.8	32.4	23.1
11	13.3	12.3	17.7	15.0	24.5	18.9	31.1	22.8	33.3	24.1
12	14.3	13.3	18.7	16.0	25.5	19.9	32.1	23.8	34.3	25.1
13	15.2	14.3	19.7	16.9	26.4	20.9	33.1	24.8	35.3	26.1
14	16.2	15.3	20.7	17.9	27.4	21.9	34.1	25.8	36.3	27.1
15	17.2	16.3	21.7	18.9	28.4	22.9	35.1	26.8	37.3	28.0
16	18.2	17.3	22.7	19.9	29.4	23.9	36.0	27.7	38.2	29.0
17	19.2	18.3	23.7	20.9	30.4	24.8	37.0	28.7	39.2	30.0
18	20.2	19.3	24.7	21.9	31.4	25.8	38.0	29.7	40.2	31.0

The obtained values of the $COPs_{HP/PVT}$ of the solar assisted HP, calculated by varying T_{amb} and G, are reported in Fig. 4.13, together with the *COPs* of a typical HP ($COPs_{ref}$, which only depends on the outdoor temperature).

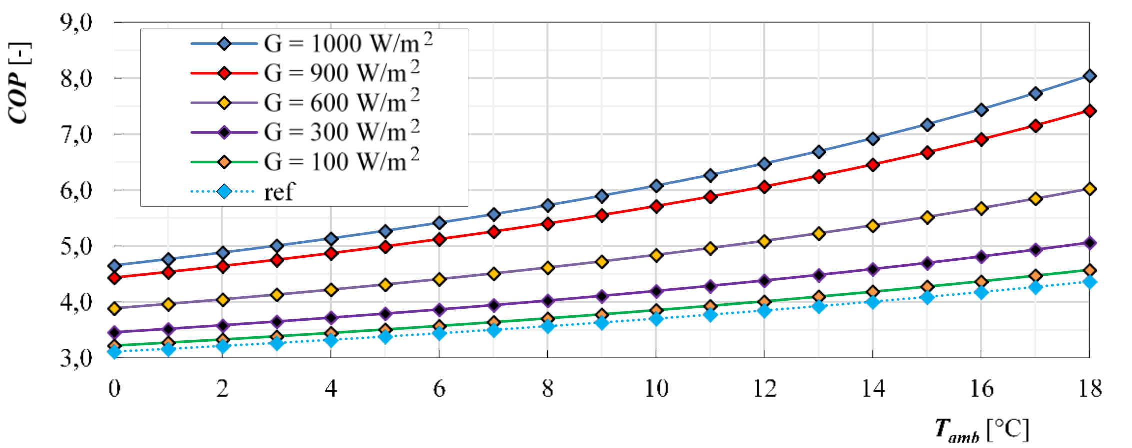

Fig. 4.13. Commercial space HP: $COP_{HP/PVT}$ and COP_{ref} (design conditions)

This figure shows the increase of the *COPs* with respect to the reference case as well as to the incident solar radiation level. Supplying the HP evaporator with air flow rate at the $T_{HP/PVT}$ temperature (Table 4.6), the *COPs* can even double the reference value. This clearly shows how remarkable energy savings can be achieved from the innovative system layout.

4.3.2. Hourly analysis

The calculated hourly heating and cooling loads of the commercial space of the examined building are depicted in

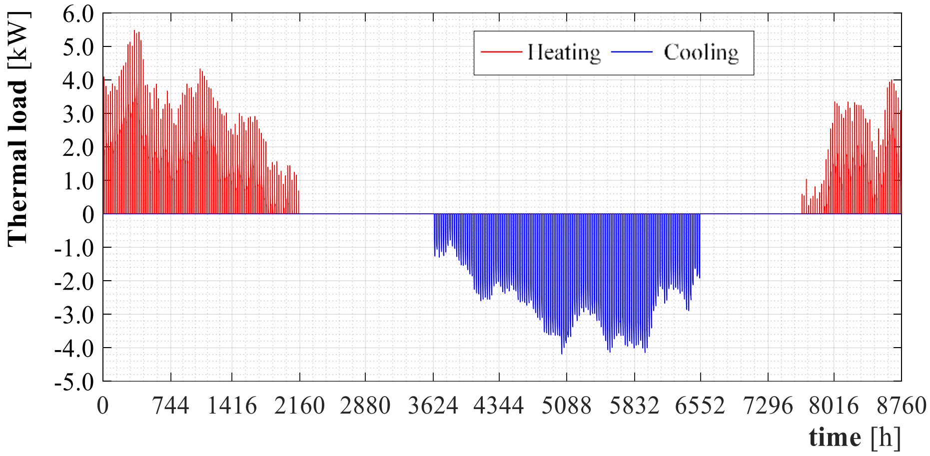

Fig. *4.14*. According to the adopted strategy considered for the case study, with the HP switched off during the summer season, the air flowing into the solar collectors is used for PV cells cooling purposes only. For this reason, the reported summer results are relative only to the electricity production of the PV/T array, whereas for the winter results the benefits due to the coupling of the PV/T collectors to the HP are also take into account (discussed at Section 4.3.1).

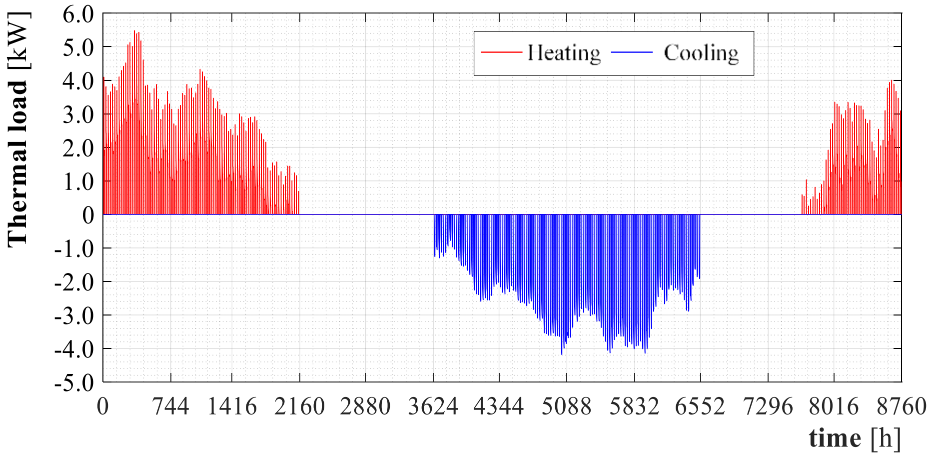

Fig. 4.14. Heating and cooling loads and demands of the considered commercial space.

In the following Figs. 6.15 - 6.23, several results relative to three summer (June the 29th and 30th, and July 1st) and winter (January the 12th, 13th and 14th) sample days are reported.

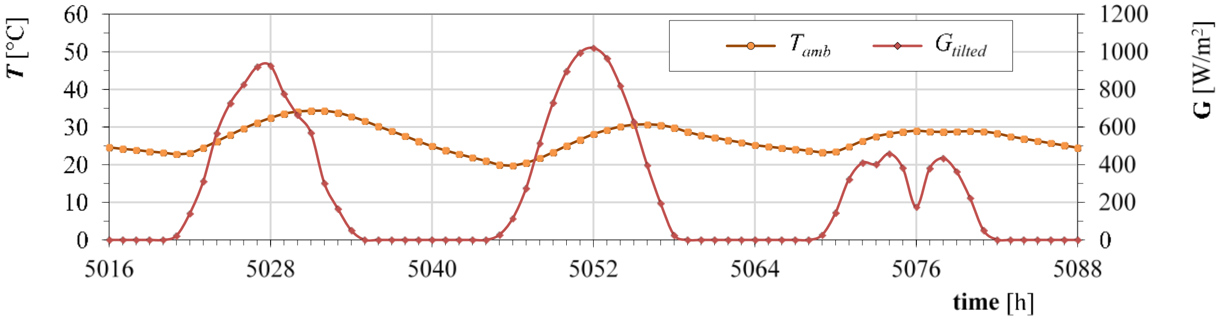

Fig. 4.15. Outdoor air and incident solar radiation at the first, third and sixth in series PV/T collector in June 29th and 30th and in July 1st.

Concerning the summer analysis, Fig. 4.15 shows the time histories of the outdoor air temperature and solar radiation incident on the panels, whereas Fig. 4.16 shows the obtained PV/T collectors outlet air and surface temperatures.

Regarding Fig. 4.16a, the reported temperature profiles are relative to the outlet air from the first, third and sixth PV/T collectors connected in series. The maximum temperature is achieved around noon (when the highest solar incident radiation occurs), while the maximum working fluid temperature (about 20.3°C on June 29th) is achieved at the outlet of the sixth PV/T panel (the last one in series for each array column). Similar comments can be carried out for the surface temperatures of the PV panels, Fig. 4.16b.

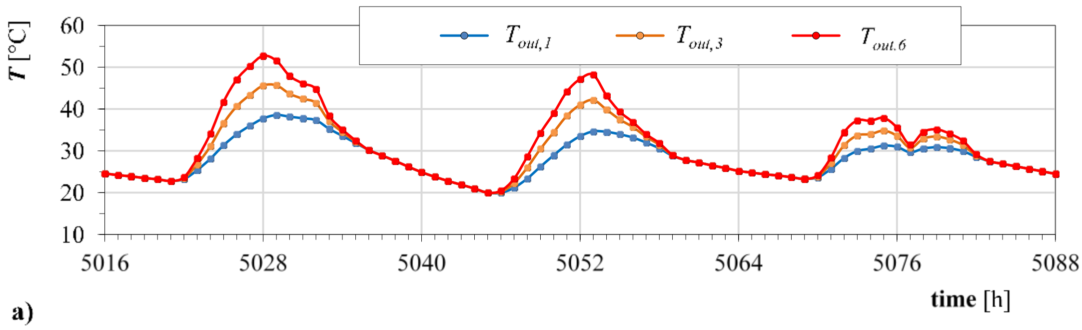

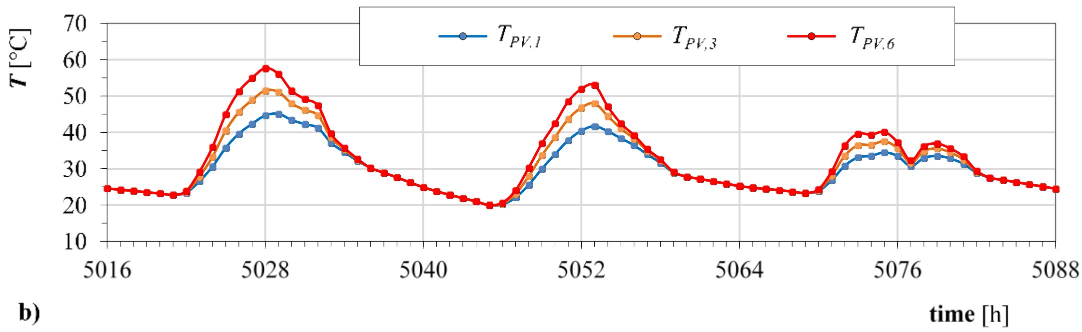

Fig. 4.16. Temperature of the outlet working fluid (a) and PV module (b), at the first, third and sixth in series PV/T collector in June 29th and 30th and in July 1st.

Fig. 4.17 shows the time histories of the extracted thermal power from the first, third and sixth PV/T collectors connected in series.

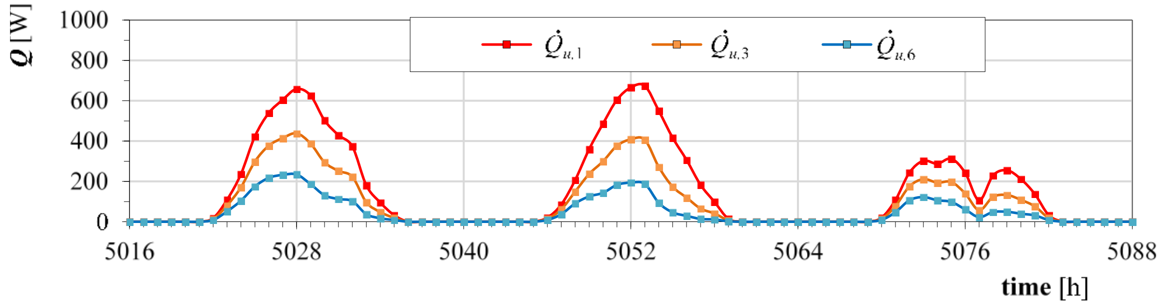

Fig. 4.17. Exhausted heat of the first, third and sixth PV/T collector in June 29th and 30th and July1st.

The heat extracted from the first PV/T collector is higher than the heat extracted from the last panel, since the thermal efficiency decreases as the temperature increases. As an example, at the 5028th hour, the extracted heat from the first PV/T collector is 625 W with respect to 234 W for the last panel.

In Fig. 4.18, the electrical efficiency of the system and the electricity production of the first, third and sixth PV/T collectors are reported for the same summer sample days. The lower the PV panel temperature, the higher the related electrical efficiencies and produced electricity. For the considered case study, a slight decrease in the electrical efficiency is detected between the first and the sixth PV/T panels connected in series (in Fig. 4.18 a maximum loss of about 5% is observed at the 5028th hour).

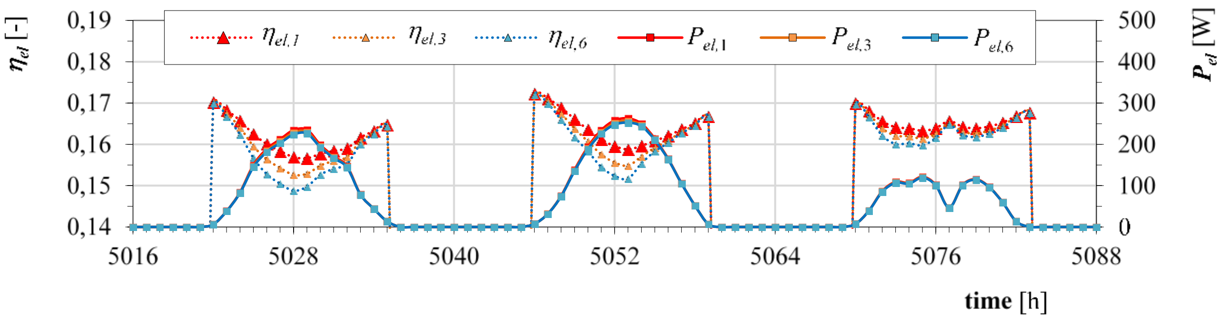

Fig. 4.18. Electrical efficiency and produced electricity of the first, third and sixth PV/T collector in June 29th and 30th and July 1st.

Shifting to the winter days, the time series of outdoor air temperatures and incident solar radiations of the three winter sample days are depicted in Fig. 4.19, whereas the obtained PV/T collectors outlet air and surface temperatures are reported in Fig. 4.20. Here, it can be observed that the temperatures are lower than those obtained during the summer time.

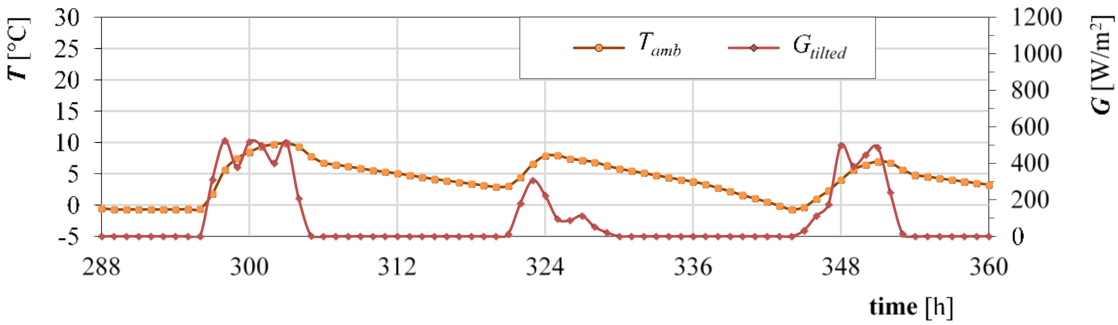

Fig. 4.19. Outdoor air and incident solar radiation at the first, third and sixth in series PV/T collector in January 12th-14th.

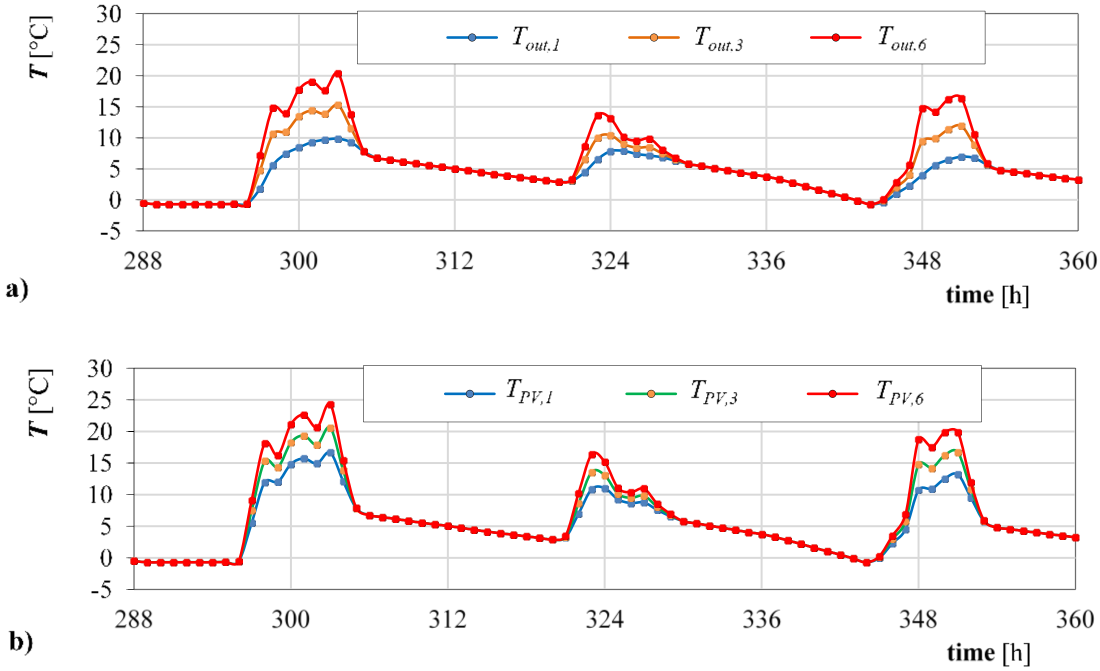

Fig. 4.20. Temperature of the outlet working fluid (a) and PV module (b), at the first, third and sixth in series PV/T collector in January 12th-14th.

Fig. 4.21a shows the time histories of the thermal efficiency and thermal power (recovered heat) from the first, third and sixth simulated PV/T collectors.

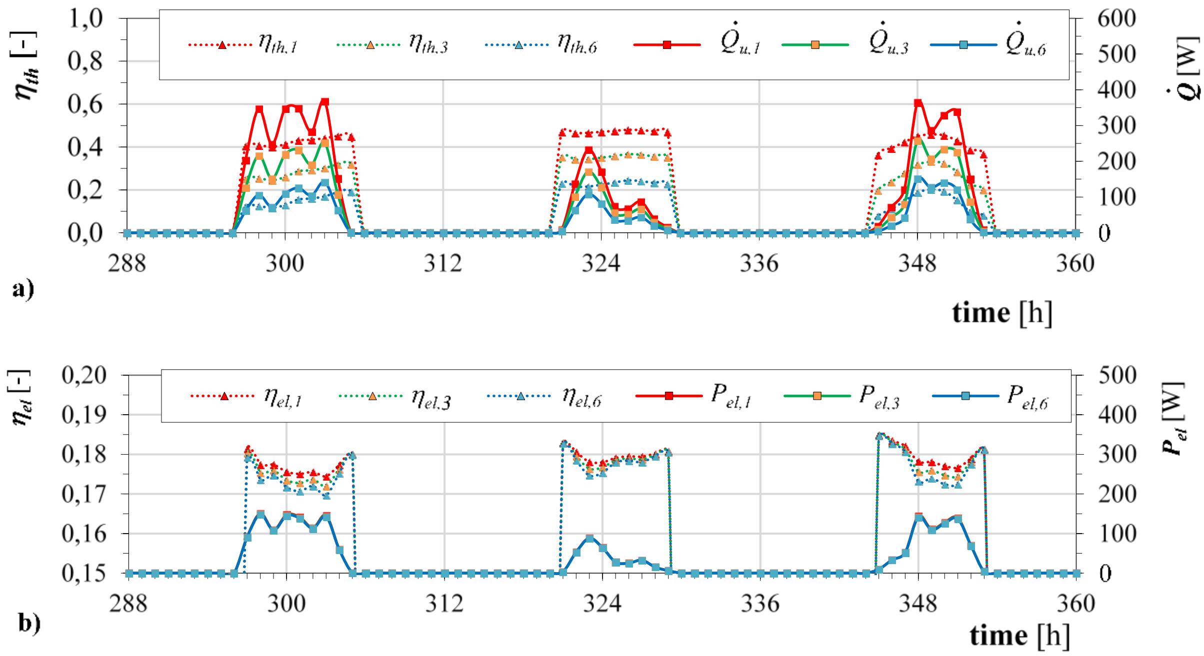

Fig. 4.21. a) Thermal efficiency and recovered heat b) electric efficiency and electricity produced, at the first, third and sixth in series PV/T collector in January 12th-14th.

The average thermal efficiency range between 20 and 40% shifting from the sixth to the first collector. The thermal power obtained from each collector in winter, is significantly lower than the corresponding thermal power obtained in summer. In Fig. 4.21b, for the same winter hours, the system electrical efficiency and the electricity production of the third and sixth PV/T collectors are reported. With respect to the summer results (Fig. 4.18), higher electrical efficiency and lower electricity production are obtained.

In Fig. 4.22, for the same winter sample days, the time histories of the electricity load/need and *COPs* are shown for the HP of the commercial space. Here, the reference case HP electricity power need ($P_{el\ HP}$) and COP_{HP} can be compared to the innovative system ones ($P_{el\ HP/PVT}$ and $COP_{HP/PVT}$). A remarkable decrease is achieved on the electricity demand of the solar assisted HP (red area in Fig. 4.22) due to the growth of the related *COP* compared to the reference system ones. As an example, for the coldest winter day (January 14th), the reference case electricity need ($E_{el,HP}$) is 3.92 kWh/day, whereas for the innovative system layout ($E_{el,HP/PVT}$) it is equal to 2.97 kWh/day, with a saving (ΔE_e) of 0.92 kWh/day (24.2%). Heat pump *PLR* conditions are taken into account in the system energy performance assessment. Specifically, in case of *PLR* conditions, lower air flow rates supplied to the HP evaporator occur. The lower the *PLR* the higher the percentage of air heated by the PV/T collectors fed to the HP evaporator. Therefore, by decreasing *PLR* higher temperatures and higher *COPs* are detected.

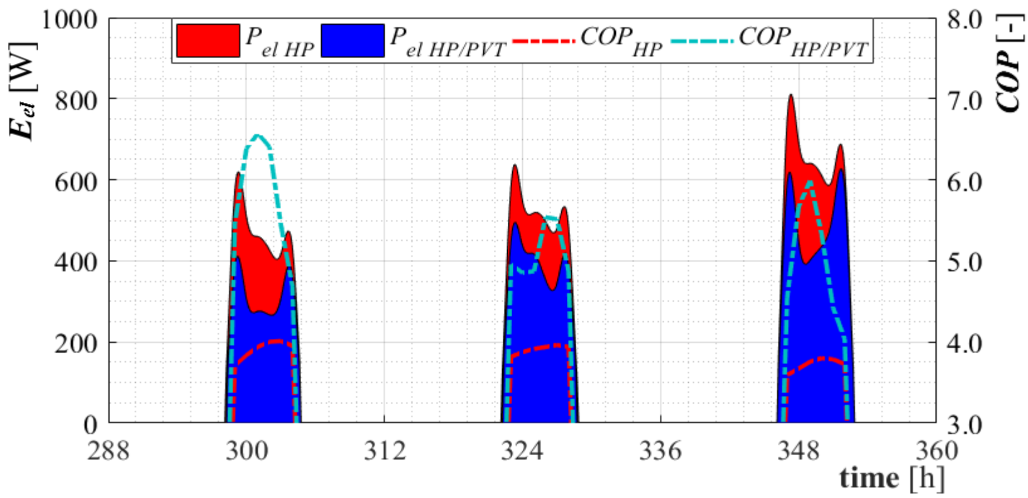

Fig. 4.22. Electricity load/need and *COP* of the commercial space HP in January 12th-14th.

For the same winter sample days, Table 4.7 shows the whole building electricity demand ($E_{el,demand}$, about 142.2 kWh - including appliances and HPs), the amount of $E_{el,demand}$ balanced by the grid ($E_{el,from\ grid}$), the electricity production from the PV/T field ($E_{el,PVTtot}$), and the amount of $E_{el,PVTtot}$ delivered to the building ($E_{el,from\ PVT}$).

Table 4.7. Whole building electricity demand and production in January 12-14th.

$E_{el,demand}$ [kWh]	$E_{el,from\ grid}$ [kWh]	$E_{el,from\ PVT}$ [kWh]	$E_{el,from\ PVT}$ [%]	$E_{el,PVTtot}$ [kWh]	$E_{el,PVTtot}$ [%]
142.2	95.9	46.3	32.6	74.4	52.3

For these days, the electricity produced by the PV/T field balance about 32.6% of $E_{el,demand}$ (about 46.3 kWh, self-consumption). The remaining amount of electricity is supplied to the building from the grid (about 59.9 kWh). It is noteworthy that although the solar collectors produce a significant amount of the building electrical demand (about 74.4 kWh, corresponding to 52.3% of $E_{el,demand}$), because of the mismatch between production and demand, a significant amount of PV electricity production is exported and sold to the grid (28.1 kWh).

To better understand the existence of renewable electricity surplus (despite the considerable building demand), a daily graph is presented. Specifically, for January 12-14th, Fig. 4.23 depicts the electricity PV/T system production and the electricity demand of the whole building (dark yellow area), as well as the electricity needs due to the solar assisted HPs of the commercial space and the house (green and red area, respectively).

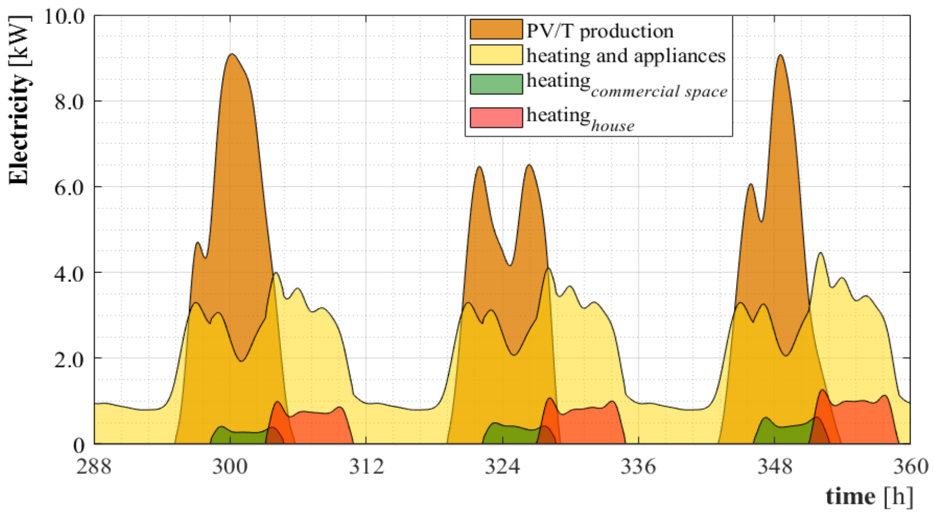

Fig. 4.23. Electricity production and demand for the whole building equipped by PV/T collectors in January 12th-14th.

Fig. 4.23 clearly shows that although remarkable building electricity needs are balanced by the PV/T collectors production, a significant surplus (exported to the grid) is observed in the central hours of the day.

4.3.3. Monthly analysis

Concerning the building commercial space, Table 4.8 shows the electricity demands for:

- space heating of the reference traditional system ($E_{el,heating}$ (ref));
- space heating of the innovative proposed system ($E_{el,heating}$ (pro));
- for space cooling ($E_{el,cooling}$).

This table clearly shows that the electricity needs of the solar assisted HP ($E_{el,heating}$ (pro)) are always lower than those of the traditional HP system ($E_{el,heating}$ (ref)). Monthly electricity savings range from 0.30 kWh/month in November to 15.0 kWh/month in January (between 10% in November and 18% in March) whereas for the proposed system the electricity needs for space cooling does not vary.

Table 4.8. Monthly electricity demands and savings of the commercial space HP/chiller.

	Jan	Feb	Mar	Apr	May	Jun	Jul	Aug	Sep	Oct	Nov	Dec
						[kWh$_e$/month]						
$E_{el,\ heating\ (ref)}$	121	71	16	-	-	-	-	-	-	-	2.8	54
$E_{el,\ heating\ (pro)}$	106	61	13	-	-	-	-	-	-	-	2.5	47
$E_{el,\ cooling}$	-	-	-	-	-	136	291	340	233	-	-	-
ΔE_{el}	15.0	10.3	2.9	-	-	-	-	-	-	-	0.30	6.1
ΔE_{el} (%)	12.3	13.9	18.5	-	-	-	-	-	-	-	10.5	11.3

Concerning the whole building equipped with PV/T collectors, Fig. 4.24. shows the monthly:

- total electricity demand ($E_{el,tot}$);

- gross produced electricity ($E_{el,field}$, computed without the electricity consumption of the PV/T fans);
- net produced electricity ($E_{el,field,net}$, computed by subtracting to $E_{el,field}$ the electricity consumption of the PV/T fans);
- electricity purchased from the grid ($E_{el,from\ grid}$, computed without net metering)
- electricity sold to the grid ($E_{el,to\ grid}$, computed without net metering).

Regarding the building electricity demands, only the electricity required by the commercial space HP varies by shifting from the reference case to the innovative one. Note that the monthly results are obtained by activating the fans of the PV/T collectors just in case of HP use. In Fig. 4.24. this is clearly visible during the winter months with $E_{el,field}$ higher than $E_{el,field,net}$. Such an operating strategy, adopted for maximizing the yearly overall energy efficiency of the coupled PV/T-HP system, is not considered in the above discussed hourly analysis (where the fans are continuously activated in sunny hours for cooling purposes). By such a low-consumption strategy, a very small amount of electricity is required by the fans (about 95.3 kWh/year), corresponding to 0.6% of the gross electricity production ($E_{el,field}$ is equal to 16.2 MWh/year). During the winter season the electricity production of the PV/T field balances the building demand ($E_{el,tot}$) from 32.9% in January to 55.1% in March; the remaining demand is balanced with electricity delivered from the grid ($E_{el,\ from\ grid}$). Note that, $E_{el,\ from\ grid}$ is rather low in the summer period, since the PV/T field produces a significant amount of building electricity needs. Nevertheless, a relevant amount of the electricity from PV/T collectors is sold to the grid ($E_{el,\ to\ grid}$), due to the mismatch between production and demand.

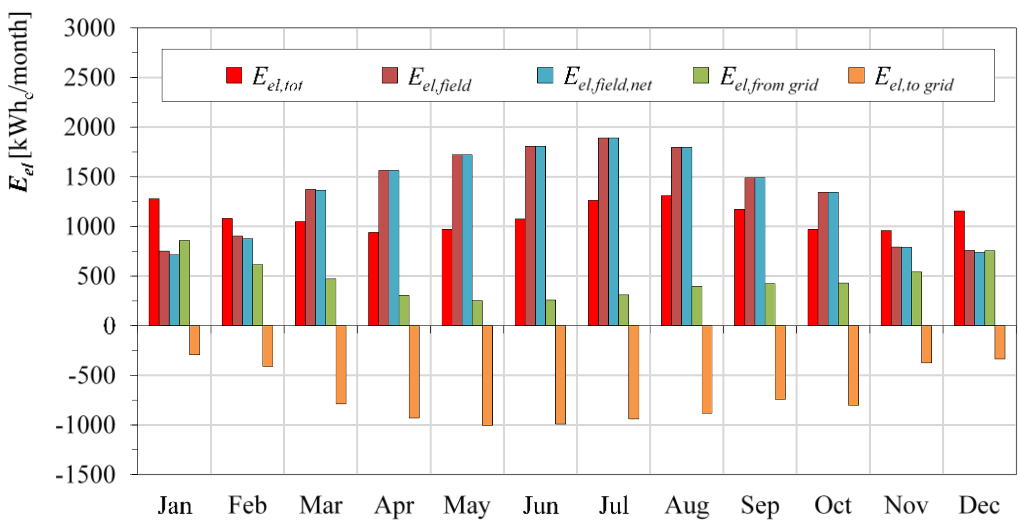

Fig. 4.24. Monthly electricity fluxes of the innovative system (no net metering).

4.3.4. Yearly analysis

The discussion of the yearly results is relative to all the 8 investigated weather zones, reported in Table 4.4. To this aim, Table 4.9 shows the electricity needs of the reference case building, due to space heating ($E_{el,\ heating}$), space cooling ($E_{el,\ cooling}$), and appliances ($E_{el,\ appliances}$).

Table 4.9. Reference case: electricity demand for the entire building.

Weather zone	$E_{el,\ heating}$ [kWh$_e$/y]	$E_{el,\ cooling}$ [kWh$_e$/y]	$E_{el,\ appliances}$ [MWh$_e$/y]
Prague	4578	44	11.43
Freiburg	3319	158	
Milan	3105	598	
Bolzano	2904	611	
Nice	734	750	
Naples	829	1000	
Athens	503	1364	
Limassol	460	1406	

Table 4.10 shows the electricity production from the PV/T collectors ($E_{el,\ field}$), the net one ($E_{el,\ field\ (net)}$) obtained by deducting the fans electricity needs ($E_{el,\ fans}$), and the savings of electricity for space heating ($\Delta E_{el,\ heating}$), also reported as percentage difference. The higher the solar radiation, the higher the electricity production by the PV/T field. Increasing the solar radiation, a non-linear growth of the electricity production is detected (because of the PV electrical efficiency decrease due to overheating). The percentage of the yearly electricity consumption related to the PV/T collectors fans, $E_{el,fan}$, calculated with respect to $E_{el,\ field}$ ranges from 0.31% in Limassol to 1.76% in Prague. Note that also the yearly results are obtained by activating the fans of the PV/T collectors just in case of HP use.

Table 4.10. Innovative system layout: electricity production and whole building saving.

Weather zone	$E_{el,\ field}$	$E_{el,\ field\ (net)}$	$E_{el,\ fan}$		$E_{el,\ heating}$	$\Delta E_{el,\ heating}$	
	[MWh$_e$/y]	[MWh$_e$/y]	[kWh$_e$/y]	[%]	[kWh$_e$/y]	[kWh$_e$/y]	[%]
Prague	11.04	10.84	195	1.76	4467	112	7.04
Freiburg	12.12	11.94	185	1.53	3224	95	8.05
Milan	12.70	12.52	174	1.37	2997	107	9.89
Bolzano	14.00	13.84	157	1.12	2804	100	10.2
Nice	16.45	16.34	106	0.64	695	39	16.6
Naples	16.20	16.10	95	0.59	795	34	12.9
Athens	16.46	16.40	69	0.42	479	24	16.9
Limassol	19.78	19.72	61	0.31	430	30	27.9

Since in Limassol the yearly heating demand is lower than that one calculated in Prague, a corresponding lower electricity consumption of these fans is detected. The energy saving due to the solar assisted HP, ranging from 7.04% in Prague to 27.9% in Limassol, clearly depends on the climate zone latitude.

In Table 4.11, the *PES* of the innovative system layout is reported for all the considered weather zones.

Table 4.11. Energy, economic and environmental analysis results.

Weather zone	ΔPE [MWh_P/y]	*PES* [%]	ΔCE [k€/year]	*SPB* [year]	$\Delta CE'$ [k€/year]	*SPB′* [year]	ΔCO_2 [t_{CO2}/year]
Prague	11.0	52	1.52	4.81	2.06	7.09	10.4
Freiburg	12.0	59	2.09	3.50	2.88	5.08	7.51
Milan	12.6	61	1.55	4.73	2.39	6.12	6.10
Bolzano	13.9	64	1.62	4.51	2.64	5.54	6.74
Nice	16.4	75	1.52	4.80	2.75	5.31	4.64
Naples	16.1	74	1.78	4.12	3.05	4.79	7.79
Athens	16.4	75	1.69	4.31	2.23	6.54	18.9
Limassol	19.7	80	2.27	3.22	2.69	5.44	8.06

The higher the HDD of the considered weather zone, the lower the corresponding *PES*. The maximum *PES* is obtained in Limassol (80%). The table also includes the results of two economic analyses relative to a very low-capital cost of the developed PV/T collector prototype (250 €/m^2, corresponding to a global investment of almost 14.6 k€) and to the electricity purchase and feed-in tariffs reported in Table 4.5.

The first analysis refers to the standard electricity purchase/selling scenario (see Section 2.2.2). In this case, the yearly ΔCE are rather low and a financial contribution on the capital costs of about 50% is taken into account for the *SPB* calculation (only assessed for the innovative system layout). The shortest *SPB*s are obtained for low HDD weather zones. The best result is achieved in Limassol with 3.22 years, whilst the worst in Prague with 4.81 years (Table 4.11). The second economic analysis refers to an ideal electricity net metering scenario (see Section 2.2.2). In this case the yearly ($\Delta CE'$) are rather high and no grant on the capital costs are considered for the calculation of the *SPB′* of the proposed system. In this case, the best result is achieved in Naples with 4.79 years and the worst in Prague with 7.09 years (Table 4.11). InTable 4.11, the ΔCO_2 are calculated as a function of the current national efficiencies for conventional electricity production and the standard CO_2 conversion factors (Table 4.5). The obtained values of ΔCO_2 range from 4.64 to 18.9 t_{CO2}/year.

4.4. Conclusions

In this work, an innovative low-cost flat-plate and air-based PV/T collector prototype is presented. Details regarding the system design as well as the construction and experimental setup are provided. The prototype is experimentally tested for various operating parameters (air flow rate, tilt angle and weather conditions).

In order to assess the energy, economic and environmental performance of the PV/T prototype, a suitable dynamic simulation model is developed in-house and successfully validated against measurements obtained during the experimental investigation conducted in Patras (Greece). The model, based on modified Hottel-Whillier-Bliss equations, is implemented in a MatLab tool. The performance of a combined system consisting of the PV/T prototype coupled with an air-to-air heat pump for space heating is also assessed. With this tool, complete energy and economic analyses of the building-HVAC system can be carried out.

In order to show the potential energy savings, economic benefits of the innovative system, and the features of the dynamic simulation code, a suitable case study analysis is conducted. An array of PV/T collectors is mounted on the tilted roof of a two-floor building, including a commercial open-space and a single-family house.

The air heated by the solar collectors is used to supply an air-to-water heat pump for the commercial space heating, whereas the produced electricity is partially self-consumed by the building. Different economic scenarios are investigated for the produced electricity surplus, such as: i) a standard electricity purchase/selling strategy, where the electricity exported to the grid is sold at the unitary national price; and ii) an ideal net metering, where the surplus of produced electricity exported to the grid can be delivered back to the building when needed. The simulation analysis is conducted for 8 different weather zones where different shares of self-consumed electricity and electricity sold to the grid are obtained. By activating the fans of the PV/T collectors just in case of heat pump use, the following main results are achieved:

- electricity production ranges from about 11.0 to 19.8 MWh/year (for the weather zone of Prague and Limassol, respectively);
- electricity demand of the heat extraction fans ranges from 195 to 61.0 kWh/year (for the weather zone of Limassol and Prague, respectively), corresponding to 1.76% and 0.31% of the system electricity production;
- *PES* ranges from 52 to 80% (for the weather zone of Prague and Limassol, respectively);
- avoided CO_2 emissions ranges from 4.6 to 10.4 t_{CO2}/year (for the weather zone of Nice and Prague, respectively);
- *SPB* period ranges from 3.2 to 4.8 years for the standard electricity purchase/selling scenario, and from 5.4 to 7.1 years for the ideal net metering scenario.

Further analyses will be carried out by taking into account whole year weather data for further enhancing the accuracy of the presented simulation tool. A suitable subroutine will be added to assess the building passive effects. A design optimization of the presented prototype will be also carried out by considering as objective functions both energy saving and *SPB*.

CHAPTER
5

5. Building energy performance simulation tool: DETECt

This chapter aims to respond to the twofold need of the research focused on BEPS tools, i.e. to develop:

- a reliable dynamic simulation tool for the building energy performance analysis capable to reliably predicting the related energy demands and the indoor environmental conditions [233-235];
- a flexible tool to be used for the implementation of new add-on models able in suitably assessing the energy performance of future building research challenges (e.g. innovative envelope integrated technologies and strategies, new energy efficiency construction materials, real users' interaction with the building indoor environmental control systems, innovative building plants, etc.) [106, 236, 237].

5.1. Aim of the work and content of the chapter

In this framework, this chapter presents the results of an empirical validation of an in-house developed building simulation model, implemented in a computer tool written in MatLab and called DETECt [231]. The presented simulation model has been used by researchers of different backgrounds in order to investigate the energy performance of novel building envelope measures and energy saving technologies, as well as innovative strategies for the hygrothermal indoor conditions control [58, 238-242]. The tool was previously and successfully verified through the results obtained by other similar models as well as the above mentioned BESTEST standard procedure, showing low or very low deviations between the obtained simulation results and those provided by test suites [58, 238-242]. The validation procedure is now completed by following the experimental approach. Specifically, in this chapter the DETECt simulation results are compared to measurements obtained through a real test-room located in Naples (South-Italy). The overall validation procedure here presented resulted more costly (in terms of required time and effort) than the comparative ones detailed in references [58, 238-242]. From this point of view this chapter and the included results can be considered as the continuation and conclusion of the starting research work reported in reference [231].

The empirical validation test of DETECt has been also conceived in order to assess the influence of building thermal properties and weather parameters on the tool reliability. The chapter includes many details and results of the experimental validation process, also describing the experimental setup design, the measured boundary conditions and the applied metrics for the empirical validation. Note that, DETECt can be coupled to additional simulation tools purposely developed for dynamically analysing traditional and innovative building systems and plants (e.g. different renewable energy technologies, HVAC systems, adaptive indoor air conditions controls, etc.). Therefore, by such complete tool, energy and economic performance analyses of whole building-plant systems can be carried out.

One of the novelties of this research consists in the development and use of a new dynamic simulation tool for assessing the energy performance of new building technologies that are not implemented yet or cannot be precisely modelled in the available simulation codes. The use of simulation tools is always required to investigate in advance the energy performance of forthcoming themes and applications, as well as future building materials and/or innovative techniques. From this point of view, in the recent years DETECt was uninterruptedly refined and updated by the authors with new functions and subroutines, and the related experimental validation has to be considered as a crucial step of the carried-out research work on developing this tool.

5.2. Model description

5.2.1. Description of the framework and general consideration

The selection of a BEPS tool highly depends on the trade-off between the accuracy of the implemented models and the computing time, whereas the reliability of simulation results + depends on the mathematical models and assumptions made to describe the occurring building physical phenomena [122]. Simulation models based on steady state methods neglect the transient effect of variables (e.g. thermal inertia) and other sensible assumptions; thus, they are not suitable for the optimal design of the building and its HVAC systems. Conversely, dynamic simulation models are capable to track peak loads and are useful to capture thermal effects, providing accurate details on how to reduce the energy demand and to improve the thermal comfort of occupants. Computational time is largely dependent on the numerical treatment of the considered structural components. In this regard, among physics-based models dealing with the spatial dependency of the thermal behaviour of buildings, different modelling approaches can be used, such as: *i)* zonal method, *ii)* thermal network, *iii)* nodal method, *iv)* Computational Fluid Dynamics (CFD).

By the zonal approach, a building is split into different thermal zones [243], where thermal and mass balances are used to determine the occurring temperature distribution.

Thermal network models are, instead, frequently used because of the related simple and efficient approach, wherein the spatial dependency is accounted by distributing resistors and capacitors in different spatial directions. Thus, as the method aims to capture the dominant building physics behaviours while ignoring nonlinearities (also necessary for the development of building control strategies [244, 245]), there is no need to solve partial differential equations, simplifying the mathematical model formulation. For example, in some building simulation tools the conduction heat transfer is solved by lumping all the building thermal masses in a single node of the considered thermal network, avoiding the adoption and the resolution of many partial differential equations [246]. Nevertheless, despite of their simplicity, lumped model approaches do not allow one to obtain details about the building surfaces temperatures, necessary for simulating the frequent rapid variation of the thermal conditions occurring in buildings as well as for indoor comfort analyses [247]. If the flow field and the spatial domain to be discretized are a priori known, thermal network-based models could be preferable than more computationally expensive and complex building thermal ones [248]. For this reason, suitable detailed mathematical algorithms / models based on the thermal network approach are more and more developed and used to predict the whole building thermodynamic behaviour and for analysing the energy performance of building-plant systems [86, 249-251]. Typically, in order to develop straightforward tools through such approach, only few system phenomena are modelled and only the most significant physical aspects occurring in the dynamic building thermal behaviour are considered. In order to simulate the building dynamic interactions within a reasonable computing time, one-dimensional modelling approaches of heat transfer phenomena within the building envelope are often employed [106, 252]. A summary about assumptions, features and limitations of such models is reported in [74, 95, 253]. The nodal method, derived from the thermal network one, considers each building zone element (i.e. indoor air, wall, etc.) as a homogeneous volume. Here, uniform state variables and appropriate heat transfer equations are applied to each node and solved by using transfer functions or finite difference methods [254]. Nodal approaches are employed by numerous BEPS tools, widely used in the research community. EnergyPlus [69] and TRNSYS [62] are two popular examples.

Tools based on the CFD approach are characterized by the highest accuracy and by long computing time, rather unsuitable to perform yearly simulations at a whole building level [83].

The thermal model implemented in DETECt is based on a nodal description of the building elements with a one-dimensional modelling of the thermal conduction phenomena (the transverse heat transfer is disregarded [255]). With the aim to analyse the effect of the spatial distribution of the heat capacity on the heat flux through the building envelope elements, the developed thermal network includes a high number of thermal capacitances, following a distributed parameters approach [256]. Specifically, in DETECt a transient distributed parameters heat transfer model is implemented for allowing accurate simulations of dynamic effects driven by the thermal mass. Such method allows one to dynamically calculate the temperature of indoor air and building surfaces, necessary for indoor comfort analyses and for simulating the temperature and flux fields of a mono-zone, multi-zone and multi-story building.

The developed simulation model is implemented in MatLab environment [257], which includes built in solvers for differential equations systems and mathematical functions. DETECt is subdivided in several sub-models, dedicated to the calculation of different phenomena. All sub-models are grouped in a single calculation tool, described in [258], whose simulator scheme is shown in Fig. 5.1. A description of the thermal model is provided hereinafter with the aim of showing the mathematical approach and algorithms included in DETECt, as well as the model assumptions that primarily influence the fidelity and accuracy of the simulation results.

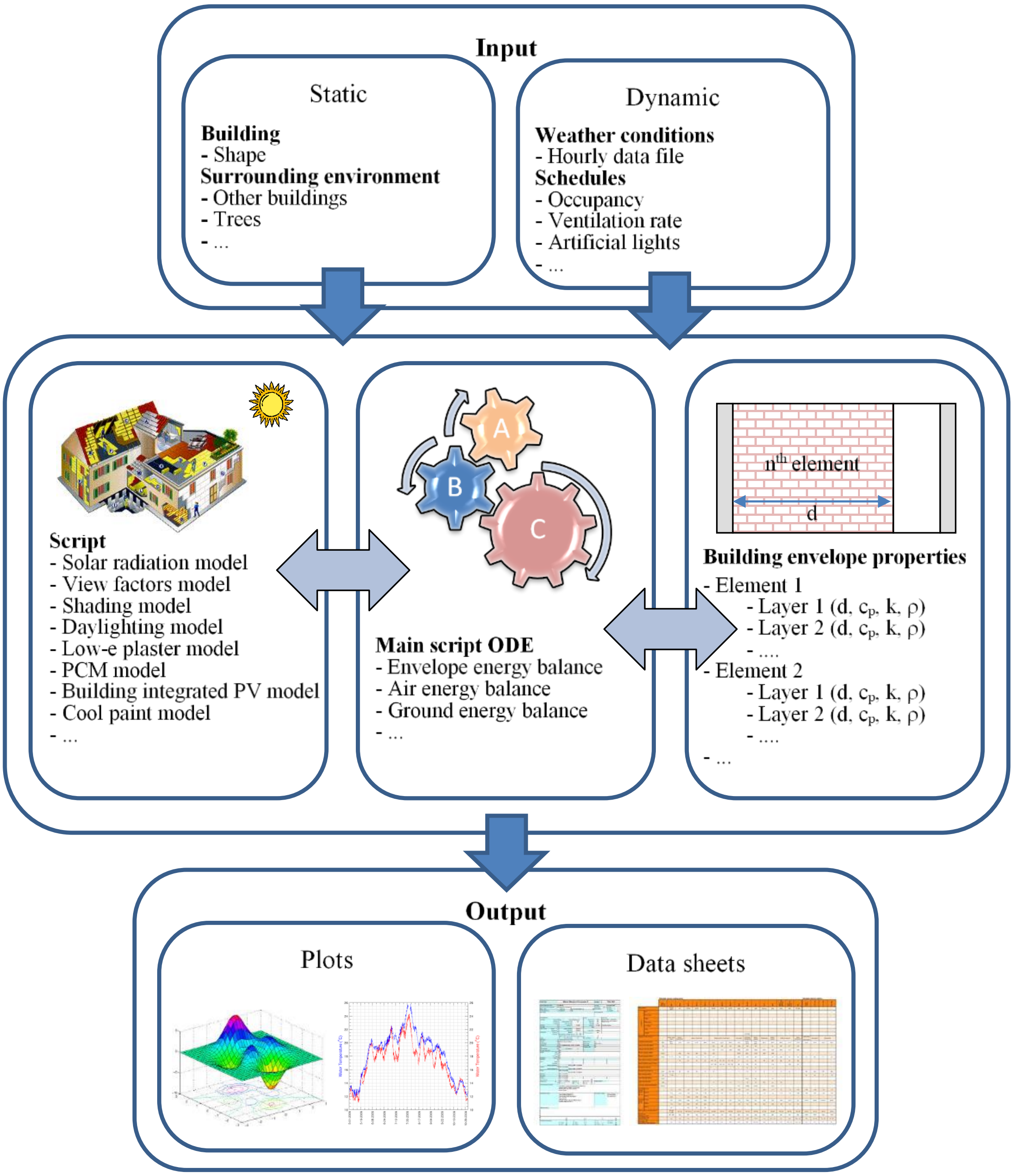

Fig. 5.1. Simulator scheme and concept.

5.2.2. Heat flow calculation procedure

The transient heat transfer through building elements is simulated by taking into account the finite difference method based on the thermal Resistance Capacitance (RC) network approach. Each thermal zone of the simulated building is modelled by lumping the indoor air mass in a single uniform temperature node, whereas each envelope elements (wall, roof, ceiling, floor, interior wall, window) is split into uniform multi-layers, where thermal masses are lumped. For homogeneous layers of different thicknesses, isotropic and time-invariant thermo-physical properties (density, specific heat and conductivity) are assumed. By following such assumptions, each n-th sub-layer ($1 \leq n \leq N$) of each m-th building element ($1 \leq m \leq M$) is modelled by a single uniform temperature node including two conductive resistances and a single lumped capacitance, as shown in Fig. 5.2. Each m-th building element includes two additional surface non-capacitive thermal nodes ($n = 0$ and $n = N+1$), considered as boundary nodes linked to the outdoor and indoor air temperatures (not shown in Fig. 5.2).

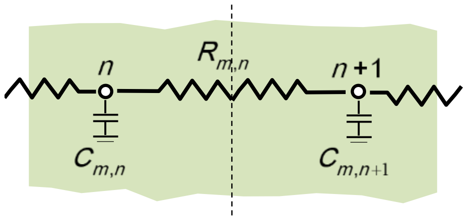

Fig. 5.2. RC thermal network: n and n+1-th nodes of the m-th building element.

Building internal and external solicitations are taken into account to assess the dynamics of the whole set of nodal temperatures of the RC network, described by a number of algebraic and differential equations (according to the discretization level, automatically selected to obtain an acceptable simulation results accuracy as well as a sufficiently short computational time [256]). A built-in ODE solver, provided by MatLab and based on variable step size Runge-Kutta and trapezoidal rule integration methods, is considered to solve the system equations [257].

The differential equation describing the heat transfer of each capacitive n-th node of the m-th building element is calculated in each t-th time step as:

$$C_{m,n} \frac{dT_{m,n}}{dt} = \sum_{j=n-1}^{n+1} \frac{T_{m,j} - T_{m,n}}{R_{m,n}^{cond}} + \gamma \cdot Q_{m,n}^{rad} \tag{5.1}$$

where T and C are the temperature and thermal capacitance, R^{cond} is the conductive thermal resistance between two nodes, Q^{rad} is the radiative forcing function acting on non-capacitive nodes ($\gamma \neq 0$ if $n = 0$ or $n = N + 1$, being $\gamma = 0$ elsewhere). Note that, Q^{rad} depends on the typology and geometry of the considered building element (assumed as either separating two indoor zones or an indoor zone from the outdoor environment). On external opaque and glazed surfaces ($n = 0$), $Q^{rad}{}_{m,0}$ includes both the solar and long wave radiations, while on inner opaque and glazed surfaces ($n = N+1$), $Q^{rad}{}_{N+1}$ account for the incident solar radiation entering through windows and the net long wave radiation load exchanged with the remaining internal surfaces of the considered thermal zone. Such terms, for each m-th building element of the heat exchange surface area, A_m, are calculated as:

$$\begin{aligned} \dot{Q}_{m,0}^{rad} &= \left[\varepsilon_m^{ext} \cdot \sigma \cdot f \cdot (T_{sky}^4 - T_{m,1}^4) + \alpha_m^{ext} \cdot I_m^{ext} \right] \cdot A_m \\ \dot{Q}_{m,N+1}^{rad} &= \left[\varepsilon_m^{int} \cdot \sigma \cdot \sum_{i=1}^{M} G_{bm} \cdot (T_{i,N}^4 - T_{m,N}^4) \ + \ \alpha_m^{int} \cdot I_m^{\mathrm{int}} \right] \cdot A_m \end{aligned} \tag{5.2}$$

where f is the external surface view factor, T_{sky} is the sky temperature, ε is the emissivity of the surface, α is the average spectral absorption factor (calculated through spectral reflectance curves integrated across the whole solar range), G_{bm} accounts for the long-wave radiation exchange on the internal surface of the considered thermal zone, I is the total solar radiation flux (depending on geometrical relationships implemented in a specific subroutine [259]). Note that further details about the solar radiation subroutine, not reported for the sake of brevity, are available in [232].

The calculation of the solar radiation entering through transparent elements and distributed within the internal space is carried out by means of the selected absorption, reflection and view factors. In particular, the total solar radiation flux striking an internal m-th surface, $I^{int}{}_{m}$, includes the solar irradiance reflected by other interior surfaces and it is calculated as:

$$\begin{pmatrix} I_1^{int} \\ I_2^{int} \\ \dots \\ I_M^{int} \end{pmatrix} = \begin{pmatrix} \left(1 - F_{11}\rho_1^S\right) & -F_{12}\rho_2^S & -\dots & -F_{1M}\,\rho_M^S \\ -F_{21}\rho_1^S & \left(1 - F_{22}\rho_2^S\right) & -\dots & -F_{2M}\,\rho_M^S \\ \dots & \dots & \dots & \dots \\ -F_{M1}\rho_1^S & -F_{M2}\rho_2^S & -\dots & \left(1 - F_{MM}\,\rho_M^S\right) \end{pmatrix}^{-1} \cdot \begin{pmatrix} I_1^0 \\ I_2^0 \\ \dots \\ I_M^0 \end{pmatrix} \tag{5.3}$$

where ρ^S are the internal surfaces solar reflectivity coefficients, F are the internal surfaces view factors, automatically calculated for parallelepipedal structures [260], I^0 is the vector of the solar radiation directly received by the interior surfaces. It is worth noting that the coefficients of the $(\overline{I} - F \cdot P_S)$ matrix shown in eq. (5.3) are calculated at the beginning of the simulation, remaining constant at each simulation time-step. The long-wave radiation exchange on the internal surfaces of the considered thermal zone is assessed through the Gebhart's absorption method [261, 262], and the G_{mb} generic coefficient of the Gebhart's matrix (namely G and consisting of several vectors) is calculated as:

$$\begin{pmatrix} G_{1m} \\ G_{2m} \\ \dots \\ G_{Mm} \end{pmatrix} = \begin{pmatrix} \left(1 - F_{11}\rho_1^{LW}\right) & -F_{12}\rho_2^{LW} & -\dots & -F_{1M}\,\rho_M^{LW} \\ -F_{21}\rho_1^{LW} & \left(1 - F_{22}\rho_2^{LW}\right) & -\dots & -F_{2M}\,\rho_M^{LW} \\ \dots & \dots & \dots & \dots \\ -F_{M1}\rho_1^{LW} & -F_{M2}\rho_2^{LW} & -\dots & \left(1 - F_{MM}\,\rho_M^{LW}\right) \end{pmatrix}^{-1} \cdot \begin{pmatrix} F_{1m}\varepsilon_m^{LW} \\ F_{2m}\varepsilon_m^{LW} \\ \dots \\ F_{Mm}\varepsilon_m^{LW} \end{pmatrix} \tag{5.4}$$

where each G_{mb} is the fraction of the radiation emitted from the interior surface and absorbed by the remaining ones, ρ^{LW} and ε^{LW} are long-wave reflectivity and emissivity coefficients. Note that, G is calculated at the beginning of the simulation, remaining constant at each time-step, as it depends on surfaces geometry and constant materials thermal properties.

Note that, in case of outer ($n = 0$) and inner ($n = N + 1$) surface non-capacitive nodes, the algebraic equation describing the heat transfer is obtained by eq. (5.1) setting the thermal capacitance, $C_{m,n}$, to zero. In this case, convective resistances can be either set as constant (based on the surface type) or calculated as a function of the surface unitary convection heat transfer coefficients (calculated by empirical relationships [231, 239]). Note that, convection heat transfer coefficients can be assumed as time variant when the wind velocity is available as input data (from measurements or weather data files); otherwise, constant coefficients are considered, by assuming a wind velocity equal to 5 m/s.

Finally, the equation describing the heat transfer of the indoor air node is calculated as:

$$C_{in}\frac{dT_{in}}{dt}=\sum_{m=1}^{M}\frac{T_{m,N}-T_{in}}{R_{m,\mathrm{int}}^{conv}}+Q_{gain}+Q_{vent}\pm Q_{hvac} \tag{5.5}$$

where C_{in} is the thermal capacitance of the zone indoor air, and R^{conv} is the internal convective resistance, assessed as a function of the surfaces inclination and flow condition, Q_{gain}, Q_{vent} and Q_{hvac} are sensible heat gains, considered as purely convective and, respectively, due to: *i)* occupants, lights and equipment, *ii)* infiltration and ventilation, and *iii)* sensible heat to be supplied to or to be removed from the building space (by an ideal heating and cooling system). Q_{hvac} is required to maintain the indoor air at the considered set point temperatures and it is calculated according to a Proportional Integral (PI) controller, whose gains vary as a function of the operating conditions [161].

Further details of the developed mathematical model and concerning the related capabilities are available in [231, 232].

5.3. Model validation

In the following, the results of a suitable empirical validation procedure conducted for assessing the DETECt reliability are detailly discussed.

It is worth noting that DETECt successfully surpassed a previous comparative validation process performed by means of the BESTEST standard procedure [101, 102, 123]. This approach includes several test cases, organized in diagnostic and qualification (mandatory) series, which allow one to analyse the influence of different physical phenomena on the numerical results provided by BEPS tools and building energy models under examination. Such test cases cover a high number of physical occurrences and model features (i.e. thermal mass, solar and internal heat gains, window-shading devices, infiltration, setback thermostat control, etc.). The BESTEST procedure has been widely adopted for assessing the accuracy of a number of building simulation tools capable to perform energy analyses [100, 120-122]. Such iterative diagnostic procedure allow codes to be examined over a broad range of parametric interactions that cannot be easily considered through experimental analyses [123].

For both the winter and summer reference days considered in the BESTEST procedure, dynamic results achieved by DETECt for the free-floating indoor air temperature and the corresponding heating and cooling requirements are always included within the BESTEST confidence intervals, confirming an initial reliability of developed code. More details about the code-to-code validation of DETECt are reported in [232].

Furthermore, an additional comparison with two commercial tools (TRNSYS and Energy-Plus) was also conducted in order to check the code reliability with respect to different building geometries and uses, HVAC activation scheduling, and weather conditions. The deviation detected between the results obtained with DETECt and with these standard tools were almost always lower than 10% [231].

5.3.1. Empirical validation procedure

In this section, details about the design of the experimental setup and the developed analyses are reported. Then, a discussion of the results obtained through the carried out empirical validation process of DETECt is provided.

Experimental set-up

The testing facility employed for the validation process of DETECt consists of a real test room located in the main building of the cluster hosting the School of Polytechnic and Basic Sciences of the University of Naples Federico II, situated in the neighbourhood of Fuorigrotta, Naples (South-Italy, 40.83999°N, 14.25176°E). Note that, a temperate climate is observed in this location, featured by rather long winters and rather hot and humid summers. Such building cluster was built in multiple phases between 1955 and 1980, and it consists of lower bodies and a main block of twelve floors (60 m height). The real test room is located at the twelfth floor of the main high-rise building, and it corresponds to a typical test cell, for its shape and features.

It is worth noting that a test-box typically consists of a single room, well insulated from its surroundings on all the related walls except one exposed to the outdoor climate conditions to allow the investigation of solar gain and temperature effects on its energy behaviour (also through the use of different windows and materials on the exposed walls) [100]. Sensors are placed throughout the room and outside to allow the data collection of temperatures, humidity, and solar radiation. The considered room is operated under free-floating temperature conditions; thus heating, cooling, and lighting system schedules are not considered.

The test room used for the presented analysis has a parallelepipedal shape (2.60 m height, 3.39 m length and 2.26 m width) and only two external walls, the South-West one including one window, and the North-West one, as shown in Fig. 5.3. The window (0.87 m length and 1.18 m height) is made of two single (8 mm thickness) glass panels (0.30 m length and 1.18 m height, for 0.6 m² area and

SHGC = 0.78), and the frame (for 0.43 m² area) is made of a traditional aluminium profile; the average U-value = 5.2 W/m²K.

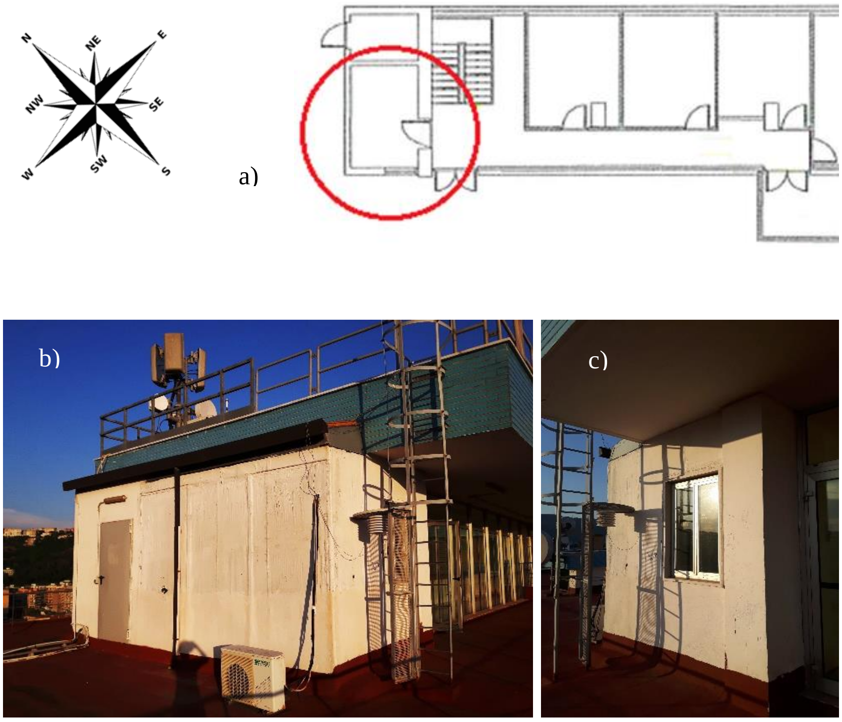

Fig. 5.3. Test-cell sketch: a) plant and orientation; b) North-West view; c) South-West view.

The South-East wall, including a wood door (2.10 m height, 0.99 m width, 0.04 m thick), is an interior wall, adjacent to a corridor of the above mentioned twelfth floor, whereas the North-East one separates the test room from another indoor space in which several machineries are continuously switched on (thus a rather high indoor temperature is observed all over the year). A 1.2 m depth horizontal overhang is located on the South-West wall. The ceiling is made for 3/5 of its surface of concrete and for the remaining part of thermally insulated aluminium sheet, and a similar thermal transmittance of such two roofs is observed.

In order to verify the layer layout of walls, ceiling and floor layers, an investigation of the available technical documentation as well as suitable low-invasive endoscopic analyses were carried out. For achieving the endoscopic investigation, several 1.5 cm diameter holes were made through the walls and the ceiling, as shown in Fig. 5.4. Here, a picture of the adopted endoscope probe (Fig. 5.4, a), the autoclaved concrete layer of the South-West and North-West walls (Fig. 5.4, b), the thermal insulation material surrounded by steel sheets of the South-West and North-West walls (Fig. 5.4, c), and the air-gap between the two semi-hollow brick layers of the South-West wall (Fig. 5.4, d), are reported. As a result of this analysis, a complete assessment of the test room envelope layout was carried out. Specifically, details about the related layers and thermophysical properties were detected.

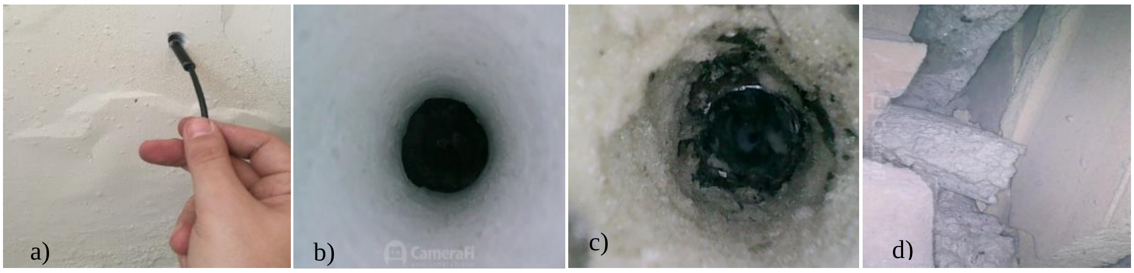

Fig. 5.4. a) Endoscope probe; b) autoclaved concrete layer; c) thermal insulation panel; d) wall air-gap.

The thermophysical properties and thicknesses of the considered test-room walls are reported in Table 5.1, whereas for the ceiling and floor they are shown in Table 5.2.

Table 5.1. Walls layers thickness and thermophysical properties (from outdoor to indoor).

South-West, North-West and North-East Walls	**Layer material**	**Thickness**	**Thermal conductivity**	**Density**	**Specific heat**
Wall thickness 0.19 m, U-value = 0.54 W/m²K		[m]	[W/(m·K)]	[kg/m³]	[J/(kg·K)]
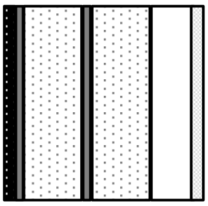	Bitumen	0.004	0.2	1075	1000
	Steel	0.0025	36	7700	500
	Thermal insulation	0.05	0.065	44	1458
	Steel	0.0025	36	7700	500
	Thermal insulation	0.05	0.065	44	1458
	Autoclaved cellular concrete	0.05	0.25	800	1000
	Plaster	0.015	0.2	1075	1000
South-East Wall	**Material layer**	**Thickness**	**Thermal conductivity**	**Density**	**Specific Heat**
Wall thickness 0.47 m, U-value = 0.57 W/m²K		[m]	[W/(m·K)]	[kg/m³]	[J/(kg·K)]
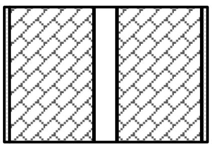	Plaster	0.015	0.35	750	1000
	Semi-hollow brick	0.20	0.32	1200	840
	Air	0.04	0.27	1.3	1008
	Semi-hollow brick	0.20	0.32	1200	840
	Plaster	0.015	0.35	750	1000

The long-wave emissivity and reflectivity (ε^{LW} and ρ^{LW}) of the interior surfaces are set to 0.9 and 0.1, respectively. The solar absorptance coefficients of the interior surfaces (α_{int}) are set to 0.25, whereas for the exterior ones (α_{est}) are set to 0.3 (walls) and 0.6 (roof).

Sensors and instrumentations applied into the test room are:

- Six thermocouples for measuring the internal surfaces temperature of the North-West, North-East, South-East, South-West walls, ceiling and floor (K-type, model TC Direct 402-805. Measuring range: from -250 to 150°C. Accuracy: ±1.0°C or ±0.75%). See Fig. 5.5a. Note that, the temperature homogeneity on the surfaces of such test room elements was repeatedly verified by means of an infrared thermo-camera (FLIR, model T335. Measuring range: from –20 to 650°C; in

3 ranges: -20 to 120°C or 0 to 350°C or 200 to 650°C. Accuracy: ±2°C or 2%. Thermal sensitivity/NETD 50 mK at 30°C. IR resolution: 320×240 pixels).

Table 5.2. Ceiling and floor layers thickness and thermophysical properties (from outdoor to indoor).

Floor	**Material layer**	**Thickness**	**Thermal conductivity**	**Density**	**Specific heat**
Wall thickness 0.48 m, U-value = 1.40 W/m²K		[m]	[W/(m·K)]	[kg/m³]	[J/(kg·K)]
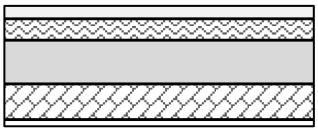	Plaster	0.015	0.35	750	1000
	Hollow block	0.18	0.6	1400	840
	Concrete slab	0.20	1.6	2200	1000
	Mortar bed	0.05	0.9	1800	1000
	Marble	0.03	1.3	2300	840
Ceiling	**Material layer**	**Thickness**	**Thermal conductivity**	**Density**	**Specific heat**
Average U-value = 0.16 W/m²K		[m]	[W/(m·K)]	[kg/m³]	[J/(kg·K)]
Horizontal attic side	Bitumen	0.02	0.20	1075	1000
	Mortar bed	0.05	0.9	1800	1000
	Concrete slab	0.20	1.6	2200	1000
	Hollow block	0.18	0.6	1400	840
Tilted aluminium sheet side	Aluminium	0.002	190	2700	900
	Polyurethane foam	0.05	0.028	44	1458
	Aluminium	0.002	190	2700	900
	Air	0.1 - 0.3	0.27	1.3	1008
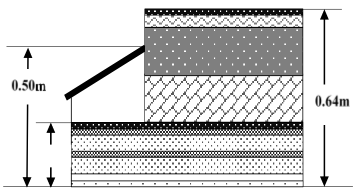	Bitumen	0.004	0.20	1075	1000
	Steel	0.0025	36	7700	500
	Thermal insulation	0.06	0.028	44	1458
	Steel	0.0025	36	7700	500
	Thermal insulation	0.06	0.028	44	1458
	Air	0.04	0.27	1.3	1008
	Plasterboard	0.015	0.21	900	840

- Three thermoresistances for measuring the temperature of internal surfaces of the door and of window glass and frame (PT 100, model TC Direct 515-680. Measuring range: from -50 to 150°C. Accuracy: ± 0.3°C at 0°C). See Fig. 5.5b.
- One hygro-thermometer for measuring the indoor air temperature and humidity (HD 9008 TRR. Platinum resistance thermometer, 100Ω. 4-20 mA output, and 10-30 VDC power supply. Temperature measuring range: -40 to 80°C. Accuracy: ±0.15°C or ±0.1%. Hygroscopic polymer humidity sensor. 4-20 mA output. Relative humidity measuring range: from 0 to 100%. Accuracy: ±1.5% in the range 0-90% and ±2.0% elsewhere. See Fig. 5.5c, right.
- One globe-thermometer for measuring the mean radiant temperature of the test room indoor surfaces, with an inside thermocouple (K-type, model TC Direct 402-805. Measuring range: from -250 to 150°C. Accuracy: ±1.0°C or ±0.75%). See Fig. 5.5c, left.

Note that, to avoid the window solar radiation effect on all such sensors, suitable shields were used during the experimental analysis (not shown on the reported pictures for the sake of clarity)

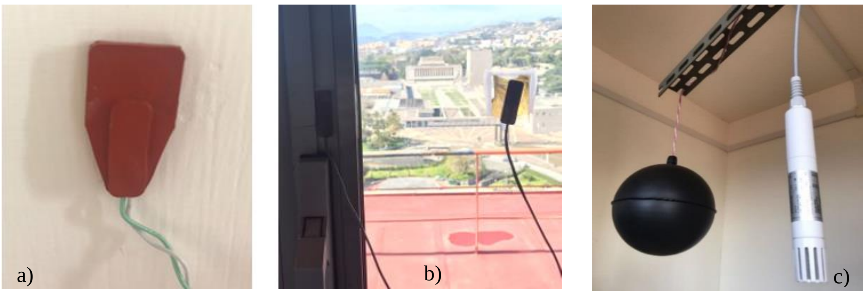

Fig. 5.5. a) Thermocouple K-type; b) thermoresistance; c) globe-thermometer and hygrothermometer. All such devices are here shown without the reflecting shielding elements used during the experimental analysis.

Sensors and instrumentations, applied to the measurements of boundary conditions, are:

- One hygro-thermometer for measuring the outdoor air temperature and humidity (HD 9008 TRR, above described), protected by a multi-plate radiation shield. See Fig. 5.6a.
- One pyranometer for measuring the horizontal global incident solar radiation (Delta Ohm, LP Pyra 02 AC. First Class pyranometer based on a thermopile sensor. 4-20 mA output. Measuring range: 0-2000 W/m^2. Operating temperature range: -40-80°C. Sensitivity: 10 μV/W/m^2. Impedance: 33-45 Ω. Device protected by two concentric domes. See Fig. 5.6b and Fig. 5.6c;
- One pyranometer for measuring the vertical South-West global incident solar radiation (Delta Ohm, LP Pyra 08 BL. Second Class pyranometer. 4-20 mA output. Measuring range: 0-2000 W/m^2. Operating temperature range: -40-80°C. Sensitivity: 15 mV/kW/m^2. Impedance: 5 Ω. Device protected by two concentric domes. Fig. 5.6b and Fig. 5.6c.
- Two hygro-thermometers for measuring the temperature and humidity boundary conditions external to the test cell. One placed in the corridor of the twelfth floor (linked to the South-West tests room wall), and the other one at the eleventh floor of the building, in the floor adjacent space to the test room (Testo 174H. 2-channel temperature and humidity mini data logger for continuous building climate monitoring. Temperature measuring range: from -20 to +70°C. Accuracy: ±0.5°C. Resolution: 0.1°C. Relative humidity measuring range: from 2 to 98%. Accuracy ±3%. Resolution: 0.1%).

Fig. 5.6. a) Thermohygrometer in a solar radiation shield. Pyranometers: b) side and c) bottom views.

All the above described sensors (except Testo 174H devices) were connected to a Compact Rio NI 9146 data logger (Fig. 5.7), linked through an Ethernet cable to a suitable dedicated PC. Note that the Testo 174 H data loggers were synchronized to the Compact Rio in order to obtain simultaneous measurement data acquisition. In order to process and convert the logged signals a suitable LabView tool was purposely developed. Such computer code was also used for real-time monitoring all the measurements of solar radiation, temperature and humidity in and out the test room. In Fig. 5.8 the front panel of such LabView tool is depicted.

The empirical analysis, conducted through the described experimental setup, was run from February to October 2018 in order to collect data in all the possible weather conditions (winter, spring, summer and autumn climates). Several logged parameters were used as input data to the DETECt simulation model, whereas other measurements were compared for validating purposes to the obtained simulation results. In the following, procedure details are provided. In addition, simulations were conducted by setting indoor gains equal at about 50W (sensible constant value due to measuring equipment), the air exchange rate at 0.2 ACH.

Fig. 5.7. Compact Rio sensors connections.

Experimental analysis

With the aim to consider dynamic weather conditions (featured by high meteorological variabilities), continuous experimental measurements were conducted between February and October 2018. For the sake of brevity, several significant days, well representing of the winter and summer climates of the considered weather zone on Naples (South-Italy), are considered in the succeeding discussion. Note that cold and temperature sunny winter days and hot sunny summer days are selected with the aim to test the code capability in simulating the solar radiation effect on the thermal behaviour of the test cell. Specifically, they refer to the following sample weeks:

- from March 23rd at 12:00 am to March 29th at 11:59 pm (winter climate time);
- from July 1st at 12:00 am to July 7th at 11:59 pm (summer climate time);

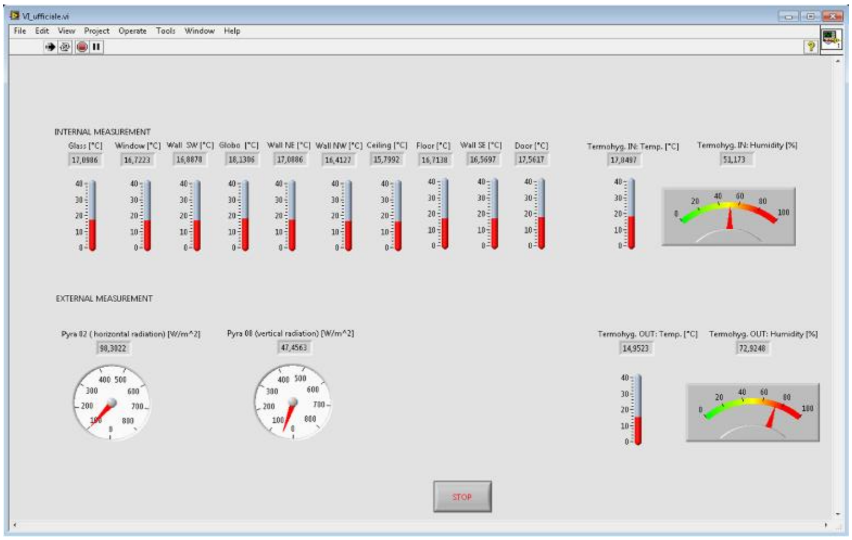

Fig. 5.8. Front panel of the developed LABVIEW tool.

During the carried-out measurements the HVAC system was switched off (free floating temperature regime). The experimental data logging time step was set at 360 seconds (i.e. records were collected each 6 minutes).

Fig. 5.9 shows, for both the selected winter and summer reference weeks, the time histories of the measured indoor and outdoor air temperatures ($T_{IN,exp}$ and $T_{OUT,exp}$, respectively) and the solar radiation on the outdoor vertical South-West façade and on the outdoor horizontal roof surface (I_{TOTver} and I_{TOThor}, respectively). In Fig. 5.9, it is possible to observe that the dynamic profile of outdoor air temperature ($T_{OUT,exp}$) coherently varies (throughout the days) according to the solar radiation trends. Note also that, the measured indoor air temperatures ($T_{IN,exp}$) peaks are time shifted with respect to the outdoor ones ($T_{OUT,exp}$). This is due to the thermal inertia phenomena of the whole test room envelope, as well as to the occurring solar radiation effect through the window, located on the room vertical South-West wall (Fig. 5.9, green line). The thermal capacitance effect of the test room envelope also softens the $T_{IN,exp}$ fluctuation in both the winter and summer weeks.

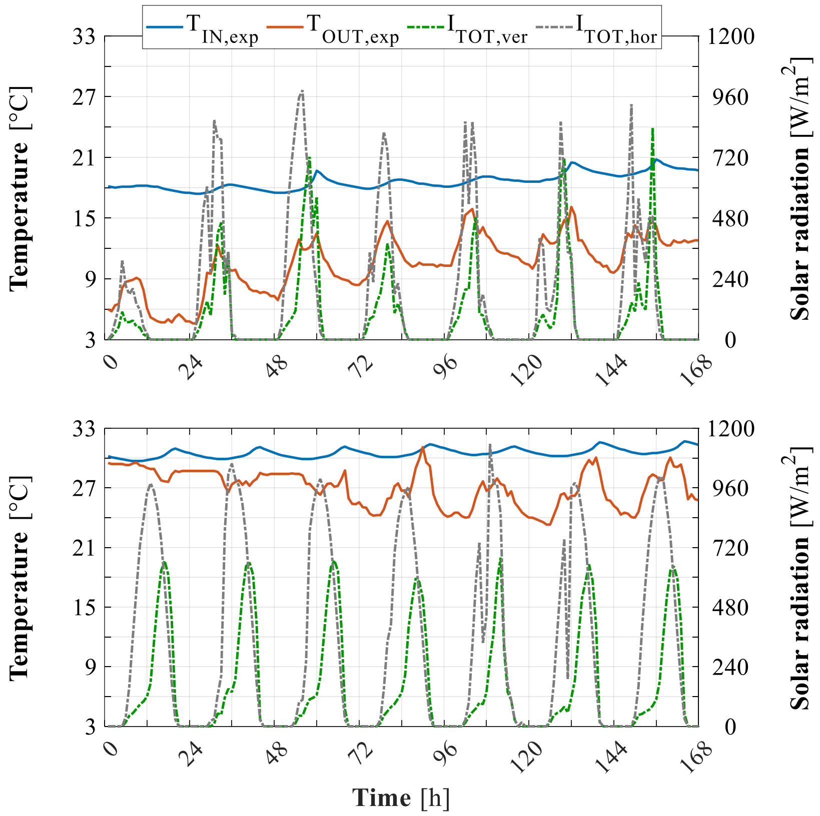

Fig. 5.9. Time histories of indoor and outdoor air temperatures and solar radiations incident on the vertical South-West façade and on the horizontal roof – Sample winter week: March 23rd - 29th (top) and sample summer one: July 1st - 7th (bottom).

Note that, the occurring indoor conditions dynamically vary according to the climate of the considered weather zone. Such result is also visible in Fig. 5.10 which shows, for the same sample weeks, the measured time histories of the indoor and outdoor relative humidity ($\phi_{IN,exp}$ and $\phi_{OUT,exp}$, respectively), together with those of $T_{IN,exp}$ and $T_{OUT,exp}$. It is noteworthy to observe that the trend of $\phi_{OUT,exp}$ highlights the presence of significant rainfall occurrences during the considered winter week (Fig. 5.10, top) and high outdoor humidity hours in summer (Fig. 5.10, bottom), as expected in a Mediterranean temperate climate.

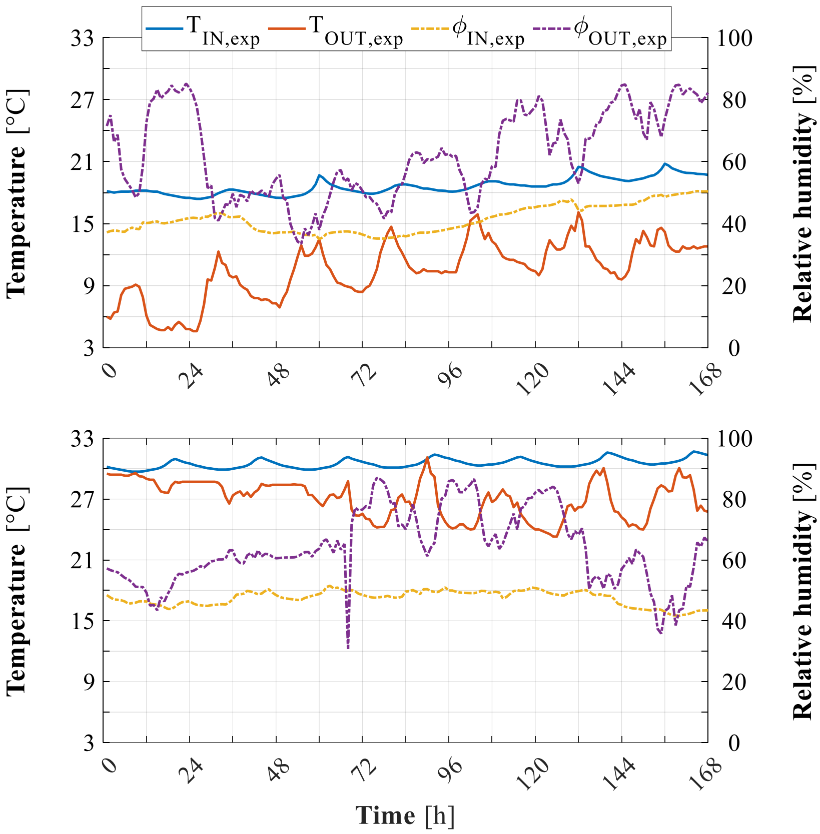

Fig. 5.10. Time histories of indoor and outdoor air temperatures and relative humidity – Sample winter week: March 23rd - 29th (top) and sample summer one: July 1st - 7th (bottom).

Fig. 5.11 shows the time histories of the internal surface temperatures of the test room walls, measured during the selected sample winter and summer weeks (Fig. 5.11, top and bottom, respectively). Since the North-East (NE) wall is adjacent to a control room in which high continuous internal thermal loads are implemented, the related surface temperature, $T_{NE,exp}$, is always the highest one during the winter time (Fig. 5.11, top) and averagely the highest one along the summer period (respect to the other measured surface temperatures). This result is clearly visible especially during night times. An exception is observed during some sunny days where $T_{NE,exp}$ is surpassed by the South-West (SW) wall temperature, $T_{SW,exp}$ (Fig. 5.11, bottom). Note that, in the carried out validation procedure, the dynamically measured $T_{NE,exp}$ temperatures are inputted in the DETECt simulation code as boundary conditions. It is noteworthy to observe that the measured surface temperatures of the South-West (SW) and North-West (NW) walls ($T_{NW,exp}$ and $T_{SW,exp}$, respectively) are remarkably variable during the daily hours (Fig. 5.11), accordingly to the relevant variations of the outdoor thermal solicitations and the low thermal capacitance of such walls. Conversely, the measured surface temperatures of the South-East (SE) wall ($T_{SE,exp}$) are weakly variable, accordingly to the related high thermal mass of such wall with respect to the other ones. Note that, the twelfth-floor corridor is confined on the SW and NE sides by a large glazed surface (Fig. 5.3). Therefore, the $T_{SE,exp}$ time profile is influenced by the correspondent solar radiation (especially during the afternoon), in both winter and summer seasons. Specifically, although $T_{SE,exp}$ shows slight fluctuations, a recurring growth is observed in afternoon times, especially in case of serene sky conditions. Note that, in the performed validation procedure, also the dynamically measured $T_{SE,exp}$ temperatures are inputted in the simulation code as boundary conditions.

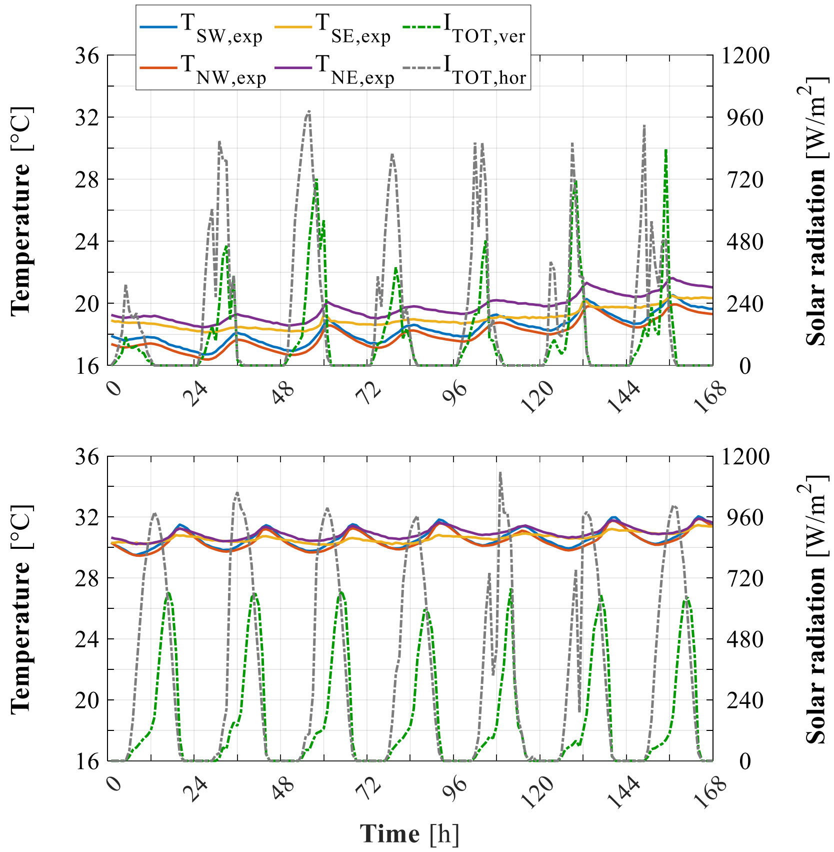

Fig. 5.11. Time histories of the internal surface temperatures of the South-West, North-West, South-East, North-East walls and of the solar radiation incident on the vertical façade and on the horizontal roof – Sample winter week: March 23rd - 29th (top) and sample summer one: July 1st - 7th (bottom).

In Fig. 5.12, a rather different behaviour is observed for the temperature of wooden door, $T_{door,exp}$, included in the SE wall (Fig. 5.3). Because of its lower thermal capacitance respect to the correspondent wall and due to highly variable thermal solicitations of the adjacent corridor, for such door a significant temperature fluctuation is observed in all the days of the summer sample week (Fig. 5.12, bottom) and in the third, fifth and sixth day of the winter one (Fig. 5.12, top). For both such weeks, Fig. 5.12 also shows the measured temperatures of the floor and ceiling surfaces ($T_{floor,exp}$ and $T_{ceiling,exp}$, respectively) together with the occurring incident solar radiations.

It is worth noting that higher (lower) floor temperatures are always detected with respect to the ceiling ones in winter (summer). Such outcome is due to the adjacency of the room floor and ceiling to an indoor space of the building and to the outdoor environment (ceiling-roof), respectively. Note that, due to the high thermal mass of the floor and to the lower one of the ceiling, the fluctuation of $T_{floor,exp}$ is always weak whilst the swing of $T_{ceiling,exp}$ is significant. This result is mostly evident in summer time, when the solar radiation is the highest temperature variation driving force, Fig. 5.12.

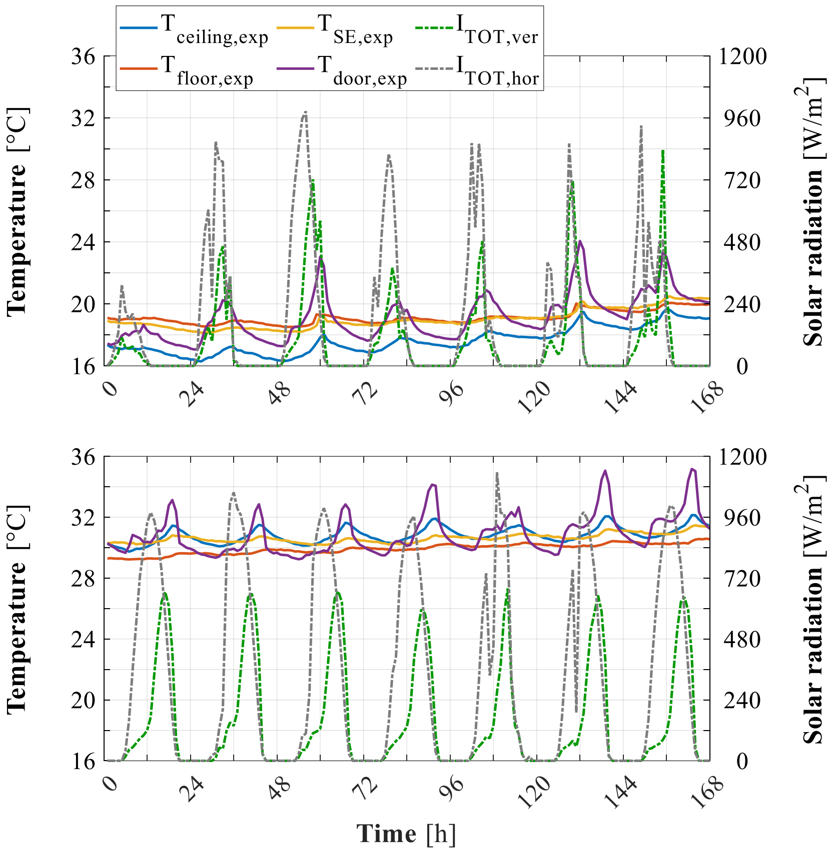

Fig. 5.12. Time histories of the internal surface of the of the ceiling, floor, South-East wall and door and of the solar radiation incident on the vertical façade and on the horizontal roof – Sample winter week: March 23rd - 29th (top) and sample summer one: July 1st - 7th (bottom)

5.3.2. Experimental vs. simulated results

In order to validate DETECt by means of measurements data, the free-floating temperatures regime of walls, floor, ceiling, and indoor air obtained by means of dynamic simulations were compared to the empirical ones achieved through the described experimental setup. To this aim, test room was suitably modelled in DETECt by implementing within the code all the related geometrical features and thermophysical properties. In addition, several measured indoor and outdoor environmental variables were assumed as dynamic input data and boundary conditions, such as the:

- global radiation on the outdoor horizontal roof surface, I_{TOThor}, and vertical South-West façade, I_{TOTver}. Note that, the global radiation on the vertical North-West façade are calculated starting from the measured global radiation on the outdoor horizontal surface;

- outdoor air temperature, $T_{OUT,exp}$;
- indoor air temperature of the corridor at the twelfth building floor limiting the SE wall (Fig. ***5.3***). Such temperature was implemented as boundary condition of the room SE wall;
- indoor air temperature of the building space at the eleventh floor. Such temperature was implemented as boundary condition of the floor partition;
- internal surface temperature of the North-East wall, $T_{NE,exp}$.

By dynamically logging such parameters a suitable data file to be inputted to DETECt, concerning all the thermal solicitations received by the test room, was obtained. As above mentioned, the test room was monitored for a long period with the aim to collect a high number of measurements (considering the different occurring meteorological conditions). The simulation time step was set, according to measurements, at 360 seconds. The initial conditions relative to all the modelled temperature were set at the starting measured temperatures collected on February 2nd.

The comparison between measured data and DETECt simulation outcomes are reported by several graphs depicted from Fig. 5.13 to Fig. 5.19. Here, for both the considered sample winter and summer weeks (March 23rd - 29th and July 1st - 7th) the time histories of the simulated indoor air and internal surfaces temperatures (red lines) are compared to the corresponding measured data (black lines). To this aim, additional lines (red dash and dot ones) are reported in these figures. They are obtained by adding and subtracting ± 1.0°C (i.e. the instrument error of the considered thermocouples) to the experimental data. Furthermore, a narrower temperature interval given by ± 0.5°C is also included (grey band) with the aim to enhance the evaluation of each simulated variable under exam.

Results for the indoor air temperature ($T_{IN,sim}$) are reported in Fig. 5.13 whereas those related to all the internal surface temperatures of the room walls, i.e. South-West ($T_{SW,sim}$), North-West ($T_{NW,sim}$), South-East ($T_{SE,sim}$), ceiling ($T_{ceiling,sim}$), and floor ($T_{floor,sim}$), are reported in Fig. 5.14, Fig. 5.15, Fig. 5.16, Fig. 5.17 and Fig. 5.18, respectively. The comparison between the simulated and empirical mean radiant temperatures is carried out too, the obtained results are depicted in Fig. 5.19.

For both the selected winter and summer periods, simulated and measured temperatures resulted very close (for the indoor air and all the considered surfaces temperatures). It is noteworthy to observe that the simulated temperatures are almost always included between the band-range of ± 0.5°C. It is noteworthy to highlight that for each investigated temperature, with respect to the accuracy required by the previously mentioned code-to-code validation procedure (i.e. BESTEST), a much higher accuracy of the simulated results is now obtained. In fact, the BESTEST validation process takes into account a ± 5°C range of variation for the obtained simulation results with respect to the reference one. Conversely, in the conducted experimental validation procedure, a definitely lower range of variation is observed, highlighting a very high accuracy of the results achieved through the DETECt dynamic simulation model.

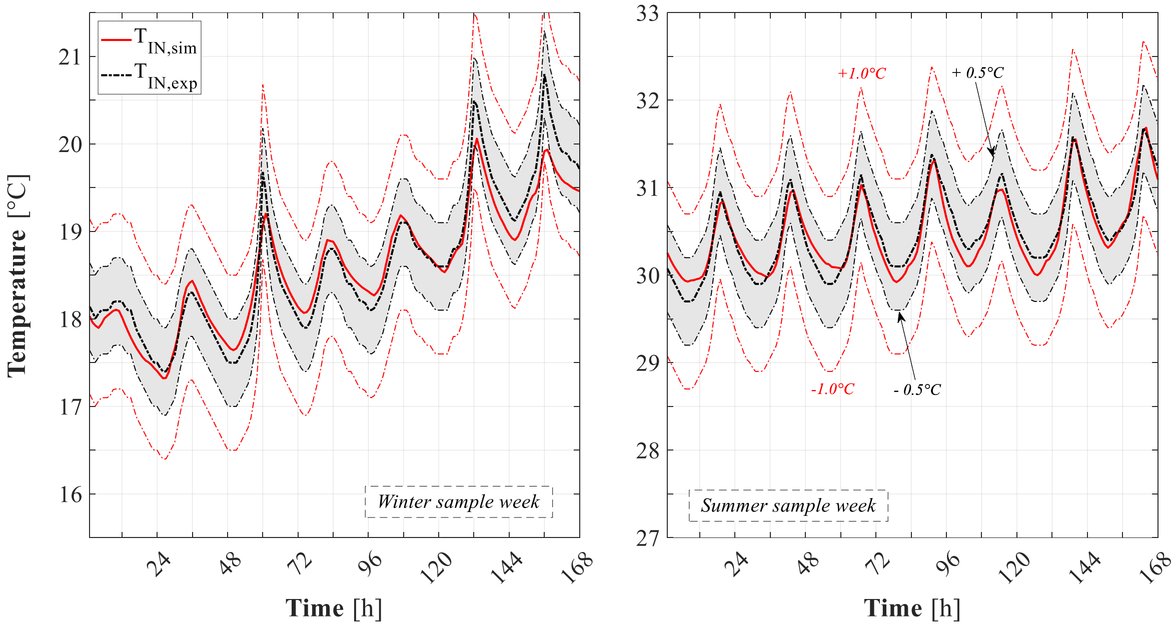

Fig. 5.13. Indoor air temperature: simulated vs. experimental results (two sample weeks)

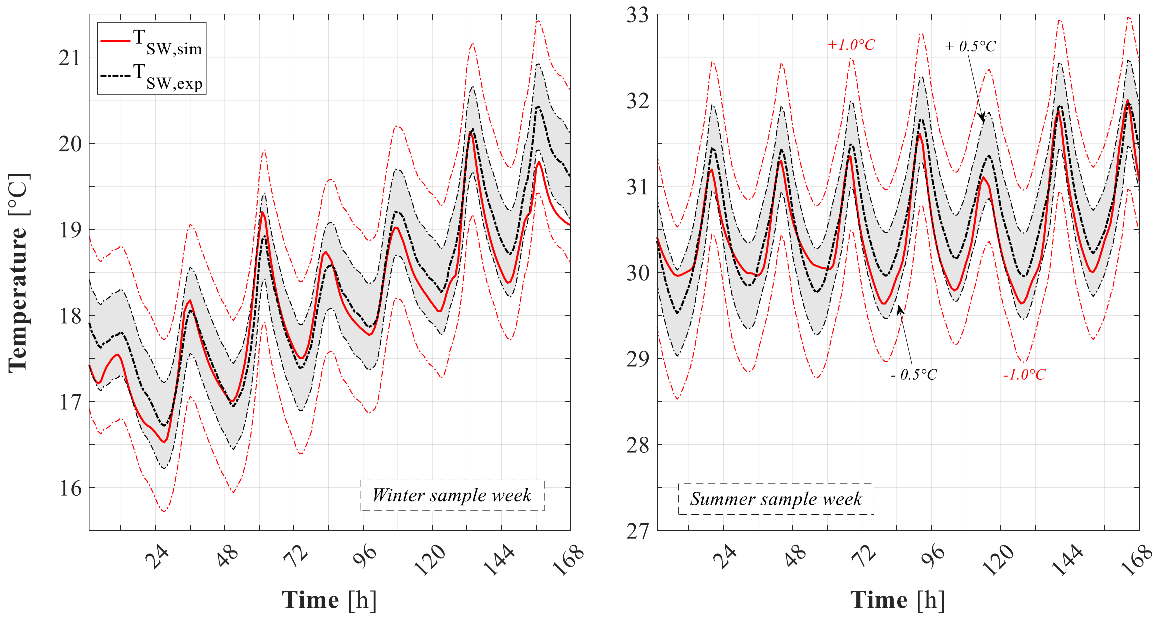

Fig. 5.14. South-West wall temperature: simulated vs. experimental results (two sample weeks)

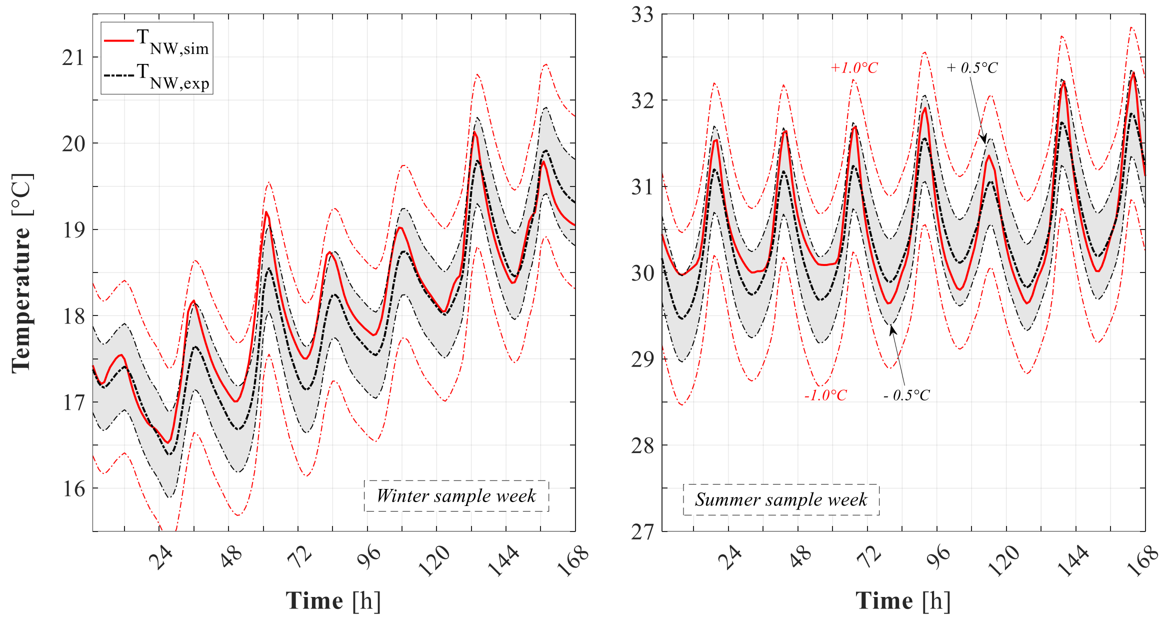

Fig. 5.15. North-West wall temperature: simulated vs. experimental results (two sample weeks)

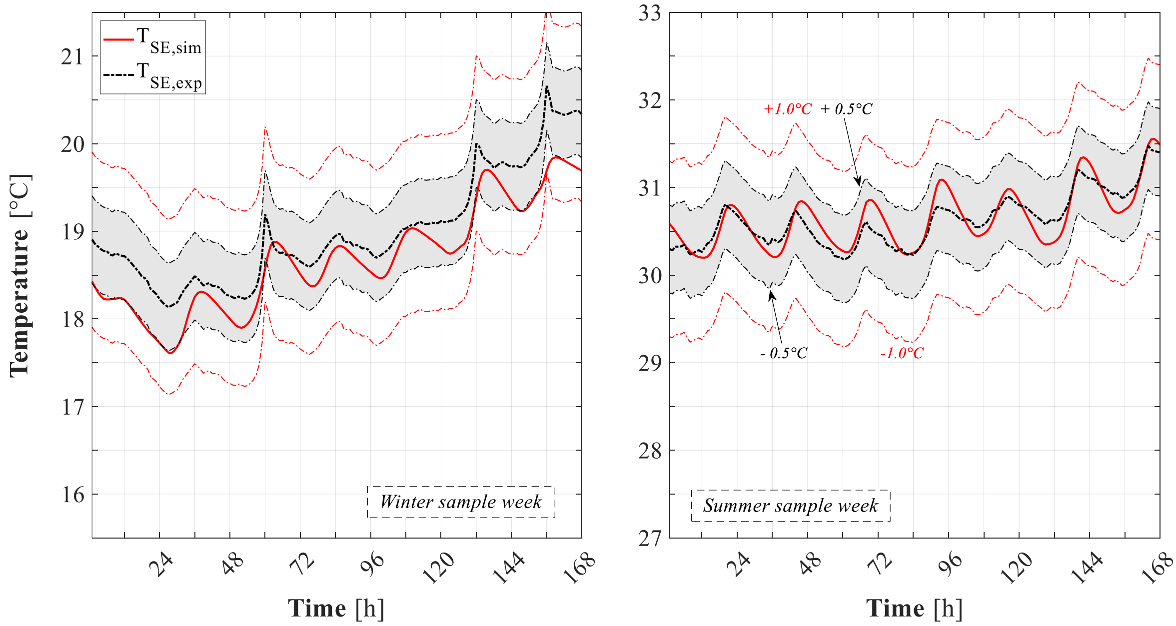

Fig. 5.16. South-East wall temperature: simulated vs. experimental results (two sample weeks).

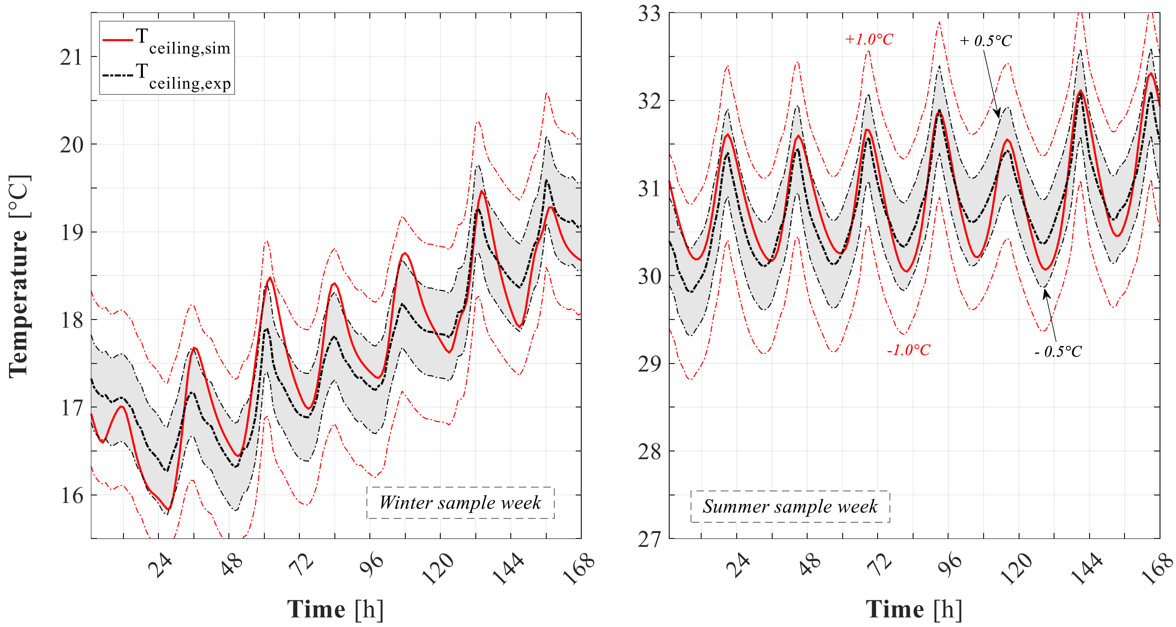

Fig. 5.17. Ceiling temperature: simulated vs. experimental results (two sample weeks).

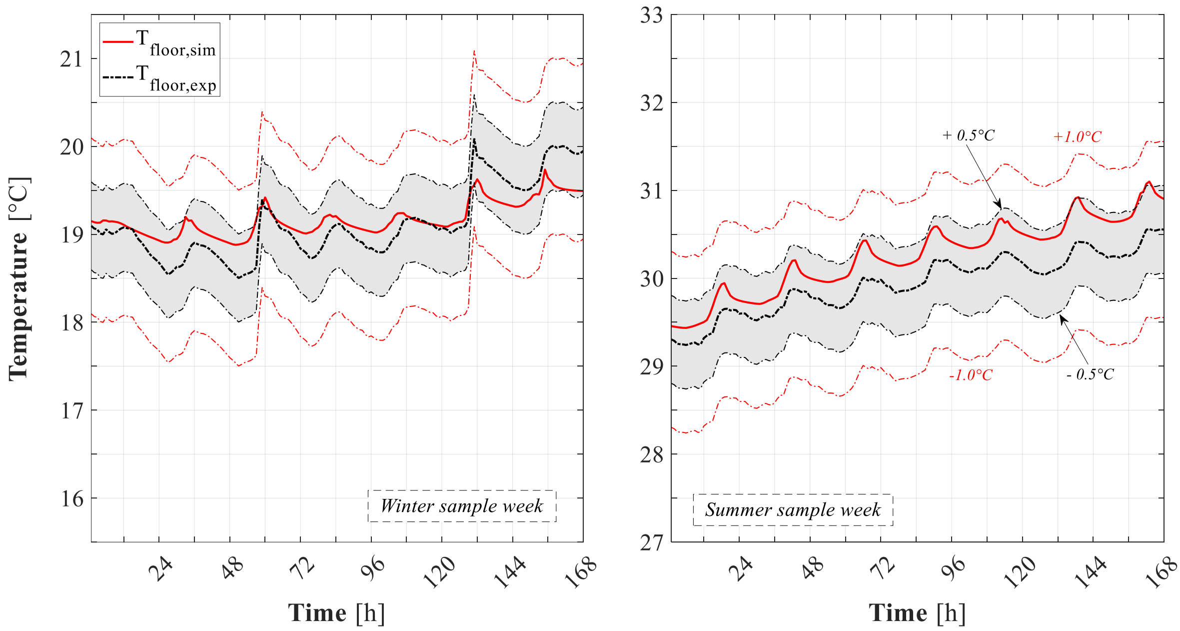

Fig. 5.18. Floor temperature: simulated vs. experimental results (two sample weeks).

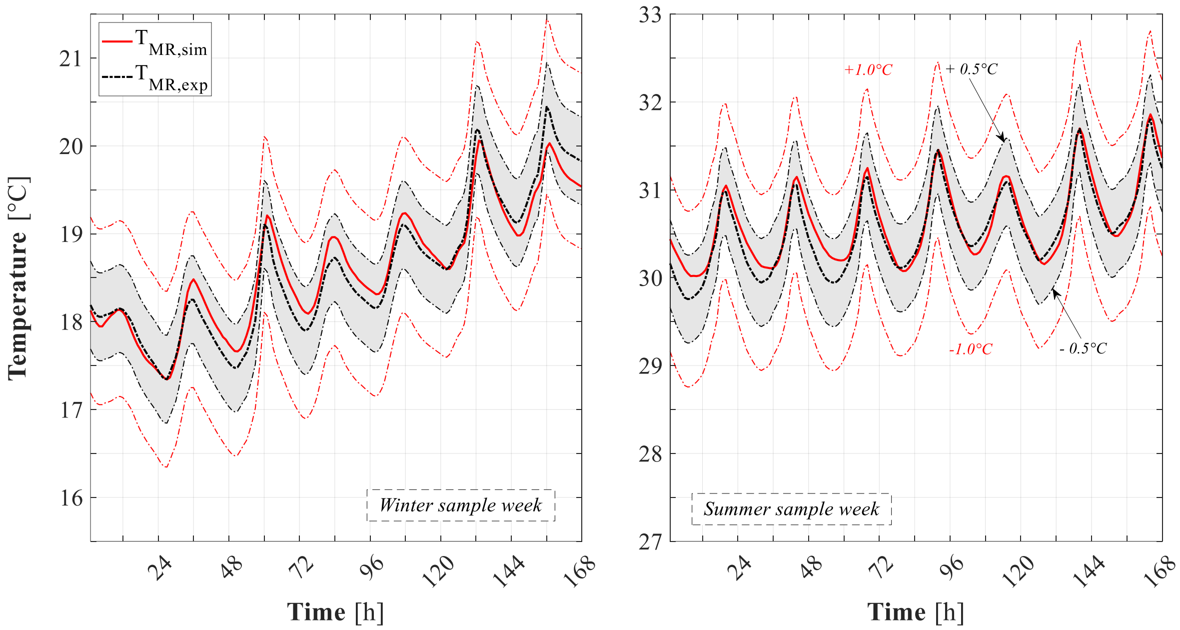

Fig. 5.19. Mean radiant temperature: simulated vs. experimental results (two sample weeks).

By such figures it can be detected that the highest differences between simulation and experimental results are obtained for the temperatures of the ceiling ($T_{ceiling}$) and of the South-East internal surface (T_{SE}), which shows the highest differences, especially during winter. On the other hand, very low variances are found out for the remaining internal surface temperatures. The lowest ones are observed for the indoor air temperature, T_{IN}, and for the mean radiant temperature, T_{MR}.

Referring to the winter season, from Fig. 5.13 to Fig. 5.18 it can be observed that the minimum temperatures are rather high respect to the expected ones. As an example, the indoor air temperature never falls under 16.8°C (Fig. 5.13). This result is due to the North-East (NE) wall that, as above mentioned, is adjacent to another room in which machineries are continuously switched on ($T_{NE,exp}$ is never lower than 18.5°C, even during winter time, see Fig. 5.11, top). Therefore, the behaviour of such element could be considered as continuous indoor thermal load acting in the test room.

The simulated and experimental indoor air and surfaces temperatures are further compared with the aim to better assess the reliability of DETECt. Specifically, for all the investigated parameters the comparison analysis is carried out for the whole period in which the investigation was conducted (from February to November 2018). From this point of view all the obtained simulation results are plotted against the corresponding measured ones. For the indoor air temperature (T_{IN}), the result of this analysis is reported in Fig. 5.20, whereas those of all the considered internal surface temperatures (i.e. T_{SW}, T_{NW}, T_{SE}, $T_{ceiling}$, and T_{floor}) and of the Mean Radiant one (T_{MR}) are shown in Fig. 5.21, Fig. 5.22, Fig. 5.23, Fig. 5.24, Fig. 5.25 and Fig. 5.26, respectively. Such figures allow one to easily detect the overall distance between simulation results (i.e. plotted points) and the bisector (corresponding measured temperatures): the lower the detected deviations, the higher the simulation reliability. Also, in this case, all these figures include the confidence instrument interval, i.e. the error band range (internal to the red dash and dot lines), obtained by shifting the bisector toward ± 1.0°C. Moreover, a narrower interval given by ± 0.5°C is included too (grey band) with the aim to enhance the reliability evaluation of the simulation results.

By such analysis it can be observed that, for almost all the simulated indoor air and surfaces temperatures, good agreements between numerical and experimental results are achieved. Almost all the simulation results are included into the band range of ± 1.0°C. Note that similar results were obtained by comparing the simulated and experimental temperatures of the window glass and frame and of the door of the considered test room (not reported for sake of brevity).

By observing Fig. 5.20 - Fig. 5.26 it can be noticed that during winter hours, temperatures are always higher than 16°C (despite of the measured much lower outdoor air temperatures). These rather high room temperatures are a consequence of the continuous (above mentioned) room thermal load due to the North-East wall. The lowest measured winter temperatures are detected on the ceiling (Fig. 5.24). During summer hours all the examined temperatures never exceed 35°C. For the South-East wall and floor, a lower number of temperature points seemingly appear in the reported plots with respect to those of the remaining building elements. In reality, the plotted points are throughout the same but those of such two elements often overlap because of the related slight time variations of temperature. This effect is due to the higher thermal inertia of South-East wall and floor versus that of the other room elements.

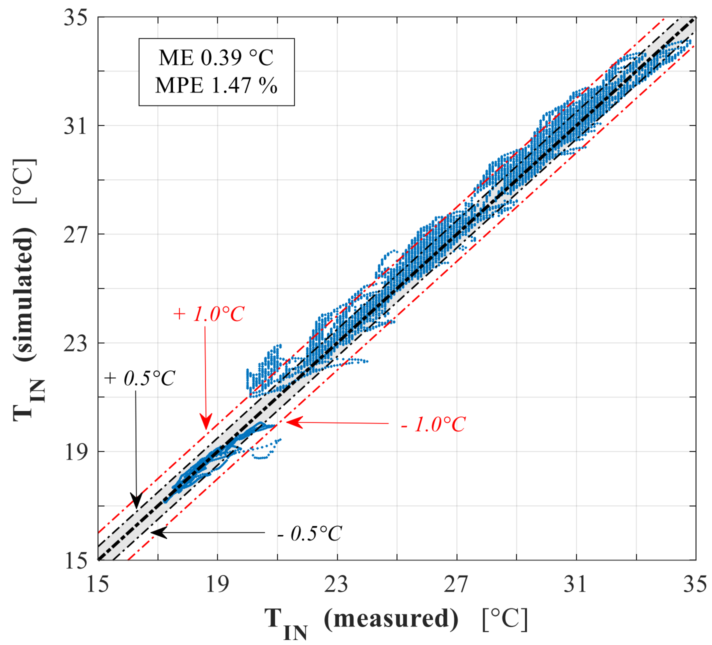

Fig. 5.20. Indoor air temperature: simulated vs. experimental results (from February to November).

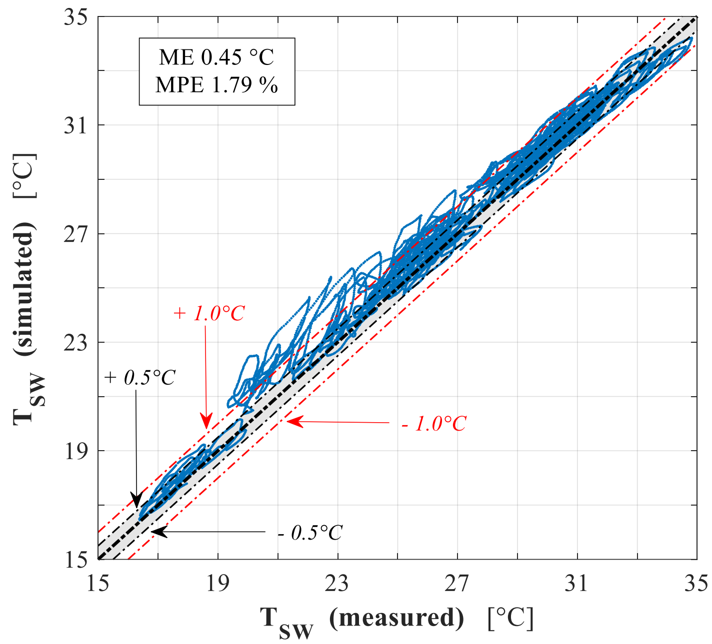

Fig. 5.21. South-West wall temperature: simulated vs. experimental results (from February to November).

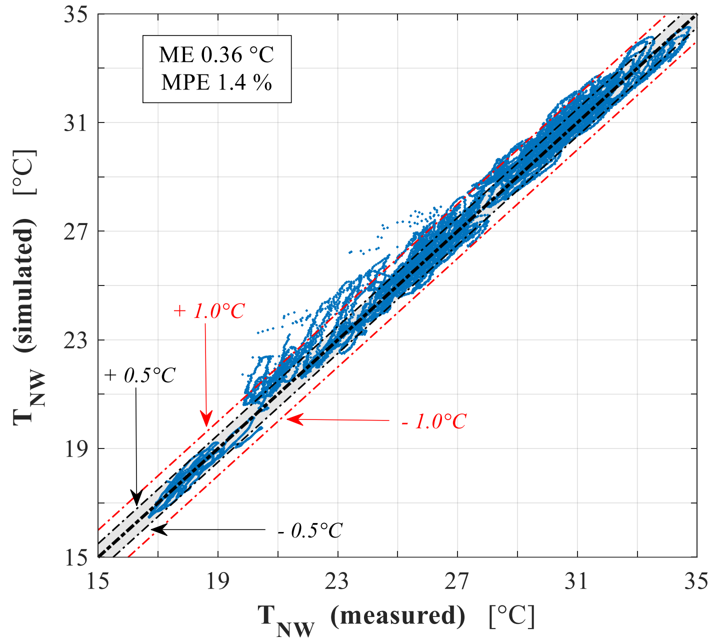

Fig. 5.22. North-West wall temperature: simulated vs. experimental results (from February to November).

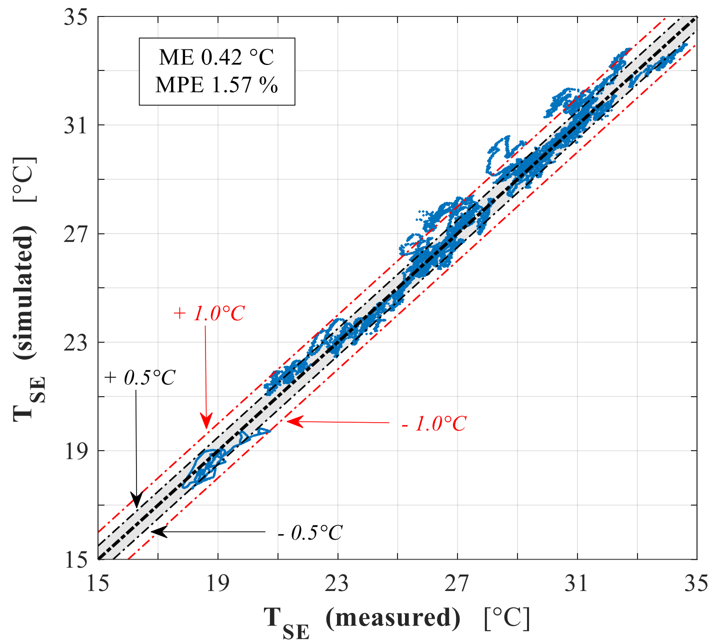

Fig. 5.23. South-East wall temperature: simulated vs. experimental results (from February to November).

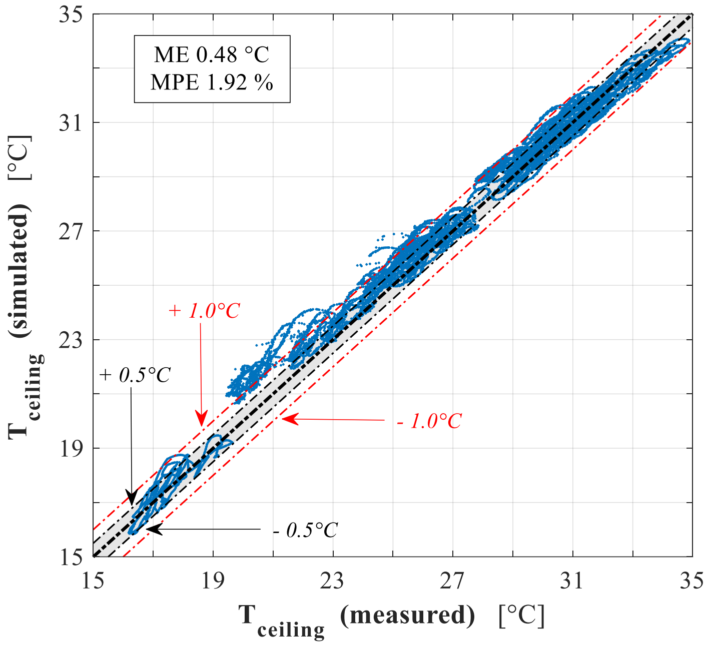

Fig. 5.24. Ceiling temperature: simulated vs. experimental results (from February to November).

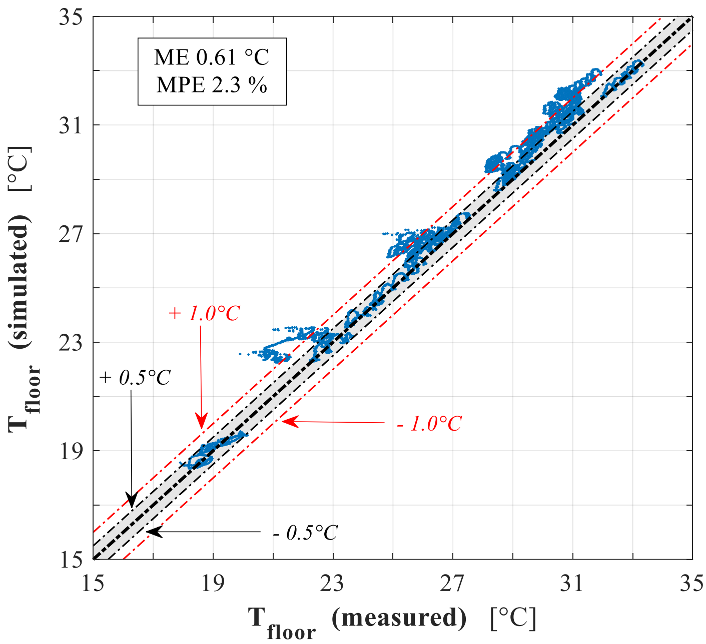

Fig. 5.25. Floor temperature: simulated vs. experimental results (from February to November).

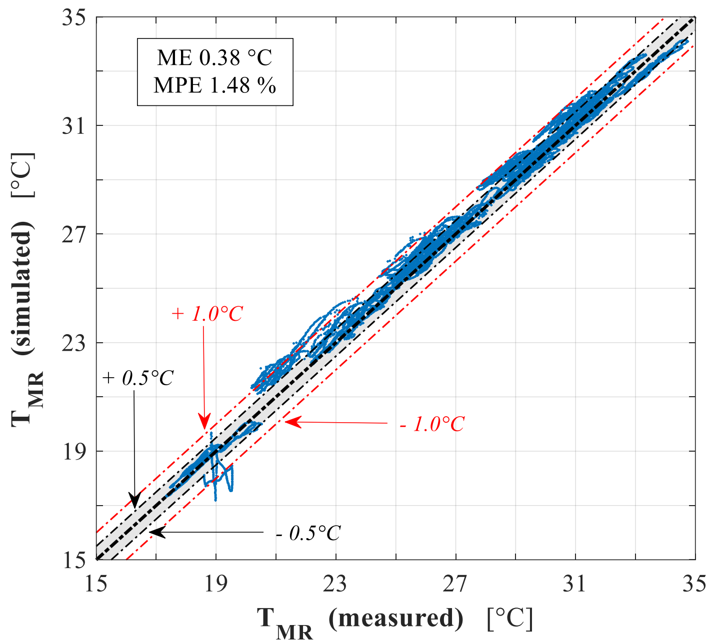

Fig. 5.26. Mean radiant temperature: simulated vs. experimental results (from February to November).

Error analysis

In order to better assess the reliability of the obtained simulation results respect to the measured ones, the related Mean Error (ME) and Mean Percentage Error (MPE), calculated on the total number of measurements (Z = 38764), are considered:

$$\mathrm{ME} = \frac{1}{Z} \cdot \sum_{z} \left| T_{sim,z} - T_{exp,z} \right| \tag{5.6}$$

$$\mathrm{MPE} = \frac{1}{Z} \cdot \sum_{z} \frac{\left| T_{sim,z} - T_{exp,z} \right|}{T_{exp,z}} \cdot 100 \tag{5.7}$$

By computing ME and MPE for all the investigated parameters from February to October 2018, very low errors are detected. Specifically, the following MEs and MPEs are obtained:

- Indoor air temperature (T_{IN}): 0.39°C and 1.47%;
- South-West wall temperature (T_{SW}): 0.45°C and 1.79%;
- North-West wall temperature (T_{NW}): 0.36°C and 1.40%;
- South-East wall temperature (T_{SE}): 0.42°C and 1.57%;
- Ceiling temperature ($T_{ceiling}$): 0.48°C and 1.92%;

- Floor temperature (T_{floor}): 0.61°C and 2.30%;
- Mean radiant temperature (T_{MR}): 0.38°C and 1.48%.

It is noteworthy to observe that MEs and MPEs are always lower than 0.5°C and 2%, respectively. An exception is obtained for T_{floor} for which the slightly higher ME and MPE values (0.61% and 2.3%) are probably due to uncertainty about the floor slab materials thermophysical properties.

5.4. Conclusions

This chapter regards the experimental validation of an in-house developed dynamic simulation model for the building energy performance analysis. This model, implemented in a MatLab tool called DETECt, is conceived for research purposes with the aim to assess the energy performance of innovative building technologies. DETECt has been uninterruptedly refined and updated by authors with new functions and subroutines, and the presented experimental validation has to be considered as one step of the conducted research work on developing this tool. DETECt can be coupled to additional tools purposely developed for simulating innovative building plants (renewable energy systems, novel HVAC system, etc.).

The reliability of the presented model to simulate the building heat transfer and thermodynamic behaviour was investigated through a suitable procedure performed by means of a purposely developed real test room located at the University of Naples Federico II, Naples, South Italy (the architectural and material features of such test room correspond to those of many Italian buildings). In the chapter, details regarding the design of the developed experimental set-up, the carried out empirical analysis, and the results of the experimental validation process are discussed.

DETECt was successfully experimentally validated. Simulated indoor air and surfaces temperatures resulted in very good agreement with the corresponding experimental data (differences between simulated and measured temperatures are often lower than 0.5°C and almost always lower than 1°C). Furthermore, very low mean absolute and percentage errors are detected (e.g. for the indoor air temperature, 0.4°C and 1.4% are achieved, respectively).

CHAPTER

6

6. Building integrated photovoltaic/thermal system (BIPV/T system)

The modelled BIPV/T system consists of a continuous air channel, obtained by BIPV/T modules connected in series in the vertical direction. A mathematical model of such system is developed with the aim to study the vertical stratification of PV and air temperatures, and to study their effects on the thermal behaviour of the adjacent indoor thermal zones and on the system electrical and thermal performances. Ultimate goal of the code is to provide a tool for the swift optimization of the BIPV/T configuration, to enhance the overall system performance as a function of the climate and building use.

6.1 Aim of the work and content of the chapter

The developed model of the BIPV/T system is based on a finite volume method for the numerical solution of the two-dimensional steady heat conduction. A resistance capacitance thermal network is modelled with the aim to describe the phenomena taking place within the PV/T system and between it and the indoor/outdoor environments. Such detailed model, also validated against experimental data published in [263], was implemented in a computer tool for the building thermal analysis (called DETECt 2.3 [231]), written in MatLab and suitably modified to allow modelling the thermal behaviour of the proposed system as a whole (i.e. coupled approach). The obtained simulation model allows assessing the BIPV/T energy performance of multi-floor buildings, by accurately calculating the thermal gradient inside the PV/T channel and the temperature stratification of the interior wall surface. This novel feature is particularly useful to assess the impact of the BIPV/T system on the building loads and occupants' comfort and to find out the BIPV/T façade inversion point. Such concept, analysed in this chapter represents the building height (i.e. channel length) at which corresponds: i) advantageous passive effects on the energy and comfort performance (i.e. heat gains in winter, cooling effect in summer); ii) the maximization of the active effects in terms of electricity production and thermal energy exploitation. All the above discussed features are new and not yet published in the available literature.

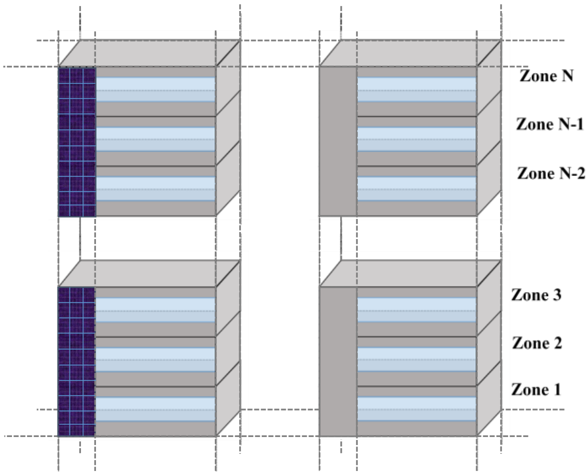

Fig. 6.1. Modelled innovative and reference building façade.

By means of the developed code, it is possible to investigate the performance of BIPV/T connected in series and mounted onto or integrated into the envelope of high-rise buildings (multi-zone and multi-floor), as sketched for a conventional and innovative façade in Fig. 6.1. In addition, differently from the majority of the commonly used commercial software, façades and roofs of a building thermal zone can be partially integrated with PV/T systems.

The developed in-house numerical model is capable to assess:

- energy fluxes, temperatures and airflow distribution within the BIPV/T system;
- active and passive effects due to the BIPV/T system on the energy performance and on the indoor thermal comfort of high-rise buildings.

In addition, a suitable tool for parametric and sensitivity analyses is implemented in the simulation code. This tool allows one to easily find out the optimal design (e.g. aspect ratio, inlet positions, etc.) and operating (e.g. air mass flow rate) parameters that minimize the overall building energy demand. Within the code, a suitable tool for the calculation of economic and environmental performance indexes is also implemented. As a result, comparative energy - as well as economic and environmental - analyses can be carried out with the aim to evaluate the overall performance of traditional and innovative building facades.

Differently from most of the papers available in literature, which focus on single aspects of BIPV/T systems without studying the system as a whole, in this chapter a comprehensive case study and a parametric analysis are presented. Such investigations also aim to show the potentiality of the model and the feasibility of façade integrated air BIPV/T system to counterbalance or overtake the building energy consumptions. The proposed air open loop BIPV/T system is applied to the perimeter zone of a high-rise office building located in several representative European weather zones, Prague (Czech Republic), Freiburg (Germany), Bolzano and Naples (Italy), Madrid (Spain), Athens (Greece), and Almeria (Spain).

The analysis of the results obtained from the case study and parametric investigation aims to provide helpful design and operating guidelines, useful for designers and practitioners working at the early design stage of innovative BIPV/T facades, also toward the achievement of the NZEB goal [238]. In fact, ultimate goal of the proposed work is to show a methodology for evaluating the magnitude of passive and active effects, as a function of the system design and operating conditions, on the indoor thermal comfort and overall energy requirements.

6.2. Simulation model

The modelled multi-floor BIPV/T façade consists of PV panels attached to a metal wall layer underneath air is drawn by mean of a mechanical fan. This ventilated air channel is created between the metal wall layer and the insulation back layer attached to the wall, as sketched in Fig. 6.2.

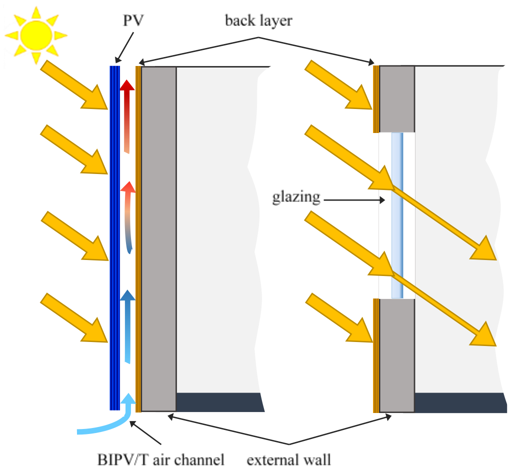

Fig. 6.2. Sketch of the modelled BIPV/T façade relative to the first floor. Sections of the two parts of wall integrating the PV/T system (left) and the opaque/glazing/opaque system (right).

To calculate the BIPV/T system energy performance, by taking into account the active and passive effects on the consumptions and of the indoor thermal comfort of the adjacent thermal zones, a suitable simulation model is developed. To this aim, the PV/T panels and the building envelope elements (e.g. wall, roof) integrating them are modelled as a whole system, whose mathematical equations (describing the thermal and electrical behaviour) are solved simultaneously. To obtain such comprehensive tool, a numerical model for calculating the energy fluxes, temperatures and airflow distribution within the BIPV/T is developed and properly implemented in a mathematical model for building energy performance analyses [231]. This building thermal model, called DETECt 2.3 and written in MatLab by following a parametric modelling approach, was validated through the BESTEST procedure [232, 238]. Its mathematical description of the heat transfer phenomena is based on a nodal description of the building elements (by using a finite difference approach based on an implicit solution scheme [231]). Thus, in this chapter the numerical building model is suitably modified with the aim to integrate the PV/T model and carry out comprehensive energy and thermal analysis of BIPV/T systems. Besides its complexness, such modelling approach, coupling both detailed models of BIPV/T systems and building envelopes, is particularly suitable in case of heavy structure building, typical in hot climates for thermal cooling, and when low or null insulation between the PV and the building element is considered (e.g. for exploiting the winter heating BIPV/T passive effects).

The simulation model developed in this work allows one to dynamically predict the thermal behaviour of mono and multi-zone buildings, as well as multi-story buildings, integrating air based open loop PV/T panels. The temperature field of a building element, integrating or not a PV/T system, can be calculated as a function of the building features (i.e. building shape and geometry, envelope materials, etc.) and weather conditions (i.e. assessing the solar radiation incident on any tilted surface by means of geometric relationships). The simulation code also includes an energy and economic assessment tool, which allows defining and simulating different operating conditions. Among others, by the presented simulation model it is possible to take into the account the heat recovered through the PV/T channel on the heating energy consumptions. Specifically, such thermal energy can be directly supplied, as free heating, to the air thermal zone or to the evaporator of a heat pump with the aim to increase its performance.

In this section, the BIPV/T model and the modification applied to the building thermal model are described. A brief description of the considered thermal comfort indexes and of the energy and economic model, implemented to assess the system energy and economic feasibility, is reported.

6.2.1. BIPV/T model

The mathematical model of the BIPV/T system is based on a finite volume approach for the numerical solution of the two-dimensional steady heat conduction. A set of equations is obtained for each node of the adopted thermal resistance capacitance (RC) network, including conductive, radiative and convective heat transfer occurring within and through the BIPV/T system. A sketch of the considered BIPV/T system thermal network used to model the system behaviour is shown in Fig. 6.3.

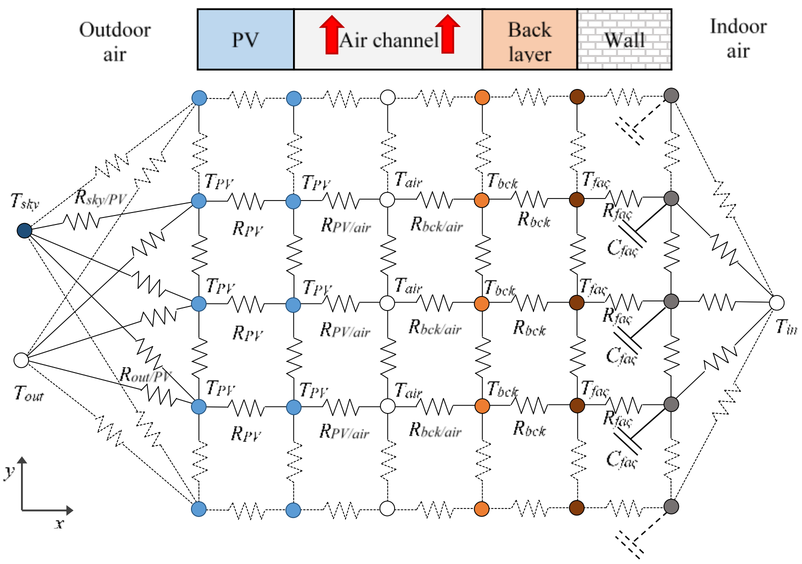

Fig. 6.3. BIPV/T system RC thermal network.

Here, a 2-D transient heat transfer is simultaneously considered for all the components of the South-façade integrating the BIPV/T system, as well as for the portion of the façade without them. A 1-D transient heat transfer is taken into account between the South-façade and the outdoor and the indoor environments. The description of the mathematical model relative to the system consisting of the external wall integrating the PV/T system is here reported. To calculate the air temperature gradient within the BIPV/T cavity, the South-façade integrating PV/T panels is discretized in a two-dimensional Cartesian coordinate system. Each element of the system (i.e. PV, air gap channel, back layer, wall) is subdivided along the vertical direction (y) in *N* equal resistive nodes. Differently from the PV, air channel, and back layer, the wall integrating the PV/T is discretized in *N* capacitive nodes to model its thermal inertia. Note that building indoor / outdoor air temperature gradients are neglected.

In each time step interval, *t*, the heat balance equation on the n-*th* PV node is:

$$\sum_{i=n-1}^{n+1}\left(\frac{T_{PV,i}-T_{PV,n}}{R_{PV\pm}^{cond}}\right)+\frac{T_{out}-T_{PV,n}}{R_{out}^{conv}+R_{PV}^{cond}}+\frac{T_{sky}-T_{PV,n}}{R_{sky}^{rad}+R_{PV}^{cond}}+\frac{T_{air,n}-T_{PV,n}}{R_{cavity}^{conv}+R_{PV}^{cond}}+\frac{T_{bck,n}-T_{PV,n}}{R_{cavity}^{rad}+R_{PV}^{cond}}+I_{sol,PV}=0 \quad (6.1)$$

where *T* refers to the nodes of the PV, the air cavity and outdoor air temperatures; *R* refers to conductive, convective and radiative thermal resistances (reported in Table 6.1) between the *n-th* node and neighbours ones (Fig. 6.3), $I_{sol,PV}$ is the net (incident minus the electricity production) incident solar radiation on the *n-th* node. The differential equation describing the energy rate of change of each control volume linked to the *n-th* air cavity temperature node is calculated as in [137]:

$$L \cdot h_{cavity,n}\left(T_{PV,n} - T_{air,n}\right) + L \cdot h_{cavity,n}\left(T_{bck,n} - T_{air,n}\right) = \dot{m}_{air} c_{p,air} \frac{dT_{air,n}}{dy} \tag{6.2}$$

According to previous studies [137, 264], in the developed model an exponential profile is taken into account for simulating the air temperature, T_{air}, in the BIPV/T cavity:

$$T_{air,n} = T_{air,n-1} \cdot e^{\left(-\frac{2 \cdot h_{cavity} \cdot L \cdot y}{\dot{m}_{air} c_{p,air}}\right)} + \left(\frac{h_{cavity} \cdot T_{PV,n} + h_{cavity} \cdot T_{bck,n}}{2 \cdot h_{cavity}}\right) \cdot \left(1 - e^{\left(-\frac{2 \cdot h_{cavity} \cdot Ly}{\dot{m}_{air} c_{p,air}}\right)}\right) \tag{6.3}$$

where h_{cavity} is the heat transfer coefficient within the cavity.

Table 6.1. Resistances [K/W].

Symbol	Expression	Symbol	Expression	Symbol	Expression	Symbol	Expression
$R_{PV\pm}^{cond}$ **	$\frac{L_{strip}}{2 \cdot k_{PV} \cdot \delta_{PV} \cdot W_{PV}}$	R_{PV}^{cond}	$\frac{\delta_{PV}}{2 \cdot k_{PV} \cdot A_{strip}}$	R_{cavity}^{conv}	$\frac{1}{h_{cavity(n)} \cdot A_{strip}}$	R_{cavity}^{rad}	$\frac{1}{h^*_{rad,cavity} \cdot A_{strip}}$
$R_{bck\pm}^{cond}$ **	$\frac{L_{strip}}{2 \cdot k_{bck} \cdot \delta_{bck} \cdot W_{bck}}$	R_{bck}^{cond}	$\frac{\delta_{bck}}{2 \cdot k_{bck} \cdot A_{strip}}$	R_{out}^{conv}	$\frac{1}{h_{out(n)} \cdot A_{strip}}$	R_{sky}^{rad}	$\frac{1}{h^*_{rad,sky} \cdot A_{strip}}$
R_{fac}^{cond}	$\frac{\delta_{fac}}{2 \cdot k_{fac} \cdot A_{strip}}$	R_{roof}^{cond}	$\frac{\delta_{roof}}{2 \cdot k_{roof} \cdot A_{strip}}$	R_{in}^{conv}	$\frac{1}{h_{in} \cdot A_{strip}}$		
		R_{floor}^{cond}	$\frac{\delta_{floor}}{2 \cdot k_{floor} \cdot A_{strip}}$				

* *linearized radiative heat transfer referring to the exchanged heat flow in previous the time-step* $h_{rad} = \dot{q}/\Delta T^{(t-1)}$

** *the symbol ± refers to bottom and top neighbour nodes. See Fig. 6.3, y-coordinate.*

The local heat transfer coefficient, $h_{cavity}(y)$, is calculated at each time step *t* as:

$$h_{cavity}(y) = \frac{k \cdot Nu(y)}{D_{eq}} \tag{6.4}$$

For comparative purposes, an average heat transfer coefficient, $\hat{h}_{cavity}$, is estimated; its value is approximated by an experimental linear correlation function of the air velocity, v_{air}. For design purposes, the following correlation is recommended [137, 264]:

$$\hat{h}_{cavity} = 3.94 \cdot v_{air} + 5.45 \tag{6.5}$$

$$v_{air} = C_d \sqrt{\Delta p / \Delta \rho} \tag{6.6}$$

where C_d depends on the channel aspect ratio, Δp, is the pressure drop along the channel and $\Delta \rho$ is the density gradient between the inlet ad outlet channel sections. For fully developed laminar flow, the local Nusselt number is calculated accordingly to [264], whereas for fully developed turbulent flow, the following relationship is taken into account:

$$Nu(\mathrm{y}) = 0.027 \cdot Re(\mathrm{y})^{0.80} \cdot Pr(\mathrm{y})^{0.33} \cdot \left(\frac{\mu_m(\mathrm{y})}{\mu_s(\mathrm{y})} \right)^{0.14} \tag{6.7}$$

For each layer, the local Reynolds number is calculated as:

$$Re(\mathrm{y}) = \frac{v_{air} \cdot D_{eq}}{v_m(\mathrm{y})} \tag{6.8}$$

The Reynolds number is compared to the critical one to estimate the flow regime. Note that it varies layer by layer due to the different temperature of the air flow and the resulting different kinematic viscosity, v_m(y).

Finally, in each time step interval t, the heat balance equation on the n-th back layer node is calculated as:

$$\begin{aligned} &\sum_{i=n-1}^{n+1} \left(\frac{T_{bck,i} - T_{bck,n}}{R_{bck\pm}^{cond}} \right) + \gamma \cdot \left(\frac{T_{out} - T_{bck,n}}{R_{out}^{conv} + R_{bck}^{cond}} + \frac{T_{sky} - T_{bck,n}}{R_{sky}^{rad} + R_{bck}^{cond}} + \frac{T_{fac,n} - T_{bck,n}}{R_{fac}^{cond} + R_{bck}^{cond}} + Q_{sol,\,faç} \right) + \ldots \\ &\ldots + (1-\gamma) \cdot \left(\frac{T_{air,n} - T_{bck,n}}{R_{cavity}^{conv} + R_{bck}^{cond}} + \frac{T_{PV,n} - T_{bck,n}}{R_{cavity}^{rad} + R_{bck}^{cond}} + \frac{T_{fac,n} - T_{bck,n}}{R_{fac}^{cond} + R_{bck}^{cond}} \right) = 0 \end{aligned} \tag{6.9}$$

where $Q_{sol,faç}$ is the solar radiation incident on each node of the back layer; γ is equal to 0 for the portion of the façade where the BIPV/T is integrated, whereas it is equal to 1 otherwise (e.g. if the back layer is external, as in case of opaque / transparent portion of the façade).

The gross electricity power production (P_{el}) of the BIPV/T systems is obtained by:

$$P_{el} = \eta_{PV} \cdot Q_{sol,PV} \cdot A_n \tag{6.10}$$

where $Q_{sol,PV}$ is the net incident solar radiation converted into electricity; $\eta_{PV} = \eta_0 - 0.005 \cdot (T_{PV} - 25)$, is the PV efficiency, assumed linearly decreasing with the increasing operating temperature, as reported in [137], η_0 is the PV efficiency in standard conditions and T_{PV} is the operating temperature. Note that the solar radiation incident on the PV modules, operating at their maximum power point condition, is assumed as uniform.

6.2.2. Modified building thermal model

The assessment of the impact of the PV/T system on the heating and cooling loads, and vice versa, is carried out by calculating the temperature of the interior wall comprising the thermal zone, including the one integrating the PV/T, and of the indoor air temperature, T_{in}. Such analysis is performed by means of the simulation model embedded in DETECt [232, 238]. Here, the discretized differential equations related to the wall integrating the PV/T devices are suitably modified. Note that, the temperature of the back layers of the PV/T (i.e. or the back layer average temperature) is considered as the boundary node for the capacitive wall integrating the PV/T. A first attempt to model and simulate, through DETECt, building roofs integrating solar thermal systems is reported in [232].

In DETECt, a nodal description of a building with a 1-D transient conduction model is assumed. Each building element material is discretized into a number, L, of thin sub-layers of different thicknesses (considered as uniform). In addition, in the modified version here presented, with respect to the portion of the wall integrating the PV/T, each l-th sub-layer is discretized along the vertical direction (y) in N equal resistive nodes (as those of the PV/T system). Each node of the considered building RC thermal network has a uniform temperature. The building is also subdivided in different thermal zones where the indoor air is considered as uniform and modelled through a single indoor air temperature node, whereas the envelope of each thermal zone is split into multi-layer elements (walls, floor, roof, horizontal and vertical internal partitions and windows).

For each building element integrating the PV/T system, the energy rate of change of each capacitive l-th node ($1 \leq l \leq L$) of the n-th layer ($1 \leq n \leq N$) is calculated as:

$$
\begin{aligned}
C_{1,n}\frac{dT_{1,n}}{dt} &= \frac{T_{fac,n}-T_{1,n}}{R_{fac}^{cond\_x}} + \sum_{j=n-1}^{n+1}\frac{T_{1,j}-T_{l,n}}{R_{j\cdot l}^{cond\_y}} + \frac{T_{2,n}-T_{1,n}}{R_{2,n}^{cond\_x}} && \text{for } l = 1 \\
C_{l,n}\frac{dT_{l,n}}{dt} &= \sum_{j=l-1}^{l+1}\frac{T_{j,n}-T_{l,n}}{R_{j\cdot l}^{cond\_x}} + \sum_{j=n-1}^{n+1}\frac{T_{l,j}-T_{l,n}}{R_{j\cdot l}^{cond\_y}} + \gamma\cdot Q_{l,n} && \text{for } 2 \leq l \leq L+1
\end{aligned}
\tag{6.11}
$$

where C and T are the thermal capacitance and the temperature of the generic node, R^{cond} is the sum of the halves sub-layers thermal resistances coupling the *l-th* node to their neighbour ones. The first capacitive node ($l = 1$) is coupled to the resistive façade temperature node, $T_{faç}$ in Fig. 6.3. For outer and inner surface non-capacitive nodes (see Fig. 6.3), the algebraic equation describing the related heat transfer is obtained through eq. (6.10) by setting the thermal capacitance $C_{l,n}$ to zero.

$Q_{,m,1}$ is the radiative forcing function, only acting on the inner non-capacitive nodes ($\gamma \neq 0$ if $l = L + 1$, being $\gamma = 0$ elsewhere), including incident solar and long-wave radiation exchange acting on outer and inner surfaces of thermal zone, assessed through the Gebhart's approach, as done in [232]. Note that further details about the assessment and handling of the solar radiation within the zone, and on calculation of the long-wave radiation exchange on the internal surfaces are available in [232]. For $l = L + 1$, R^{cond_x} becomes an equivalent (conductive plus convective) thermal resistance connecting the boundary non capacitive L node to that one related to the indoor air temperature node of the adjacent thermal zone. Note that for assessing the internal convective thermal resistance, the unitary convection heat transfer coefficient depends on the slope of the surfaces and the heat flux direction. Note also that the portion of the wall non integrating PV/T panels is only discretized along the x direction (i.e. only into L thin sub-layers); more details are reported in [232].

Finally, the differential equation on the thermal network node of the indoor air, T_{in}, is calculated as:

$$C_{in}\frac{dT_{in}}{dt}=\sum_{j=1}^{N}\left(\frac{T_{L+1,j}-T_{in}}{R_{j\cdot l}^{cond}+R_{in}^{conv}}\right)+\frac{T_{L+1,op}-T_{in}}{R_{fac,op}^{cond}+R_{in,op}^{conv}}+\frac{T_{L+1,tr}-T_{in}}{R_{fac,tr}^{cond}+R_{in,tr}^{conv}}+\dots$$
$$\dots+\sum_{m=1}^{M}\frac{T_{m,N}-T_{in}}{R_{in,m}^{conv}}+Q_g+Q_v\pm Q_{HVAC} \tag{6.12}$$

where C_{in} is the thermal capacitance of the zone indoor air, whose temperature, T_{in}, is assumed as homogeneous in the space. The indoor air node exchanges heat with: i) the N internal surfaces nodes of the portion of wall integrating the PV/T, ii) the internal surfaces nodes of the opaque and transparent façade portion (see Fig. 6.2), iii) the M internal surfaces nodes or the considered thermal zone. Note that the internal convective resistances, R_{in}^{conv}, are calculated as a function of the surfaces condition (e.g. ascendant or descendant flow, wall inclination). In addition, with the exception of the radiative thermal load, all sensible heat gains are considered as purely convective and networked to the indoor air node only. Such sensible heat gains are: Q_g, the internal gains due the occupants, lighting and electrical appliances; Q_v, the ventilation thermal load (including both the infiltration and ventilation terms); Q_{HVAC}, the sensible heat to be supplied to (Q_h) or to be removed from (Q_c) the building space by an ideal heating and cooling system (necessary to maintain the indoor air at the desired set point temperatures). Further details on the building thermal model are available in [232].

6.2.3. Thermal comfort model

The dynamic calculation of comfort indexes is carried out to assess the thermal comfort of occupants. To this purpose, the hygrothermal conditions inside the occupied spaces are calculated through DETECt by following the approach reported in [231, 238]. The thermal comfort model consists of several comfort indexes calculated as:

i) Predicted Mean Vote (PVM). This index represents the mean thermal sensation vote on a standard scale for a group of building occupants, exposed to a certain environment. The comfort perception, based on steady-state heat transfer between the body and the environment, is obtained for any given combination of environmental variables, prevailing activity levels and clothing. The *PMV* is a function of the air temperature (T_{in}), the mean radiant temperature (T_{mr}), relative air velocity (v)

and air humidity (in terms of vapour pressure, p_a), as well as the activity level (i.e. metabolic rate, M and the clothing insulation (I_{cl}), as:

$$PMV = f\left(T_{in}, T_{mr}, v, p_a, M, I_{cl}\right) \tag{6.13}$$

ii) Predicted Percentage of Dissatisfied (*PPD*). This index represents the predicted percentage of dissatisfied people at each *PMV*. The relationship between *PPD* shows that the *PPD* value decreases when *PMV* converges to zero, contrarily it increases in either the positive or negative direction. Note that the *PPD* also indicates that even at thermal neutrality (i.e. *PMV* = 0), about 5% of the people may be dissatisfied. The *PPD* index is calculated as:

$$PPD = 100 - 95 \cdot \exp\left(-0.03353 \cdot PMV^4 - 0.219 \cdot PMV^2\right) \tag{6.14}$$

iii) Mean radiant temperature (T_{mr}) of the indoor building space. It is defined as the uniform temperature of an ideal enclosure (where occupants stay) in which the radiant heat transfer from the human body is equal to the radiant heat transfer occurring in the real non-uniform enclosure. In DETECt, by assuming a simplified approach, T_{mr} is calculated as a function of the temperature of each surface (T_m) of the considered thermal zone (indicated with m), the view factor between, ($F_{p\text{-}m}$) a person (considered as a sphere in the middle of the zone) and the m-th surface, as:

$$T_{mr} = \sum_m \left(T_m \cdot F_{p-m}\right) \tag{6.15}$$

Further details on comfort indexes calculation are available in [265]. Finally, note that the comfort analysis is carried out by taking into account both indoor air temperature and humidity, which are controlled at a desired set point. From this point of view, in each simulation time step interval the space moisture balance on the indoor space air is calculated by following a decoupled approach. Further details are as reported in [231, 238].

6.2.4. Energy and economic model

The energy and economic feasibility of the investigated BIPV/T system is carried out by means of a thermo-economic model, here described. For comparison purposes, a conventional building system (without PV/T) is simulated and considered as Reference System (REF). Here, space heating and cooling is provided by the electric heat pump/chiller powered by the national grid, whereas in case of the investigated BIPV/T system a share of electricity is also covered by the PV electricity production. Energy indexes are calculated, for both the BIPV/T system and the REF one, assuming the same building occupancy, indoor gains, infiltration rates, and indoor air set points. The yearly Primary Energy Saving (*PES*) of the BIPV/T system with respect to the REF one is calculated as:

$$PES = \frac{1}{\eta_{el}} \cdot \sum_{t=1}^{Y} \left(P_{el,PV} - E_{el,aux} + \frac{Q_{h,REF}}{COP_{h,REF}} + \frac{Q_{c,REF}}{COP_{c,REF}} - \frac{Q_{h,BIPV/T}}{COP_{h,BIPTV/T}} - \frac{Q_{c,BIPV/T}}{COP_{c,BIPV/T}} \right) \cdot \frac{\Delta t}{3600} \qquad (6.16)$$

where $P_{el,PV}$ is the PV electricity produced by the BIPV/T system before described; $E_{el,aux}$ is the electricity supplied to the auxiliary devices (e.g. fans); $Q_{h,REF}$ and $Q_{c,REF}$ are the heating and cooling loads of the REF system, whereas $Q_{h,BIPV/T}$ and $Q_{c,BIPV/T}$ are those of the BIPV/T system; η_{el} is the national thermoelectric efficiency; COP_h and COP_c are the coefficient of performance of the considered heat pump/chiller.

In the simulation model, the heat pump / chiller is modelled as black-box, therefore COP_h and COP_c can be calculated by means of two different approaches: i) manufacturers' data, ii) recommended analytical equations. By the first method, *COP* values, condenser/evaporator and electrical outputs are obtained as a function of the occurring operating conditions (evaporator inlet and condenser outlet temperatures) and the part-load ratio (f_{PLR}), by means of data (e.g. characteristic curves) provided by manufacturers. Starting from manufacturers' data, the heat pumps/chillers performance is then easily obtained, for all the simulated operating conditions. By the second approach, the analytical equations recommended by the UNI/TS 11300 (Italian release of ISO EN 13790) are taken into account. As a result, starting by the nominal coefficient of performance (COP_N) and energy efficiency ratio (EER_N), obtained by the constructors for a device with a specific power, the system heating and cooling performance are calculated as:

$$\begin{aligned} COP_h &= \frac{COP_N}{COP_{max}} \cdot \frac{\vartheta_c + \Delta\vartheta_c}{\left(\vartheta_c + \Delta\vartheta_c\right) - \left(T_{out} - \Delta\vartheta_f\right)} \cdot \frac{4 \cdot f_{PLR}}{0.1 + 3.6 \cdot f_{PLR}} \left[1 - 0.25 \cdot \left(1 - 4 \cdot f_{PLR}\right)\right] \\ COP_c &= EER_N \cdot \frac{\vartheta_e - \vartheta_c + T_{out} + \vartheta_e}{2 \cdot \left(\vartheta_c - \vartheta_e\right)} \cdot \left(a \cdot f_{PLR}^3 + b \cdot f_{PLR}^2 + c \cdot f_{PLR} + d\right) \end{aligned} \qquad (6.17)$$

where f_{PLR} is the part-load ratio, T_{out} the outdoor air temperature, θ_c and θ_f the condenser/evaporator temperatures, respectively. Further details are available in [238].

To assess the economic feasibility of the system, the investigated system capital costs are taken into account. The extra capital cost of the BIPV/T system (with respect to the REF one), $C_{BIPV/T,tot}$, includes the capital costs of PV/T collectors, fans, and auxiliaries, and it is calculated as a function of the solar field surface area, as:

$$C_{BIPV/T,tot} = j_{PV/T} \cdot A_{PV/T} \qquad (6.18)$$

where $j_{PV/T}$ is the BIPV/T capital cost per square meter.

The BIPV/T system yearly economic savings are reported in terms of operating costs with respect to those of the reference system, REF. The PV electricity production is used to balance the building final energy use, whereas the surplus is delivered to the national grid, sold at the feed-in tariff, $c_{el,ft}$. The avoided cost due to the electricity self-consume is calculated at the purchase tariff, $c_{el,pur}$. The difference between the BIPV/T system operating costs and those of the REF system, ΔC, is calculated by taking into account the net electricity consumptions. Note that in the REF system, only the heat pump/chiller electricity consumptions are taken into account, whereas electricity consumptions due to fans and PV production are also considered for the BIPV/T case. Thus, the yearly economic savings are calculated as:

$$\Delta C = \sum_{t=1}^{Y} \left[\left(P_{el,PV} - \dot{E}_{el,aux} + \frac{\dot{Q}_{h,BIPV/T}}{COP_{h,BIPV/T}} + \frac{\dot{Q}_{c,BIPV/T}}{COP_{c,BIPV/T}} - \frac{\dot{Q}_{h,REF}}{COP_{h,REF}} - \frac{\dot{Q}_{c,REF}}{COP_{c,REF}} \right) \cdot c_{el} \right] \cdot \frac{\Delta t}{3600} \tag{6.19}$$

where c_{el} is equal to $c_{el,ft}$ if in the considered time interval, t, there is surplus of PV electricity production, otherwise c_{el} is equal to $c_{el,pur}$.

To assess the economic profitability, the main economic indexes are calculated, such as the Simple and Discounted Pay Back period (*SPB* and *DPB*):

$$\begin{aligned} SPB &= \frac{C_{BIPV/T,tot}}{\Delta C} \\ DPB &= -\frac{log\left(1 - SPB \cdot a\right)}{log\left(1 + a\right)} \end{aligned} \tag{6.20}$$

where a is the interest rate. At last, Net Present Value (*NPV*) and Profit Index (*PI*) are also evaluated as:

$$\begin{aligned} NPV &= \Delta C \cdot \left\{ \frac{1}{a} \cdot \left[1 - \frac{1}{\left(1+a\right)^N} \right] \right\} - C_{BIPV/T,tot} \\ PI &= \frac{NPV}{\left| C_{BIPV/T,tot} \right|} \end{aligned} \tag{6.21}$$

6.3. Experimental verification

To verify the reliability of the simulation model, the obtained simulation results are compared with experimental data previously obtained at the Solar Simulator Laboratory at Concordia University, and published in [263]. The model inputs are set accordingly to the experimental tests. In particular, the tested BIPV/T system consists of two mono-crystalline PV panels with a transparent backing, 4 mm thick, connected in series and mounted above a layer of insulation and plywood separated by an air channel. The BIPV/T system has the following dimensions: length of 2.039 m (i.e. each panel is 1.0 m length), width of 0.529 m, air channel depth of 45 mm for a total thickness of 87 mm. Measurements are gathered by taking into account the air channel mass flow rate equal to 232 kg/h and by assuming, as boundary conditions, the outside air temperature set at 20°C and the solar radiation set at 1030 W/m². Additional details are reported in Table 6.2.

Table 6.2. Experimental conditions.

Parameter	**Unit**	**Value**
BIPV/T width	m	0.529
BIPV/T height	m	2.039
PV thickness	mm	4.0
Emissivity	-	0.89
Air channel depth	mm	45
Mass flow rate	kg/h	237
Outside air temperature	°C	20.0
Sky temperature	°C	14.3
Solar irradiation	W/m²	1030
Wind speed	m/s	2.2

In Fig. 6.4 the temperature trends for the PV panel and the air flowing through the channel are shown. Here, a good agreement between the measured data (obtained from the experimental set up [263], relative to blue diamond markers for the PV temperature and orange diamond markers for the air temperature) and simulated ones (red line for PV temperature and black line for air temperature) can be observed. Note that simulations are obtained by discretizing each BIPV/T element in 300 nodes, to get a continuous trend. An average good agreement between simulated and measured is achieved for both the PV and the air channel temperature. A higher discrepancy is observed at the inlet section (i.e. at height 0 m) and at the joint section among the two panels (i.e. at height 1.0 m), highlighted with the coloured blue regions in Fig. 6.4.

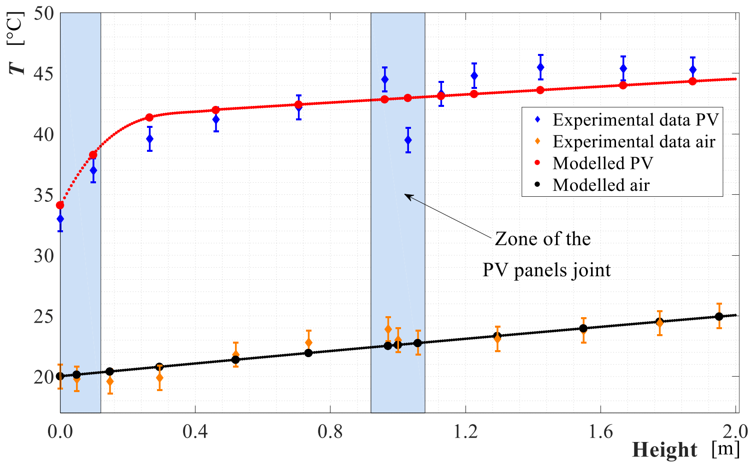

Fig. 6.4. Comparison between measured and calculated temperatures.

Here, the temperature drops at the centre of the BIPV/T system (at height = 1.0 m) relative to the experimental data trend is due to the gap in the PV cells between the two connected PV panels, as discussed in [263]. In fact, at the junction between the two PV panels, such gap (due to the packing factor of the PV cells between the two PV panels) did not prevent the solar radiation to transmit through the PV layer, causing an increase of the measured air channel temperature and a drop in the PV one, with respect to the simulated ones.

By comparing the simulated and experimental data, measured with T-type thermocouples (12 for the PV panel and 13 for the air channel, uniformly distributed along the PV panel), with an accuracy of ±1°C [263], an acceptable average error of 2.4 and 1.9% for T_{PV} and T_{air} is achieved, calculated as:

$$e_{\%} = \frac{\frac{1}{n} \cdot \sum_{i=1}^{n} \left| X_{\text{exp}}^{(i)} - X_{\text{sim}}^{(i)} \right|}{\overline{X}_{\text{exp}}} \cdot 100 \tag{6.22}$$

The main cause of discrepancy between simulated and experimental data, observed for the PV panels, was estimated to be the heat transfer coefficient. Therefore, an additional comparison between experimental data and simulation results, relative to the calculated heat transfer coefficients within the air channel ($h_{c,cavity}$(y)), is carried out. Simulated and experimental results are reported in Table 6.3. Here, the estimation of the air channel heat transfer coefficient is done through measures obtained during experimental tests carried out on the same BIPV/T system and reported in [266]. Here, the used outside average heat transfer coefficients ($\hat{h}$), for the PV and the back (insulation) layers of the BIPV/T system, are calculated by the knowledge of the temperature of each BIPV/T element and their heat transfer.

Table 6.3. Experimental verification assumptions. Numerical (sim) and experimental (exp) parameters.

Parameter	**Symbol**	**Unit**	**Value**	**Percentage error [%]**
Mass flow rate	$\dot{m}$	kg/h	232	
Average air velocity	v_{exp}	m/s	2.3	2.6
	v_{sim}	m/s	2.24	
Reynolds Number	Re_{exp}	-	12365	0.6
	Re_{sim}	-	12287*	
Heat transfer coefficient of PV	$\hat{h}_{exp}$	W/(m²·K)	15.55	1.4
	$\hat{h}_{sim}$	W/(m²·K)	15.34*	
Heat transfer coefficient of back layer	$\hat{h}_{exp}$	W/(m²·K)	5.67	4.2
	$\hat{h}_{sim}$	W/(m²·K)	5.43*	

**average value (300 nodes)*

In the developed simulation model, differently from these measured average heat transfer coefficients, local absolute heat transfer coefficients are calculated. Although this difference, a good agreement is observed, with encouraging low discharges of the percentage error, as shown in Table 6.3. Nevertheless, further investigation will be carried out from both numerical and experimental points of view.

6.4. Case study

The developed case study analysis refers to a ten-floor building with its longitudinal axis-oriented East–West. Simulations are carried out for the South facing perimeter thermal zones, consisting of thermal spaces adjacent to the investigated South-façade. Here, the modelled façade is split in two parts, one integrating the BIPV/T system and the other one consisting of an opaque/glazing/opaque wall structure, as shown in Fig. 6.5.

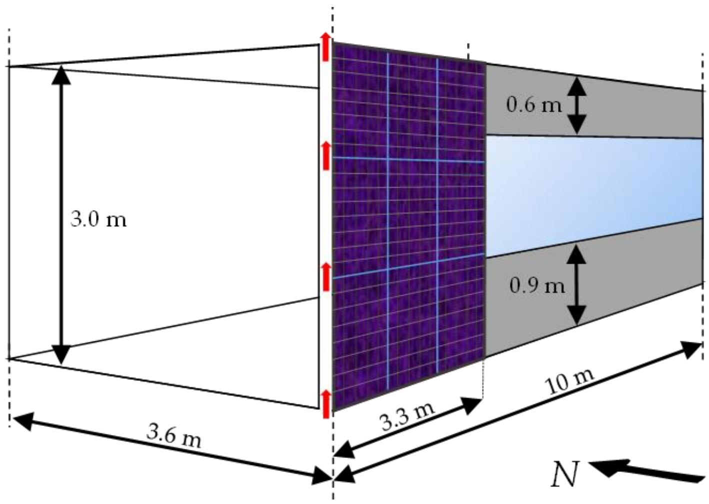

Fig. 6.5. Perimeter zone of one sample building floor.

For comparison purposes, both the proposed innovative building, i.e. BIPV/T, and the reference one, REF, are modelled and simulated. The sketch of the simulated BIPV/T and REF buildings are shown in Fig. 6.1. Note that the simulated modular BIPV/T system is based on mono-crystalline silicon cells (156 x 156 mm) PV solar panels, whose features are reported in Table 6.4. Each panel of the BIPV/T system is approximately 1.0 m length, with a width of 0.53 m, and an air cavity depth of 45 mm.

Table 6.4. BIPV/T features.

Parameter	Symbol	Unit	Value
Gross area	A_{PV}	m^2	99.0
Thickness	t_{PV}	mm	5.0
Nominal efficiency*	η_{PV}	-	0.147
Cell peak power*	$P_{PV,nom}$	W	205
Absorbance	α_{PV}	-	0.92
Tilted angle	θ	°	90
Temperature coefficient	β_{ref}	°C^{-1}	0.0045

**STC conditions: temperature at 25°C and solar radiation flux 1000 W/m^2.*

The thicknesses of building walls (U-value = 1.32 W/m^2·K) and floor/ceiling (U-value = 1.10 W/m^2·K) are 30 and 25 cm, respectively. The wall layers include hollow bricks (λ = 0.33 W/m·K, ϱ =

1600 kg/m^3, c = 1200 J/kg·K) and thermal insulation (λ = 0.05 W/m·K, ϱ = 13.0 kg/m^3, c = 1100 J/kg·K). The absorptance of the opaque external surfaces is 0.3. The direct solar radiation is transferred through the windows to the inside zones, assuming an absorbing coefficient for the floor and the interior walls equal to 0.35 and 0.18, respectively. The glazing surface consists of a 4-6-4 air filled double-glazed system, with U-value = 2.8 W/m^2·K and SHGC equal to 0.5 (simulating a translucent surface, to prevent glare discomfort by diffusing the transmitted light). Interior walls are modelled as adiabatic. For such thermal zones, considered as office spaces, a ventilation rate equal to 1.0 Vol/h and a crowding index of 0.12 person/m^2 are considered. The interior thermal loads include people (95 W/p at 26°C, varying with T_{in}), lighting, and equipment (for a total 9.0 W/m^2). The heating and cooling set points are 20 and 26°C, whereas the heating and cooling system is switched on from 09:00 to 19:00 (week days only). Both the simulated innovative and reference buildings are heated through air-to-water electric heat pumps and chillers, sized on the maximum load, supplying hot and cold water to a fan-coils system. For the proposed innovative building, outlet air from the BIPV/T system is exploited to supply the evaporator of the heat pump for space heating (the potential direct free heating, for T_{outlet} > 20°C, is neglected). Note that, the air mass flow rate flowing through the BIPV/T cavity is considered as driven by natural or mechanical ventilation. If the stack effect is not sufficient to ensure the air channel velocity set point, the fan is activated to boost the air flow through the channel; vice versa it is switched off. A minimum air channel speed of 0.5 m/s is taken into account in the simulations. Note also that for the assessment of heat pumps and chillers performance, the manufacturer data look up approach is used; the main system features are shown in Table 6.5. Further and detailed features of heat pumps/chiller are available in the manufacturer's data sheet (i.e. Clivet Spa – ELFOEnergy Extended Inverter series).

Table 6.5. Main features of heat pump/chiller (Clivet® Series WSAN-XIN).

	Power		COP_N*	EER_N**	Nominal Air flow
	Heating	**Cooling**			
	[kW]	[kW]	[-]	[-]	[l/s]
Mod 41	9.0	12.0	6.12	6.27	1389
Mod 51	12.0	15.0	5.53	5.31	1389
Mod 61	15.0	21.0	5.80	6.19	2778
Mod 71	18.0	23.0	5.71	5.85	2778

*evaluated at $T_{evaporator}$ = 7°C and f_{PLR} = 100%
**evaluated at $T_{condenser}$ = 20°C and f_{PLR} = 100%

Yearly simulations (from 0:00 of January 1st to 24:00 of December 31st) are carried out by taking into account Meteonorm data files. The modelled buildings are simulated as located in seven different weather zones, shown in Fig. 6.6, featuring cold, temperate, and hot climates.

Fig. 6.6. Investigated climatic zones.

Through such weather data files, calculated heating and cooling degree days (HDD and CDD), incident solar radiation (ISR), and heating and cooling periods are reported in Table 6.6.

Table 6.6. Climatic zones and indexes, and system schedules.

Climatic zones		**HDD** [Kd]	**CDD** [Kd]	**ISR** [kWh/(m²·y)]	**Heating**	**Cooling**
Prague	(CZ)	3853	149	998	No limitations	
Freiburg	(DE)	3110	253	1114	No limitations	
Bolzano	(IT)	2641	475	1251	10/15 - 4/15	6/01 - 9/30
Madrid	(ES)	2174	687	1659	10/15 - 4/15	6/01 - 9/30
Naples	(IT)	1479	727	1529	11/15 - 3/31	6/01 - 9/30
Athens	(GR)	1060	1201	1561	11/15 - 3/31	6/01 - 9/30
Almeria	(ES)	783	961	1724	12/01 - 3/31	6/01 - 9/30

Moreover, note that national primary energy and carbon oxide (CO_2) emission conversion factors, as well as energy tariffs are taking into account, as reported in Table 6.7. Note also that the BIPV/T capital cost per square meter ($j_{PV/T}$ in eq. (6.18)) is considered equal to 250 €/m^2.

Table 6.7. National primary energy and carbon oxide conversion factors, and energy tariffs.

Parameter	**Unit**	**CZ**	**DE**	**ES**	**GR**	**IT**
PE conversion factor	[kWh_e/kWh_P]	0.324	0.389	0.395	0.368	0.460
CO_2 conversion factor	[g_{CO2}/kWh_e]	0.950	0.624	0.440	1.149	0.483
Feed-in tariff	[€/kWh_e]	0.079	0.100	0.079	0.073	0.039
Purchase tariff	[€/kWh_e]	0.188	0.239	0.187	0.136	0.189

Finally, to show the potentiality of the developed simulation model and the feasibility of the proposed BIPV/T system configuration, including an air to water heat pump supplied by war exhausted air by the PV/T channel, a parametric analysis on the BIPV/T system performance is carried out. Such analysis aims at maximizing the overall primary energy savings, by optimizing the BIPV/T system design based on both its active and passive effects. To this purpose a thirty-floor building is modelled and simulated. The obtained results could be useful for designers and stakeholders of innovative BIPV/T façades, which may take into consideration the proposed approach during the design stage of such innovative façades.

6.5. Results and discussion

The analysis of the active and passive effect due to the building integration of PV/T panels into the façade of a high-rise building is carried out by means of dynamic simulations. Through the developed simulation model, hourly and cumulative (e.g. monthly, yearly) heating and cooling requirements and demands can be calculated for both the innovative and reference buildings, as a function of the building feature, BIPV/T geometry, and weather conditions.

Energy, comfort, and economic results are obtained for an air open loop BIPV/T system with a single opening integrated on the South façade of a ten-floor building. In addition, a parametric analysis is carried out to evaluate the influence of the BIPV/T design on the overall energy performance. For both the investigations, yearly thermo-economic results are obtained for the European climatic zones reported in Table 6.6.; whereas, thermal and comfort hourly, daily and monthly results are only provided for the weather zone of Naples, for the sake of brevity.

6.5.1. Analysis of passive effects

Temperatures analysis

To evaluate the impact due to the building integration of PV/T panels on the thermal behaviour of the whole building and of each thermal zone, it is of interest the study of the vertical temperature gradient of the PV panels and of the air flowing along the channel. Fig. 6.7 shows the temperature profiles of the PV panels (Fig. 6.7,a) and of the air channel (Fig. 6.7,b) vs. the channel length (building height) and vs. the time, for a winter sample day (January 10th).

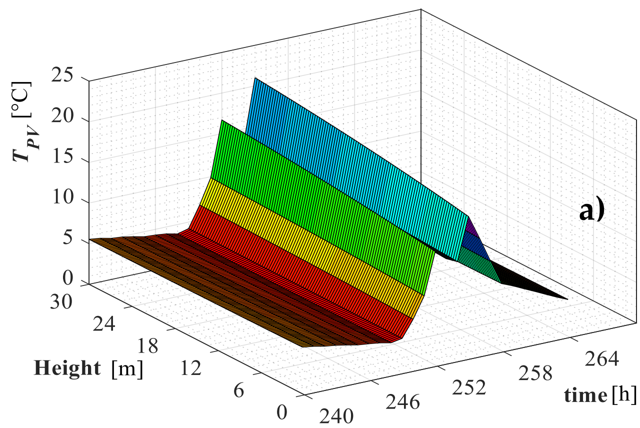

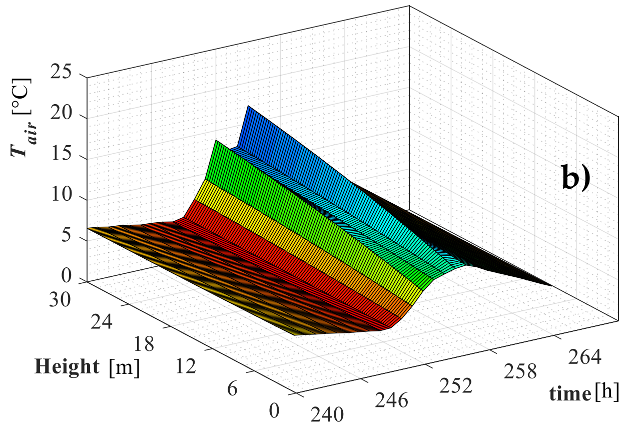

Fig. 6.7. Temperatures of PV panels (a) and channel air (b). January 10th - Naples.

As expected, the air channel temperatures follow and approach the PV panels ones (ranging between 15 and 21°C, Fig. 6.7, a). In this sample day, due to the air velocity minimum level (set at 0.50 m/s) and the occurring weather conditions, the maximum temperature growth, i.e. calculated difference between the inlet and outlet channel sections, is about 17°C, corresponding to an average temperature increase of 0.9°C per building floor. Although slight, the increase of the air channel temperature occurs even in cold winter days, as that one of Fig. 6.7. In fact, in this selected sample winter day, the maximum incident solar radiation on the South façade is 187 W/m^2, whereas the minimum and the maximum outdoor air temperatures are 5.1 and 10.8°C, respectively. In this figure, it is also possible to note that during the night, when the channel is closed, the PV temperature is lower than the outdoor air one (i.e. reported in night hours as air channel temperature only for graphical purposes). This is due to the long-wave infrared radiative heat exchange between the building external surfaces and the sky. Because of this phenomenon, the calculated night-time temperature of the PV panels could be lower than that one of the portions of the corresponding opaque envelope of the reference building.

For two sample winter and summer hours, January 13th at 13:00 and June 29th at 10:00, Fig. 6.8 shows the temperature profiles of BIPV/T panels, air channel and outdoor air versus the length of the BIPV/T system (i.e. building height). Note that in such sample hours, the incident solar radiation on the South façade is 506 (winter day) and 415 (summer day) W/m^2, whereas the outdoor air temperature is 12.2°C (winter day) and 32.4°C (summer day). This figure displays the increase of the air temperature inside the channel, with a great potential in assisting space heating (in winter).

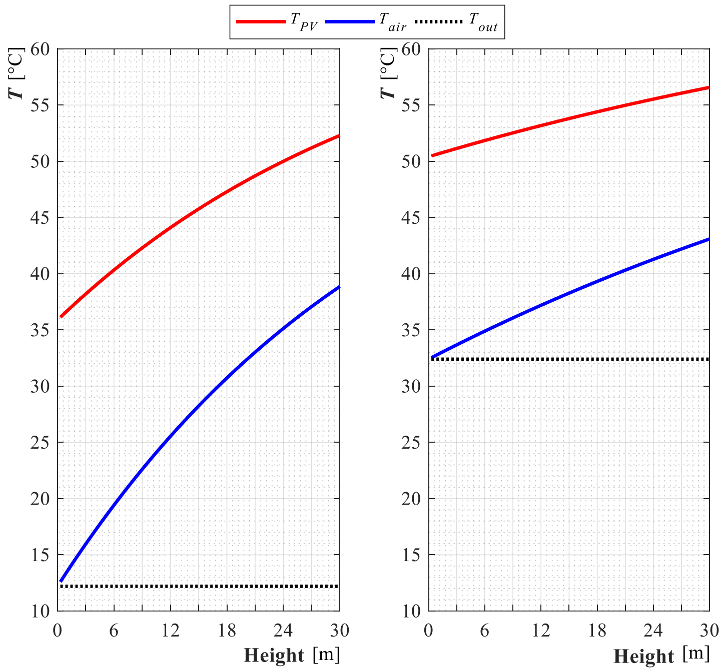

Fig. 6.8. Temperatures of the PV panels, channel and outdoor air for a sample winter (left, January 13th at 13:00) and summer (right, June 29th at 10:00) hour - Naples.

At the same time, the air flowing through the channel cools the PV panels by extracting heat from them and resulting in the increase of the PV electrical efficiency (with respect to the BIPV case). In this figure it can be also observed that during winter (Fig. 6.8, left), where space heating potentials can be exploited, the air channel temperature reaches the selected indoor air set point (20°C) at a building height equal to 6 m, corresponding to the end of the 2nd floor (note that the height of each floor is 3 m, Fig. 6.5). Note that such result depends on the occurring weather conditions, such as the inlet outdoor air temperature (12°C in Fig. 6.8, left) and the incident solar radiation. The outdoor air is gradually heated along the BIPV/T channel length, and the produced thermal energy is usefully recovered by supplying such air to the heat pump evaporator, increasing its COP. Note that in this case study the winter BIPV/T system active effect consists of the enhanced heat pump efficiency obtained by exploiting the recovered heat, as discussed in the next subsections.

The PV panels and air channel temperatures influence the thermal behaviour of the building envelope. To evaluate the magnitude of this passive effect, the following figures display the sketched visual and calculated thermal images of the external and internal South building façade, including the PV/T panels and the alternating opaque / transparent sections. Note that for comparison purposes, the thermal images refer to the same temperature distribution (i.e. colormap set from 10 to 15°C).

Fig. 6.9 shows, for the same sample winter hour of a cold day (January 10th at 13:00, i.e. the incident solar radiation on the South façade is 153 W/m^2 and the outdoor air temperature is 8.8°C), the visual and thermal images of the external South building façade.

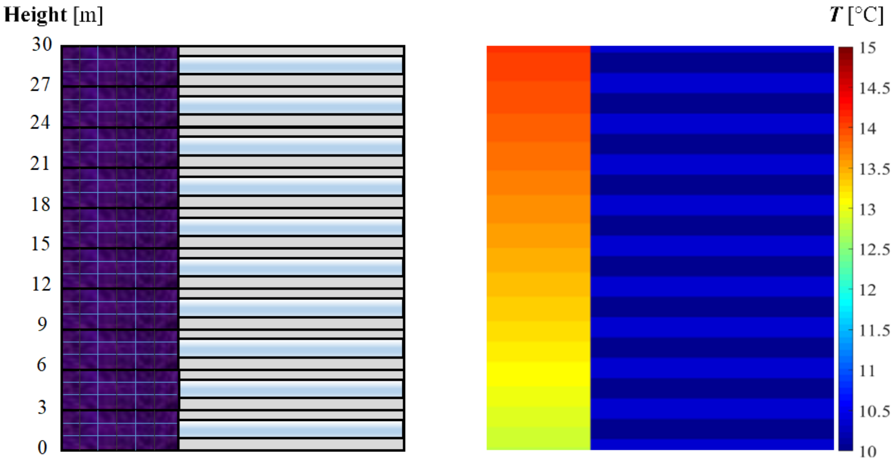

Fig. 6.9. Thermal map of the South building façade for BIPV/T configuration (January 10th at 13:00) - Naples.

The PV temperature increases from 10.5°C (at the channel inlet section, y = 0 m) to 13.5°C (at the channel outlet section, y = 30 m), Fig. 6.9 right. For the same cold sample hour, the visual and thermal images of the internal surface of the South-façade are shown Fig. 6.10. Here, the temperature vertical gradients of the internal surface with (Fig. 6.10, top) and without (Fig. 6.10, bottom) BIPV/T systems are compared (to estimate the passive effect due to the presence of the BIPV/T system on the external surface). At the inlet section of the BIPV/T channel (at y = 0 m), the internal surface air temperature is 14.2°C, about 1.9°C higher than that one calculated on the internal surface relative to the opaque portion of the wall without BIPV/T (as well as on the reference building opaque façade). In addition, the internal surface relative to the portion of the façade integrated with BIPV/T panels shows a temperature stratification along the building height, i.e. from 14.0°C (at y = 0 m) to 14.9°C (at y = 30 m). Consequentially, although slight, such increase of the average temperature of the internal surface of the South-façade causes a reduction of the thermal load and an increase of the thermal comfort of occupants. Obviously, the higher is the incident solar radiation the higher is the expected temperature rise. Similarly to Fig. 6.9, Fig. 6.11 shows the visual and thermal images of the external South building façade for a sample summer hour (July 29th at 10:00, i.e. the incident solar radiation on the South façade is 293 W/m^2 and the outdoor air temperature is 21.4°C). The PV temperature ranges between 37°C (at y = 0 m) to 44 °C (at y = 30 m).

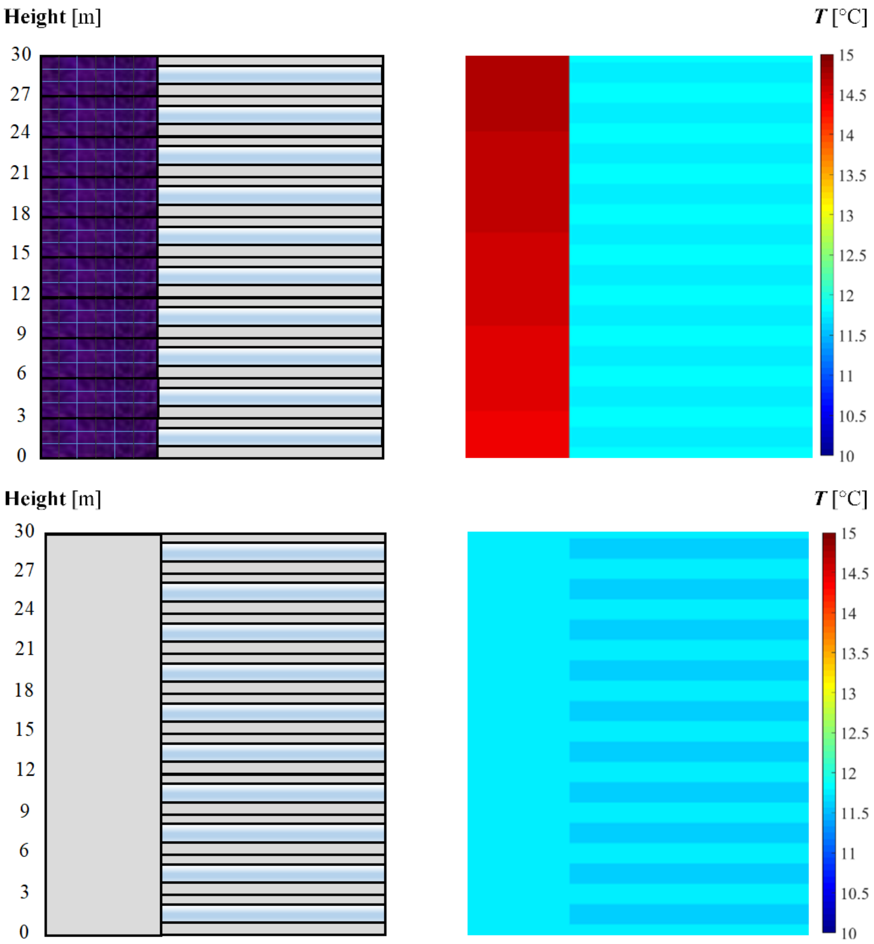

Fig. 6.10. Thermal map of the interior south building façade for BIPV/T configuration (top) and reference ones (bottom). Sketch of the external façade (left) and interior wall surface (right) temperature map (January 10th at 13:00) - Naples.

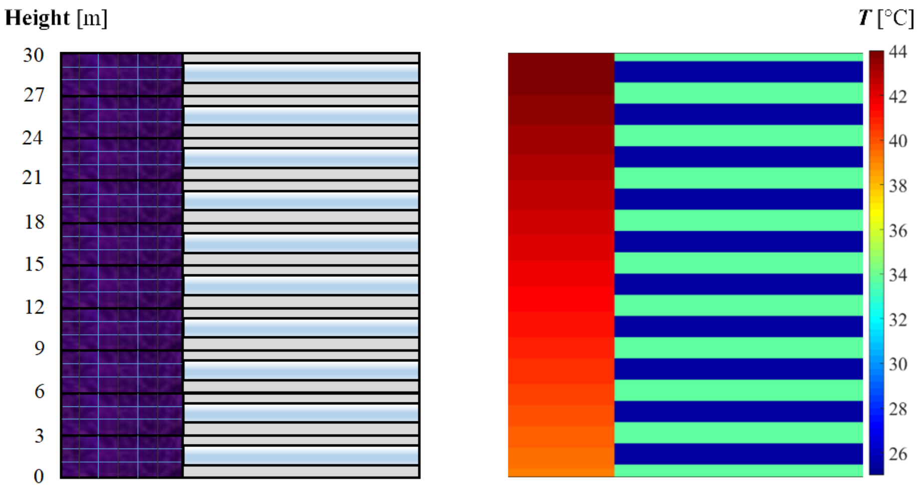

Fig. 6.11. Thermal map of the South building façade for BIPV/T configuration (July 29th at 10:00) - Naples.

Likewise to Fig. 6.10, the passive effect due to the BIPV/T panels the internal surface air temperature is shown in Fig. 6.12.

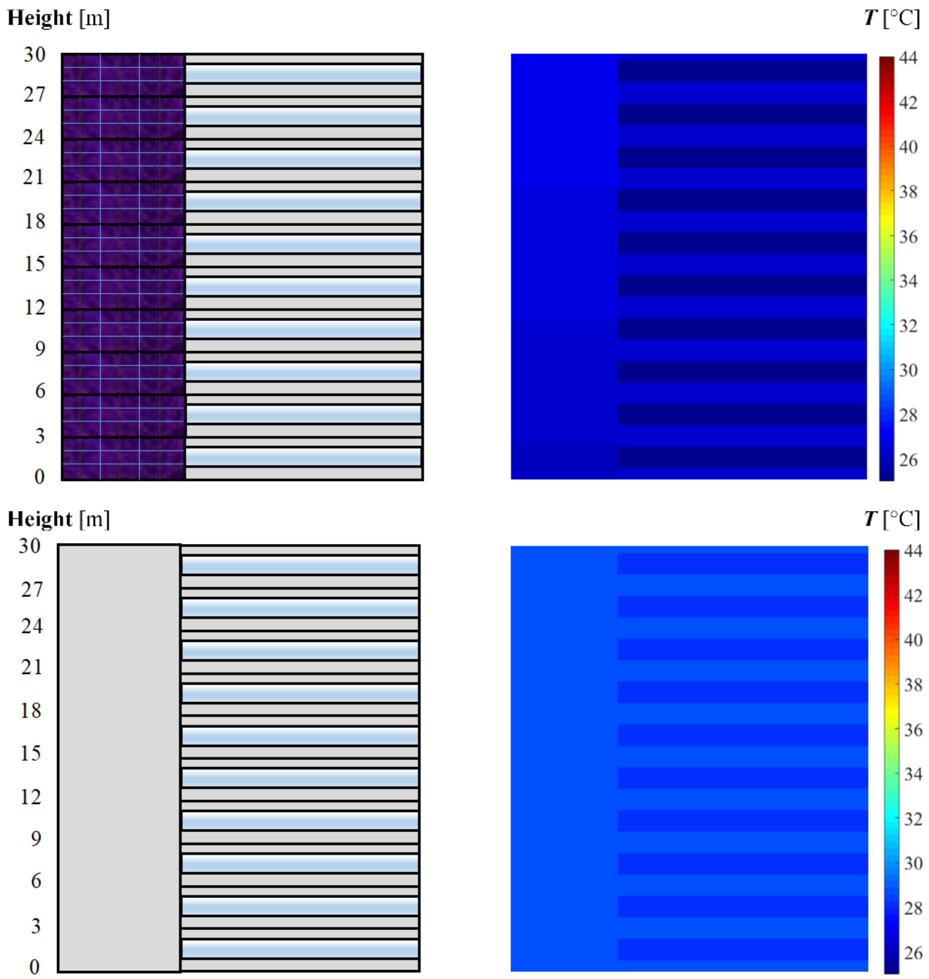

Fig. 6.12. Thermal map of the interior south building façade for BIPV/T configuration (top) and the reference ones (bottom). Sketch of the external façade (left) and interior wall surface (right) temperature map (July 29th at 10:00) – Naples

Here, the temperature of internal surface of the wall integrating the PV/T panels ranges between 25.2°C (at y = 0 m) to 27.2°C (at y = 30 m), reaching 26.5°C at y = 9 m. Such intermediate value is the average temperature of the internal surface of the opaque façade (without BIPV/T) of the reference building. Therefore, for the first three building floors, the average radiant temperature of internal surface of the wall integrating the PV/T panels decreases, and the cooling loads too, as expected. In case of high-rise buildings, the use of modular BIPV/T systems connected in series with a single inlet channel may cause an overheating effect at building heights higher than the height linked to this intermediate value. Such height is here called inversion point, and its influence on the building thermal and energy performance is discussed in the following paragraphs.

The increase of the average temperature of the internal surface of the South-façade has a significant impact on the indoor air temperature, as well as on the thermal loads. Given the thermal space dimensions, the larger is the portion of the wall integrating PV/T panels, the higher is their passive effect impact. This behaviour can be observed in Fig. 6.13, where for the simulated 9th building floor and for five winter and summer sample days (i.e. January 10th - 14th (top) and June 26th - 30th (bottom)), the time history of the indoor air temperature is shown (for both innovative and reference buildings). Note that at the top label of Fig. 6.13, the indoor air temperature of the 9th floor thermal zone (innovative building), calculated on the whole year, is also shown. By comparing the innovative building with the reference one, an increase of the free-floating indoor air temperature is obtained during switched off HVAC system hours. In fact, thanks to the thermal inertia of the wall integrating the PV/T panels, the daily stored heat gains are shifted in time toward the interior thermal zone. Therefore, lower heating loads are obtained in the early morning when the HVAC system is switched on. Such effect becomes negative during summer, when higher (free floating) temperatures cause higher cooling requirements and loads.

Heating and cooling loads

The variation of the indoor air temperature, as shown in Fig. 6.13, implies the variation of the heating and cooling loads.

Fig. 6.14 shows the sensible thermal loads (Q_{HVAC}) trends relative to the innovative and reference building configurations, calculated for the same sample winter and summer days of Fig. 6.13, (i.e. January 10th - 14th (top) and June 26th - 30th (bottom)). During the heating season, a reduction of the thermal loads (comparing the innovative building with the reference one) is obtained thanks to the positive BIPV/T system passive effects (Fig. 6.14, top). Conversely, during the summer hours in which the HVAC is running, the passive effect due to the BIPV/T system causes space overheating and, thus, a slight increase of the cooling loads (Fig. 6.14, bottom).

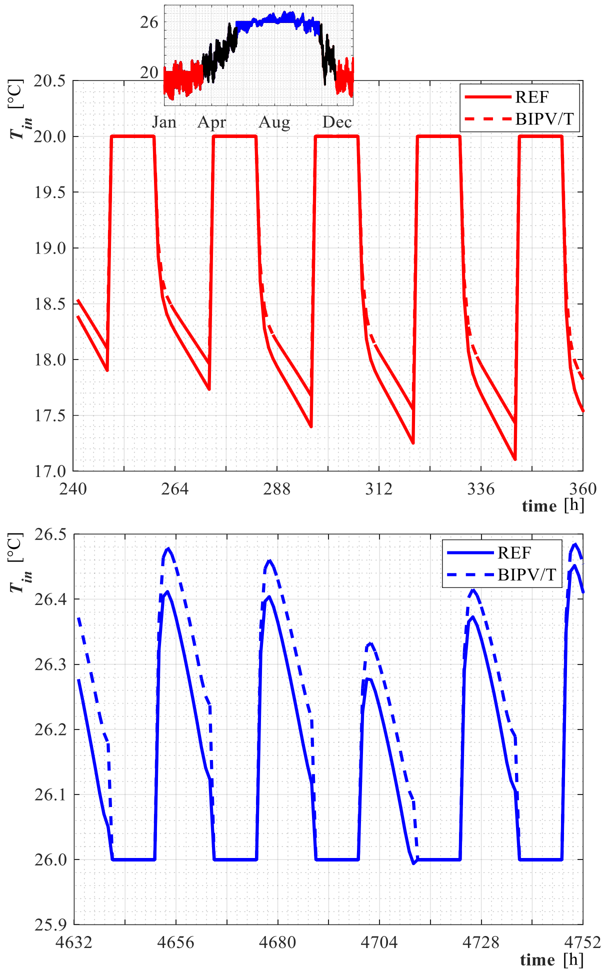

Fig. 6.13. Indoor air temperatures (9th floor). January 10th - 14th (top) and June 22th - 26th (bottom) - Naples.

Dynamic yearly heating and cooling requirements of such thermal zone (innovative building) are shown at the top label of Fig. 6.14, top. For the weather zone of Naples, Fig. 6.15 shows the monthly heating and cooling requirements for both building configurations. In this figure, the passive effects due to the BIPV/T systems can be analysed.

Positive passive effects due the BIPV/T system on the monthly heating requirements are obtained during the winter season. This is particularly evident in the coldest months, where the innovative building configuration shows the lower energy requirements versus those calculated for the reference building. On the contrary, the use of the BIPV/T system always produces an overall overheating summer effect, resulting in slightly higher monthly cooling requirements. On the yearly time basis, in case of the BIPV/T building configuration, the reference building heating and cooling requirements, about 4.3 MWh/y and 10.5 MWh/y, respectively decreases and increases of about 25.6 and 0.95%.

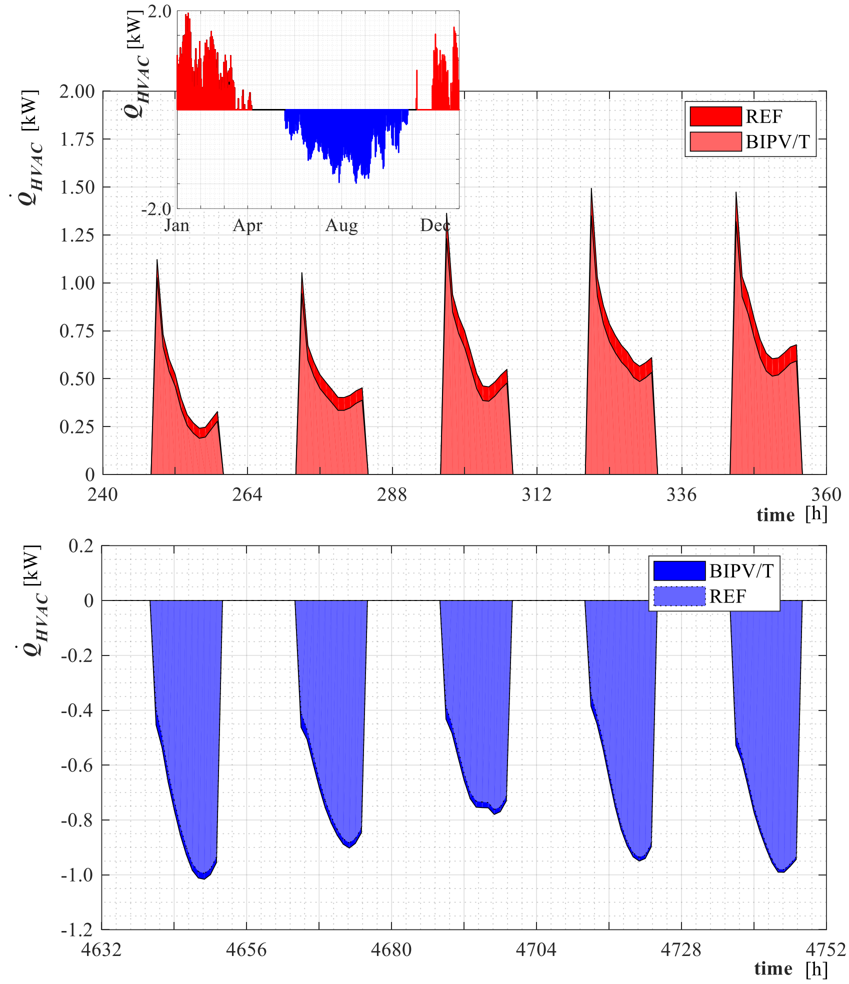

Fig. 6.14. Sensible thermal loads (9th floor). January 10th - 14th (top) and June 22th - 26th (bottom) - Naples.

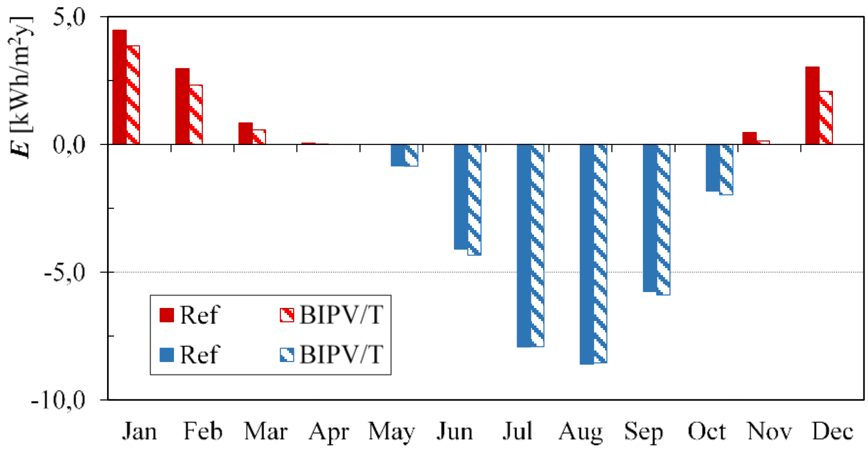

Fig. 6.15. Monthly heating and cooling requirements of the whole building – Naples.

It is worth noting that this result seems unexpected; in fact, the use of open loop air BIPV/T systems generally produces passive cooling to the adjacent thermal zones [132], mainly due to the lower solar energy input (i.e. due to the conversion of part of the solar radiation in electricity) and to the removed heat with the cooling medium. Nevertheless, in case of high-rise buildings (i.e. a ten-floor perimeter zone building is here taken into account), simulation results show a different influence of the BIPV/T system on the cooling loads, as expected and discussed hereinafter. Finally, the total and specific (i.e. per unitary surface area) yearly heating and cooling requirements, calculated for each floor and for both the innovative and reference buildings, are shown in Table 6.8.

Table 6.8. Yearly total and per unitary surface area heating and cooling requirements - Innovative and reference building – Naples.

	Prague		**Freiburg**		**Bolzano**		**Madrid**		**Naples**		**Athens**		**Almeria**	
	H	C	H	C	H	C	H	C	H	C	H	C	H	C
Innovative							[kWh/(m²·y)]							
Floor 1st	74.2	-1.8	52.7	-5.8	42.7	*-16.2*	31.2	-20.1	9.6	*-28.1*	5.6	*-41.4*	0.2	*-33.6*
Floor 2nd	74.0	-1.9	52.5	-5.9	42.5	-16.5	31.0	-20.4	9.5	*-28.5*	5.5	-41.8	0.2	*-34.0*
Floor 3th	73.6	-2.0	52.1	-6.1	42.1	-16.7	30.8	-20.6	9.3	*-28.8*	5.3	-42.0	0.2	*-34.3*
Floor 4th	73.3	-2.0	51.8	-6.2	41.8	-16.9	30.5	-20.8	9.1	-29.2	5.2	-42.3	0.2	*-34.6*
Floor 5th	73.0	-2.1	51.6	-6.3	41.6	-17.1	30.3	-21.0	9.0	-29.5	5.1	-42.5	0.2	-34.9
Floor 6th	72.8	-2.2	51.4	-6.4	41.3	-17.3	30.2	-21.2	8.8	-29.8	5.0	-42.8	0.2	-35.1
Floor 7th	72.6	-2.2	51.2	-6.5	41.1	-17.5	30.0	-21.4	8.7	-30.0	4.9	-43.0	0.2	-35.4
Floor 8th	72.4	-2.3	51.0	-6.6	40.9	-17.6	29.9	-21.5	8.6	-30.3	4.8	-43.2	0.2	-35.6
Floor 9th	72.2	-2.3	50.9	-6.7	40.7	-17.8	29.8	-21.7	8.5	-30.5	4.8	-43.3	0.1	-35.8
Floor 10th	72.1	-2.4	50.8	-6.8	40.6	-17.9	29.7	-21.8	8.4	-30.6	4.7	-43.5	0.1	-35.9
Reference							[kWh/(m²·y)]							
Floor nth	81.4	-1.7	58.7	-5.6	47.1	-16.4	36.9	-19.7	11.8	-29.1	7.1	-41.7	0.3	-34.7
							[MWh/y]							
Innovative	26.3	-0.8	18.6	-2.3	15.0	-6.2	10.9	-7.6	3.2	-10.6	1.8	-15.3	0.1	-12.6
Reference	29.3	-0.6	21.1	-2.0	17.0	-5.9	13.3	-7.1	4.3	-10.5	2.6	-15.0	0.1	-12.5
							[%]							
ΔQ_{HVAC}	10.2	-33.3	11.8	-15.0	11.8	-5.1	18.0	-7.0	25.6	-1.0	30.8	-2.0	0.0	-0.8

* *italic and underlined values refer to floors of the innovative building with cooling requirements lower than those of the average reference building floor*

The obtained results vary as a function of the building floor height, due to the different temperatures of the portion of the internal surface of the South façade integrating the BIPV/T system calculated along the height channel (as discussed in Fig. 6.10 and Fig. 6.12, i.e. inversion point). According to Fig. 6.10, the heating requirements of the innovative building are always lower than those of the reference one (positive ΔQ_{HVAC}), for each floor and for the whole building. Conversely, according to Fig. 6.12, the cooling requirements of the innovative building are generally higher than those of the reference building (negative ΔQ_{HVAC}); the only exceptions regard the first floors (i.e. underlined values) of the innovative buildings located in Almeria, Athens, Naples, and Bolzano. Note that in case of the BIPV/T system, the reduction of the building heating requirements is higher than the increase of the cooling ones.

Passive effect inversion point

The concept of the inversion point is here described. To this purpose, Fig. 6.16 shows the cooling load (Q_{HVAC}) trends versus the building floor, calculated for the reference (without BIPV/T) and the innovative one (with BIPV/T) building, for a sample summer hour (July 29th at 10:00). In this figure, it is possible to note that for the first four (almost five) floors, the cooling load of the BIPV/T configuration is lower than the cooling load of the reference one. The opposite behaviour occurs after the 5th floor, where passive effects become negative (i.e. overheating).

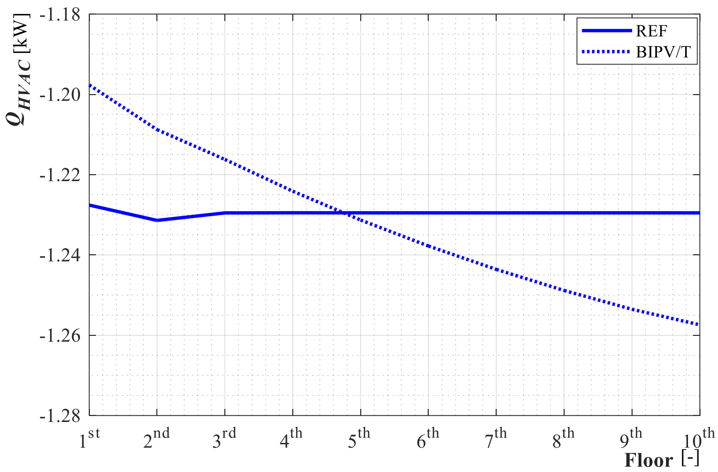

Fig. 6.16. Cooling load vs. building floor. Sample summer hour (July 29th at 10:00) - Naples.

At higher floors, i.e. along the flow path of the air channel, the increase of the air channel and PV temperatures produces an increase of the cooling load of the innovative building versus the reference one. The inversion of the trend of the passive effects on the cooling loads (i.e. from positive to negative) is observed at a specific height of the BIPV/T channel, i.e. close to the 5th floor for the considered case study. Such height corresponds to the here called inversion point.

This result suggests an interesting approach that could optimize the passive and active effects due to the thermal stratification of the BIPV/T components. In fact, thanks to the use of a modular BIPV/T system, due to its broken lines among PV/T panels, it is possible to take into account different openings on the PV/T system along the flow path of the air channel, as recently proposed in [149]. Such method, being a feasible and interesting solution for helping to prevent excessive heat, could yield to lower internal radiant and lower PV temperature, resulting in higher PV efficiencies, and optimized space heating potentials. In this regard, by taking into account Fig. 6.16, to obtain a cooling effect of the BIPV/T system on the cooling thermal loads of all the building floors, it could be advisable to consider at least an additional inlet at the 5th floor (i.e. obtaining a two inlet system configuration for the investigated ten-floor building located in Naples). During summer, for the climate of Naples, the use of a multiple openings, used as air inlets, could result in increased electrical and thermal performances (i.e. fresh air cools the PV panels and reduces the average radiant temperature of the wall internal surface). It is worth noting that without a suitable control strategy, the inversion point must be calculated by means of a yearly analysis, taking into account both the heating and cooling loads. Such analysis carried out for the weather of Naples is shown in Fig. 6.17.

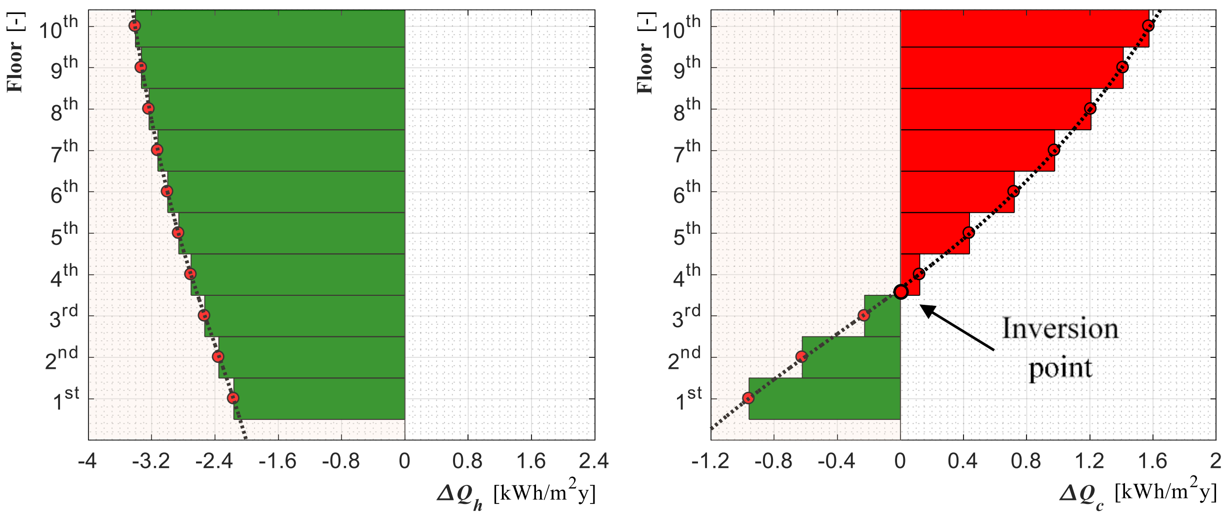

Fig. 6.17. Yearly difference of heating (ΔQ_h, left) and cooling (ΔQ_c, right) requirements for each floor - Naples.

Here, for each building floor, the difference between the yearly heating and cooling requirements of the innovative building versus those of the reference one (i.e. heating: $\Delta Q_h = |Q_{h,BIPV/T} - Q_{h,REF}|$ - Fig. 6.17, left) and (cooling: $\Delta Q_c = |Q_{c,BIPV/T} - Q_{c,REF}|$ - Fig. 6.17, right) are shown. In this figure, the inversion trend of ΔQ_c (Fig. 6.17, right), calculated on a yearly basis, is detected between the third and fourth floor. Obviously, the inversion point height calculated on the yearly basis is different from that one observed for a sample hour (e.g. Fig. 6.16), which is influenced by the boundary conditions of the specific simulated hour (i.e. solar radiation, wind velocity, outside air temperature). During winter (Fig. 6.17, left), by taking into account a single inlet, a positive heating effect (heating gain) is achieved for all the building floors. On the contrary, during summer a positive effect (cooling) can be obtained only for the first, second, and third floors, a progressive negative effect (overheating) occurs from floor 4th to floor 10th. Given the potentials of such approach for BIPV/T system applications, the multiple inlet method needs to be further investigated [57, 149]. Nevertheless, its importance on the passive effects of BIPV/T systems on the heating and cooling loads is of interest, as discussed in this chapter. In addition, it is worth noting that, besides an accurate air flow and wind analysis (e.g. in [149]), a complete investigation of the multiple inlet strategy must include the capital and operating cost and energy consumptions of the multiple fans, necessary to address the optimal configuration, as discussed in the following sections.

The same analysis reported in Fig. 6.17 for the weather zone of Naples is carried out for several European weather zones, which are shown in Fig. 6.6 and climatically characterized in Table 6.6. For each building floor and corresponding height, the trends of ΔQ_c, calculated for all the investigated weather zones, are shown in Fig. 6.18.

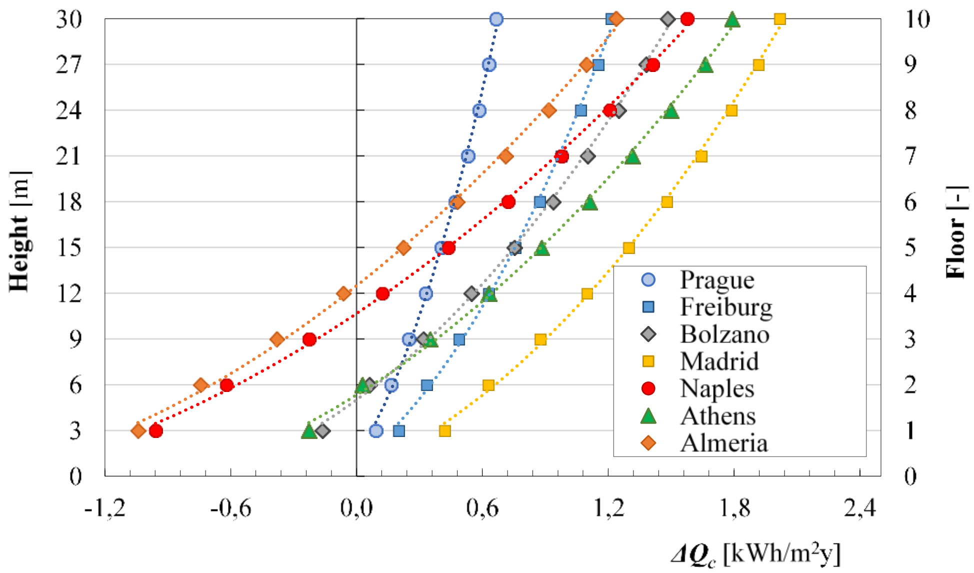

Fig. 6.18. BIPV/T cooling effect on cooling requirements for each climatic zone.

Here, the inversion points relative to the cooling loads vary as a function of the climate, being generally higher at warmer weather zones. Such analysis shows how the concept of the inversion point is of particular interest for hot and temperate climates, and how the use of dynamic simulations is crucial for its assessment, which is to be based on yearly energy performance.

<u>Indoor thermal comfort</u>

The temperature stratification of the internal surface of the wall integrating PV/T panels has a significant influence on the thermal comfort of occupants as well. For a sample winter and summer day, the PMV and PPD for the 1st, 5th and 10th floors, for both the investigated buildings, are shown in Fig. 6.19. Note that PMV and PPD are calculated by assuming the metabolic rate (M) equal to 70 W/m^2, the air velocity (v_{air}) equal to 0.16 m/s in winter and to 0.23 m/s in summer, and the clothing insulation (Cl) equal to 0.155 clo in winter and to 0.110 clo in summer (according to the EN ISO 7730:2005 standard on ergonomics of the thermal environment). In Fig. 6.19, the light blue area represents the range of PMV to which corresponds the comfort zone, i.e. PMV $\in$ [-0.5; +0.5] and PPD $\leq$ 15%. During the winter season, due to the BIPV/T panels, the increased average radiant temperature produces for all floors a PMV higher than that one obtained for the reference building.

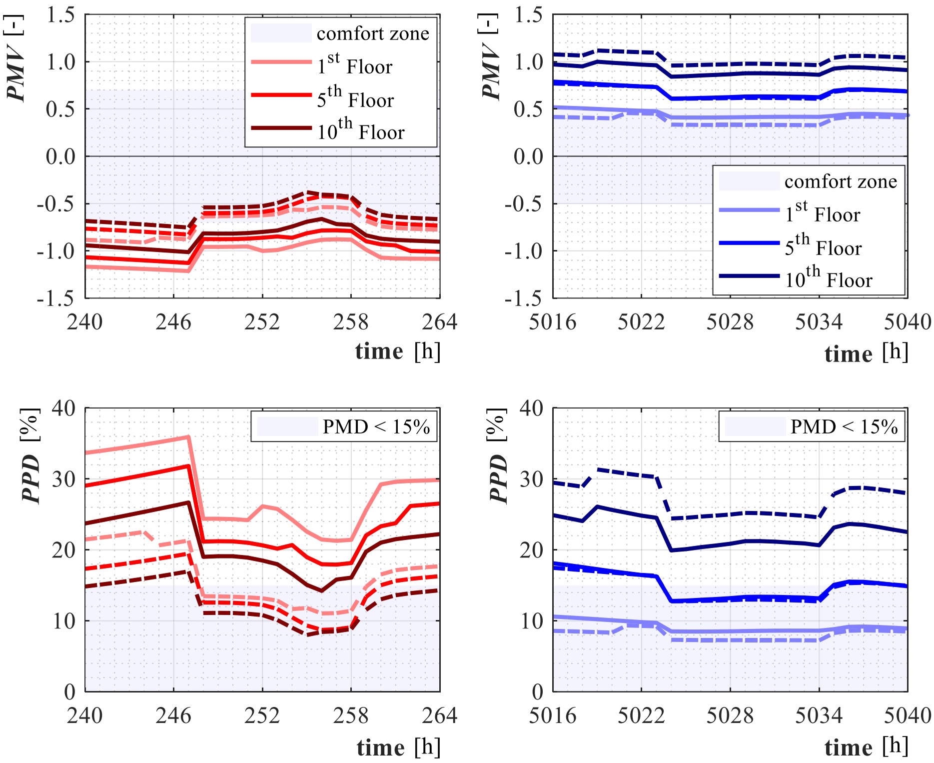

Fig. 6.19. PMV and PPD. 1st, 5th and 10th floors (reference system - solid line, BIPV/T system - dashed line). Sample winter and summer days (January 10th and in July 29th) - Naples.

As a result, in all the thermal zones (i.e. ten floors) a higher winter thermal comfort is achieved. Conversely, during summer, according to the trend of the cooling loads shown in Fig. 6.16, at the 1st floor a better PMV of the BIPV/T configuration versus that one achieved in case of the reference building is achieved. The opposite occurs for the 5th and 10th floors.

Similarly, the calculated PVM values for the 5th floor are similar for both buildings, whereas for the 10th floor the BIPV/T building configuration worse PMV values are achieved. For each floor, Fig. 6.20 and Table 6.9 show the seasonal and yearly comparison among discomfort hours calculated for the reference and BIPV/T configuration. During the winter season, the use of BIPV/T panels provides a gradual reduction of the number of discomfort hours, i.e. an average reduction of about 58% is obtained. During the summer season, according to the results shown in Fig. 6.19, the trend of discomfort hours is rather different. For the first three floors, thanks to the cooling effects of the BIPV/T systems (the average radiant temperature decreases), a reduction of discomforts hours is calculated (i.e. ranging between -42 and -4%), whereas from the remaining floors an increase of discomfort hours occurs (i.e. ranging between 1.5 and 12%). On the other hand, by considering the comfort performance on the entire year, i.e. cumulating winter and summer season performance, an overall reduction of discomfort hours is observed at each floor (i.e. ranging between -48 and -11%).

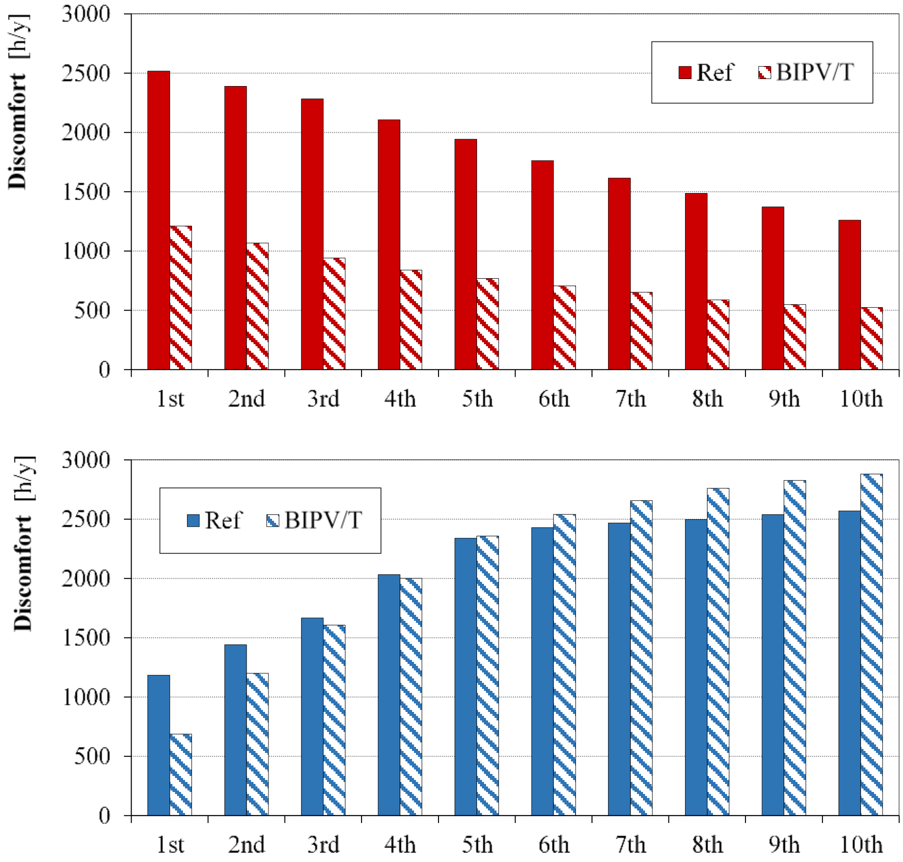

Fig. 6.20. Discomfort hours per year calculated for the winter (top) and summer (bottom) seasons - Naples.

Table 6.9. Discomfort hours per year per floor – Naples.

Winter season		**Floor1st**	**Floor2^{n}**	**Floor3^{r}**	**Floor4th**	**Floor5th**	**Floor6th**	**Floor7th**	**Floor8th**	**Floor9th**	**Floor 10th**
REF	[h/y]	2516	2389	2282	2106	1943	1762	1614	1486	1371	1261
BIPV/T		1210	1068	941	839	768	707	653	587	548	523
Δ	[%]	-52	-55	-59	-60	-61	-60	-59	-60	-60	-60
Summer season		**Floor1st**	**Floor2nd**	**Floor3rd**	**Floor4th**	**Floor5th**	**Floor6th**	**Floor7th**	**Floor8th**	**Floor9th**	**Floor 10th**
REF	[h/y]	1184	1441	1667	2000	2357	2428	2467	2497	2537	2569
BIPV/T		687	1199	1606	2032	2298	2539	2657	2760	2827	2879
Δ	[%]	-42	-17	-4	+1.5	+2.5	+5	+7	+10	+11	+12
Entire year		**Floor1st**	**Floor2nd**	**Floor3rd**	**Floor4th**	**Floor5th**	**Floor6th**	**Floor7th**	**Floor8th**	**Floor9th**	**Floor 10th**
REF	[h/y]	3700	3830	3949	4106	4300	4190	4081	3983	3908	3830
BIPV/T		1897	2267	2547	2871	3066	3246	3310	3347	3375	3402
Δ	[%]	-48	-41	-35	-30	-28	-22	-19	-16	-13	-11

6.5.2. Analysis of active effects

Thermal and electrical efficiency and production

For the two sample winter and summer hours of Fig. 6.8 (i.e. January 13th at 13:00 and June 29th at 10:00), the electrical efficiency profiles of the PV panels versus the length of the BIPV/T system (i.e. building height) is shown in Fig. 6.21.

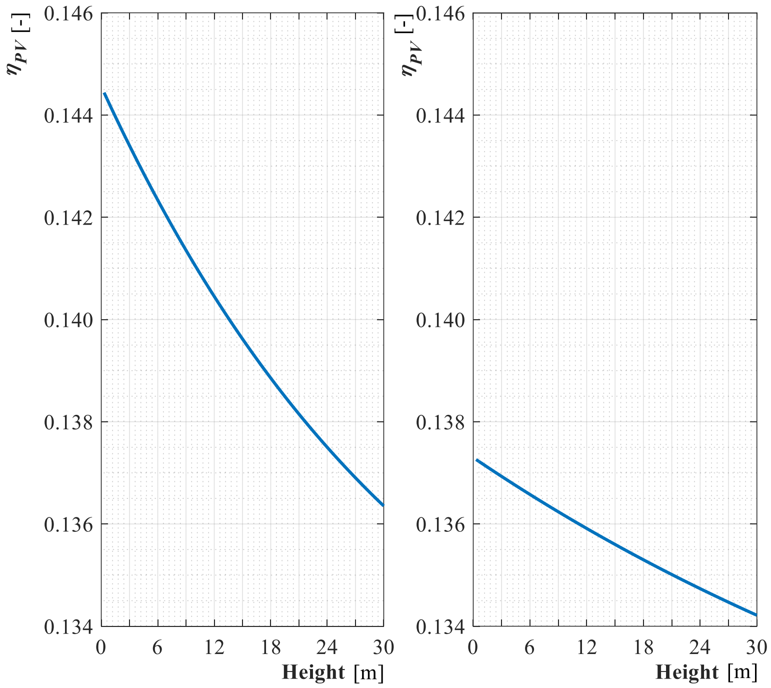

Fig. 6.21. Electrical efficiency of the PV panels for a sample winter (left, January 13th at 13:00) and summer (right, June 29th at 10:00) hour - Naples.

This figure shows the reduction of the electrical efficiency along the channel height, due to the increase of the temperature of the air flowing through the channel (while extracting heat from the PV panels), as shown in Fig. 6.8. Note that for the winter and summer hours, the incident solar radiation is equal to 526 and 415 W/m^2, resulting in electricity production (electrical efficiency) equal to 7.3 kW (14.0%) and 5.3 kW (12.3 %), respectively.

For the same sample hours, by taking into account the temperature difference between the air channel temperature at the outlet (at y = 30 m) and at the inlet (at y = 0 m) sections it is possible to calculate the thermal energy extracted from the PV (i.e. transferred to the air flowing through the channel). The calculated heat extractions (thermal efficiency) are equal to 3.2 kW (6.2%) and 1.5 kW (3.7%), respectively for the winter (i.e. thermal energy production) and the summer (i.e. exhausted thermal energy) hour. Note that for the winter and summer sample hours, the air channel mass flow rate is about 440 and 521 kg/h, and the air channel temperature difference is equal to 26.3 and 10.6 °C.

On the yearly basis, the calculated electrical and thermal efficiencies of the investigated BIPV/T system configuration are equal to 13.9 and 30.1 %. It is worth noting that such low values are influenced by the vertical inclination of the PV/T panels (i.e. integrated in the building façade), and by the latitude of the investigated location (i.e. 40.8 °N, Naples). Higher results can be obtained with lower tilt angles or higher latitudes.

The yearly PV electricity productions, calculated for all the considered European weather zones (see Fig. 6.6 and Table 6.6.), are reported in Table 6.10.

Table 6.10. BIPV/T system: electricity production.

		Prague	**Freiburg**	**Bolzano**	**Madrid**	**Naples**	**Athens**	**Almeria**
Floor 1st	[$kWh_e/(m^2 \cdot y)$]	26.9	29.0	34.8	31.6	37.5	35.7	41.2
Floor 10th	[$kWh_e/(m^2 \cdot y)$]	26.6	28.7	34.3	31.3	36.9	35.2	40.7
Whole building	[MWh_e/y]	9.6	10.4	12.4	11.3	13.4	12.8	14.7

This table also includes the yearly production per unitary PV area obtained at the 1st and 10th floors. As expected, the lowest electricity production is obtained at the last floor (due to the decreased PV efficiency along the flow path of the BIPV/T air channel, e.g. Fig. 6.21) for all the weather zones, whereas at higher ISR, higher electricity productions are achieved (i.e. the highest value is calculated for Almeria – 14.7 MWh/y).

6.5.3. Energy, economic and environmental performance

Combined passive and active effects

By taking into account the electrical energy needs for heating and cooling, calculated for all the investigated weather zones, the assessment of the passive and active effects due to the BIPV/T system is carried out. To this aim, Table 6.11 shows the yearly heating and cooling electricity needs of the reference case (E_{el}) and the percentage difference between the yearly heating and cooling electricity needs calculated for the reference and the BIPV/T building system configurations (ΔE_{el}). Positive (negative) ΔE_{el} values refer to the percentage increase (decrease) of electricity needs.

To evaluate the passive and active effects, outlet air from the PV/T channel is alternatively considered as:

exhausted toward the outdoor environment. This mode, namely BIPV/T exhausted, is taken into account during the heating and cooling seasons. Heating and cooling, and total (passive), percentage differences, ΔE_{el}, allow one to assess the impact due to the BIPV/T passive effect on the energy needs;

i) supplied to the evaporator of the heat pump (mixed to outdoor air to fulfil the required flow rate). This mode, namely BIPV/T with heat recovery, is taken into account during the winter season only. Heating and cooling percentage differences, ΔE_{el} (calculated between the BIPV/T with heat recovery mode performance and the BIPV/T exhausted mode ones), allow assessing the impact due to the BIPV/T active effect only on the energy needs. Total (passive + active) ΔE_{el} combine both the BIPV/T passive and active effects on the energy needs.

Table 6.11. Electrical energy demands for heating, cooling and total (heat + cool). Comparison among reference and innovative building façades with and without heat recovery.

	Reference			**BIPV/T exhausted**		*Total (passive)*	**BIPV/T with heat recovery**		*Total (passive + active)*
	Heating	Cooling	Total	Heating	Cooling		Heating	Cooling	
	E_{el} [MWh/y]			ΔE_{el} [%]					
Prague	12.70	0.12	12.82	-12.6	22.7	*-12.3*	-3.1	-	*-15.0*
Freiburg	8.39	0.40	8.80	-11.8	13.3	*-10.7*	-3.8	-	*-13.8*
Bolzano	6.71	1.29	8.00	-8.1	3.5	*-6.2*	-6.8	-	*-11.4*
Madrid	5.01	1.99	7.00	-21.6	5.5	*-13.9*	-4.1	-	*-16.2*
Naples	1.35	2.65	4.01	-25.6	0.1	*-8.6*	-6.6	-	*-10.2*
Athens	0.77	3.67	4.44	-17.6	1.5	*-1.8*	-8.0	-	*-2.9*
Almeria	0.03	2.74	2.77	-46.8	-0.4	*-0.9*	-4.2	-	*-0.9*

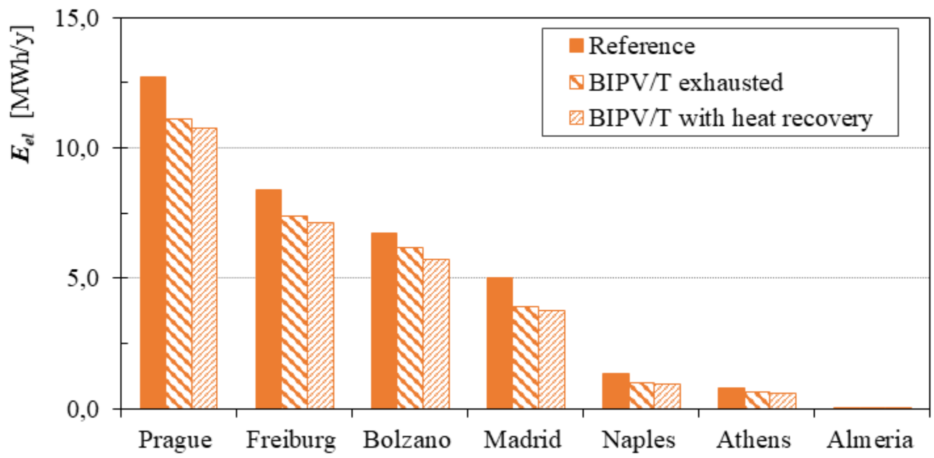

Fig. 6.22. Heating electrical energy needs for the reference and innovative building façades with and without heat recovery.

The obtained results show that for the exhaust mode, the percentage difference of electricity needs for heating range between -8.1% (Bolzano) and -25.6% (Naples), resulting in energy savings only due to the passive effect offered by the BIPV/T system (reduction of thermal loads). When the outlet air from the BIPV/T channel is supplied to the heat pump evaporator to offset the heating load, an additional advantage, i.e. active effect, can be achieved. In fact, the recovered thermal energy produces a further decrease of heating electricity needs (with respect to the BIPV/T exhausted mode), ranging between -3.1% (Prague) and -8.0% (Athens). For sake of completeness, the yearly heating electrical needs calculated for the reference case and BIPV/T one in exhausted and heat recovery modes (relative to the passive and active effects due to the PV/T building integration) are shown in Fig. 6.22. Here, it is clearly shown that the higher is the HDD, the higher is the energy saving, whereas the lower is the influence of the active effects (lower effective recovered heat). In fact, the lower the heating energy requirements are, the higher are the energy savings or energy recovery potentials. Similarly, during summer (Table 6.11), a very slight reduction of cooling electrical needs is obtained in case of Almeria (-0.4%). In all the investigated weather zones, an increase of electricity is achieved, up to +22.7% (Prague). As expected, the lower the cooling energy requirements are, the higher is the impact of the BIPV/T passive effects on the energy needs. Note that the combined heating and cooling percentage ΔE_{el} values (i.e. total (passive + active), Table 6.11), are encouraging, ranging between -0.9 in Almeria and -16.2% in Madrid.

It is also worth noting that the influence of the building floors height on the overall final energy needs is very weak. This can be observed by taking into account the yearly net final electricity uses reported in Table 6.12 for all the investigated weather zones.

Table 6.12. Final electricity use.

	Prague		**Freiburg**		**Bolzano**		**Madrid**		**Naples**		**Athens**		**Almeria**	
	REF	BIPV/T	REF	BIPV/T	REF	BIPV/T	REF	BIPV/T	REF	BIPV/T	REF	BIPV/T	REF	BIPV/T
	[kWh$_e$/(m^2·y)]													
Floor 1st	54.4	23.6	44.5	13.9	42.9	6.9	43.4	10.3	36.2	-2.1	43.4	7.2	38.9	-2.5
Floor 2nd	54.5	23.6	44.6	13.9	43.0	7.0	43.4	10.4	36.3	-1.9	43.5	7.3	38.9	-2.2
Floor 3rd	54.4	23.6	44.6	13.9	42.9	7.0	43.4	10.5	36.2	-1.8	43.5	7.5	38.9	-2.1
Floor 4th	54.4	23.6	44.6	13.9	42.9	7.0	43.4	10.6	36.2	-1.7	43.5	7.6	38.9	-1.9
Floor 5th	54.4	23.5	44.6	13.9	42.9	7.1	43.4	10.6	36.2	-1.5	43.5	7.7	38.9	-1.7
Floor 6th	54.4	23.5	44.6	13.9	42.9	7.1	43.4	10.7	36.2	-1.4	43.5	7.8	38.9	-1.6
Floor 7th	54.4	23.5	44.6	13.9	42.9	7.1	43.4	10.7	36.2	-1.4	43.5	7.9	38.9	-1.4
Floor 8th	54.4	23.5	44.6	13.9	42.9	7.2	43.4	10.8	36.2	-1.3	43.5	8.0	38.9	-1.3
Floor 9th	54.4	23.4	44.6	14.0	42.9	7.2	43.4	10.8	36.2	-1.2	43.5	8.1	38.9	-1.2
Floor 10th	54.4	23.4	44.6	14.0	42.9	7.2	43.4	10.9	36.2	-1.1	43.5	8.1	38.9	-1.1
	[MWh$_e$/y]													
Whole building	19.6	8.5	16.0	5.0	15.5	2.5	15.6	3.8	13.0	-0.6	15.6	2.8	14.0	-0.6
ΔE_{el} [%]	56.8		68.8		83.5		75.5		104.2		82.2		104.4	

The calculated results include the PV electricity production and consumptions due to the electric heat pump/chiller (for heating and cooling), channel air fans, building lighting and equipment. It is worth noting to observe that, for all the investigated weather zones, the use of the BIPV/T systems helps reaching the nearly or net zero energy building (ZEB) target. Moreover, in Naples and Almeria, the PV electricity production is higher than the building overall electricity demands (reaching the net positive ZEB target): electricity surplus of 0.5 MWh$_e$/y (Naples) and 0.6 MWh$_e$/y (Almeria) are achieved. In Naples, as an example, the PV electricity production is about 13.4 MWh$_e$/y, whereas the final electricity use of the reference building is about 13.0 MWh$_e$/y, resulting in a negative final electricity use (including passive and active effects). The use of the BIPV/T system causes a decrease of the share of electricity due to heating and cooling, as shown in Fig. 6.23.

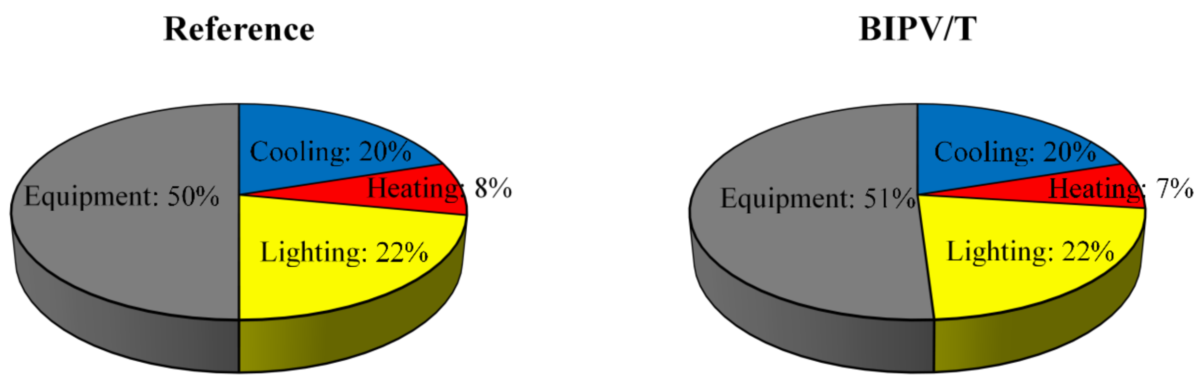

	Value	Unit
Total energy	13.0	[MWh$_e$/y]

	Value	Unit
Total energy	12.8	[MWh$_e$/y]
PV production	13.4	

Fig. 6.23. Final electricity use for the weather zone of Naples.

Here, the share and total final electricity use of both the BIPV/T and reference building configurations are reported. In case of the reference building, the heating and cooling electricity needs are respectively 1.1 MWh$_e$/y and 2.6 MWh$_e$/y, decreasing to 0.9 MWh$_e$/y and 2.6 MWh$_e$/y in case of the BIPV/T configuration, which shows a reduction of both the heating and cooling needs (up to 14.0% and 1.8%). Finally, a swift and simplified economic analysis is carried out by taking into account national electricity fees and feed-in tariffs, as reported in Table 6.7, and the capital cost of the BIPV/T system equal to 25 k€. Satisfactory paybacks (simple – SPB, discounted – DPB), net present values (NPV), and internal rates of return (IRR) are achieved, as reported in Table 6.13.

Table 6.13. Economic indexes.

		Prague	Freiburg	Bolzano	Madrid	Naples	Athens	Almeria
SPB	[y]	3.9	3.1	3.4	3.7	3.3	4.7	3.1
DPB	[y]	4.5	3.5	3.8	4.2	3.7	5.5	3.4
NPV*	[k€]	7.9	12.1	10.6	8.8	11.0	5.3	12.4
IRR	[%]	21.8	29.6	26.9	23.5	27.6	16.7	30.0
PI	[%]	95.7	146.8	129.0	106.7	133.4	64.1	150.0

* *discount rate = 5%, time of the cash flow = 10 years*

As an example, the SPB varies from 3.1 (in Freiburg and Almeria) to 4.7 (in Naples) years. Table 6.14 include the yearly primary energy savings and avoided overall CO_2 emissions for all the investigated weather zones. Remarkable primary energy savings and encouraging results in terms of avoided CO_2 are obtained, confirming the overall feasibility of the proposed technology. Note that conventional national electricity production efficiencies and emissions factors for electricity generation, reported in Table 6.7, are taken into account (according to EU Eurostat - energy price statistics).

Table 6.14. Primary energy savings and avoided CO2 emissions.

	Prague		**Freiburg**		**Bolzano**		**Madrid**		**Naples**		**Athens**		**Almeria**	
[kWh_p/y]	REF	BIPV/T	REF	BIPV/T	REF	BIPV/T	REF	BIPV/T	REF	BIPV/T	REF	BIPV/T	REF	BIPV/T
Floor 1st	167.8	72.9	102.4	31.9	93.3	14.9	109.8	26.1	78.8	-4.5	118.0	19.5	98.5	-6.3
Floor 2nd	168.1	73.0	102.5	32.0	93.4	15.1	110.0	26.4	78.8	-4.2	118.2	20.0	98.6	-5.7
Floor 3rd	167.9	72.8	102.5	32.0	93.4	15.2	109.9	26.6	78.8	-3.9	118.1	20.3	98.5	-5.2
Floor 4th	167.9	72.7	102.5	32.0	93.4	15.3	109.9	26.8	78.8	-3.6	118.1	20.7	98.5	-4.7
Floor 5th	167.9	72.6	102.5	32.0	93.4	15.4	109.9	26.9	78.8	-3.4	118.1	21.0	98.5	-4.3
Floor 6th	167.9	72.5	102.5	32.0	93.4	15.5	109.9	27.1	78.8	-3.1	118.1	21.3	98.5	-4.0
Floor 7th	167.9	72.5	102.5	32.0	93.4	15.5	109.9	27.2	78.8	-2.9	118.1	21.5	98.5	-3.6
Floor 8th	167.9	72.4	102.5	32.1	93.4	15.6	109.9	27.3	78.8	-2.8	118.1	21.8	98.5	-3.3
Floor 9th	167.9	72.4	102.5	32.1	93.3	15.7	109.9	27.4	78.8	-2.6	118.1	22.0	98.5	-3.1
Floor 10th	168.0	72.4	102.5	32.1	93.4	15.7	109.9	27.5	78.8	-2.4	118.1	22.1	98.5	-2.9
Whole building														
[MWh_e/y]	60.5	26.1	36.9	11.5	33.6	5.5	39.6	9.7	28.4	-1.2	42.5	7.6	35.5	-1.5
Δ[t_{CO2}/y]	10.6		6.9		6.2		5.2		6.6		14.8		6.4	

Finally, by a simplified green analysis, the environmental impact of the proposed energy efficiency solution is estimated. Specifically, the average amount of acres necessary to sequestrate the avoided CO_2 is calculated by taking into account the carbon dioxide sequestered by average forestry acres (i.e. 0.947 metric ton CO_2 acre/year, according to the inventory of greenhouse gas emissions (from 1990 to 2013) of the US Environmental Protection Agency). A swift calculation shows that, thanks to the BIPV/T systems, the avoided CO_2 emissions (Table 6.14) correspond to average annual sequestrations of carbon ranging from 4.9 (Madrid) to 14.0 (Athens) acres of average forest.

6.5.4 BIPV/T system – parametric analysis

By following the aforementioned discussion about the cooling inversion point (e.g. Fig. 6.16, Fig. 6.17, and Fig. 6.18), a further investigation is carried out. In particular, the possibility of applying the multiple opening concept, also known as multiple openings system [57, 149, 150], on the modular BIPV/T facades is analysed. For this purpose, a suitable parametric analysis is carried out by varying the number of openings, used as inlet sections, with the aim to find out the optimal BIPV/T design configuration which implies the minimum heating and cooling demands, and overall building electricity consumptions.

Simulation assumptions

The investigated parameter is the number of the openings on the façade BIPV/T façade, (ξ), assumed as inlet section. The parametric analysis is carried by taking into account the same assumptions considered for the ten-floor building and BIPV/T system of the case study reported in Section 6.4. Nevertheless, to increase the level of detail of the parametric study, a thirty-floor high rise building (with the South façade integrating the BIPV/T system) is modelled and simulated. The simulated layouts, defined as a function of the number of active openings, are calculated by dividing the floors number of the considered high-rise building for its integer divisors. Thus, eight BIPV/T system layouts with 1, 2, 3, 5, 6, 10, 15, and 30 openings, (ξ), are obtained. Simulations are carried out for the weather zones of Naples (featuring mild winters and hot summers) and Freiburg (featuring mild rainy winters and temperature summers).

Fig. 6.24 shows the sketch of the configuration layout relative to the typical BIPV/T system (with one opening, Fig. 6.24, left), and the BIPV/T system configuration with multiple openings (Fig. 6.24, right – showing 1 opening for each building floor, for a total of 30 openings).

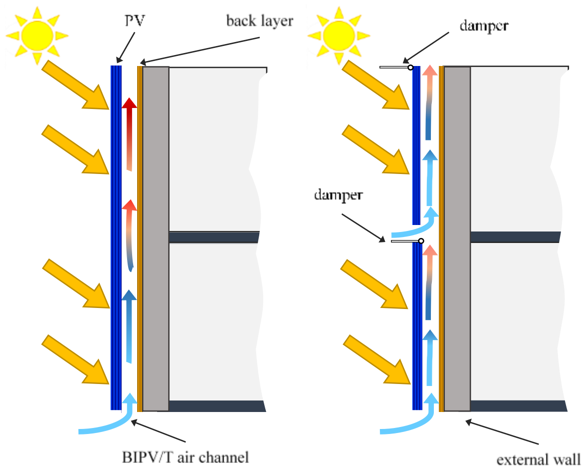

Fig. 6.24. Sketch of the modelled BIPV/T façade relative to the first and second floors. Sections of the wall integrating the PV/T system with a single opening (left) and multiple openings (right).

The thermal and energy performance of each BIPV/T system layout is compared to that one obtained for the reference case (without BIPV/T). The obtained results are reported in terms of heating and cooling requirements, electricity, and primary energy percentage difference. Such index is calculated by the ratio of the difference between the values of the considered variable, calculated for the reference (X_{REF}) and multi-opening (X_{PRO}) layouts, to the reference one (X_{REF}), as:

$$\Delta X = \frac{X_{REF} - X_{PRO}}{X_{REF}} \cdot 100 \tag{6.23}$$

The parametric analysis is carried out by taking into account the same heat pumps/chiller implemented for the reference case. Heat pumps/chiller features are summarized in Table 6.5, whereas the HVAC layouts for the investigated zones and building are reported in Table 6.15.

Table 6.15. HVAC system layouts.

		Naples	Freiburg
Peak load	**Heating** [kW]	43.2	91.4
	Cooling [kW]	49.4	29.5
Number of selected heat pumps/chillers	**Mod 41** [-]	2	2
	Mod 51 [-]	1	2
	Mod 61 [-]	1	2
	Mod 71 [-]	1	2

Heating and cooling requirements

The impact of the number of openings (ξ) on the heating and cooling requirements is analysed hereinafter. In particular, Fig. 6.25 shows the heating requirements percentage variation (ΔQ_h) as a function of ξ, calculated by comparing the eight multiple openings BIPV/T layouts versus the reference (without BIPV/T) one, for both the investigated weather zones.

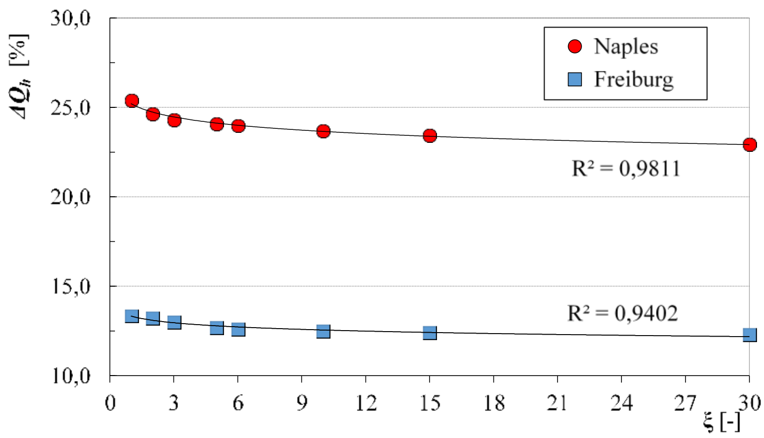

Fig. 6.25. ΔQ_h vs. number of openings (ξ).

As expected, by increasing the number of openings, a remarkable reduction of ΔQ_h is obtained, due to the reduction of the air channel temperature (also due to the reduced stack effect). For both the investigated weather zones, the higher is ξ, the lower is the impact of the BIPV/T on the heating loads. Thus, since passive effects are mitigated, an increase of the heating requirements is achieved. In Naples, the percentage variation of heating requirements, ΔQ_h, ranges from 23.0% (at $\xi = 30$) to 25.4% (at $\xi = 1$). In Freiburg, ΔQ_h ranges from 12.3% (at $\xi = 30$) to 13.3% (at $\xi = 1$). Note that, the differences between the ΔQ_h calculated for the investigated zones are ascribed to the higher influence of the BIPV/T system (i.e. energy savings or energy recovery potentials) in case of lower heating energy requirements.

The percentage variation of cooling requirements (ΔQ_c) as a function of ξ, is shown in Fig. 6.26.

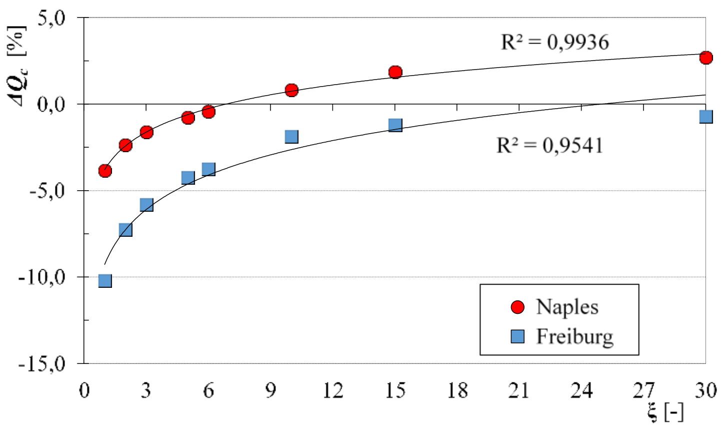

Fig. 6.26. ΔQ_c vs. number of openings (ξ).

Hare, as expected, increasing the number of openings, ξ, helps preventing the impact of passive effects (e.g. overheating) at the higher floors (according to the findings about the inversion point reported in Section 5.1). This leads to the increase of ΔQ_c, which ranges from -3.8% (at $\xi = 1$) to 2.7% (at $\xi = 30$) for the weather zone of Naples, and from -7.2% (at $\xi = 1$) to 1.2% (at $\xi = 30$) in Freiburg. Note that negative ΔQ_c values indicate that the BIPV/T system negative passive effects (i.e. overheating), occurring at the higher floors, overtake the positive passive effects (i.e. cooling), taking place at the lower floors. By Fig. 6.26, according to the outcomes of Fig. 6.18, it is possible to note that the use of multiple openings for the weather zone of Naples produces a reduction of the building cooling requirements, and that by using six openings (one each five floors) the overheating effects are counterbalanced by the cooling ones. Increasing the number of openings, an additional slight advantage in terms of cooling requirement reduction is observed (up to 2.7% at $\xi = 30$). In Freiburg, according to Fig. 6.18, during summer the use of multiple openings only allows reducing the overheating effects (no cooling effects are observed).

PV Electricity production

The number of openings on the BIPV/T façade also influences the PV electricity production. Fig. 6.27 shows the percentage variation of electricity production ($\Delta E_{el,PV}$) versus the number openings, ξ. Note that for the calculation of this index, the reference value (X_{REF} in eq.(6.23)) is the electricity production obtained in case of the BIPV/T layout with a single opening. By increasing the number of openings, ξ, on the BIPV/T system, the PV panels operate at lower temperatures with respect to those observed in case of the typical BIPV/T system configuration (with single opening).

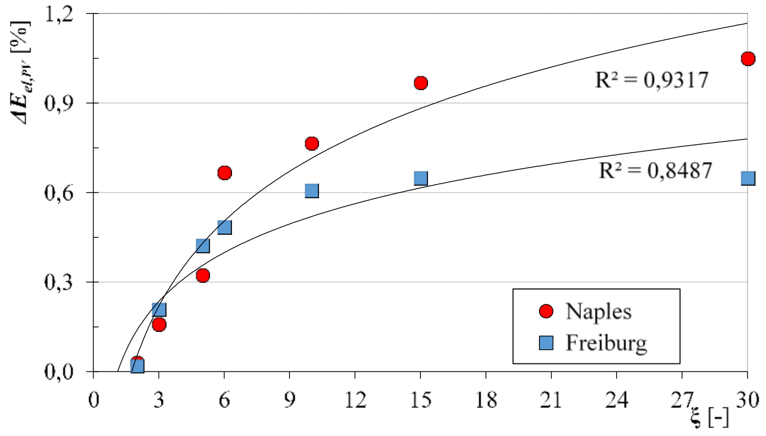

Fig. 6.27. $\Delta E_{el,PV}$ vs. number of openings (ξ).

In fact, by increasing ξ, the air flowing through the channel has a lower average temperature with higher heat extraction potentials, leading to higher PV efficiencies as discussed regarding Fig. 6.21. A percentage increase of PV electricity production ranging from 0.2% (at $\xi = 2$) to 1.1% (at $\xi = 30$) is calculated for the weather zone of Naples. In Freiburg, a minor $\Delta E_{el,PV}$ increase is observed, reaching a maximum of 0.6% (at $\xi = 30$).

Electrical requirements

By taking into account the electrical needs due to the operation of the HVAC system (for heating and cooling) and the operation of the air channel fans, the percentage electricity variation ΔE_{el} versus ξ is show in Fig. 6.28.

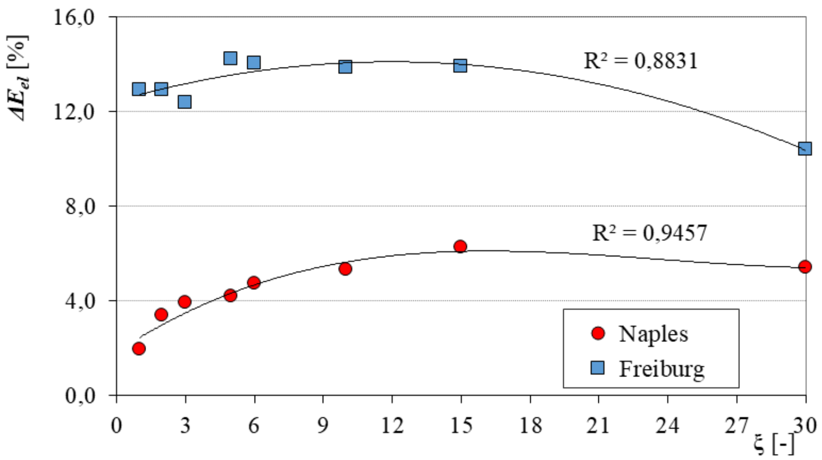

Fig. 6.28. ΔE_{el} vs. number of openings (ξ).

Here, it is possible to note that the trend of ΔE_{el} versus ξ shows a maximum value. This behaviour is caused by different significant aspects, playing opposite roles on the electrical needs. In particular, the increase of the number of openings implies:

i) the variation of the heat pump, COP_h, which depends on conditions of the air from the PV/T cavity channelled to the heat pump evaporator. Such conditions are characterized by the total air channel mass flor rate and by its average temperature, calculated at the outlet sections of the obtained parallel air channels. Note that by using multiple openings, the modular PV/T panels can be considered in parallel and series operation, thus, the total air channel mass flor rate increases as ξ increases, whereas the average air channel temperature decreases as ξ increases;

ii) the increase of the final electricity use due to fans, caused by the reduced stack effect inside the channel.

It is worth noting that as the number of ξ increases, the air flowing through the BIPV/T cavity is channelled to the HVAC system (heat recovery mode) with lower temperature and higher flow rate. Nevertheless, as well known, the contribution of the BIPV/T system to the increase of the heat pumps COP_h (i.e. active effect) is limited to the operating flow rate and to the maximum temperature at the evaporator (i.e. 20°C as provided by manufacturers). Therefore, by taking into account a multiple openings strategy, the optimal number of openings depends on the trade-off between the increase of the *COP* (achieved with a suitable combination of outlet air temperature and flow rate) and the increase of electricity needs due to the multiple openings fans. As shown in Fig. 6.28, the maximum obtained ΔE_{el} is equal to 6.3% (at $\xi = 15$) in Naples and to 14.2% (at $\xi = 6$) in Freiburg.

Primary energy saving

Finally, it is interesting to assess the percentage variation of the primary energy saving (ΔPES) as a function of the number of multiple openings. The slight trend of ΔPES versus ξ is shown in Fig. 6.29.

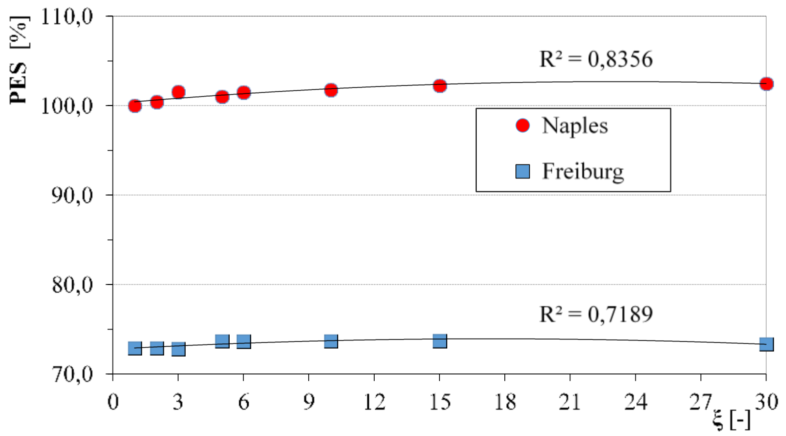

Fig. 6.29. *PES* vs. number of openings (ξ).

This minor variation is mainly due to the primary energy linked to the PV electricity production and electrical loads, which smooth the influence due to the passive and active BIPV/T effects. The ΔPES

ranges from 100% (at $\xi = 1$) to 102.5% (at $\xi = 30$) in Naples (where the positive net ZEB goal is achieved), and from 72.8% (at $\xi = 1$) to 73.7% (at $\xi = 30$) in Freiburg.

Estimated trends of ΔQ, $\Delta E_{el,PV}$, ΔE_{el}, and ΔPES versus ξ

The results obtained from the parametric analysis can be useful for designers and benchmark purposes, in case of the implementation of air open loop BIPV/T systems on the façade of new or refurbished buildings. To this aim, several equations, defined by the trends of ΔQ, $\Delta E_{el,PV}$, ΔE_{el}, and ΔPES versus ξ, are estimated. Despite of the limitation of such approach, restricted to the case study building use and to the investigated BIPV/T system, such easy to use correlations can be taken into account as swift tools for the assessment of the percentage variation of heating and cooling requirements, PV electricity production, electrical needs, and primary energy savings, as a function of the number of openings on the BIPV/T façade.

In particular, for both the considered weather locations, by taking into account the trends of ΔQ_c *and* ΔQ_h (see Fig. 6.25 and Fig. 6.26), and the one of $\Delta E_{el,PV}$ (see Fig. 6.27) versus ξ, a logarithmic profile is detected. In addition, very high root means square errors, R^2, are calculated, ranging from 94 to 99%. The obtained trends can be characterized by the logarithmic equation reported in Table 6.16. The table also provides the values of the coefficients *a* and *b*, to be selected as a function of the investigated parameter.

Similarly, the trends of ΔE_{el} (see Fig. 6.28) and ΔPES (see Fig. 6.29) as a function of ξ show a parabolic profile, also detected with satisfactory R^2, ranging from 0.71 to 0.88%. The obtained trends can be estimated through the parabolic equation reported in Table 6.16. Also, in this case, the coefficients *a*, *b*, and *c*, are provided in the table as a function of the investigated parameter.

Table 6.16. Estimated equations and coefficients.

Equations	**Heating and cooling requirements**				**PV electricity production**		**Electrical needs**		**Primary energy**	
	logarithmic trend: $a \cdot ln(\xi) + b$						parabolic trend: $a \cdot \xi^2 + b \cdot \xi + c$			
Parameters	**Heating - ΔQ_h**		**Cooling – ΔQ_c**		**PV – $\Delta E_{el,PV}$**		**HVAC – $\Delta E_{el,HVAC}$**		**Building - ΔPES**	
	Naples	**Freiburg**	**Naples**	**Freiburg**	**Naples**	**Freiburg**	**Naples**	**Freiburg**	**Naples**	**Freiburg**
a	-0.67	-0.34	25.2	2.52	0.42	0.24	-0.011	-0.015	-0.005	-0.004
b	1.97	13.3	3.80	9.50	-0.25	-0.04	0.45	0.28	0.22	0.13
c	-	-	-	-	-	-	2.22	12.5	100	72.8

6.6. Conclusions

In this chapter, a dynamic simulation model for the energy performance assessment of an active open-loop air building integrated photovoltaic/thermal (BIPV/T) system is presented. The developed model allows assessing both the active and passive effects due to the integration of BIPV/T systems in new or renovated buildings. To this aim, the developed model is implemented in a computer tool, written in MatLab and called DETECt, appositely modified for performing comprehensive building-plant energy performance analysis. By means of the tool, a particular attention is paid to the analysis of the BIPV/T system thermal and electrical performance in case of high-rise building façades. The whole simulation model is capable to provide useful guidelines for preliminary feasibility studies.

To perform a comparative analysis and to show the potentiality of the presented tool, a suitable and comprehensive case study, relative to a ten floor office building, is carried out. A particular attention is paid to the analysis of the BIPV/T passive effects on the heating and cooling loads and requirements (the heat transfer through the integrating façade produce heat gains in winter and cooling/overheating in summer) and active ones consisting of PV electricity production and PV panels heat extraction (exploited by a heat pump). The thermal, electrical, and environmental performance of the proposed innovative building, integrating BIPV/T systems in the South façade, are compared to those achieved by a reference building envelope. With the aim to show the influence of the weather conditions on the energy and economic performance of the proposed building façade, both reference and innovative buildings are simulated in seven different European weather zones.

Interesting performance of the proposed innovative building vs. the reference one, in terms of energy efficiency, thermal comfort, economic indexes and avoided CO_2 emissions, are obtained. Simulation results show that the BIPV/T panels integrated on the building South façade are an effective solution for the reduction of the final building energy demand. Depending on the weather conditions, thermal active and passive effects can reduce the final energy demands up to 16%, whereas the amount of electricity produced by PV panels allows reaching the net and positive zero energy, as well as zero carbon, building goals.

In the investigated heating dominated weather zone, the BIPV/T passive and active effects have a similar influence on the reduction of the heating electricity needs. As an example, in Bolzano (cold winter), the passive effects produce a percentage reduction of the heating electricity needs of about 8%, whereas the active effects produce an extra percentage reduction equal to 6.8%. For all the investigated weather zones, by combining passive, heating and cooling, and active heating effects, the investigated total reduction of heating and cooling electricity needs ranges from a minimum of 1 to a maximum of 16%.

Finally, by means of the developed simulation model, it is possible to calculate the cooling inversion point, i.e. channel length beyond which the positive passive effects (i.e. cooling) become negative (i.e. overheating), influencing the indoor thermal comfort and the heating and cooling loads of the adjacent thermal zone, and consequently the building energy demands. To investigate the significance of this concept, a parametric analysis is carried out with the aim to find out the number of openings along the BIPV/T channel minimizing the heating and cooling demands, and the net overall building electricity consumptions. Such analysis shows that a slight decrease on the overall heating and cooling requirements, and a minor increase of the PV electricity production is obtained by the multiple opening system design. By increasing the number of openings, a maximum percentage increase of the PV electrical productions of about 1% is obtained, with a maximum percentage reduction of the overall electrical needs of 2.5%.

In addition, several relationships are identified in order to provide swift tools, useful for designers and benchmark purposes, for the assessment of the percentage variation of heating and cooling requirements, PV electricity production, electrical needs, and primary energy savings, as a function of the number of openings along the BIPV/T façade.

The proposed methodology can be useful for designers and practitioners in order to evaluate the magnitude of passive and active effects due to the building integration of air PV/T systems on the overall energy requirements and indoor thermal comfort, as a function of the system design and operating conditions.

CHAPTER

7

7. Building to vehicle to building (V2B^2)

As buildings play a crucial role in fossil fuel consumption and carbon dioxide emissions, the development of integrated sustainable energy strategies, from energy generation to storage and transportation, has gained a great attention. In this regard, solar houses, sustainable mobility and electric storage systems are considered as effective strategies toward the goal of a sustainable built environment and a cleaner mobility.

In net or Nearly Zero Energy Buildings (NZEB), the energy generated by off-site resources should be matched or even exceeded by on-site renewable generation, designated for the building itself or exported to the grid. To this aim, NZEBs could effectively take advantages from plug-in electric vehicles, which can be considered as additional high-power appliances (increasing the residential electricity consumption) and as house electricity sources (accelerating the development of NZEBs and promoting the deployment of renewable energy sources).

This chapter focus on the implication of distributed electric storages, building energy use and power generation, which arise within the general frameworks of Vehicle To Home (V2H) and NZEBs.

7.1. Aim of the work and content of the chapter

In this framework, this chapter aims to extend the existing concepts of V2H and ZEB to a novel framework by defining a new zero energy paradigm where buildings are not considered as autonomous entities and the potentiality of EVs are exploited at a micro-grid level. Such new concept focuses on the impact of the efficiency of renewable energy sources and the energy consumption of transportation on the energy performance of a new whole system. Specifically, such whole energy system is linked to human activities consisting of different users, such as buildings and electric vehicles. As well known the energy demand of such whole energy system is highly influenced by occupants' behaviours and by daily mobility patterns, set out by the distance between the buildings where human activities occur.

Key aspect of this new paradigm is the possibility to transfer electricity within such micro-grid by means of an EV, optimizing the utilization of power generation at a system level. In particular, the electricity generated by PV panels located on a building is transferred off-site to other buildings through the EV electricity storage devices. By such system, alternative to the electricity transfer through conventional power grids, the reduction of initial and operating costs of electricity can be obtained in several building combinations such as the classical binomial "house-office". Here, the installation of a PV field can be economically optimized by avoiding a double plant construction (saving the initial costs by selecting and operating just one PV system installation at house or at office). Other additional different potential benefits that can be obtained by such novel concept are: i) a reduced stress on the grid (limiting the peak of load especially during hours of high energy use); ii) a reduced risk of blackout for the involved users (supported by a backup power system in case of power outage); iii) supplying users in case of peak of electricity power needs (often users have low electricity power supply contracts whilst sporadic higher power peak are required); iv) supplying users where the grid is absent or too far (avoiding unsustainable capital costs for grid-user connection); v) supplying occasional users avoiding the constant and operating costs of grid (holiday houses or similar buildings occupied and utilised several days per year only).

No rules are available at this moment on this topic by national governments and authorities. In the next future, from one hand they should stimulate and facilitate users to develop the above described concept in order to decongest the national grids and to stimulate the use of EVs by giving them an additional role (electricity vector). On the other hand, a potential concurrent energy market can be foreseen against the present energy players that could restrain and counteract such new idea. A possible solution could be a novel regimentation of such new way to transfer the electricity, mostly if the economic convenience of the related technology will be reached in the next years by the cost decrease of PV panels, batteries and electric vehicles.

In order to show the potentiality of the proposed concept by taking into account an accurate prediction of the profiles of building electric loads, EV consumption and PV generation (filling the gap of the available literature), a dynamic simulation model is developed. The model, implemented in MatLab, allows one to study the role of EVs as electricity vector among buildings integrating PV panels and electrical storages. Therefore, a novel relevant case study analysis, based on three different management systems, is carried out aiming to analyse the energy and economic performance of the proposed novel vehicle to building (or home) concept.

The analysed new zero energy scheme includes three main electrical users, such as a residential building, an office building, and an electric vehicle. The selected users can be considered as the basic nucleus of human-linked energy systems connected in a micro-grid. A dynamic vehicle commute distance profile is simulated in order to assess the effect of vehicles use on the proposed novel vehicle to building operation. Three different scenarios, relative to location of PV and energy storage strategies, are simulated and compared to a reference conventional case by taking into account energy and economic indexes. The case study analysis aims to show the potentiality of the proposed energy scheme, namely Building To Vehicle To Building strategies ($V2B^2$), to provide swift design guidelines and to assess how it allows the fully utilization of the electricity generation, maximizing the self-production of building integrated RES toward the ZEB goal evaluated at a micro-grid level.

7.2. System description

The classical Vehicle To Building (V2B) idea introduces significant contributions to simultaneously enhance the power system and support the buildings integration of renewable technologies. Nevertheless, it is not yet clear how the Electric Vehicle (EV), acting as energy user, storage point and energy vector, may contribute to the zero energy concept, specifically to the achievement of the net or nearly zero energy building target. In this regard, by considering the EV not only as a storage system but also as a transfer device capable to use, store and transport electricity from a building to another, a novel dynamic model for energy and economic simulation analyses is here presented. It aims to investigate the implication of a new concept in reaching the net-zero energy balance, by matching as much as possible the energy demand of a whole energy system linked to human activities consisting of three main users: the house, the electric vehicle, and the office. By exploiting the concept of net or nearly zero energy building, authors aim to complete it by defining a new zero energy paradigm (focused on such whole system) where buildings are not considered as autonomous entities. This suggest to take into account the efficiency of renewable energy sources as well as the energy consumption of transportation, which is highly influenced by daily mobility patterns due to the distance between residential and work place buildings.

From this point of view, a new acronym can be conceived by taking into account that the energy exchange can be among the EV and two buildings ($V2B^2$, that means Building To Vehicle To Building). The proposed simulation model is capable to investigate the best configuration of this micro-grid, considered as a crucial solution for supporting the high EV penetration toward the establishment of the new V2B² concept, through which optimizes the integration of the EV into the power system as well as into the net or Nearly ZEB balance at a micro-grid scale.

7.2.1. EVs for the NZEB goal at micro-grid level

To provide insight of the energy performance of these typical future micro-grids, including PV panels and electrical storage systems, suitable numerical assessments are carried out and discussed. To this aim, different sample system layouts are modelled and dynamically simulated through the developed model. In general, the investigated micro-grid consists of:

- two different building users: a single-family house (namely House) and an office space (namely Office), where HVAC system and appliances are supplied by electricity;
- PhotoVoltaic (PV) panels, integrated either in the house roof or in the office façade;
- electricity storage devices. Specifically, a main House System Battery (HSB) and an Electric Vehicle Battery (EVB);
- an Electric Vehicle (EV).

Fig. 7.1 shows the schematic diagram of the general energy management system of the proposed V2B² scheme, showing how electrical renewable generation (from PV), demands (of both the buildings within the micro-grid) and supply (from the grid and/or the stationary and mobile storage devices) are managed toward the maximum exploitation of renewable energy and the self-consumption of RES. In particular, the system control logic acts on the energy storage systems in order to reduce the energy provided from and delivered to the main power grid at a micro-grid level (minimizing the impact of intermittent RES [267]), while reducing the overall buildings energy consumptions (achieving the NZEB goal at the micro-grid level). According to the storage devices capacities (State Of Charge, SOC), and to the maximum power constraints, the instantaneous power demand of the two buildings (i.e. House and Office), is satisfied by the distributed generation within the microgrid (i.e. PV generation produced on site at the main building), the power drawn by the batteries (both the stationary, HSB, and the mobile one, EVB), and the power provided by the grid. It is worth noting that the bidirectional operation of the batteries allows the balance condition of the microgrid to be satisfied at the best. In fact, by taking advantage of the bidirectional operation of the batteries, it is possible to minimize or nullify the energy from the power grid. In addition, by using the energy stored within the EVB, both buildings can effectively take advantage by the renewable energy provided by the renewable energy system (i.e. PV field installed at the main building, e.g. either on the roof of the house or on the façade of the office). The general microgrid system control logic proposed in this chapter is described in Fig. 7.1, which shows how all the electrical flows interact among the delivery and consumptions points.

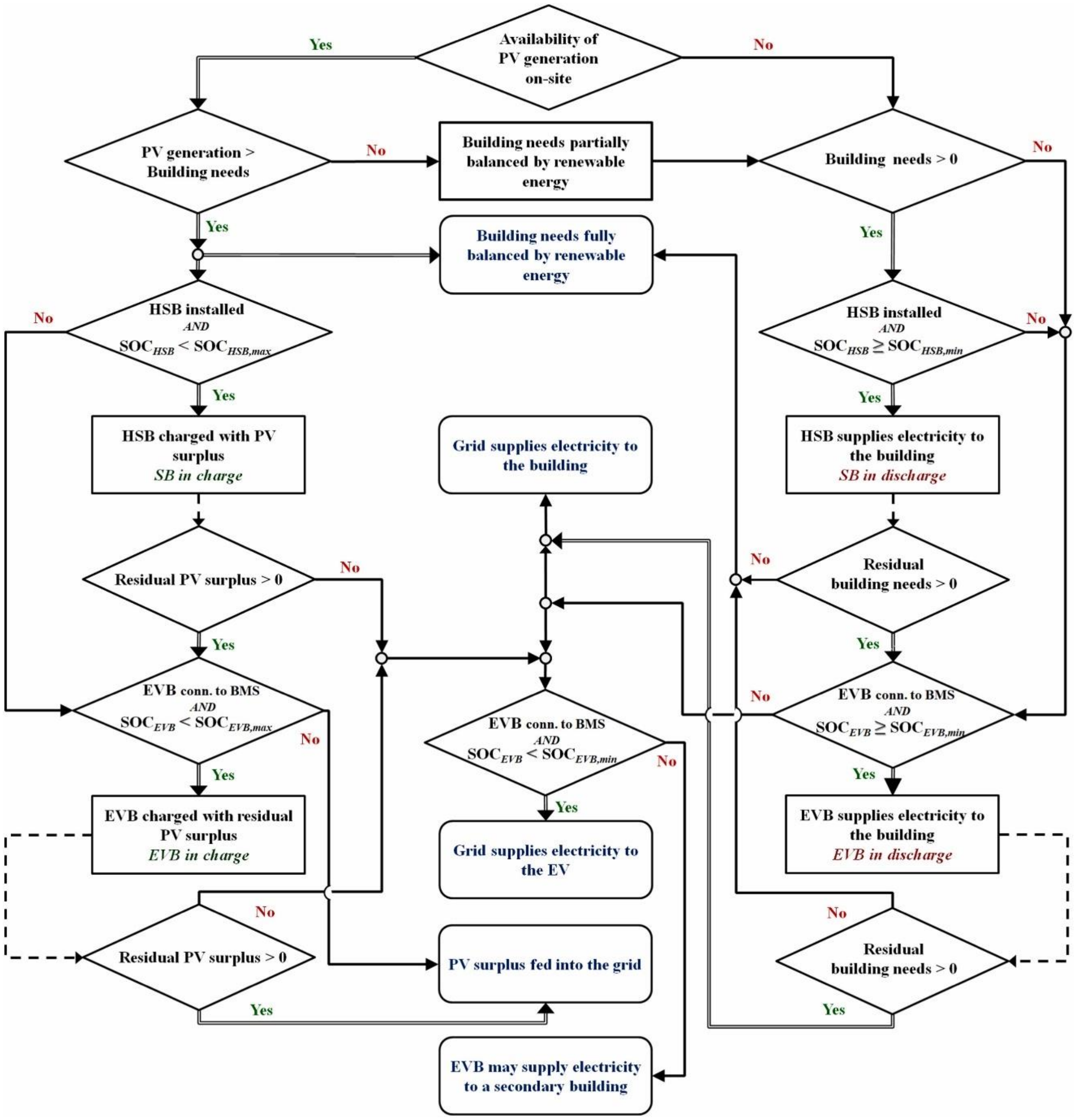

Fig. 7.1. Flow chart of the general energy management system of the proposed V2B2 scheme.

In particular, if the instantaneous PV generation is higher than the main building needs (i.e. sum of all electricity demands), they are fully covered by renewable energy, while the surplus of PV generation is stored within the EVB (if connected to the Building Management System (BMS) of the building itself) until the minimum storage capacity is reached ($SOC_{EVB,min}$); the remaining PV electrical surplus is stored within the HSB unless its capacity is lower than the maximum constraint level ($SOC_{HSB,max}$), while further PV generation is stored in the EVB (surpassing its minimum level, limited by driving needs). Energy stored within both the batteries is used in different times of the day as a function of the buildings requests and the EV location. When the $SOC_{HSB,max}$ is reached, the surplus of renewable energy is either continuously stored within the EVB (if connected to the BMS system) or fed into the national power grid. Conversely, when no PV generation (at the main building power station) or HSB (at the secondary building) are available, if the EV is connected to the BMS of a building (either the house or the office, depending on the occurring condition) and its capacity is higher than the minimum constraint value ($SOC_{EVB,min}$), the EVB acts as a source of electricity used to cover the electrical building needs. Finally, the power grid acts as auxiliary system, supplying electricity to both the buildings and the EV for its own motion.

7.2.2. System layout

With the aim to study the role of electric vehicles as alternative electricity vector among buildings integrating PV panels, a suitable analysis is carried out. It refers to three different cases studies (hereinafter referred to as Case 1, Case 2 and Case 3) to be compared to a reference traditional one without PV panels (referred to as Case 0), sketched in Fig. 7.2. Such analysed system layouts differ from each other in:

- the EVB operation (i.e. charging and discharging process). Note that, the EVB is alternatively considered as additional storage point for the two investigated building users, in this case House and Office. The EVB can receive electricity from the HSB, acting as a load point while in charging mode, or provide electricity to buildings and EV, as active sources, in discharging mode;
- the site in which the renewable generation system is placed. The PV system, located on the House roof or on the Office façade, provides electricity to all the building users (i.e. heating, cooling, equipment, lights) and to the EV, whereas its surplus is fed to the power grid (namely Grid), which transfers power back to the users when needed.

By considering the EV as only conceived for transportation from/to House to/from Office and by varying the PV panels site and the batteries features, the obtained system layouts are:

- *Case 0*, considered as the reference layout, represents the conventional unidirectional Vehicle to Building (V2B) system operation (Fig. 7.2, Case 0). Here, the plug-in EV is linked with the power grid by acting as a power load. The EV is charged through a home charger and no renewable energy systems and batteries are installed on-site (neither on the House or Office buildings). House and Office electricity loads are balanced by the grid;
- *Case 1* represents a novel concept of bidirectional Building To Vehicle To Building (V2B²) system operation (Fig. 7.2, Case 1). The plug-in EV is linked with the power grid acting as a power load as well as a source for the House building, and as a source only for the Office space. A renewable energy system, consisting of PV panels, is on-site installed on the tilted roof of the House building.

The House is also equipped with an HSB, which can also feed the EVB (in case of available stored energy, otherwise the EVB is conventionally supplied by the grid). An additional novelty is here represented by the transfer to Office through EVB of the electricity potentially produced by the House PV panels. The EVB can be also charged at Office, if necessary. Auxiliary electricity for House and Office loads is balanced by the power grid.

A priority sequence "House – HSB – EVB – power grid" is assumed to dispatch PV generation. In particular, when the EV is disconnected from House, PV, HSB and power grid are considered as the only available House energy sources. The amount of generated PV electricity is self-consumed by the House (for its energy needs), whereas electricity surplus from the PV field (PV production minus total House electricity need) if fed to and stored within the HSB. If a surplus of power generation occurs when the HSB is fully charged, it is exported to the grid. Conversely, in case of no PV production (i.e. no solar radiation availability), the House is powered by the HSB until its complete discharge (then, the grid supplies the remaining electricity for the House demand). When the EV is connected to the House, the surplus of generated electricity (i.e. PV production is higher than House needs and the HSB, preferentially charged, is full) is delivered to the EVB. Such stored energy is used for the EV motion and, if sufficient, transferred to the Office load, which can benefit of the solar energy collected at House. In other words, by this strategy, the electricity generated off-site to the Office is here exploited by transferring it through the EV, to be considered as an electricity network alternative to the grid. When the EV returns back to the House, if the EVB state of charge is higher than the minimum threshold, the EVB acts a source of electricity for the House, and its residual electricity needs (not balanced by the HSB) can be balanced by the EVB until it reaches the minimum state of charge, after that any residual energy need is provided by the power grid.

Note that, electricity stored within the batteries can be supplied to the considered users down to their minimum SOC level which, for the EV battery, depends on the daily amount of electricity necessary to drive the vehicle (plus an additional amount of electricity, referred to as safe level – batteries are never fully discharged). The minimum electricity charge level necessary for the EV trips is guaranteed by the grid (the EV battery are possibly supplied in specific time intervals depending on the amount of electricity need and charger power). Note that during night hours, if the HSB SOC is higher than the EVB one, electricity from HSB is supplied to the EVB (if the vehicle is connected to the House).

- *Case 2* represents a novel concept as well of bidirectional Building To Vehicle To Building (V2B²) system operation, based on swappable batteries (Fig. 7.2, Case 2). The system operation follows that of Case 1, thus the plug-in EV is connected to the power grid acting as a power load as well as a source for the House building, and as a source only for the Office space. PV panels are installed on the House tilted roof. The difference with Case 1 relies on the batteries, specifically, in Case 2 the House is equipped with a battery identical to the EV one and a quick swap of batteries is allowed between EV and House. The swapping option prevents the need of energy transfer from the HSB to the EVB (when EVB charge is required), and thus the related losses. As for Case 1, the electricity potentially produced by the House PV panels is transferred to Office through the EVB. The EV can be charged both at the House and Office buildings (the charge at Office is also here required just for car-moving purposes).

Note that, the SOCs of the two above mentioned identical batteries are compared before the EV motion at the morning of each day. Here, the battery featured by the highest SOC level is assumed to be placed on the EV (the other one, is left at House, acting as a HSB, also for charging purposes) and vice versa.

- *Case 3* represents a different novel concept of bidirectional V2B² system operation (Fig. 7.2, Case 3). The main difference with the previous Cases regards the site of the PV panels, which are installed on the façade of the Office space, where no dedicated battery (i.e. HSB) is considered (solar energy is stored directly into the EVB). The plug-in EV communicates with the power grid acting in this case as a power load as well as a source for the Office space, and as a source only for the House building. In Case 3, the novelty is represented by the possible transfer to House through EVB of electricity produced by the Office PV panels (the EVB energy, that is potentially produced by the Office PV panels, is here used primarily for Office needs and for EV motion and then for House needs). The EV can be charged both at the House and Office buildings (the grid charge at House is here considered just for car-moving purposes). Note that, the EVB is fed by DC electricity surplus from the Office PV field. In particular, the available surplus (PV production minus total Office electricity need) supplies the EVB as a function of the related SOC.

In all the Cases 1, 2 and 3 the final remaining PV energy production surplus is exported to the grid (by selling it at the current hourly price). These scenarios can also be considered as a reliable energy source in case of emergency, such as a power outage. In general, HSB and/or EVB power to buildings is provided by reducing the stress on the grid. Note that, the DC current produced by the PV panels or supplied by the HSB and EVB is converted into AC current by an inverter. Such device also works as a suitable regulator conceived to: i) maximize the current (produced by the PV field) provided to the users or delivered to the grid; ii) prevent an early degradation of batteries.

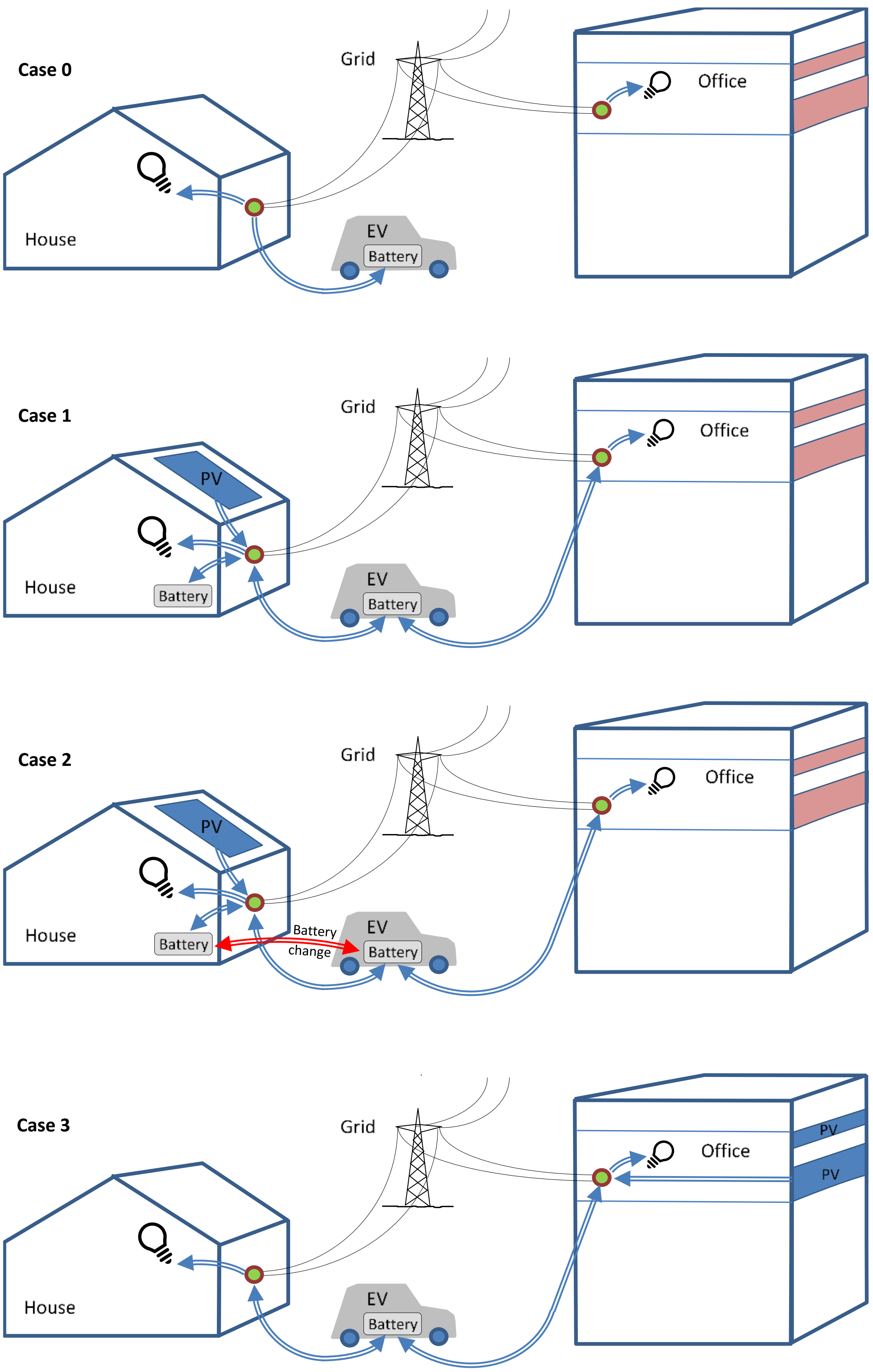

Fig. 7.2. Investigated micro-grid system layouts.

7.3. Dynamic simulation model

The simulation model of the investigated V2B² system layouts is implemented in a previously developed simulation model, developed for performing building-system dynamic simulations. Details about capabilities and validation procedures are reported in [268, 269].

Through the simulation model, the energy and economic performance of the investigated V2B² layouts, i.e. Case 1, Case 2, and Case 3, and of the reference one, Case 0, are suitably assessed.

Specifically, through energy balances the electrical demands of the investigated buildings, House and Office, and of the electric vehicle, EV, are calculated in order to identify the energy exchanges (produced, delivered, exported, and consumed energy) between PV system, buildings, HSB, EVB and grid.

This section describes the mathematical models and operating logic of the main components of the investigated layouts, i.e. buildings, batteries, and vehicle operation.

7.3.1 Building load calculation model

The prediction of dynamic energy demand of the two buildings, House and Office, where PV panels are integrated, is performed by a computer simulation code, called DETECt 2.3, previously developed to carry out dynamic building energy performance analyses [231, 270]. The simulation model, implemented in MatLab environment, has been conceived for research purposes to investigate novel building envelope integrated technologies [58, 166], operating energy saving strategies [238, 271], operating energy saving strategies [240, 242, 268] toward the NZEB target. The simulation model has been validated by following the BESTEST procedure [123, 231, 232, 270], showing also a very good agreement with measured data. Subsequently, DETECt was also experimentally validated.

DETECt has been modified in order to allow the simulation of multiple buildings, independent or mutually interacting. The temperature field of each multi-zone and multi-floor building is calculated as a function of its features, occupancy schedules, weather conditions and location data. The influence of a building on the others in terms of cast shadows is also calculated. The mathematical model is based on a nodal description of the buildings, modelled through resistive-capacitive (*RC*) thermal networks obtained by discretizing the heat transfer equation and considering distributed parameters (thermal masses and conductivities are uniformly discretised) [256]. The adopted scheme allows subdividing each building into several thermal zones (assuming perfect indoor air mixing), delimited by different multi-layer building elements (walls, roof, windows, etc.) consisting of numerous sub-layers which constitute the nodes of the *RC* thermal network.

For each simulated building, the system of equations describing the heat transfer (discretized by means of the finite difference method) of each n-th node ($1 \le n \le N$) of the m-th building element ($1 \le m \le M$) of each thermal zone, modelled with a single indoor air temperature node, is written as:

$$
\begin{aligned}
& C_{m,n}\frac{dT_{m,n}}{dt} = \sum_{j=n-1}^{n+1}\frac{T_{m,j}-T_{m,n}}{R_{m,j}^{eq}} && \textit{(capacitive nodes)} \\
& \sum_{j=n-1}^{n+1}\frac{T_{m,j}-T_{m,n}}{R_{m,j}^{cond}} + \chi\cdot Q_{m,n} = 0 && \textit{(non capacitive nodes)} \\
& C_{in}\frac{dT_{in}}{dt} = \sum_{m=1}^{M}\frac{T_{m,N}-T_{in}}{R_{m,N+1}^{conv}} + \frac{\left(T_{out}-T_{in}\right)}{R_v} + Q_{pp} + Q_{appliances} \pm Q_{HC}^{s} && \textit{(indoor air node)}
\end{aligned}
\tag{7.1}
$$

where C, T, and R are thermal capacitances, temperatures, and resistances; Q is a forcing function including the incident solar and long-wave radiation exchange; Q_{pp} and $Q_{appliances}$ are the sensible heat gains due to people, and appliances (lighting and equipment), networked to the indoor air node only; $\dot{Q}_{HC}^{s}$ is the sensible heat to be supplied to (or removed from) the thermal zone by an ideal heating and cooling system, aiming at maintaining the indoor air at the desired set point temperature [231]. Further details about the thermal network describing the thermal behaviour of a single thermal zone and details about the numerical integration methods implemented in DETECt, are extensively reported in [166, 238, 270].

As the simulated building are assumed as heated and cooled by electrical devices (i.e. heat pumps/chillers), in each time step, the calculation of the heating and cooling electrical needs, $P_{heating}$ and $P_{cooling}$, of each building (B) is obtained as a function of Q^{S}_{HC} (given for each thermal zone of the simulated buildings) and of the HVAC conversion efficiency (i.e. COP), such as:

$$
\begin{aligned}
P_{Heating} &= \frac{\sum_B \max(0, Q_{HC}^{s})}{COP_{heat}} \\
P_{Cooling} &= \frac{\sum_B \min(0, Q_{HC}^{s})}{COP_{cool}}
\end{aligned}
\tag{7.2}
$$

Similarly, the electrical power due to appliances, $P_{appliances}$, is obtained by the knowledge of the electrical power of Q_{APP}.

7.3.2 PV production

Due to the RC thermal networks scheme, the implementation of building integrated solar systems (PV panels) modelled as non-capacitive external building envelope layers can be suitably carried out. In particular, a Building Integrated PhotoVoltaic (BIPV) system [1] is modelled by taking into account the following assumptions: i) one dimensional heat transfer, ii) isothermal surfaces of the PV module, iii) neglected system edge heat losses [272, 273]. It is worth noting that the PV module temperature strongly affects its electrical efficiency [274, 275], thus it is assessed by taking into account the system conductive, convective and radiative thermal exchanges accounted within the thermal networks terms.

The interaction between the electrical and thermal efficiencies is properly modelled by taking into account the thermal and optical properties of the PV modules and the incident solar radiation. The thermal behaviour can be assessed by accurately modifying the second equation of the system reported in eq. (7.1), by considering the PV node as resistive only. The operating cell temperature (T_{PV}) is calculated in each time step by solving the heat balance equation:

$$\frac{T_{out}-T_{PV}}{R_{out}^{conv}+R_{PV}^{cond}}+\frac{T_{sky}-T_{PV}}{R_{sky}^{rad}+R_{PV}^{cond}}+\frac{T_{m,1}-T_{PV}}{R_{PV}^{cond}}+I_{PV}\cdot A_{PV}=0 \tag{7.3}$$

where R are conductive, convective and radiative thermal resistances, and I_{PV} is the effective absorbed solar radiation per unit of PV cell gross area, A_{PV}, calculated as:

$$I_{PV}=(K_{\theta}\cdot\alpha_{PV}-\eta_{PV})\cdot I_{m}^{\text{ext}} \tag{7.4}$$

where α_{PV} is the PV cell absorptance, η_{PV} is the PV module efficiency, I_{PV}^{ext} is the global incident solar radiation (calculated for any tilted surface by means of geometric relationships [259]), and K_{θ} is the Incident Angle Modifier (IAM), defined as the ratio between the radiation absorbed by the cell divided at the occurring incident angle and the radiation absorbed by the cell at normal incidence ($K_{\theta}=\tau(\vartheta_i)/\tau(0)$) [276].

Given the cell temperature, a linear expression of photovoltaic cell efficiency, η_c, is taken into account, such as [274]:

$$\eta_c=\eta_{ref}\left[1-\beta_{ref}\cdot(T_{PV}-T_{ref})\right] \tag{7.5}$$

where η_{ref} is the cell electrical efficiency, provided by manufacturers, calculated at the reference temperature (T_{ref} at 25°C) and solar radiation flux (1000 W/m²), β_{ref} is the temperature coefficient which depends on the temperature at which the PV efficiency drops to zero [276].

The module efficiency is calculated as: $\eta_{PV} = \eta_{c} \cdot \eta_{mod}$, where η_{mod}, is the module conversion efficiency. Finally, the net power (P_{PV},) produced by the system is obtained by the gross electrical power produced by the PV module minus the electricity loss due to the inverter efficiency, and it is calculated as:

$$P_{PV}=\left(\eta_{PV}\cdot I_{m}^{ext}\right)\cdot\eta_{inv}\cdot A_{PV} \tag{7.6}$$

7.3.3 Electrical vehicle model

The key component of an electric vehicle EV is the battery (EVB), impacting on the grid as well as on the building energy management. The higher the EVB capacity and the charging demand, the severely higher is its impact on the grid (due to the higher drawing of current). Within the simulation model, the bidirectional EVB operations, charging and discharging modes [277], are modelled by taking into account their characteristic curves. In charging mode, the battery stores energy drawn from the charging station, i.e. storing power output either from PV or grid acting as an electricity load. Conversely, in discharging mode the battery acts as an electricity source, releasing its stored energy to supply energy either to the vehicle electric engine or to the building to partially or fully balance its load.

In this chapter, the EVB (e.g. a Li-ion battery) is modelled by using the modified Shepherd model proposed in [278] and also considered in [208]. Therefore, according to [278], the behaviour of a battery cell is modelled with respect to the terminal voltage, discharge/charge current and state of charge. In particular, the charging mode is simulated by taking into account the power demand of the EVB charger, i.e. home station, modelled considering the EV charger characteristic reported, as an example, in Fig. 7.3. The EV charger is modelled as operating on a constant current (e.g. 16.75 A) and constant voltage (e.g. 415.28 V) charging cycle, with a nominal charge power AC of 7.5 kW, an overall efficiency factor 0.94, Fig. 7.3. Note that the AC charger power profile provides the indication of the amount of time necessary to the EV battery to be fully charged at its maximum capacity.

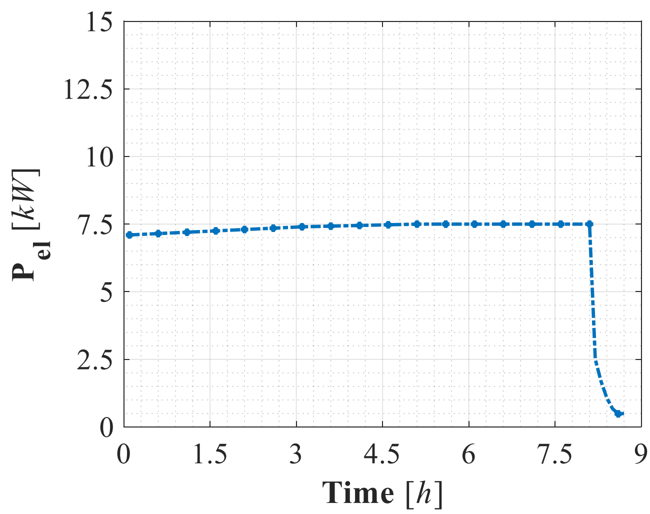

Fig. 7.3. Power demand of the EV charger vs. time [208].

In discharging mode, a constant current is also assumed [278]. When the EVB acts as a source for fulfilling the buildings load, the discharge characteristics of the battery pack for discharge rates of 0.2

C (30.36 A) is assumed, as modelled in [208]. When the EVB provides energy to the vehicle motion, the power consumption is a function of the driving speed. According to the approach proposed in [279], the energy losses for a EVs are considered as a function of the driving velocity, being distributed in different categories, such as aerodynamic, tire, drivetrain, and ancillary losses, as reported in Fig. 7.4.

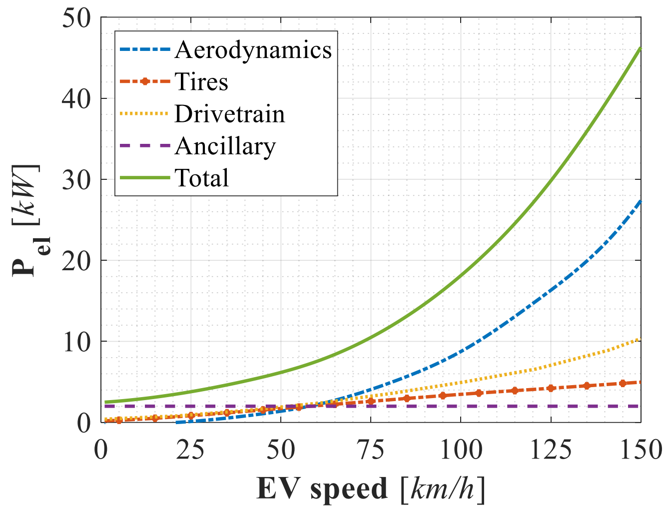

Fig. 7.4. EV power consumption vs. driving speed (Tesla Motors).

7.3.4 Electrical home battery model

The home battery, HSB, is modelled by means of an equivalent circuit of a Li-ion battery, by taking into account a scaled model directly linking the internal charge curve of the battery with the operating power [280]. According to [281], the implemented characteristic curve of the battery charge power is shown in Fig. 7.5.

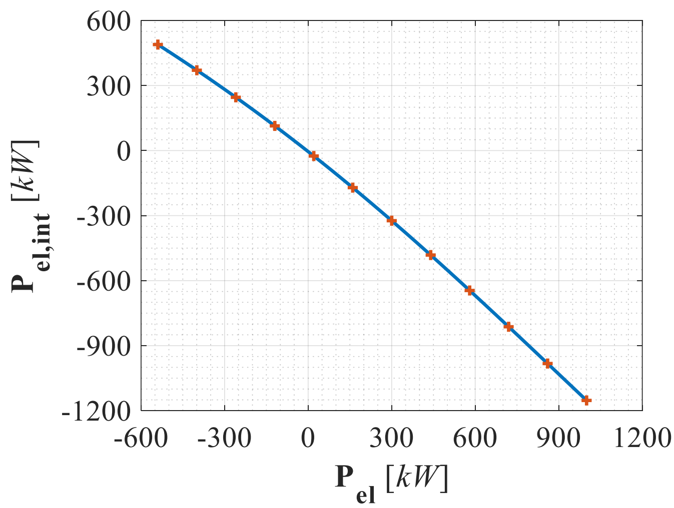

Fig. 7.5. Main battery characteristic HSB charge.

7.4. Case study scenarios

In order to study the role of electric vehicles as electricity vector among buildings integrating PV panels, a suitable comprehensive case study analysis is carried out. Such case study analysis also aims to analyse the energy and economic performance of the proposed V2B² systems, consisting of the main energy users linked to the human activities, such as a house, an office and an electric vehicle. By means of the developed case study, the energy consumptions due to the operation of the house and office buildings, and due to the daily mobility patterns (linked to the distance between residential and work places) are investigated toward a new zero energy paradigm including the whole system and its energy storage technologies, considered as crucial to reach sustainability at a micro-grid level.

To this aim, the above presented V2B² scenarios, sketched in Fig. 7.2, Case 1, Case 2 and Case 3 are compared to the reference one, Case 0 (i.e., a standard scenario with an unidirectional electric vehicle charged at home only by the power grid as no renewable energy sources considered).

For all the investigated scenarios, simulation assumptions regard design and operating parameters, linked to the two investigated buildings, a residential single-family house (hereinafter referred to as the House) and an office space (namely Office), and an electric vehicle (namely EV). The main simulation assumptions are given in the following:

- *House*: two-floor single family residential building with its longitudinal axis East–West oriented. The building has a pitched building roof (Fig. 7.2) where, only in the scenarios Case 1 and Case 2, Building Integrated PV panels (BIPV) are installed (no PV are considered in Case 0 and Case 3). The House building is occupied by a typical family with 5 members spending daytime hours outside; a family member leaves the House in the morning to reach his office (i.e. Office, afterwards described) by EV, coming back home after work late in the afternoon (one hour later the other members). The main features of the considered House are reported in Table 7.1, whereas the related operating assumptions are depicted in Table 7.2.
- *Office*: a single intermediate floor office space of a multi-floor building with its longitudinal axis East–West oriented. The Office space is simulated as a South facing perimeter thermal zone, with internal walls considered as adiabatic (adjacent to thermal zones with the same indoor air temperature). The modelled façade consists of an opaque/glazing/opaque wall structure (split in three horizontal strings, Fig. 7.2). The opaque strings, only in the scenario Case 3 scenario, integrate BIPV panels (no PV are considered in Case 0, Case 2 and Case 3). The Office space is occupied during daytime hours by 6 people. The family member leaving the House building

reaches the Office work place where the car remains parked until the end of the business day. The main features of the considered Office are reported in Table 7.1 whilst the related operating assumptions are depicted in Table 7.2.

- *EV*: The electric vehicle is only used for home-work commuting, between the House and the Office. This assumption allows focusing on the behaviour of the system consisting of House-EV-Office and on its energy consumptions, disregarding the random use of the vehicle for personal mobility. The EV driving distance, from House to Office, is 13 km per trip (26 km/day, Table 7.3), considered as an average distance, also according to the distribution of daily driven distance [279]. The EV leaves the House and the Office at 8:00 a.m. and 17:00 p.m., respectively. The EV is parked at the House garage (or similar) from 17:30 p.m. to 8:00 a.m. and at the Office place from 8:30 a.m. to 17:00 p.m. (plugged to their building management systems in Case 1, Case 2 and Case 3).
- *PV panels*: the BIPV field is made of mono-crystalline silicon panels including cells of 156 x 156 mm. The main features of the BIPV system are reported in Table 7.2. BIPV panels are installed on the pitched roof of the House (tilt angle 30°) in Case 1 and Case 2, and on the vertical façade of the Office in Case 3. Note that for both integration cases (on the roof and on the façade), BIPV panels are South oriented. Finally, the sizing of the PV field is based on the available surface area of the house roof and of the single office façade, Table 7.3. The resulting PV peak power is lower than a typical solar roof mounted system for a two-floor single family house, and it allows the PV field to provide sufficient electricity for the house, office, and electric vehicle needs. It is worth noting that both active and thermal passive effects are taking into account in the simulations.
- *On-site battery:* this on-site House System Battery (HSB) is a Li-ion battery with a charging/discharging characteristic curve, developed according to [281], shown in Fig. 7.5. Depending on the simulated scenarios, HSB has different maximum capacities, as reported in Table 7.3, whereas a 5.0 kW home/office charger is taken into account. HSB features are reported in Table 7.3. Note that the minimum and maximum state of charge of the HSB correspond to the 5% and 95% of its nominal capacity.
- *EV battery*: the EV battery of Case 1, Case 2 and Case 3 simulates a battery pack of 6831 cells, 18650 form factor Li-Ion battery, following an 11S 9S 69P configuration [282] with a capacity of about 50 kWh. For Case 0, a similar car with a smaller capacity battery, 30 kWh, is taken into account. The EV charging and discharging behaviour is modelled according to [208]. The EV battery is in discharge mode as a function of the driving path features, shown in Fig. 7.6 (EV motion power peak is equal to 6.2 kW). Note that the charger nominal power is 7.5 kW and the minimum and maximum state of charge of the EVB (also namely safe level) correspond to the 5% and 95% of its

nominal capacity. Details about EV operations are reported in Table 7.3

Table 7.1. Buildings envelope features.

Parameter	House	Office
Number of floors	2	1
Height of each floor [*m*]	3.5	4.0
Useful surface area of each floor [m^2] (length × width [*m*])	64 (8 × 8)	90 (15 × 6)
Total useful surface area [m^2]	128	
Window U-value (4-6-4 air filled double-glazing) [$W/(m^2 \cdot K)$]	2.1	
Window to vertical Wall Ratio, WWR [-]	0.23	0.55
Wall U-value [W/m^2K] and (thickness [*cm*])	0.34 (30)	
Wall hollow bricks conductivity [$W/(m \cdot K)$]	0.33	
Wall hollow bricks density [kg/m^3]	1600	
Wall hollow bricks specific heat [$J/(kg \cdot K)$]	1200	
Wall insulation conductivity [$W/(m \cdot K)$]	0.05	
Wall insulation density [kg/m^3]	13.0	
Wall insulation specific heat [$J/(kg \cdot K)$]	1100	
Wall absorptance (to solar radiation through windows) [-]	0.2	
Floor/ceiling U-value [$W/(m^2 \cdot K)$] and (thickness [*cm*])	0.68 (25)	
Floor absorptance (to solar radiation through windows) [-]	0.4	

Table 7.2. Buildings operating assumptions.

Parameter	House	Office
Ventilation rate [*Vol/h*]	0.5	0.7
Crowding index [$person/m^2$]	0.04	0.06
Occupancy and appliances schedule [*hours*]	18-8	9-18
Thermal load due to people (variable as a function of the indoor air temperature) [*W/person*]	95 (at 26 °C)	
Thermal load due to lighting and equipment [W/m^2] (scheduled as a function of the occupancy [*hours*])	10	9 (9-13) 15 (14-18)
Heating set-point [*°C*]	20	
Cooling set-point [*°C*]	26	
Heating period [*month/day*]	11/15th - 3/31st	
Cooling period [*month/day*]	6/01st - 9/30th	
HVAC system schedule [*hours*]	7-8, 18-22 8-10, 17-20 (weekend)	9-12, 13-18
HVAC system capacity (air-to-air electric heat pump/chiller) [*kW*]	12	
HVAC system COP	Variable COP (provided by manufacturers) as a function of the occurring operating conditions, and the part-load ratio f_{PLR} [46].	
South-oriented BIPV surface area (Case Study 1, 2 and 3), A_{PV} [m^2]	28	
BIPV panels peak power [*kW*]	5.5	
BIPV panels nominal efficiency (mono-crystalline silicon cells of 156 × 156 mm @ STC conditions: temperature at 25°C and solar radiation flux 1000 W/m²), η_{PV} [-]	0.195	
BIPV panels thickness [*mm*]	5.0	
BIPV panels slope [°]	30	90
BIPV panels absorptance, α_{PV}[-]	0.92	
BIPV temperature coefficient, B_{ref} [$°C^{-1}$]	0.0045	

Table 7.3. Batteries and electric vehicle operations.

Parameter	House	Office	EV
EV trip from/to House to/from Office (from Monday to Friday at an average speed of 50 km/h) [*km*]	-	-	26
Case study 0 battery [*kWh*]	-	-	30
Case study 1 battery [*kWh*]	2 x 13.5	-	50
Case study 2 battery [*kWh*]	50	-	50
Case study 3 battery [*kWh*]	-	-	50
EV battery charge schedule [hours]	From 2 to 7	When necessary	-

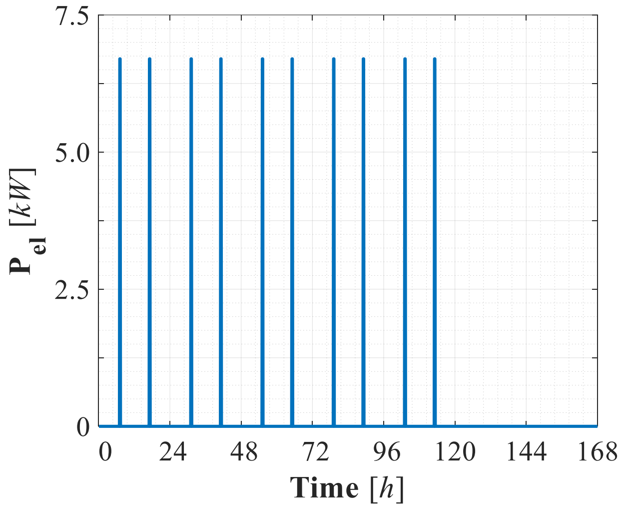

Fig. 7.6. EV power consumption.

Finally, each simulation starts on 0:00 of January 1st and ends at 24:00 of December 31st. Dynamic simulations are carried out through DETECt 2.3 (a 7.5 minutes time step is assumed) by taking into account hourly Meteonorm data files. In particular, simulations refer to the weather zone of Naples (Italy), being the heating and cooling degree days (HDD and CDD) equal to 1479 and 727 Kd, and the incident solar radiation equal to 1529 kWh/m²y.

It is worth noting that the office and house buildings selected for the case study are typical buildings for the considered country (Italy). In particular, their thermophysical properties are selected according to the EU requirements concerning energy performance of buildings toward the NZEB target [161]. In this regard, the house typology represents the largest number of significant experience of NZEB designs and constructions, especially in case of new houses, in the Mediterranean climate. In addition, new houses are expected to be construct in residential neighborhoods (far from the city center), while office buildings (mainly represented by high-rise buildings, especially if new) are and will be mostly located in the city center or in business neighborhoods [163]. Thus, current parking and daily driving patterns of Italian (and European) car drivers seem to be consistent with current models of electric vehicles, whose uptake appears to be promising for the coming years [283]. Finally, both buildings operating parameters are consistent with their usage, while their features are suitable for PV installation and for the access to a charging station for their own parking lots (particularly necessary at home for every electric driver).

7.4.1. Energy and economic performance indexes of the proposed V2B² systems

With the aim to compare the performance of the proposed layouts, Case 1, Case 2 and Case 3, to the reference Case 0 one, from the energy and economic point of views, several parameters / indexes are calculated.

As all energy users of the considered system layouts are supplied with electricity, the yearly Energy Consumption (*EC*) is easily calculated as:

$$EC = \sum_{t=1}^{Y} \left(P_{Grid \to House} + P_{Grid \to Office} + P_{Grid \to EV} \right) \tag{7.7}$$

where P_{grid} is the electricity required from the power grid by the House, Office, and EV loads, i.e. $P_{grid \to house}$, $P_{grid \to Office}$, and $P_{grid \to EV}$. *EC* represents the electricity delivered from the grid to the main users of the investigated V2B² systems.

Given *EC*, the yearly Self-Electricity Consumption (*SEC*) is the net energy between PV system electricity production, due to the PV panels (E_{PV}), and the energy delivered from the grid (*EC*). As a result, the Energy Saving (*ES*) and the Relative Energy Saving (*RES*) of each proposed layout (Case 1, Case 2, Case 3, namely Case X) with respect to Case 0 are calculated as:

$$\begin{aligned} ES &= EC_{Case\ 0} - EC_{Case\ X} \\ RES &= 1 - \frac{EC_{Case\ X}}{EC_{Case\ 0}} \end{aligned} \tag{7.8}$$

To evaluate the economic profitability of the investigated V2B² system layouts, a detailed economic analysis is included in the simulation model. With respect to the reference system, (V2B, Case 0), which only includes the electric vehicle, the V2B² systems (Case 1, Case 2 and Case 3) include the electric vehicle and combine technologies for power production (PV field) and electric storage (HSB). It also worth noting that with respect to Case 0, for V2B² cases a higher capacity EV battery is taken into account, being the systems conceived to transport electricity by the vehicle from a building to another. Therefore, the capital costs of the V2B² layouts include the costs of PV field and HSB, as well as the additional cost of the EVB calculated with the respect to the one of the reference system Case 0.

Therefore, to calculate the total investment cost (*IC*) of the V2B² system layouts, the cost of PV solar field, HSB / EVB batteries, and inverter / regulator are taken into account by means of capital cost functions, as detailed hereinafter.

The PV panels and inverted capital cost is calculated as a function of their specific cost ($IC_{PV,sp}$) per rated power (P_{PV}), as:

$$IC_{PV} = IC_{PV,sp} \cdot P_{PV} \tag{7.9}$$

The capital cost of the batteries (HSB and EVB, $C_{HSB,EVB}$) is calculated as a function of the specific cost ($IC_{BAT,sp}$) per kWh of energy capacity ($Cap_{HSB,EVB}$), as:

$$IC_{HSB,EVB} = IC_{BAT,sp} \cdot Cap_{HSB,EVB} \tag{7.10}$$

The capital cost of the inverter (IC_{inv}), is calculated as a function of its specific cost ($IC_{inv,sp}$) per peak power (P_{PV}, kW) of PV panels [284], as:

$$IC_{inv} = IC_{inv,sp} \cdot P_{PV} \tag{7.11}$$

The economic yearly saving of the V2B² system takes into account the economic gains and operating costs calculated with respect to those of V2B reference system (Case 0), by considering time-dependent tariffs applied to the electricity exchanged with the national grid.

The net operating costs depends on the amount of electricity purchased from and sold to the national grid. The electricity purchased from the national grid ($E_{grid\rightarrow house}$, $E_{grid\rightarrow Office}$ and $E_{grid\rightarrow EV}$) is calculated by considering the hourly purchase price, $j_{el.grid}$, namely Purchase Grid Electricity, *PGE*. Similarly, the economic incomes due to the Feed to Grid Electricity, $FGE_{PV,}$ due to the energy exported to the national grid, $E_{PV\rightarrow grid}$, are calculated by taking into account a time-dependent tariffs, the hourly National Single Price, $j_{el.NSP}$ (NSP, the feed in tariff per electricity). It is worth noting that the amount of electricity sold to the grid represents an avoided cost due to the generated PV Electricity Self-Consumed (E_{PV} - $E_{PV\rightarrow grid}$), ESC_{PV}.

The system Operating Costs, *OC*, are due to the amount of electricity purchased by ($E_{grid\rightarrow house}$ + $E_{grid\rightarrow Office}$ + $E_{grid\rightarrow EV}$) and sold ($E_{PV\rightarrow grid}$) to the grid, plus a yearly Maintenance cost, *M*, for the PV field. *OC* is calculated as:

$$OC = PGE - FGE_{PV} + M = \left[(E_{House} + E_{Office} + E_{EV}) \cdot j_{el,grid} - ESC_{PV} \right] - FGE_{PV} + M \tag{7.12}$$

The yearly Economic Savings (*EcS*) and the Relative Economic Saving (*REcS*) achieved by the V2B² system with respect to the reference V2B one, are calculated as:

$$EcS = OC_{Case\ 0} - OC_{Case\ X}$$
$$REcS = 1 - \frac{OC_{Case\ X}}{OC_{Case\ 0}} \tag{7.13}$$

The economic analysis is performed through the calculation of several indexes. The first one is the Simple PayBack (*SPB*) index, which represents the length of time required to recover the cost of the investment, calculated as:

$$SPB = \frac{IC}{\left(\mathrm{OC}_{Case\ 0} - \mathrm{OC}_{Case\ X}\right)_{\mathrm{year}}} \tag{7.14}$$

where *IC* is the investment capital costs of the V2B² layouts (Case 1, Case 2 and Case 3).

The second one is the Net Present Value (*NPV*) index, useful to assess the profitability of the investment. The *NPV* is calculated as the difference between the present value of cash inflows and the present value of cash outflows over a period of time (~20 years), as:

$$NPV = \sum_{t=1}^{N} \frac{EcS}{(1+r)^t} - IC \tag{7.15}$$

Where r is the discount rate (equal to 5%). Note that given the *NPV* it is possible to assess the Internal Rate of Return (*IRR*), being the discount rate that makes the *NPV* equal to zero.

Finally, the Profitability Index (*PI*), useful to assess the profitability of the investment, as well as to rank the proposed layouts by quantifying the amount of value created per unit of investment, is calculated as:

$$PI = \frac{\sum_{t=1}^{N} \frac{EcS}{(1+r)^t}}{IC} \tag{7.16}$$

The *PI* is assessed by considering a discount rate equal to 5% and a time horizon of 20 years.

For the proposed case study scenarios, the economic analysis is performed by taking into account a specific cost per kWh of energy capacity, $PI_{BAT,sp}$, of the batteries (HSB and EVB) equal to 260 €/kWh [284], whereas the specific costs per rated power of PV panels and the inverter, $IC_{PV,sp}$, are set to 1000 €/kW (500 €/kW considering a 50% reduction of capital investment for PV panels, according to the Italian regulation in case of building renovations), respectively. Moreover, a hourly purchase price, $j_{el,grid}$, for the purchase of electricity from national grid (averagely equal to 0.20 €/kWh for the House and 0.18 €/kWh for the Office) and a time-dependent tariff for the feed in tariff per electricity, $j_{el,NSP}$ (known as hourly National Single Price,NSP, shown in Fig. 7.7) are taken into account.

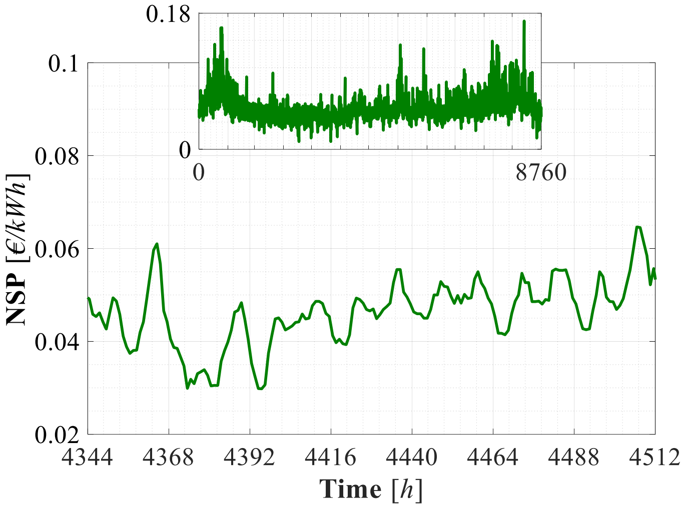

Fig. 7.7. National Single Price (NSP) of electricity – July 1st -7th.

7.4.2. Load and grid matching indexes

In order to analyse the matching electricity performance of the whole system, V2B², consisting of House + EV + Office, as a general zero energy balance, two relevant indexes are calculated with the aim to evaluate the self-consumption of the on-site renewable energy production and the on-site matching capability [169]. Such indexes describe the temporal matching between the building (or the whole V2B² system) electrical load and the PV generation, and between the fluctuation of the energy exchange of the system with the grid. Such indexes provide an insight on the ability of the building to work in synergy with the grid [169]. The use of the electric vehicle battery (EVB), together with the one installed at home (HSB), aims to enhance the matching between load and generation, reducing the necessity of the House and Office buildings to rely on the grid, increasing the overall self-consumption.

Such indexes are commonly used in the NZEB evaluation and comparison. The first index measures the degree of the utilisation of on-site energy generation related to the energy demand, and it is known as load matching index, f_{load}, varying between 0 and 1 (or 100%). The surplus of energy production (neither consumed on-site or stored in the batteries), exceeding the load, is considered as part of the grid electricity, thus the maximum f_{load} becomes 1 (or 100%). Obviously, the value of the index highly depends on the evaluation period. The higher f_{load} over the considered time interval, the better is the coincidence between load and on-site generation.

For the investigated system, f_{load} is calculated as respect to the whole system V2B² (House + EV + Office), $f_{load,V2B^2}$, as well as only to the House, $f_{load,House}$, and Office, $f_{load,Office}$, buildings, such as:

$$
\begin{aligned}
f_{load,V2H^2} &= \frac{1}{N}\cdot\sum min\left[1,\frac{E_{PV}(t)+E_{HSB\rightarrow House}(t)+E_{HSB\rightarrow EVB}(t)+E_{EVB\rightarrow House}(t)+E_{EVB\rightarrow Office}(t)}{E_{House}(t)+E_{Office}(t)+E_{EV}(t)}\right] \\
f_{load,House} &= \frac{1}{N}\cdot\sum min\left[1,\frac{E_{PV}(t)+E_{HSB\rightarrow House}(t)+E_{EVB\rightarrow House}(t)}{E_{House}(t)}\right] \\
f_{load,Office} &= \frac{1}{N}\cdot\sum min\left[1,\frac{E_{PV}(t)+E_{EVB\rightarrow Office}(t)}{E_{Office}(t)}\right]
\end{aligned}
\tag{7.17}
$$

Where N is the number of time intervals, t, in the evaluation period (i.e. day, hour), E_{PV} is the energy produced by the PV systems, $E_{HSB\rightarrow House}$ is the energy transferred from the house battery HSB to the House to balance its demand, $E_{HSB\rightarrow EVB}$ is the energy transferred from HSB to the electric vehicle battery EVB, $E_{EVB\rightarrow House}$ and $E_{EVB\rightarrow Office}$ are energy transferred from the EVB to the House and Office demands, E_{House}, E_{Office} and E_{EV} are the energy demands of House, Office and EV, respectively.

The second index measures the exchange of energy between the whole system and the grid, calculated by knowing the import/export building profile, and it is called grid interaction index, f_{grid}. It represents the variability of the normalized net export energy flow, and it is calculated as the ratio between net export from a building compared to the maximum/minimum within an annual cycle. The net export from the whole system (or a building) is defined as the difference between exported and delivered energy within a given time interval (e.g. monthly). A positive value of f_{grid} describes a net exporting system, whereas low values implies almost constant export or import.

For the investigated system, f_{grid} is calculated with respect to the whole system V2B² (House + EV + Office), $f_{grid,V2B^2}$, as well as only to the, House, $f_{grid,House}$, and Office, $f_{grid,Office}$, buildings, such as:

$$
\begin{aligned}
f_{grid,V2H^2} &= STD\left[\frac{E_{PV\rightarrow Grid}(t)-E_{Grid\rightarrow House}(t)-E_{Grid\rightarrow Office}(t)-E_{Grid\rightarrow EV}(t)}{\left|\max\left[E_{PV\rightarrow Grid}(t^y)-E_{Grid\rightarrow House}(t^y)-E_{Grid\rightarrow Office}(t^y)-E_{Grid\rightarrow EV}(t^y)\right]\right|}\right] \\
f_{grid,House} &= STD\left[\frac{E_{PV\rightarrow Grid}(t)-E_{Grid\rightarrow House}(t)}{\left|\max\left[E_{PV\rightarrow Grid}(t^y)-E_{Grid\rightarrow House}(t^y)\right]\right|}\right] \\
f_{grid,Office} &= STD\left[\frac{E_{PV\rightarrow Grid}(t)-E_{Grid\rightarrow Office}(t)}{\left|\max\left[E_{PV\rightarrow Grid}(t^y)-E_{Grid\rightarrow Office}(t^y)\right]\right|}\right]
\end{aligned}
\tag{7.18}
$$

Where t^y refers to the yearly interval, and, in the considered time interval (t or t^y), $E_{PV\rightarrow Grid}$ is the exported energy from PV to the grid (electricity produced in excess with respect to the users demands and battery capacities), $E_{Grid\rightarrow House}$, $E_{Grid\rightarrow Office}$, $E_{Grid\rightarrow EV}$ are the energies delivered from the grid to the House, Office, and EV to balance their demands.

7.5. Result and discussion

7.5.1. Generation and loads

Simulation results, related to the weather zone of Naples (South-Italy), are here presented and discussed in order to evaluate the performance of the proposed V2B² concept, by taking into account the energy demands of both the buildings (House and Office), the electric vehicle (EV) and the renewable energy availability (PV installed on the roof of the house building and on the South facing façade of the office space).

The dynamic yearly profiles of electric needs for equipment, heating, and cooling for the House and Office buildings are shown in Fig. 7.8.

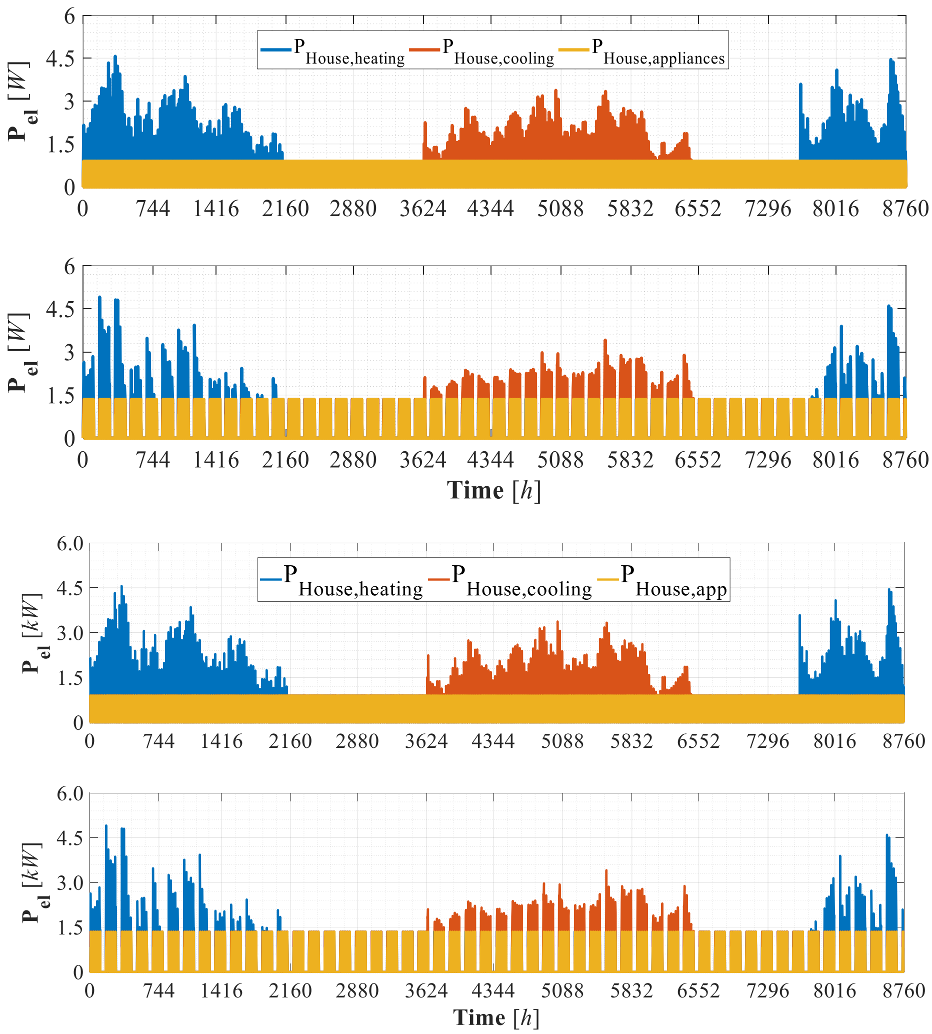

Fig. 7.8. House (top) and Office (bottom) building electrical yearly demand.

Such figure clearly shows that the House and Office peak heating and cooling loads are almost similar, whereas a higher demand for appliances is obtained by the office space. For both the buildings, the simulated electric heating peak loads are higher than the cooling ones. Note that during the weekend no loads are observed in the Office case. Yearly electrical heating, cooling and appliance peak loads and demands for each user are reported in Table 7.4. House heating and cooling electrical needs are about 5.0 and 3.4 kWh_{el}/m^2, whereas Office heating and cooling electrical needs are equal to 2.4 and 4.3 kWh_{el}/m^2.

Table 7.4. Yearly electrical heating, cooling and appliance peak loads and demands.

User	$P_{heating,max}$ [kW]	$P_{cooling,max}$ [kW]	$P_{appliances,max}$ [kW]	**Total peak** [kW]	$E_{heating}$ [MWh/y]	$E_{cooling}$ [MWh/y]	$E_{appliances}$ [MWh/y]	**Total energy** [MWh/y]
House	3.67	2.48	0.90	4.56	0.64	0.44	2.00	3.08
Office	3.56	2.06	1.35	4.37	0.30	0.55	2.73	3.58
EV	-	-	-	6.70	-	-	-	6.99

Yearly total electricity needs (due to heating, cooling, and household appliances) are equal to 3.08 and 3.58 MWh/y, respectively for the House and the Office. The third key user of the proposed systems is the EV, with a peak demand of 6.7 kW_{el}, Fig. 7.6 (@ an average speed of about 50 km/h, Fig. 7.4) and an yearly energy consumption of 6.99 MWh/y, corresponding to about 51.2% of the whole system energy demand (equal to about 13.65 MWh/y). Fig. 7.9 shows, for a sample winter week-day, the typical profile of the total electrical demands due to the three users of the V2B² system (i.e. P_{House}, P_{Office} and P_{EV}). Here, an almost continuous electrical load required by the buildings can be noted, whereas the electricity from grid to the EVB occurs, as scheduled, in the early morning ($P_{Grid\rightarrow EV}$); it is worth noting that $P_{Grid\rightarrow EV}$ corresponds to the EV electricity from power grid of the reference Case 0.

Depending on the considered case study, PV panels are installed on the roof (30° tilted) of the House building (Case 1 and Case 2) and on the South façade of the Office building (Case 3). Although both the solar fields consist of the same number of solar panels (same caption area, 28 m²), the amount of incident global solar radiation over the whole year considerably changes due to the different PV tilts, as clearly reported in Fig. 7.10.

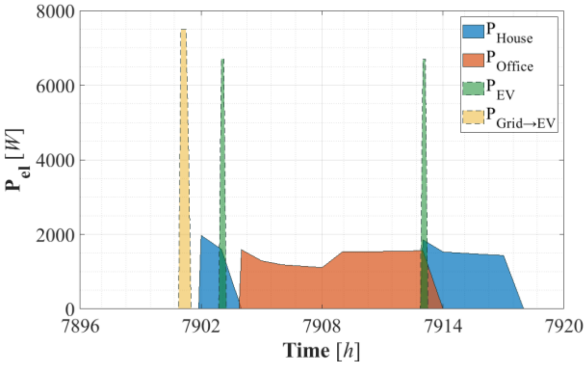

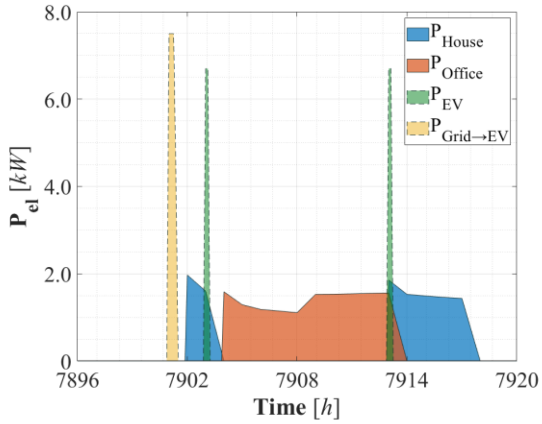

Fig. 7.9. Electrical daily demands of House, Office, EV and power grid supply to EV– winter sample day (November 25th).

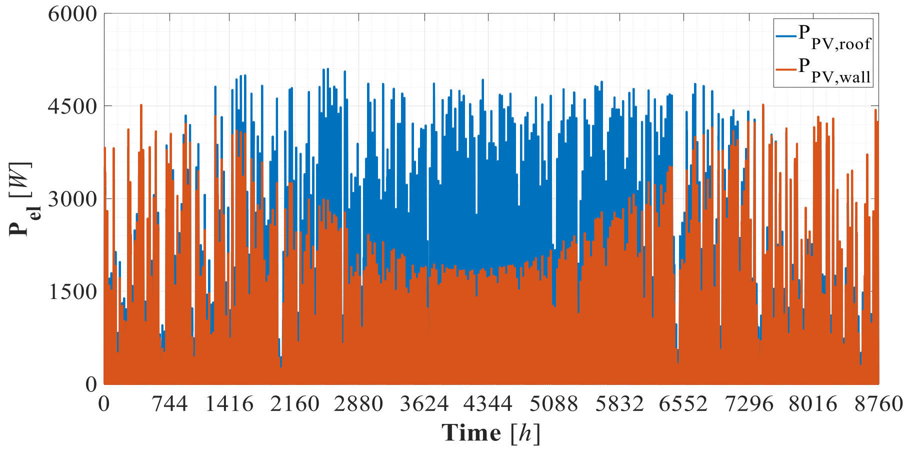

Fig. 7.10. PV yearly power production – PV integrated on the tilted roof of the House (Cases 1 and 2) and PV integrated on the vertical wall of the Office (Case 3).

The solar exploitation is maximized when the PV panels are on the tilted roof, at the latitude of Naples (40.85°), especially during the summer season, when the PV power production surpasses the House and Office loads.

Table 7.5. Monthly electrical energy needs and PV productions.

	Jan	Feb	Mar	Apr	May	Jun [kWh]	Jul	Aug	Sep	Oct	Nov	Dec
E_{House}	366.4	291.2	231.3	164.6	170.1	248.8	320.3	311.6	224.3	170.1	228.6	351.5
E_{Office}	356.9	268.3	240.2	219.4	240.2	306.2	390.5	426.2	323.1	240.2	253.4	312.8
E_{EV}	77.1	67.0	73.7	70.4	77.1	70.4	73.7	77.1	67.0	77.1	73.7	70.4
Total	*800.4*	*626.4*	*545.2*	*454.3*	*487.4*	*625.3*	*784.5*	*814.8*	*614.4*	*487.4*	*555.6*	*734.6*
$E_{PV,roof}$	353.5	427.7	670.5	791.0	890.7	946.5	983.5	927.0	761.0	675.8	390.2	359.2
$E_{PV,wall}$	338.9	363.2	496.0	459.8	435.7	406.7	443.0	500.3	516.7	576.6	358.0	363.4

The monthly matching of overall electricity demands of each user (House, Office and EV) and on-site generation for the PV fields (PV installed on the roof and on the façade) under investigation is reported in Table 7.5 and Fig. 7.11.

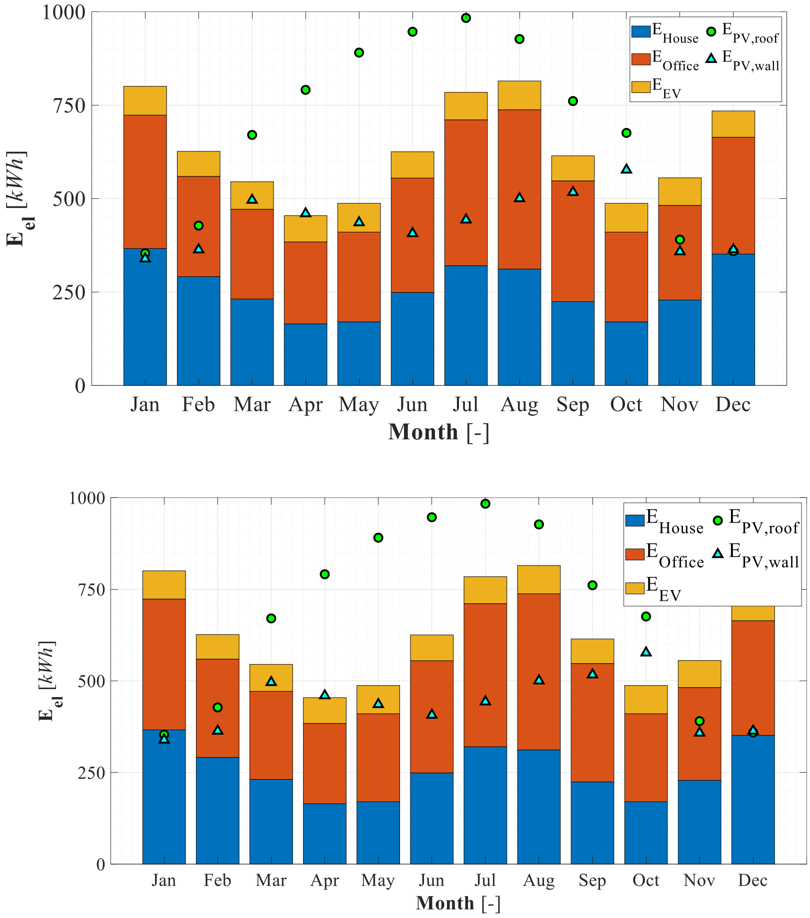

Fig. 7.11. House and office buildings electrical monthly energy consumptions and PV production of roof and wall mounted fields.

It is interesting to analyse the cumulative annual PV electricity generation and system load profiles, as reported in Fig. 7.12. The electricity generation is always lower than the total load in case of solar field installed on the wall (Case 3), whereas for the roof installation (Case 1 and Case 2), the cumulate generation surpasses the load after April. Note that the calculated yearly PV electricity production of the solar field installed on the roof, $E_{PV,roof}$, is equal to 5.18 MWh/y (peak load = 5.10 kW), whilst for the solar field installed on the façade, $E_{PV,wall}$ it is equal to 5.26 MWh/y (peak load = 4.5 kW).

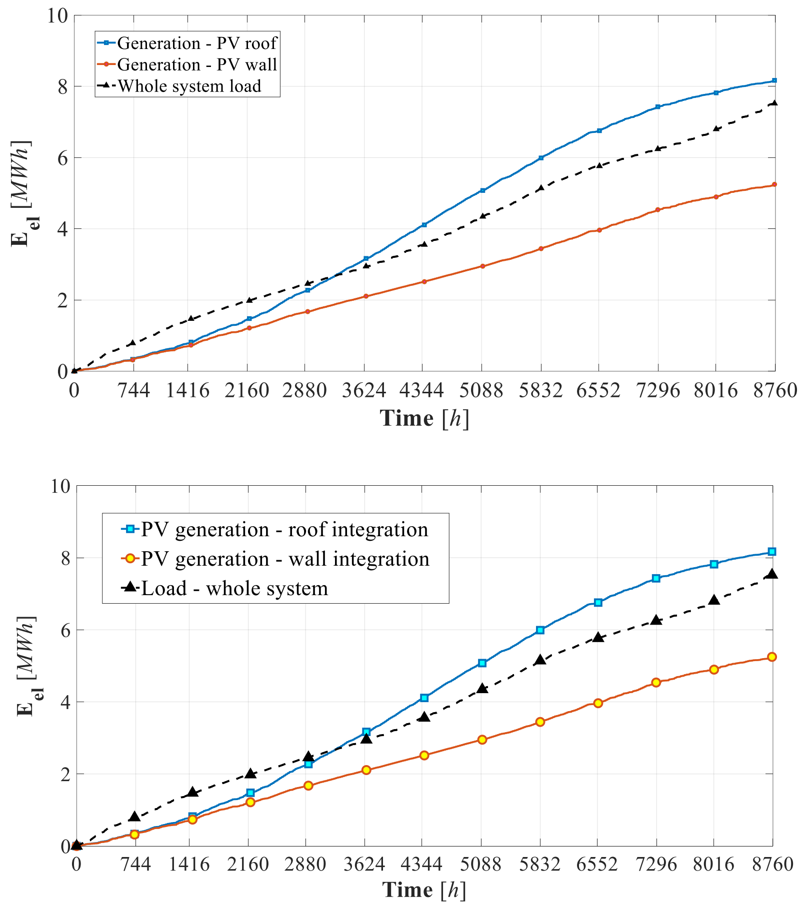

Fig. 7.12. Cumulative annual electricity generation and loads profiles of simulated cases.

7.5.2. Energy analysis

Given the electricity loads and generations of the proposed system, it is of high interest to investigate the possibility to store as much energy as possible, in order to better match renewable production with demand and to reduce the need of electricity from the national power grid. To this aim, the presented case studies include different storage and delivery strategies. To better understand the electrical behaviour of the investigated system layouts, the time histories of the main electricity flows are reported for four summer sample days in Fig. 7.13 for Case 1, in Fig. 7.14 for Case 2 and in Fig. 7.16 for Case 3. The selected sample days (Friday July 27th – Monday 30th) include weekdays and weekend days.

The top graphs of Fig. 7.13, Fig. 7.14 and Fig. 7.16 shows the time histories of:

i) PV power production (P_{PV}) together with the surplus of PV electricity (equal to max[0, (P_{PV} – P_{House})] for Case 1 and 2, and to max[0, (P_{PV} – P_{Office})] for Case 3), delivered to the house battery ($P_{PV\rightarrow HSB}$), the EV battery ($P_{PV\rightarrow EV}$), the power grid ($P_{PV\rightarrow Grid}$);

ii) the electrical flows required to balance the EV demand by the power grid (charged at the house, $P_{Grid\rightarrow EV,House}$, and charged at the office, $P_{Grid\rightarrow EV,Office}$), and the electrical flow to the HSB from the

EVB ($P_{HSB \rightarrow EVB}$). Note that $P_{Grid \rightarrow EV}$ is considered as the power production delivered to the EV, which is previously provided by the grid and stored in a dedicated battery;

iii) the state of charge of the HSB (SOC_{HSB}) and the EVB one (SOC_{EVB}), together with the safety level (minimum SOC) of EV charge ($SOC_{safe\ level}$).

The middle graphs of Fig. 7.13, Fig. 7.14 and Fig. 7.16 shows the time histories of:

i) PV power production (P_{PV}) and House demand (P_{House}), together with the electrical flows required to balance the House demand by PV ($P_{PV \rightarrow House}$), by EV battery ($P_{EVB \rightarrow House}$), by HSB ($P_{HSB \rightarrow House}$), and by Grid ($P_{Grid \rightarrow House}$).

The bottom graphs of Fig. 7.13, Fig. 7.14 and Fig. 7.16 shows the time histories of:

i) PV power production (P_{PV}) and Office demand (P_{Office}), together with the electrical flows required to balance the Office demand by PV ($P_{PV \rightarrow Office}$), by EV battery ($P_{EVB \rightarrow Office}$), and by the Grid ($P_{Grid \rightarrow Office}$).

For the simulated Case 1, see Fig. 7.13 top, at the beginning of the first weekday, when the sun rises and the solar radiation reaches the PV panels, the buildings loads is still null and PV production is delivered to the House battery ($P_{PV \rightarrow HSB}$) with a consequent increase of the SOC_{HSB}. When the building load becomes positive (P_{House} at 7:00 a.m., Fig. 7.13 middle) the PV generation of electricity is firstly delivered to the house load ($P_{PV \rightarrow House}$), as shown in Fig. 7.13 middle. As the PV generation is not sufficient to balance the House load, electricity from the HSB is delivered to the House ($P_{HSB \rightarrow House}$), causing a slight decrease of the SOC_{HSB}. At the same time, the EV battery is charged by the Grid ($P_{PV \rightarrow EV}$, Fig. 7.13 top), increasing the SOC_{EVB} to the charge level necessary for the EV motion, as shown in Fig. 7.13 top. In fact, when P_{EV} is required and provided by the Grid (both in the early morning at the House, $P_{Grid \rightarrow EV,house}$, and in the afternoon at the Office, $P_{Grid \rightarrow EV,office}$), the SOC_{EVB} returns to the level of charge occurring before the charge. Just after the EV leaves, the House load becomes zero (P_{House}, Fig. 7.13 middle) as all occupants leave it. Thus, all the PV panels generation is supplied to the HSB, until its state of charge level, SOC_{HSB} reaches the maximum value (i.e. 1 or 100%), as shown in Fig. 7.13 top. Afterward, PV panels power production is fed to the Grid ($P_{PV \rightarrow Grid}$). With the House load (P_{House}) occurring in the afternoon, when occupants and the EV comes back home, the House load is firstly balanced by the PV panels generation ($P_{PV \rightarrow House}$), then by the HSB ($P_{HSB \rightarrow House}$), and at last by the Grid ($P_{Grid \rightarrow House}$), as shown in Fig. 7.13 middle. The Office is totally balanced by the Grid ($P_{Grid \rightarrow Office}$), since the EVB is not sufficiently charged (no renewable energy is stored).

As the weekend starts, referring to the second day reported in these graphs, the EV is stationary at the House and connected to the building management system, therefore the surplus of PV panels generation is firstly delivered to the HSB ($P_{PV \rightarrow HSB}$), and when the SOC_{HSB} reaches the maximum level, it is supplied to the EVB ($P_{PV\rightarrow EVB}$), increasing the SOC_{EVB}, Fig. 7.13 top, to a level sufficient to avoid the need of the Grid on Monday morning (the last plotted day), when $P_{Grid\rightarrow EV,House}$ and $P_{Grid\rightarrow EV,Office}$ are null. The same before discussed behaviour occurs in both the weekend days, where thanks to the possibility to charge the EVB by PV panels generation, the Grid is never used to balance the House load. In fact, as shown in Fig. 7.13 middle, the House load (P_{House}) is firstly balanced by the PV generation ($P_{PV\rightarrow House}$), then by the HSB ($P_{HSB\rightarrow House}$, causing its discharging), then by the EVB ($P_{EVB\rightarrow House}$, causing its discharging) and at last by the Grid ($P_{Grid\rightarrow House}$).

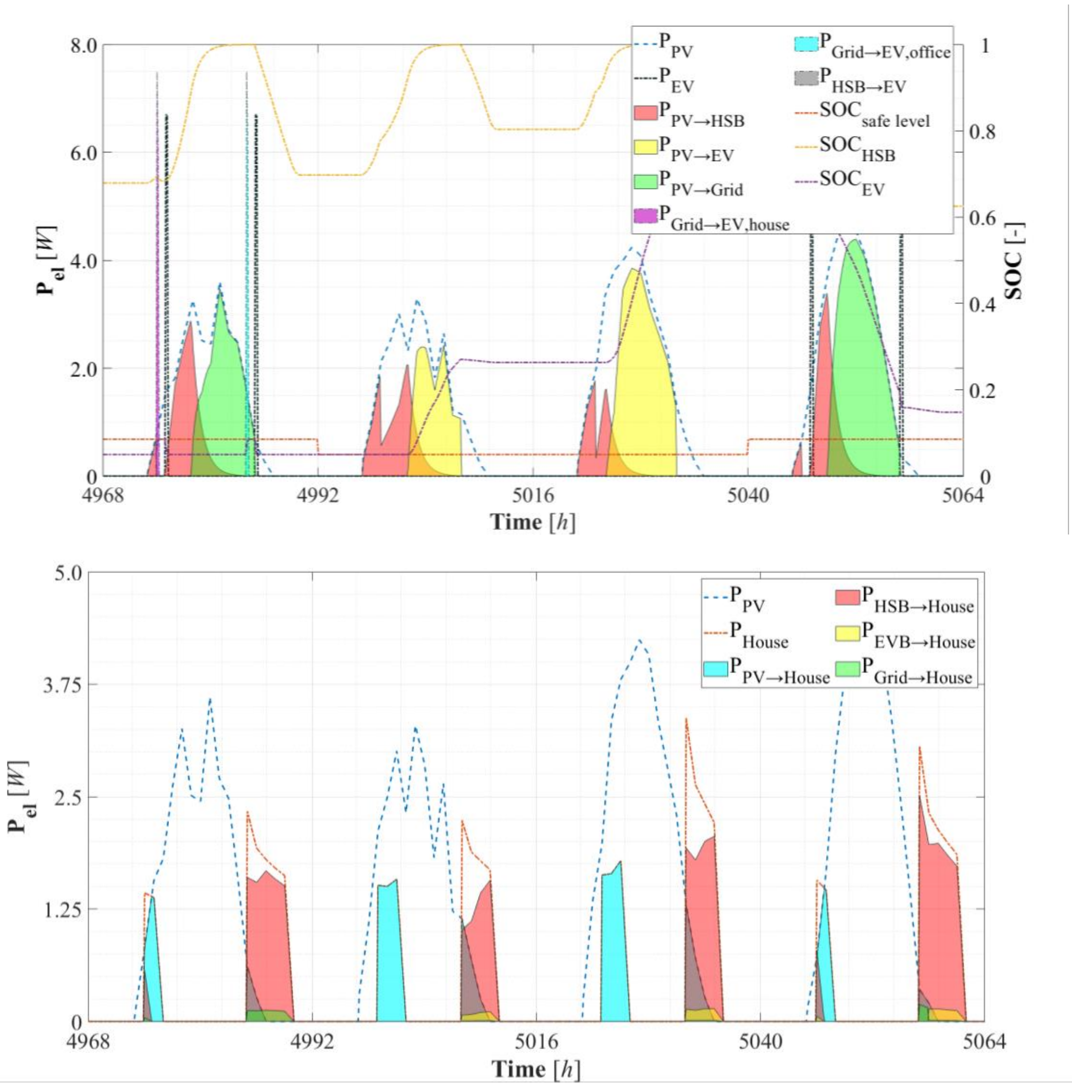

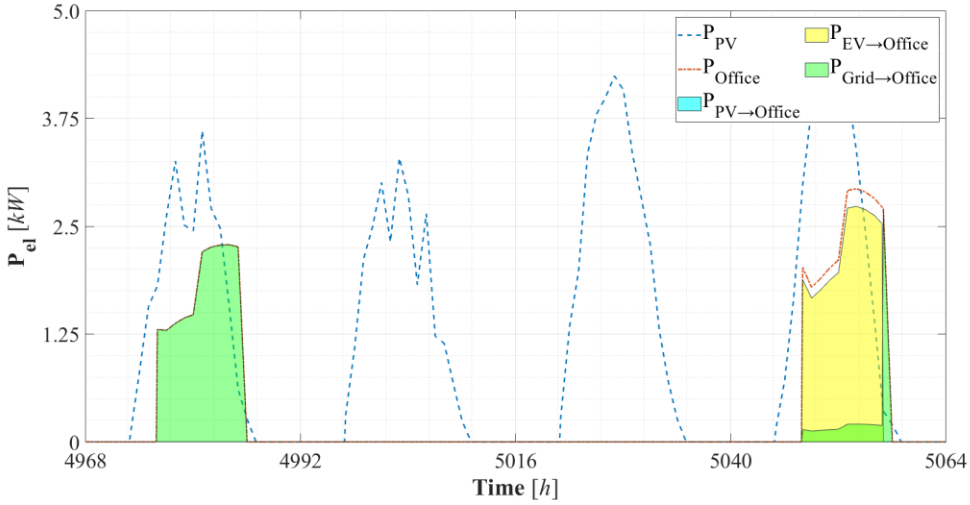

P_PV
P_Office
P_PV→Office
P_EV→Office
P_Grid→Office
P_el [kW]
5.0
3.75
2.5
1.25
0
4968
4992
5016
5040
5064
Time [h]

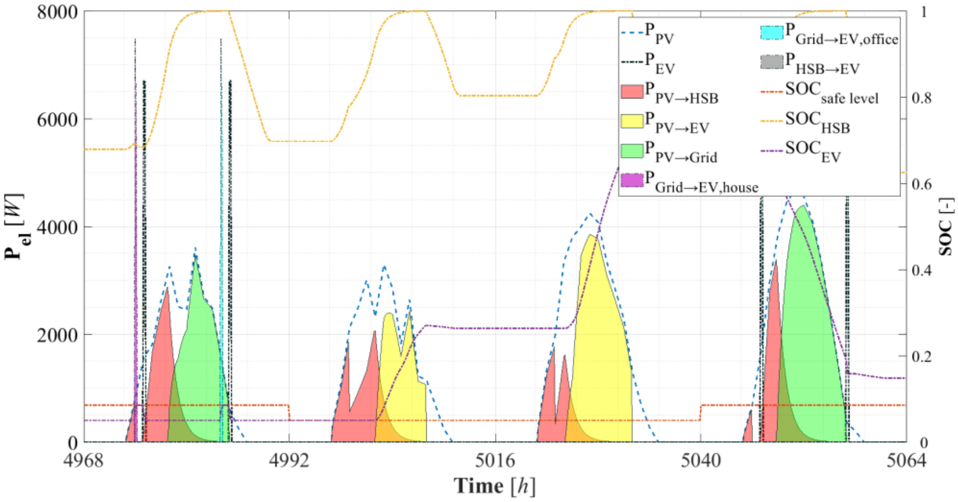

P_PV
P_EV
P_PV→HSB
P_PV→EV
P_PV→Grid
P_Grid→EV,house
P_Grid→EV,office
P_HSB→EV
SOC_safe level
SOC_HSB
SOC_EV
P_el [W]
SOC [-]
8000
6000
4000
2000
0
1
0.8
0.6
0.4
0.2
0
4968
4992
5016
5040
5064
Time [h]

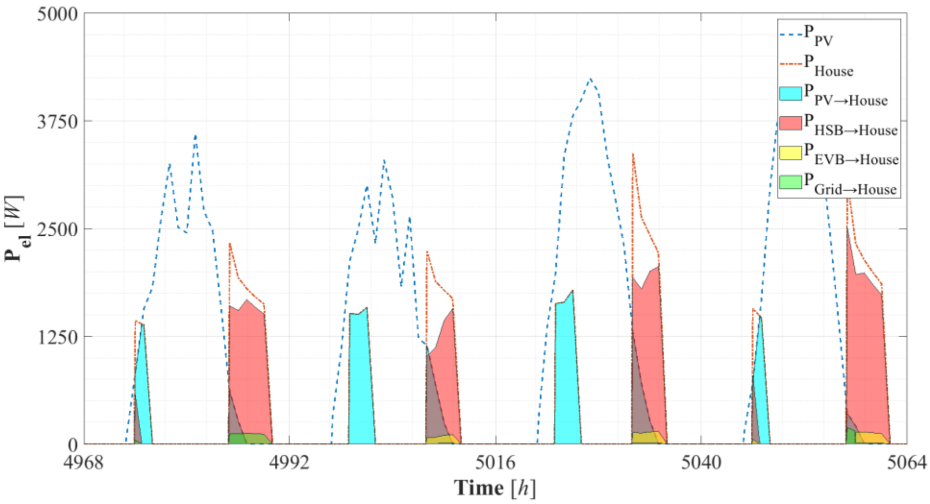

P_PV
P_House
P_PV→House
P_HSB→House
P_EVB→House
P_Grid→House
P_el [W]
5000
3750
2500
1250
0
4968
4992
5016
5040
5064
Time [h]

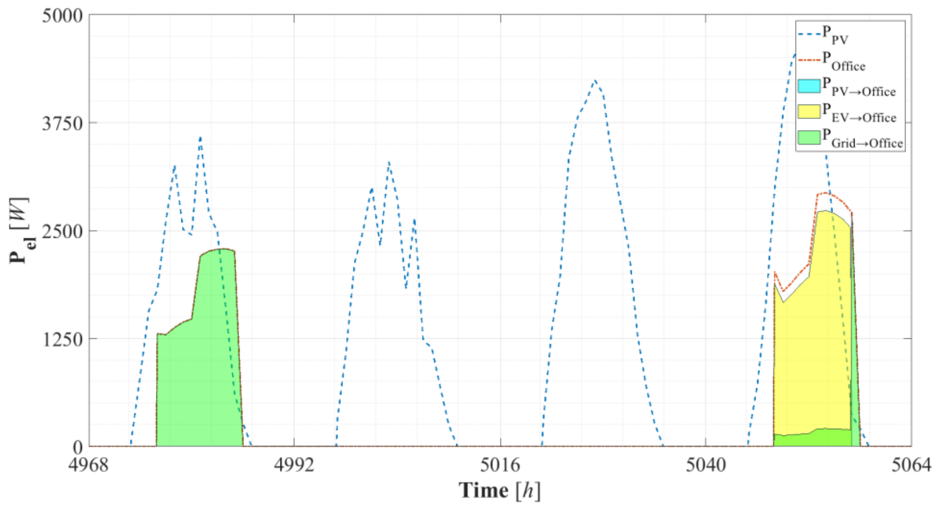

Fig. 7.13. Case 1 - Daily dynamic profiles of system electrical flows and battery state of charge (top of the figure only) – July 27th -30th.

As the SOC_{EVB} reaches a high level, the EVB is capable to provide electricity to the Office load (on Monday), thus the electricity produced by PV panels located on the House roof is transferred to the Office ($P_{EV\rightarrow Office}$), see Fig. 7.13 bottom.

Similar behaviours can be observed for Case 2 and Case 3, Fig. 7.14 and Fig. 7.16, respectively. The main differences with Case 1 consists of the diverse electrical storage strategies. In particular, for Case 2 (i.e. battery swap option), see Fig. 7.14 top, two batteries, namely EBV1 and EVB2, with the same capacity of the EVB of Case 1 are taken into account. Therefore, when the House is unoccupied, all PV generation is delivered to the currently on-site battery (acting as HSB, $P_{PV\rightarrow HSB}$, being the battery double in capacity with respect to the HSB considered in Case 1), there is no electricity exported to the Grid. During the second weekend day (Sunday), when the EVB2 (the on-site battery) is full (SOC_{EV2} equal to 1 or 100%), PV generation is delivered to the battery located on the EV, EVB1 (acting as EVB of Case 1, $P_{PV\rightarrow EVB}$).

In addition, as the electricity exported to the Grid considerably decreases in Case 2 with respect to Case 1, the EV is mostly carrying a battery sufficiently charged to provide electricity to the Office. In fact, in Fig. 7.14 top, the EVB delivers electricity to the Office ($P_{EVB\rightarrow Office}$) to balance its load ($P_{Office}$) also on the first day (i.e. Friday) of plotted ones, reducing the Grid supply ($P_{Grid\rightarrow Office}$) with respect to Case 1 (Fig. 7.13 bottom).

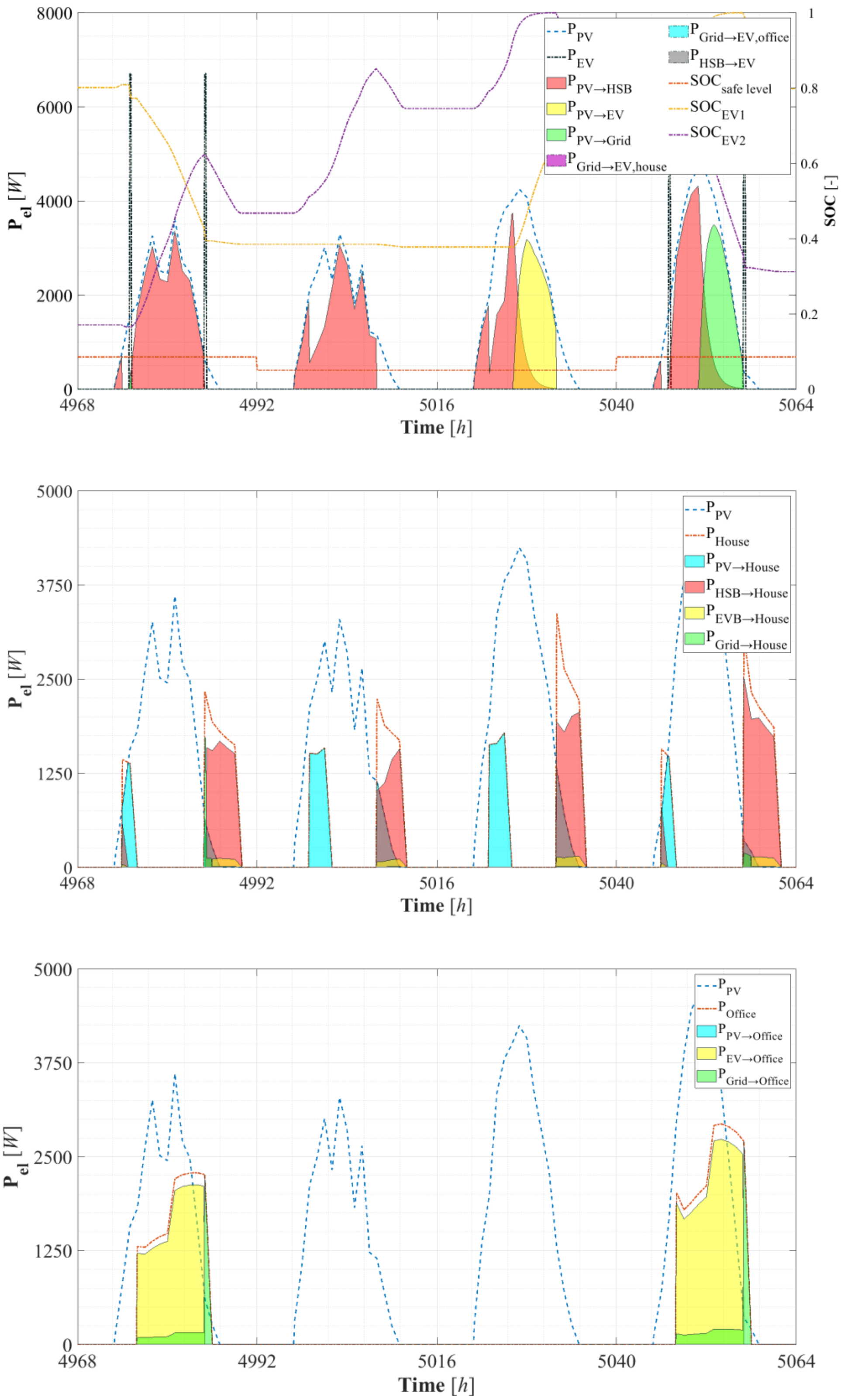

Fig. 7.14. Case 2 - daily dynamic profiles of system electrical flows and battery state of charge (top of the figure only) – July 27th -30th.

It is interesting to note how the swap of the two batteries (Case 2) occurs, as shown in Fig. 7.15. Specifically, before the EV motion, the battery currently on-site, referred to EVB1 (initially on-site located, Fig. 7.14 top), has a SOC level higher than the battery on the EV (i.e. EVB2); thus, the EV position is equal to 1 in Fig. 7.15 (i.e. the EVB2 is on the EV). Therefore, just before the EV motion, the batteries are swapped, the EV position becomes equal to 0 in Fig. 7.15, meaning that the EVB1 becomes the EV battery (acting as EVB) and the EVB2 becomes the on-site battery (acting as a HSB). According to Fig. 7.14 top, EVB2 (still on-site) increases its SOC level through weekend days, whereas SOC_{EVB1} (i.e. EVB1) starts increasing only on Sunday afternoon when the SOC_{EVB2} reaches 1 (or 100%, i.e. EVB2 is full). A second swap of batteries occurs on Monday morning, when the batteries SOC levels are compared again before the morning EV motion, Fig. 7.15.

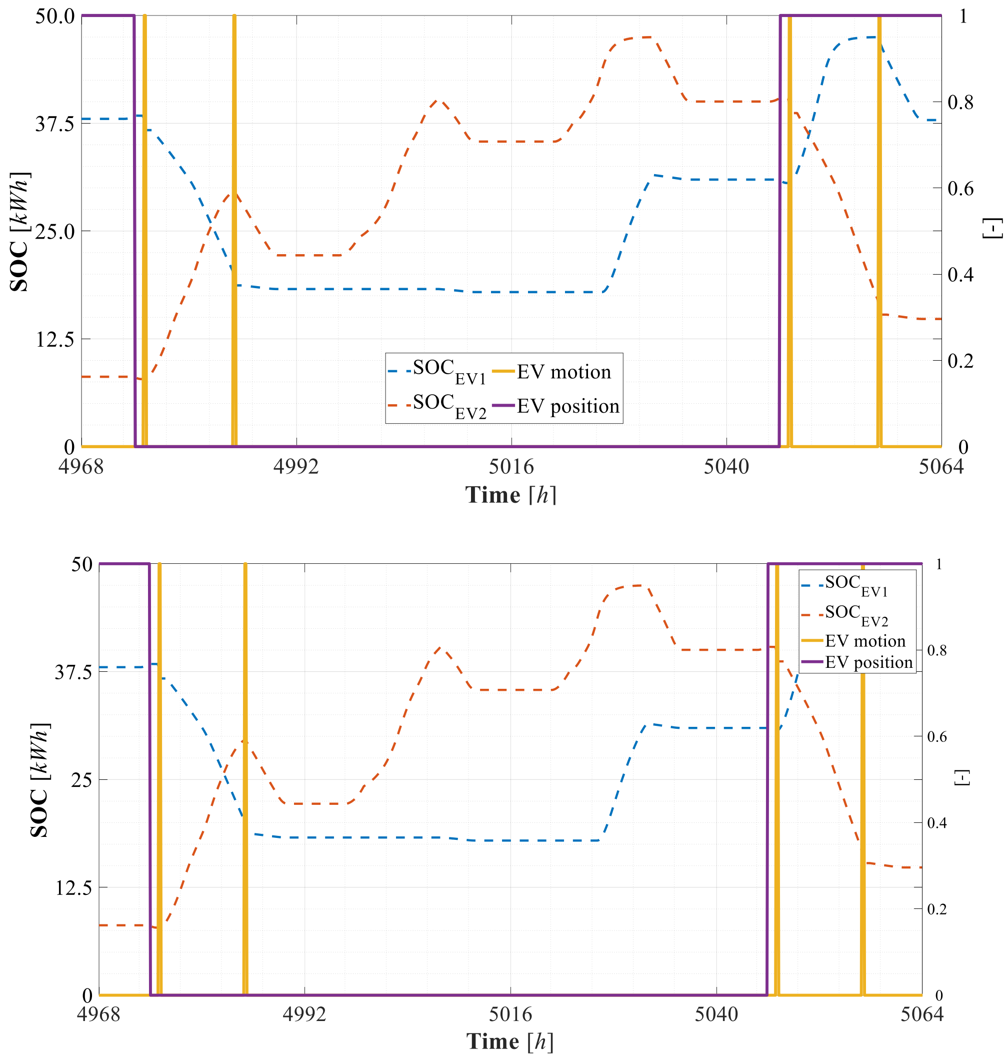

Fig. 7.15. Case 2 – Position of batteries (i.e. 1 means EVB1 on vehicle and vice versa), EV motion, and daily profiles of batteries state of charge – July 27th -30th.

Concerning Case 3 (i.e. no on-site batteries and PV located on the Office South-façade are considered), see Fig. 7.16, in weekdays the PV power production is delivered to the Office to balance its load ($P_{PV\rightarrow Office}$), whereas its surplus is delivered to the EVB ($P_{PV\rightarrow EVB}$) and then to the Grid ($P_{PV\rightarrow Grid}$).

On a weekly basis, the distribution of delivered electricity from all the considered sources (i.e. PV, Grid, EVB and HSB), necessary to balance E_{House}, E_{Office}, and E_{EV} demands are shown in Fig. 7.17, Fig. 7.18, and Fig. 7.19, respectively. Fig. 7.17 clearly shows that to balance the House demand (E_{House}), in Case 1 and Case 2 the PV panels generation ($E_{PV \rightarrow House}$) is significantly exploited, particularly during the summer weeks, when the solar availability increases. For such case studies (Case 1 and Case 2), the HSB also plays a crucial role in balancing the House demand ($E_{HSB \rightarrow House}$) throughout the whole year, whereas a small amount of electricity is provided by the Grid ($E_{Grid \rightarrow House}$) and by the EVB ($E_{EVB \rightarrow House}$). Differently from Case 1 and Case 2 (i.e. PV panels integrated on the House tilted roof), for Case 3 (i.e. PV panels integrated on the Office façade) the major provider is the Grid, which covers the House demand almost completely during the summer weeks. It is worth noting that the tilt angle of solar panels (90°) disadvantaging the summer solar production (i.e. low sun height on south-vertical façades). On the other hand, such tilt angle maximizes the solar exploitation during winter weeks, therefore a significant contribution by the EV to the House demand ($E_{EVB \rightarrow House}$) is achieved. The EVB stores PV generation when plugged at the Office BMS and transfer it (by the EV) to the House.

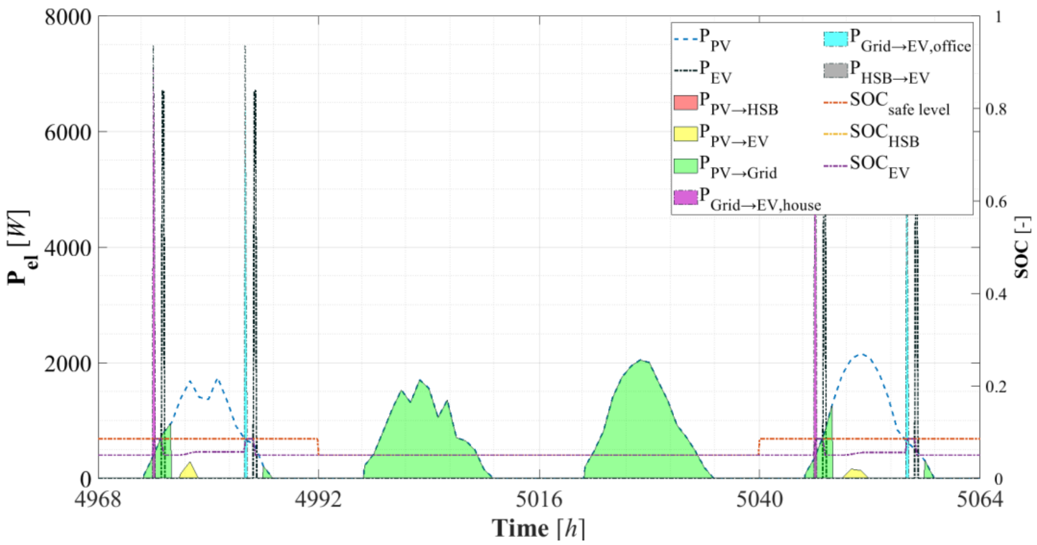

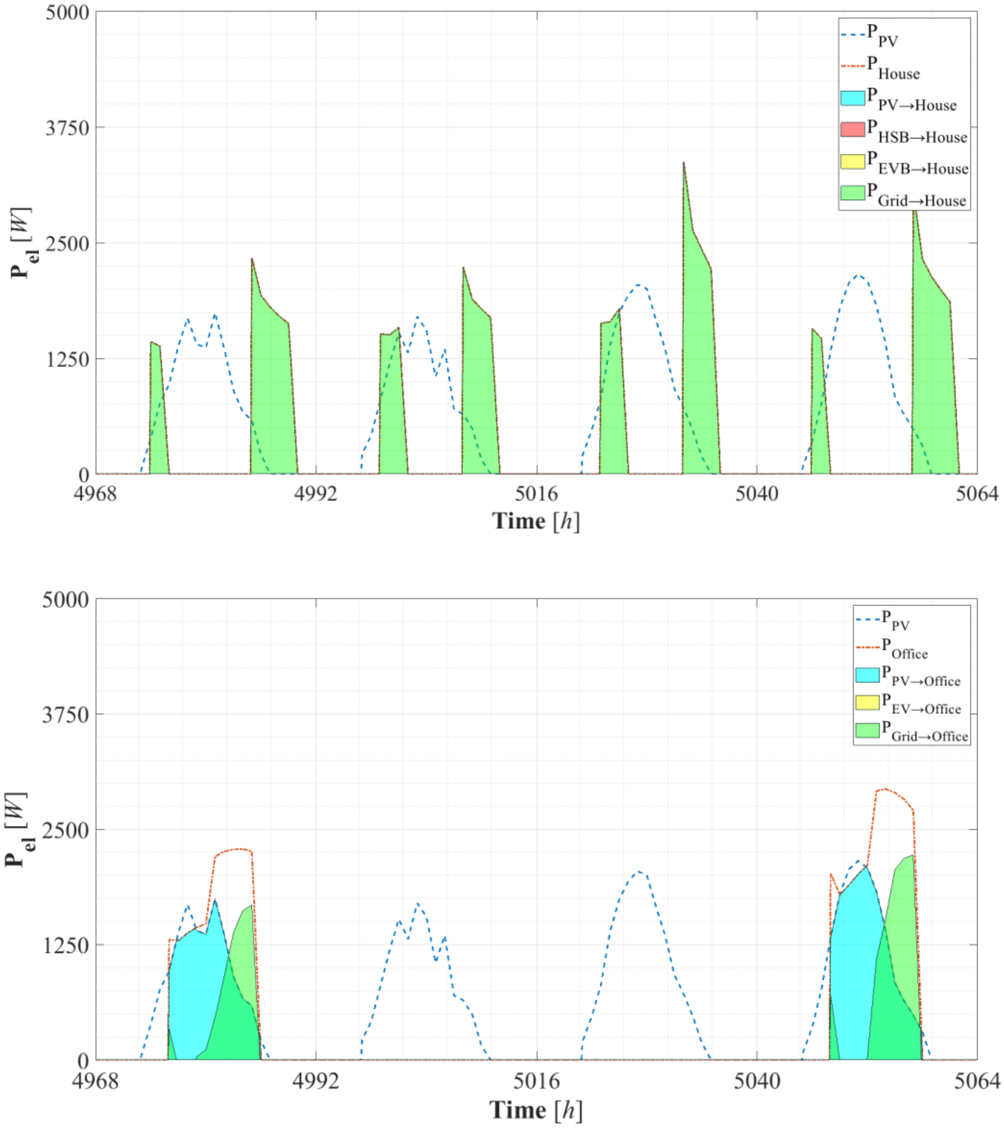

Fig. 7.16. Case 3 - daily dynamic profiles of system electrical flows and battery state of charge (top of the figure only) – July 27th - 30th.

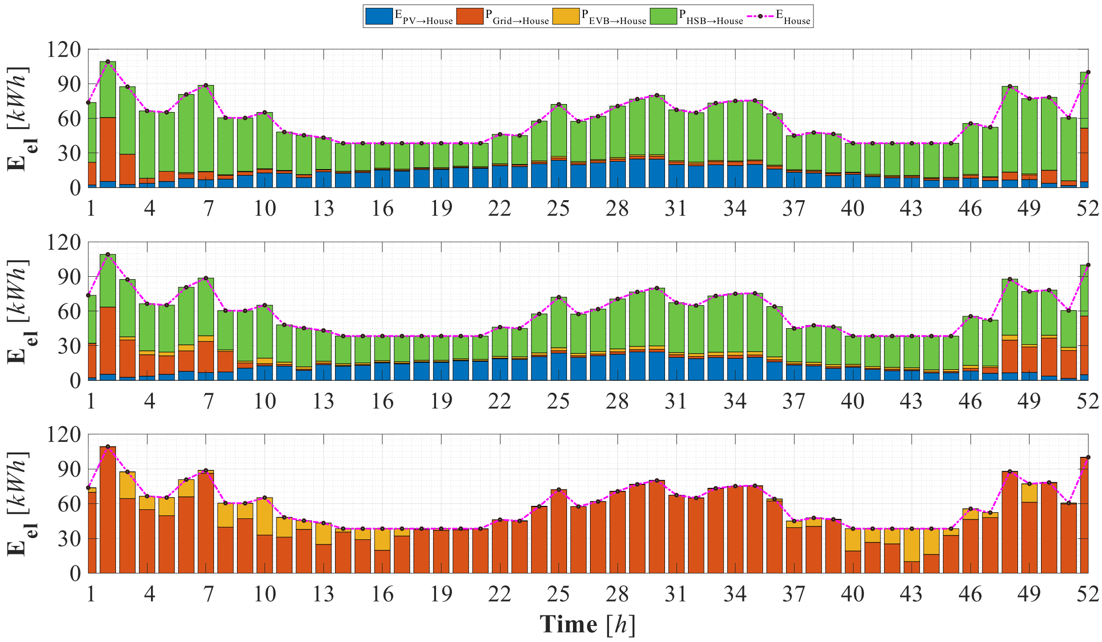

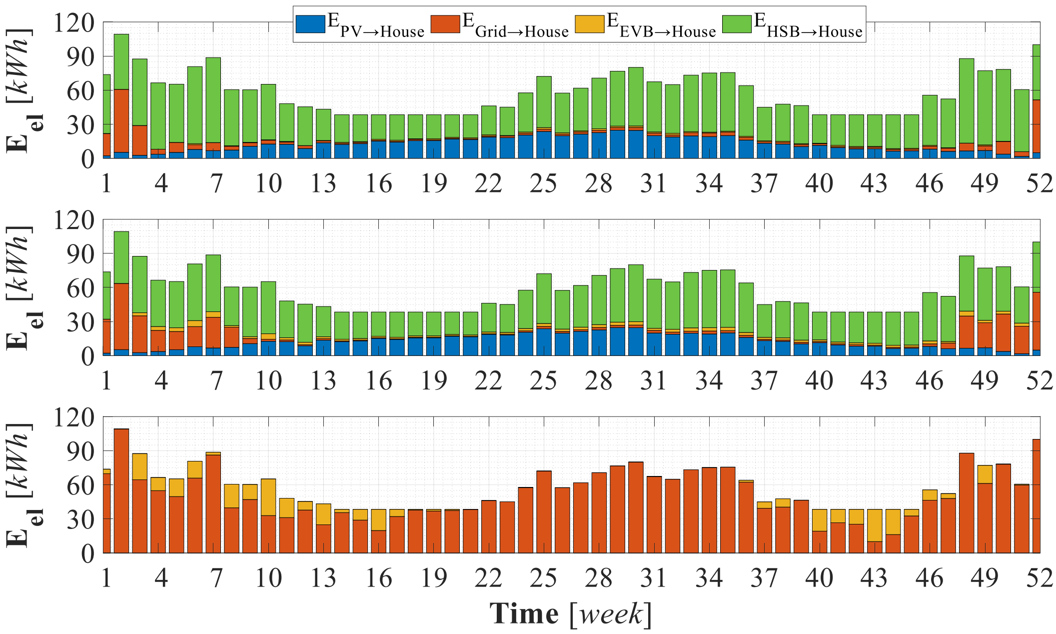

Fig. 7.17. House demand balance: weekly electricity flows – Case 1 (top), Case 2 (middle), Case 3 (bottom).

Concerning the Office demand (E_{Office}), see Fig. 7.18, in Case 1 and Case 2, electricity is greatly provided by the EV, which effectively acts as energy vector. A more significant contribution of the EVB to the Office demand ($E_{EVB \rightarrow Office}$) can be noted for Case 2 where the use of two high capacity batteries, suitably swappable, increases the electrical storage capability, and consequently the possibility to better match the House and Office demands. EVB also contributes to power the Office in Case 3, although the major energy provider is the PV field ($E_{PV \rightarrow Office}$), which constantly (according to the PV power production, see Table 7.5) contributes to balance the Office demand.

Finally, Fig. 7.19 , relative to the EV demand (E_{EV}), shows that Case 2 represents the better strategy for storing and transporting electricity, being the EV always equipped with the battery with the highest capacity. As a result, the major part of E_{EV} is balanced by PV panels generation ($E_{PV\rightarrow EVB}$), whereas the contributions to the Grid ($E_{Grid\rightarrow EVB,house}$ and $E_{Grid\rightarrow EVB,office}$) occurs only in winter weeks. Differently from Case 2, Case 1 and Case3 show a significant contribution of the Grid to the EV demand during the year.

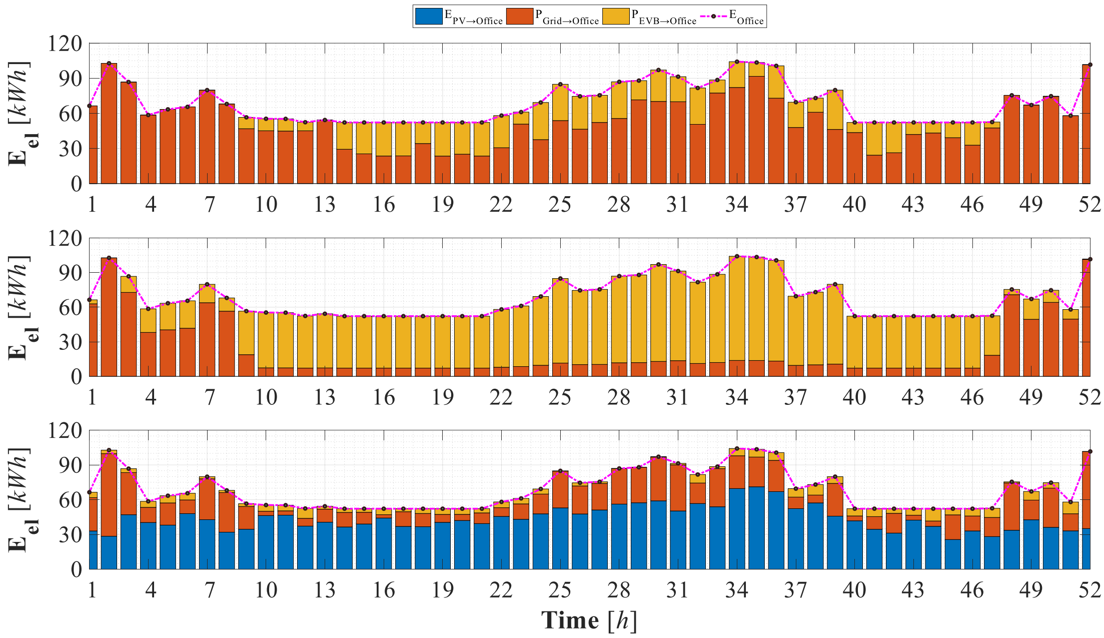

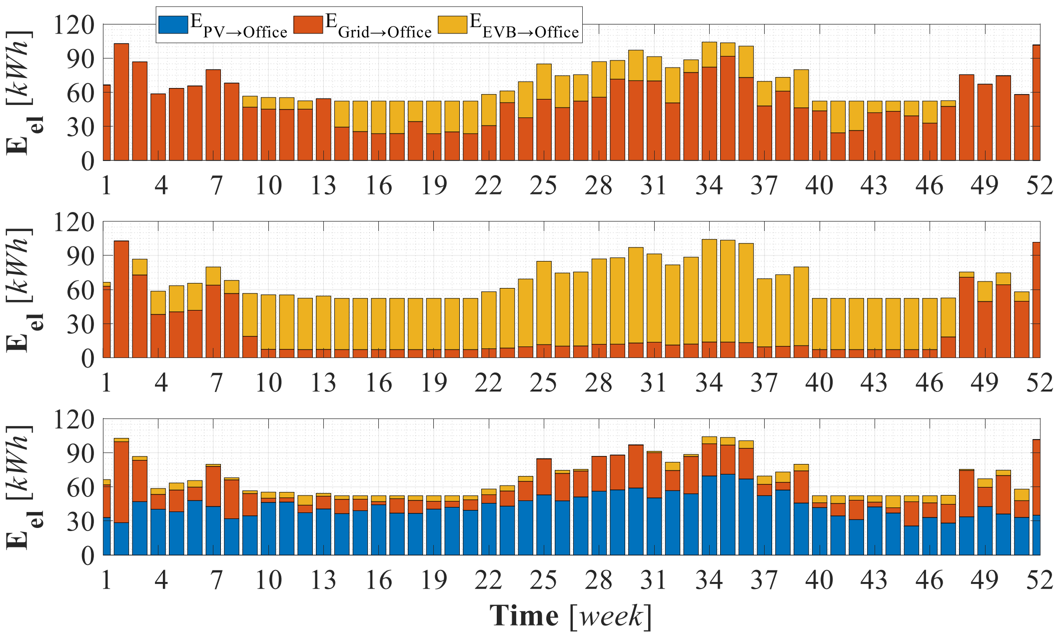

Fig. 7.18. Office demand balance: weekly electricity flows – Case 1 (top), Case 2 (middle), Case 3 (bottom)

Case 2 storage strategy results the optimal one for reducing the Grid supply for the whole system, not only for the EV. This can be observed by analysing the demand of electricity from the Grid delivered to the three users, House, Office and EV, as shown in Fig. 7.20.

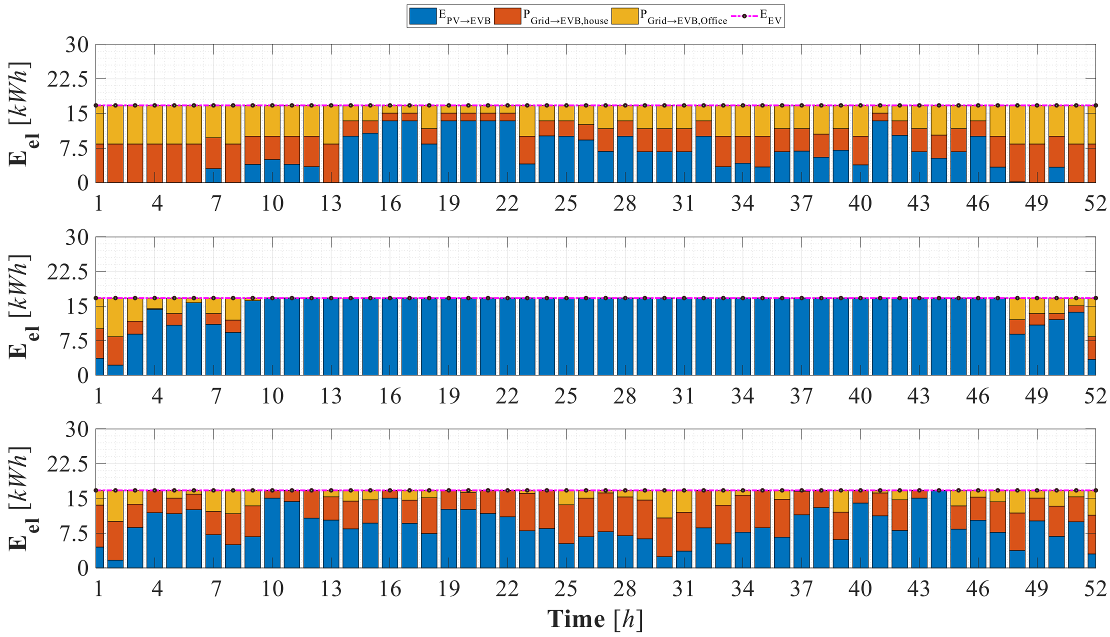

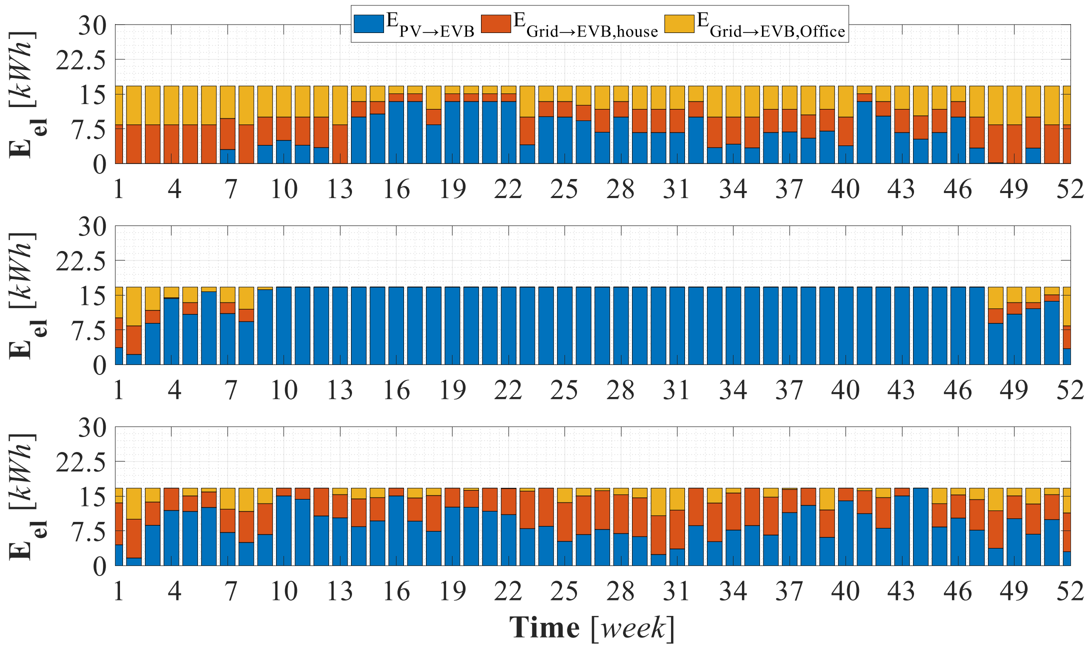

Fig. 7.19. EV demand balance: weekly electricity flows – Case 1 (top), Case 2 (middle), Case 3 (bottom)

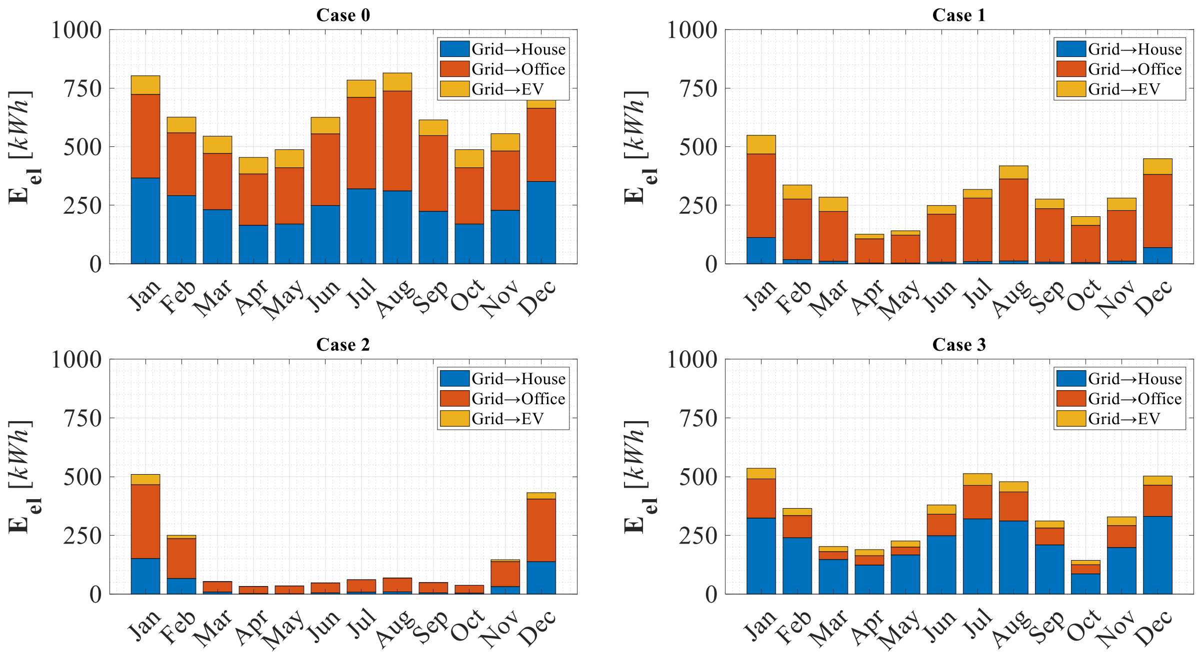

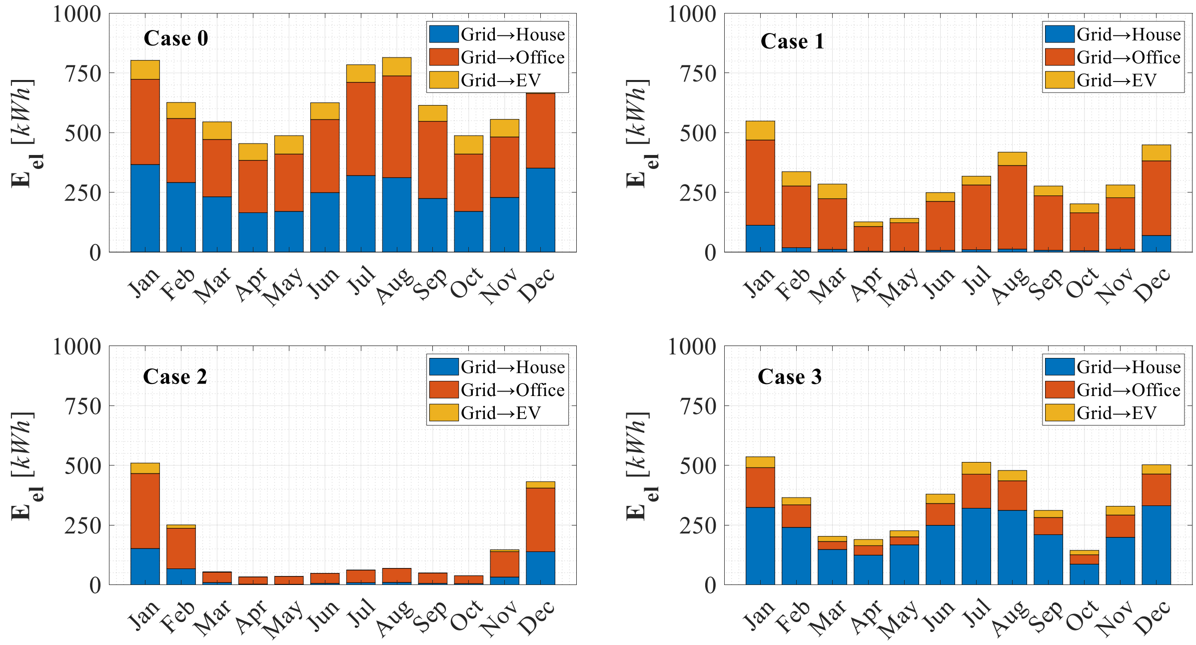

Fig. 7.20. Monthly electrical energy from the Grid

Specifically, with respect to the reference Case 0, the lowest electricity demand from the Grid occurs for Case 2. Here, with the exception of the winter months (January, February, November and December), Grid energy is weakly required. Case 1 and Case 3, besides the significant difference in the monthly PV generation, almost require the same amount of electricity from the Grid, meaning that a better management of electrical flows is achieved in Case 3. Case 1 also shows that the Office demand is matched by the electrical energy stored into the EVB, and transported by the EV from the House, mostly during spring and autumn months, due to the reduction of House demand (no heating and cooling is required), which increase the chances of the EV to power the Office.

Although the achieved reduction of electricity from the Grid (for all investigated V2B² scenarios) and the enhancement of the matching between generation and load due to the proper management of storage batteries, a significant amount of PV production is exported to the Grid. In this regard, electricity produced by PV panels is partially self-consumed by the users (House, Office, and EV) while the rest is exported to the Grid. In this regard, Fig. 7.21 shows the monthly and yearly produced, self-consumed and exported amounts of PV panels generation for all investigated cases. By comparing Case 1 and Case 2, it is clear that the amount of exported energy significantly decreases, due to the higher storage capability of Case 2 with respect to Case 1, as well as to the EV battery swap option which increases the amount of electricity transported by the EV and delivered to the Office. During winter months, there is no exported electricity by Case 2. Case 3 shows, as expected, the lowest amount of PV production and self-consumed energy with respect to Case 1 and Case 2. In addition, the yearly exported energy of Case 3 is comparable to Case 2 one, although the related lowest PV panels generation. This is due to the better winter exploitation of solar energy (according to the PV panels tilt angle) as well as to the occupancy schedule of the Office, which is not occupied during weekends when the produced electricity is directly exported to the Grid (not self-consumed neither stored in the EVB).

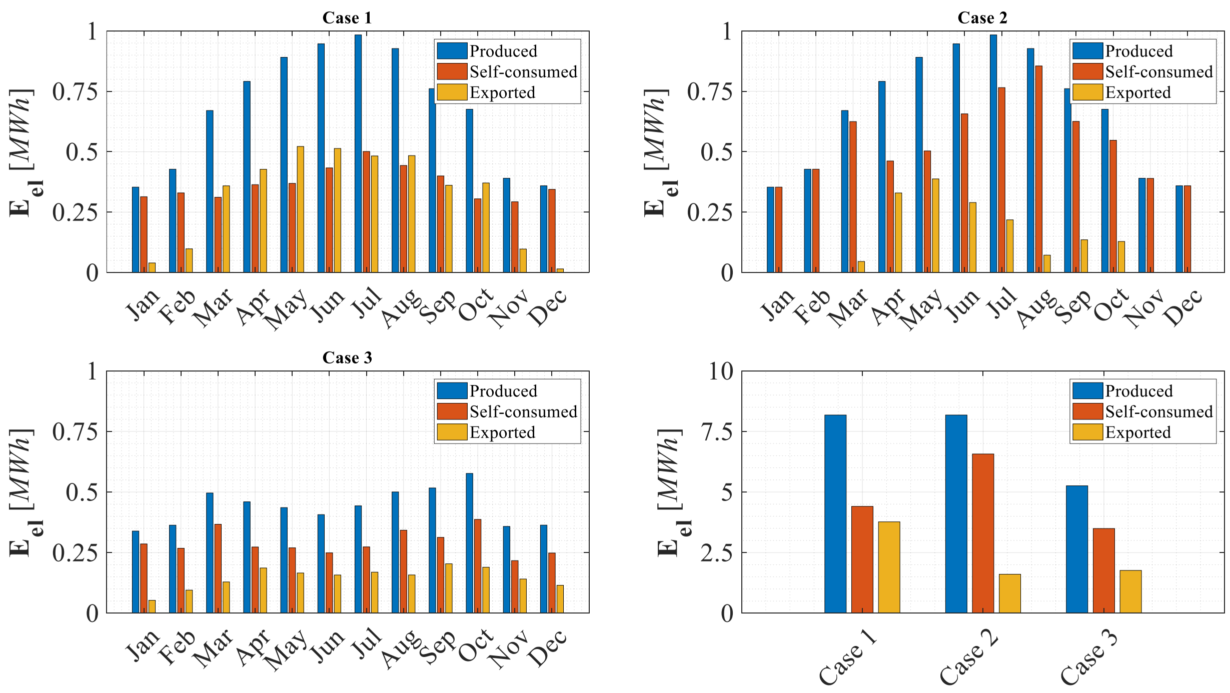

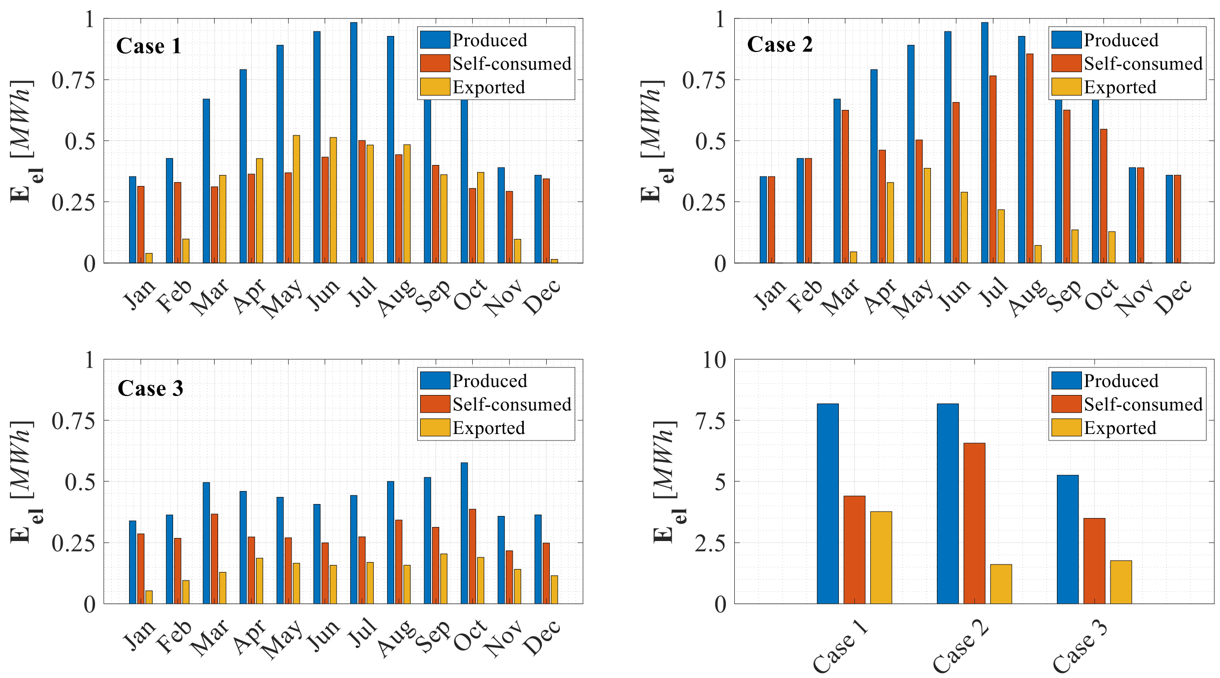

Fig. 7.21. Monthly and yearly renewable energy produced by PV, consumed on sites (by House, Office and EV) and exported to Grid.

Yearly results (see Fig. 7.21, the bottom right) clearly show that the best energy matching between generation and loads is achieved in the Case 2 scenario. However, an interesting performance can be observed for Case 3, where the amount of self-consumed electricity is comparable to the one calculated for Case 1 (which has a much higher PV panels production), suggesting a high matching between generation and loads (pursued with the installation of PV panels at the Office where the EV is parked for most of the time). Moreover, Case 3 exported energy is slightly higher than the one calculated for Case 2 (though the significant Case 3 weekend days exports), resulting in a similar economic income due to the selling electricity to the grid, as better discussed in the next paragraph.

Yearly results related to all the discussed electricity flows are reported in Table 7.6 for the reference Case 0 and the proposed V2B² layouts. The table also includes the PV panels production (E_{PV}) and the users demand (E_{House}, E_{Office}, E_{EV}). By analysing the yearly overall results, it is interesting to note that the House total electrical consumption ($E_{Grid \rightarrow House}$), originally equal to 24.1 kWh_{el}/m^2 (typical value of net or nearly zero energy buildings [163, 166]) is now very close to zero for the simulated Cases 1 and 2, being equal to 2.1 and 2.9 kWh_{el}/m^2, and equal to 21.2 kWh_{el}/m^2 for Case 3. Concerning the Office total electricity consumption ($E_{Grid \rightarrow Office}$), originally equal to 39.7 kWh_{el}/m^2, is equal to 31.0 kWh_{el}/m^2 for Case 1, to 13.2 kWh_{el}/m^2 for Case 2, and to 11.8 kWh_{el}/m^2 for Case 3. By considering both buildings, House and Office, as one single building user, the final electricity consumption ($E_{Grid \rightarrow House}$ + $E_{Grid \rightarrow Office}$), equal to 30.6 kWh_{el}/m^2 for the reference Case 0, becomes equal to 14.0 kWh_{el}/m^2 for Case 1, 7.2 kWh_{el}/m^2 for Case 2, and 17.3 kWh_{el}/m^2 for Case 3. These very low values of electricity consumption per square meters suggests that the solar fields, regardless of the power production, are capable to significantly balance the electrical energy needs of the considered single user (House + Office) to values typical for net or nearly zero energy buildings [163].

The overall electricity from Grid for each investigated V2B² scenarios and for each user, reported in Table 7.6, also shown in Fig. 7.22, is considerably reduced with respect to Case 0.

Table 7.6. Yearly energy results.

Parameter	**Case 0**	**Case 1**	**Case 2**	**Case 3**
		[MWh/y]		
E_{PV} (PV prod)	-	8.18	8.18	5.26
E_{House} (House demand)	3.08	3.08	3.08	3.08
E_{Office} (Office demand)	3.58	3.58	3.58	3.58
E_{EV} (EV demand)	0.87	0.87	0.87	0.87
$E_{PV \to House}$ (from PV to House)	-	0.65	0.65	-
$E_{PV \to Office}$ (from PV to Office)	-	-	-	2.28
$E_{PV \to HSB}$ (from PV to House battery)	-	2.30	4.84	-
$E_{PV \to EVB}$ (from PV to EV battery)	-	1.19	0.66	1.13
$E_{PV \to Grid}$ (from PV to Grid)	-	3.77	1.61	1.76
$E_{EVB \to House}$ (from EV battery to House)	-	0.03	0.08	0.37
$E_{EVB \to Office}$ (from EV battery to Office)	-	0.79	2.37	0.24
$E_{EVB \to HSB}$ (from EV battery to House battery)	-	-	-	-
$E_{HSB \to House}$ (from House battery to House)	-	2.12	1.98	-
$E_{HSB \to Office}$ (from House battery to Office)	-	-	-	-
$E_{HSB \to EVB}$ (from House battery to EV battery)	-	-	-	-
$E_{Grid \to House}$ (from Grid to House)	3.08	0.27	0.37	2.71
$E_{Grid \to Office}$ (from Grid to Office)	3.58	2.79	1.19	1.06
$E_{Grid \to EVB,house}$ (from Grid to EV battery – at house)	0.88	0.28	0.12	0.31
$E_{Grid \to EVB,office}$ (from Grid to EV battery – at office)	-	0.29	0.04	0.10

The overall electricity from Grid is decreased by 47.9% for Case 1 (3.92 MWh/y), by 77.0% for Case 2 (1.73 MWh/y) and by 44.5 % for Case 3 (4.18 MWh/y) with respect to the reference Case 0 (requiring 7.53 MWh/y). Specifically, by considering a single user, the electricity from Grid decreased as reported:

- $E_{Grid \to House}$ (3.08 MWh/y, Case 0) is decreased by 91.2 % in Case 1 (0.27 MWh/y), by 85.8% in Case 2 (0.37 MWh/y), and by 12.1% in Case 3 (2.71 MWh/y);
- $E_{Grid \to Office}$ (3.58 MWh/y, Case 0), is decreased by 22.0% in Case 1 (2.79 MWh/y), by 66.5% in Case 2 (1.19 MWh/y), and by 70.3% in Case 3 (1.06 MWh/y);
- $E_{Grid \to EV}$ (0.88 MWh/y, Case 0) is decreased by 35.2% in Case 1 (0.57 MWh/y), by 81.8% in Case 2 (0.16 MWh/y), and by 53.4% in Case 3 (0.41 MWh/y).

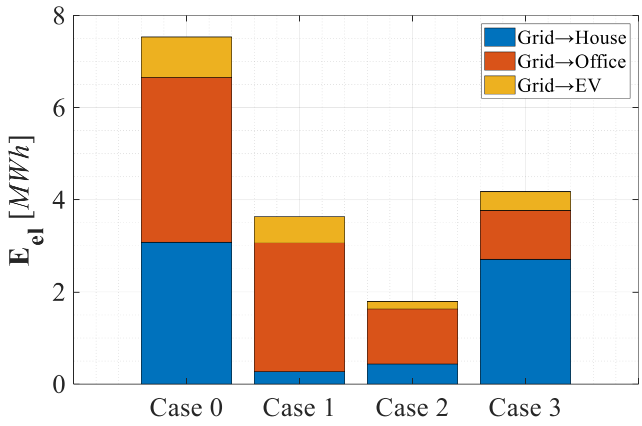

Fig. 7.22. Yearly electricity energy from Grid (see Table 7.6).

For each investigated case, the shares of yearly electricity delivered to each user, House, Office and EV, by PV panels, HSB, EVB and Grid are reported in Fig. 7.23, Fig. 7.24, and Fig. 7.25, respectively. The House demand (3.08 MWh/y, E_{House}), see Fig. 7.23, is balanced by 8% and 12% by the Grid in Case 1 and 2, and by 88% in Case 3.

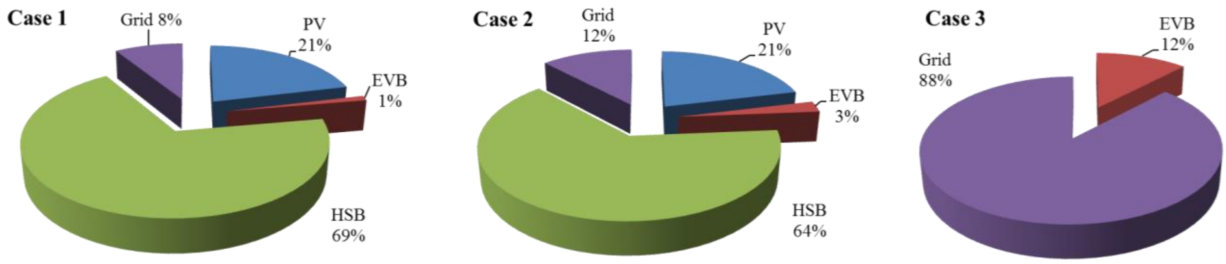

Fig. 7.23. Share of yearly electricity delivered to House (yearly electricity demand equal to 3.08 MWh/y -Table 7.6) by PV panels, HSB, EVB and Grid.

The PV panels generation directly covers the House demand by 21% in Case 1 and Case 2 (PV panels installed on the House roof). The EVB provides the 1, 3 and 12% of E_{House} for Case 1, Case 2 and Case 3, respectively. Conversely, the EVB provides about 22, 66 and 6% of the Office demand (3.58 MWh/y, E_{Office}) for Case 1, Case 2 and Case 3, respectively, see Fig. 7.24 (significantly reducing the power grid integration). PV panels production covers about 64% of E_{Office} in Case 3. The EV demand (0.88 MWh/y, E_{EV}), see Fig. 7.25, is balanced by PV electricity stored within the EVB by 35% in Case1, 82% in Case 2, and 54% in Case 3, with a remarkable reduction of electricity from Grid on which the EV relies when connected to the BMS of both House and Office buildings.

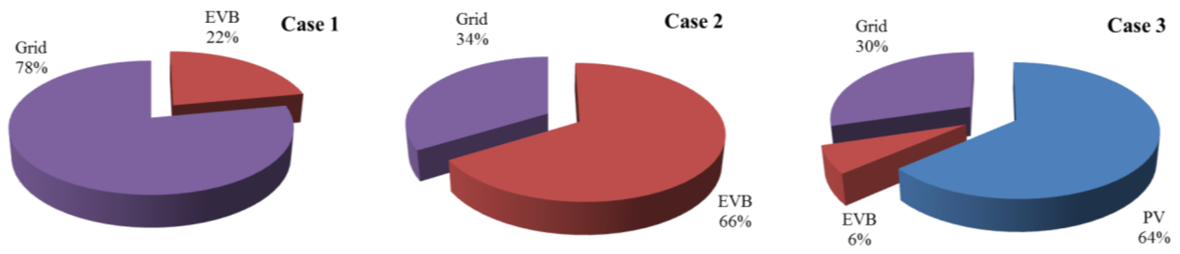

Fig. 7.24. Share of yearly electricity delivered to Office (yearly electricity demand equal to 3.58 MWh/y --Table 7.6) by PV panels, EVB and Grid.

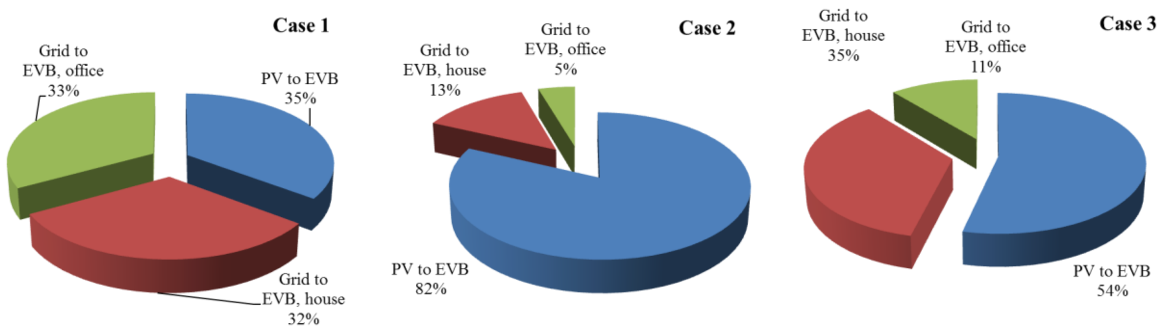

Fig. 7.25. Share of yearly electricity delivered to EV (yearly electricity demand equal to 0.88 MWh/y - -Table 7.6) by PV panels and Grid.

The share of yearly electricity delivered to the whole system from each energy source, i.e. PV panels and Grid, is reported in Fig. 7.26 for the investigated layouts, such as Case 0 and V2B² scenarios (Case 1, Case 2 and Case 3). Here, electricity by each source is split according to the selected user. The main electricity consumer of the considered system, reference Case 0, is the Office, requiring about 47 % of the total energy supplied by the grid; the second consumer is the House, requiring 41% of electricity, and then the last one is the EV, with 12% of the consumed electricity. Fig. 7.26 clearly shows how the weight of the Office demand delivered by the Grid decreases i) to 36% and 15% in Case 1 and Case 2, respectively, thanks to the electricity transferred and delivered by the EVB, and ii) to 14% in Case 3 thanks to the PV panels production. Similarly, the House demand delivered by the grid decreases to i) 4% and 5% in Case 1 and Case 2, respectively, thanks to the PV panels production, which is directly delivered to the House load and stored into the HSB, supplied back to the House and, in Case 1, to the EVB; ii) to 36% in Case 3 thanks to the electricity transferred and delivered by the EVB. The EV demand decreases from 12% to 7%, 2% and 4%, respectively in Case 1, Case 2 and Case 3.

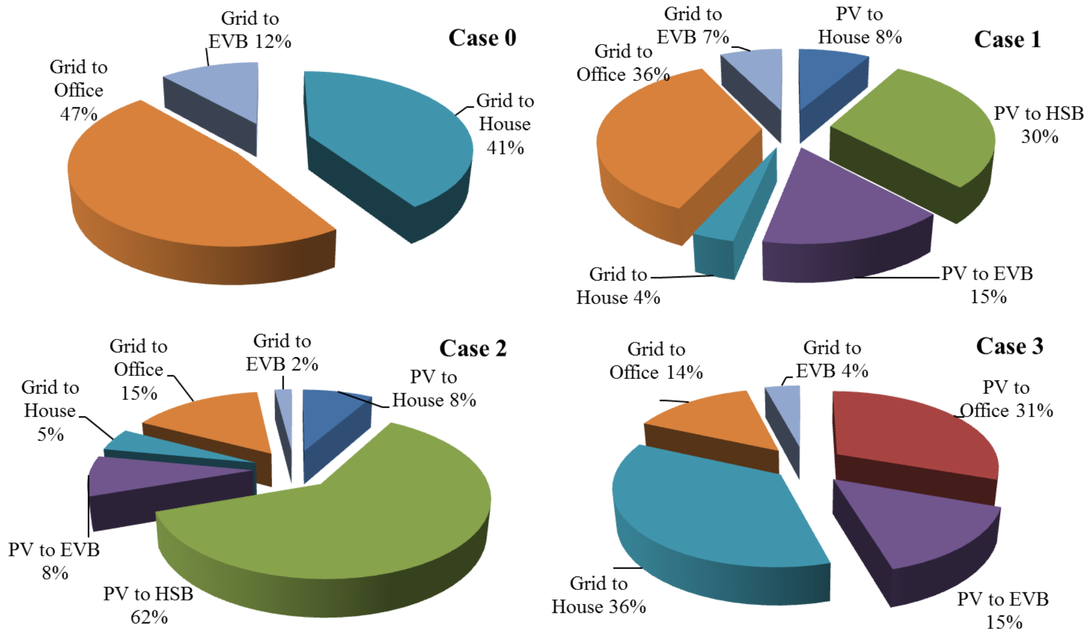

Fig. 7.26. System balance - House (3.08 MWh) + Office (3.08MWh) + EV (0.22 MWh), equal to 6.87 MWh: shares of electricity by source.

It is of interest to see how the two batteries of Case 2, EVB1 and EVB2, because of the swap option, are almost equally used, as reported in Fig. 7.27. Such figure shows the outlet electricity flows (EV→House, EV→Office, EV→EVB) and percentage of inlet electricity by PV panels (PV→EV), by grid (Grid→EVB,house and Grid→EVB,office), and by the battery acting, time by time, as on-site house (HSB→EVB). The major outlet electrical flow for EV1 and EV2 is the energy delivered to the Office, EV→Office (equal to 1.32MWh/y for EV1 and to 1.23 MWh/y for EV2), followed by EV→House and to the energy required for the EV motion, EV→EVB. Outlet electricity flows are balanced by the inlet ones. Specifically, electricity from PV panels accounts for about 97% of the total inlet flows, whereas the remaining amount of electricity (about 3%) is delivered by the Grid mostly when the EV is connected to the House BMS.

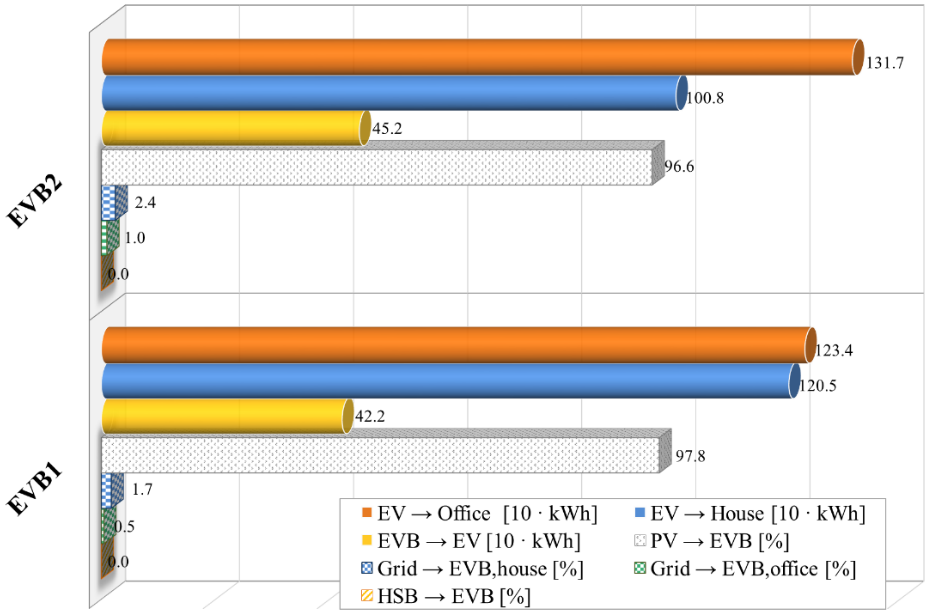

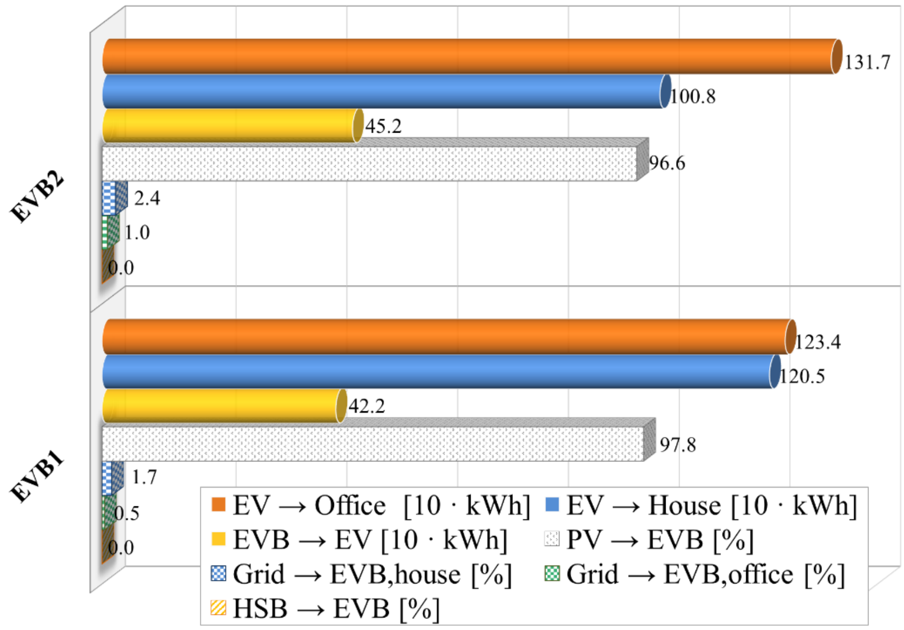

Fig. 7.27. Energy balance on batteries of Case 2: outlet electricity flows and shares of inlet electricity by PV panels, HSB and Grid.

Finally, in order to analyse the matching between the load and the generation, by means of the load matching and grid interaction indexes (see eqs. 7.7 and 7.8), presented in the previous section, the amount of exported and imported (or delivered) energy must be analysed. To this aim, Fig. 7.28 shows the cumulative delivered and exported electricity profiles for all the investigated systems. According to the results reported in Fig. 7.21, Case 2 shows the best exploitation of the renewable source (lowest delivered energy from Grid), thanks to the batteries swap option, leading to a remarkable reduction of the electricity exported to the Grid. In this regard, the worst performance is achieved by Case 1, which shows the highest exported energy to the Grid. In addition, a remarkable increase of the exported electricity is observed during spring and summer months, when heating and cooling loads are null, and the PV panels generation highly surpasses the system demand. Similarly, the increase of delivered electricity occurs mainly during summer and winter, when there are heating and cooling demands in both House and Office. A constant delivery is observed in Case 2, being the high capacity of EVB1 and EVB2 swappable batteries capable to enhance the matching between PV generation and loads. Case 3 outperforms Case 1 in terms of exported electricity, while its requires more electricity from the Grid with respect to Case 1 during the summer season (due to the lowest vertical PV panels production and to the unexploited use of electricity produced by the solar field in the weekend days).

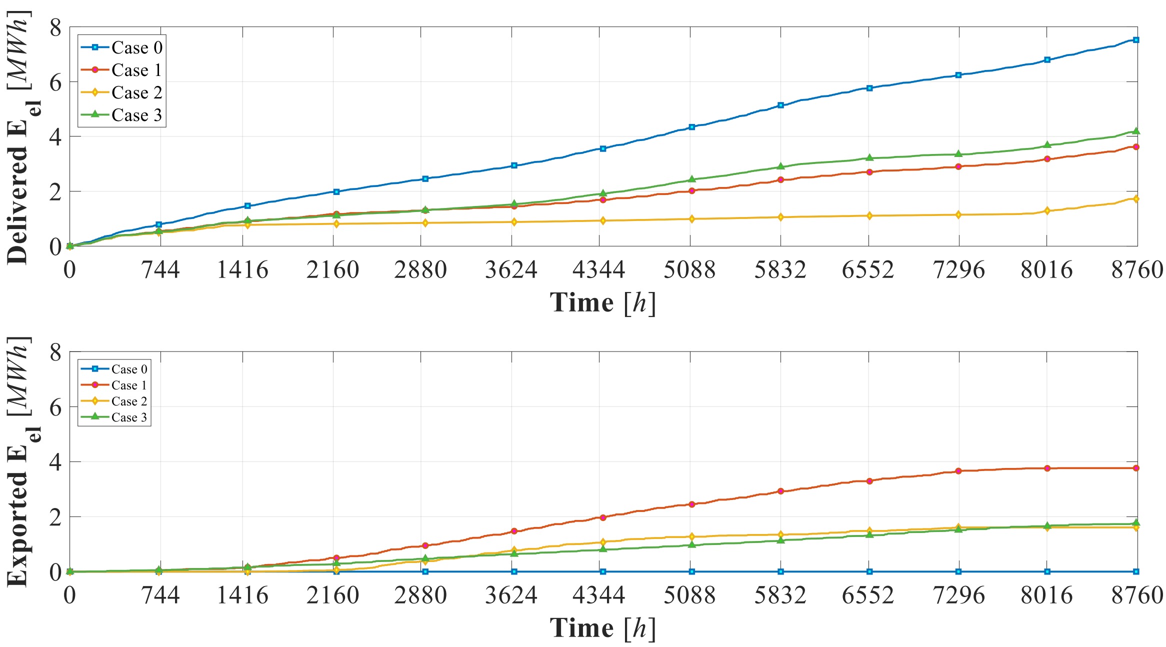

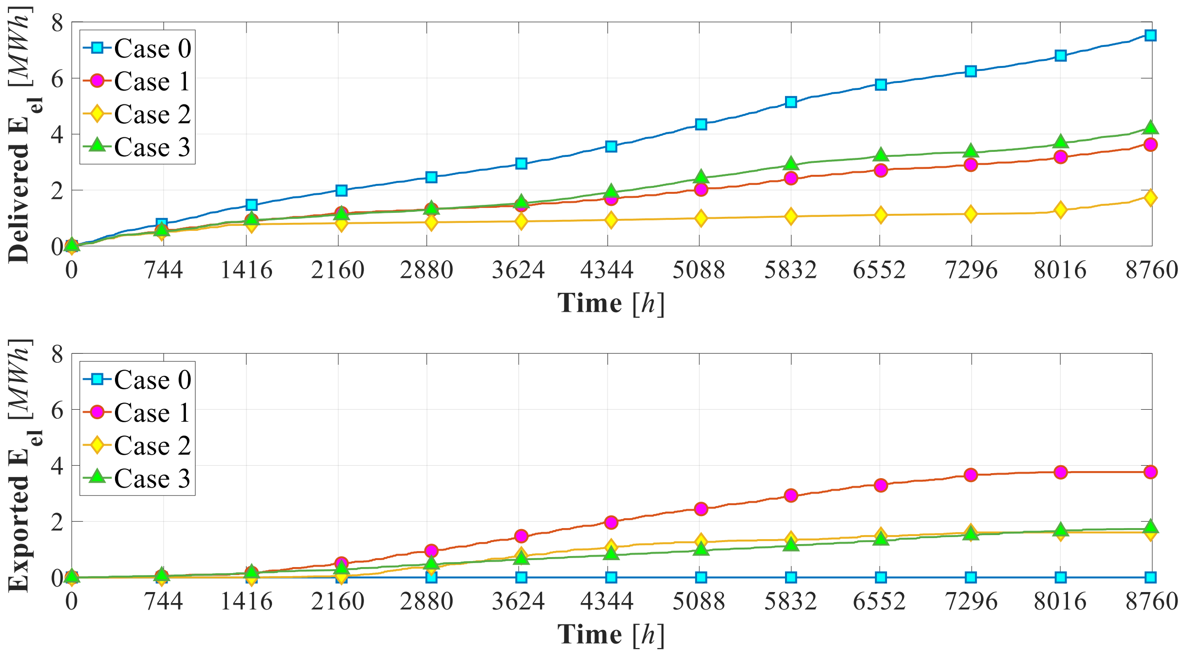

Fig. 7.28. Cumulative delivered and exported electricity to and from the investigated system.

The value of f_{load} and f_{grid}, calculated on annul resolutions for the whole system as well as for the House and Office buildings of the V2B² scenarios (Case 1, Case 2 and Case 3) are reported in Table 7.7. In addition, Fig. 7.29 shows the profile of f_{load} and f_{grid}, calculated on hourly and daily basis.

The values of f_{load}, measuring the amount of electricity load balanced through PV panels generation (also known as solar fraction [168]), calculated on hourly basis (Fig. 7.29), show a high utilization of electricity production, being often reached the 1 (or 100%). On the annual basis, the maximum f_{load} values are largely obtained by Case 2, whereas values lower than 50% are obtained by Case 3 and for the Office.

Table 7.7. Load matching (f_{load}) and grid interaction (f_{grid}) indexes.

Parameter	**Case 0**	**Case 1**	**Case 2**	**Case 3**
	[%]			
V2H²				
$f_{load,V2B^2}$ (annual basis)	-	57.83	59.45	40.43
$f_{grid,V2B^2}$ (annual basis)	-	10.50	8.00	9.36
House				
$f_{load,House}$ (annual basis)	-	63.23	62.82	46.31
$f_{grid,House}$ (annual basis)	-	21.39	14.69	17.85
Office				
$f_{load,Office}$ (annual basis)	-	44.18	46.05	42.73
$f_{grid,Office}$ (annual basis)	-	19.94	16.24	15.90

For all the proposed scenarios, f_{grid} calculated on the annual basis (annual standard deviation), describes the V2B² scenarios as net exporting systems (positive values). Nevertheless, increasing the assessment time resolution, it is possible to note the occurrence of electricity export and import, with a higher fluctuation on the hourly basis with respect to the daily one (Fig. 7.29). A lower fluctuation is observed for Case 2, as expected, being its storage capability the most effective one to reduce the Grid interaction (matching the loads with the PV panels generation). Note that the differences among the storage scenarios seem to not result in remarkable differences of export/import, when f_{grid} is evaluated on the annual basis (a higher resolution is desirable).

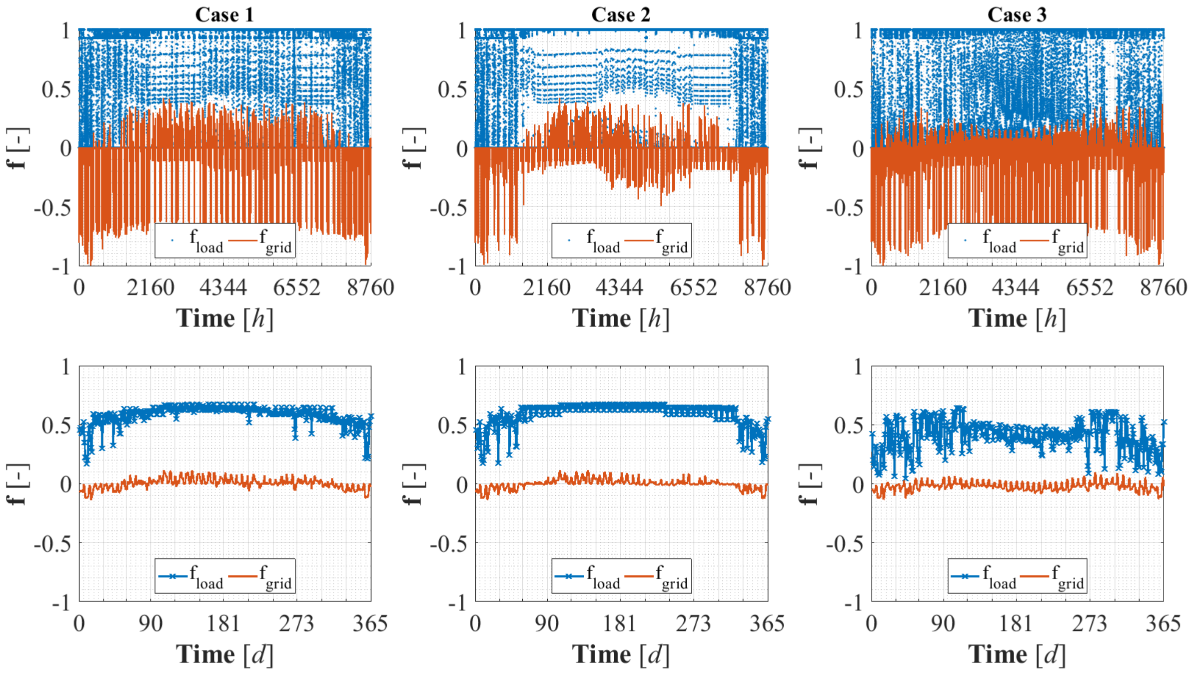

Fig. 7.29. Load matching (f_{load}) and grid interaction (f_{grid}) indexes for Case 1, Case 2 and Case 3.

7.5.3. Economic analysis

The positive energy findings obtained by the V2B² scenarios do not necessarily imply the economic profitability of the proposed systems. These include the capital costs of a bidirectional converter, an energy storage system, and a solar field (with respect to the standard V2B reference Case 0). In addition, V2B² also requires an advanced management system capable to track all energy transfers (between the House, HSB, EVB, Office and Grid). Therefore, the economic analysis is mandatory required to assess the feasibility of the proposed V2B² scenarios with respect to the conventional one.

Table 7.8 summarizes the main annual energy and economic indexes calculated for all scenarios. The analysis shows that all the proposed V2B² are high efficient, with the best outcome achieved by

Case 2 scenario (*RES* = 77%). Thus, the lowest operating costs are calculated for Case 2, which shows the highest ESC_{PV} (i.e. economic value of self-consumed PV panels generation, considered as avoided cost). Nevertheless, all cases show small economic revenues due to the electricity sold to the Grid. As an example, FGE_{PV} reaches the maximum value in Case 1, about 180 *k€/y*, which does not counterbalance the higher operating cost (e.g. with respect to Case 2). In general, the economic analysis shows that, although the use of batteries leads to a very high self-consumed electricity, reducing the dependence on the Grid, the high investment costs, *IC*, make the *SPB* very remarkable for all scenarios, ranging between 10.9 and 15.2 years. *IC* are significant, especially for Case 1 and Case 2, about 14.5 *k€* and 20.2 *k€*, respectively. Lower *IC* values are calculated for Case 3 (about 7.9 *k€*), where the on-site battery is not considered, whereas the highest *IC* is that one of Case 2 (with the highest storage capacity). The high capital cost of batteries, nowadays about 260 €/*kWh*, leads to not very profitable systems, though the significant economic savings (*EcS*), leading to negative (for Case 1 and Case 2) of very low positive (Case 3) Net Present Values, *NPV*, calculated by considering a discount rate equal to 5% and a time horizon of 20 years.

Table 7.8. Yearly energy results.

Parameter	Case 0	Case 1	Case 2	Case 3
EC ($E_{Grid \rightarrow House,Office,EV}$) [*MWh/y*]	7.53	3.92	1.73	4.18
SEC ($E_{House,Office,EV}$) [*MWh/y*]	-	4.06	6.56	3.49
ES [*MWh/y*]	-	3.61	5.80	3.36
RES [%]	-	51.8	77.00	44.56
OC [*k€/y*]	1.44	0.66	0.32	0.81
FGE_{PV} [*€/y*]	-	182.2	64.51	92.48
ESC_{PV} [*€/y*]	-	770.5	1111.5	623.0
EcS [*€/y*]	-	952.8	1179.5	715.5
REcS [%]	-	66.4	82.2	49.9
IC [*k€*]	-	14.52	20.20	7.85
SPB [*y*]	-	15.2	17.1	10.9

Therefore, in order to evaluate the economic profitability as a function of the future cost of the storage system, a sensitivity analysis is carried out. In particular, by varying the capital cost of the electric storage capacities ($IC_{HSB/EVB}$ or *BCI*), from 80 €/*kWh* (target cost) to 260 €/*kWh* (actual cost), the variation of the *SPB* is shown in Table 7.9. The *SPB* decreases to values lower than 7 years at the target price of the batteries. It is worth noting that future lower costs of PV panels, inverter and BMS could be taken into account, further reducing the *SPB* of the proposed system.

Similarly, Fig. 7.30 shows the variation of the *NPV* versus the discount rate (*NPV* vs. *r*) as a function of the Battery Capital Cost (*BCI*). Here, it is clear that with the reduction of *BCI* an increase of the *NPV* is expected. For the target price of the batteries (i.e. 80 €/*kWh*), the *NPV* becomes positive for discount rates lower than 9.5%, coincident with *IRR*. By considering the actual *r* equal to 5%, for a

BCI lower than 125 €/*kWh*, positive NPV are obtained for Case 1 and Case 2 scenarios. For the scenario with the lowest investment, Case 3 (scenario without on-site battery), the *NPV* is positive for all the considered battery costs for discount rates higher than 5%. Fig. 7.30 also shows how the profitability index, *PI*, varies as a function of $IC_{HSB/EVB}$, and it is always positive. Its slope is constant for Case 3, while it increases at lower $IC_{HSB/EVB}$ for Case 1 and Case 2 (scenarios with on-site battery).

Table 7.9. SPB calculated for different price of electric storage ($IC_{BAT,sp}$).

Parameter	Case 1	Case 2	Case 3
$IC_{BAT,sp}$ [€ /*kWh*]		[*y*]	
80	6.61	6.83	5.94
125	8.77	9.40	7.20
170	10.93	11.98	8.46
215	13.08	14.55	9.71
260	15.24	17.13	10.97

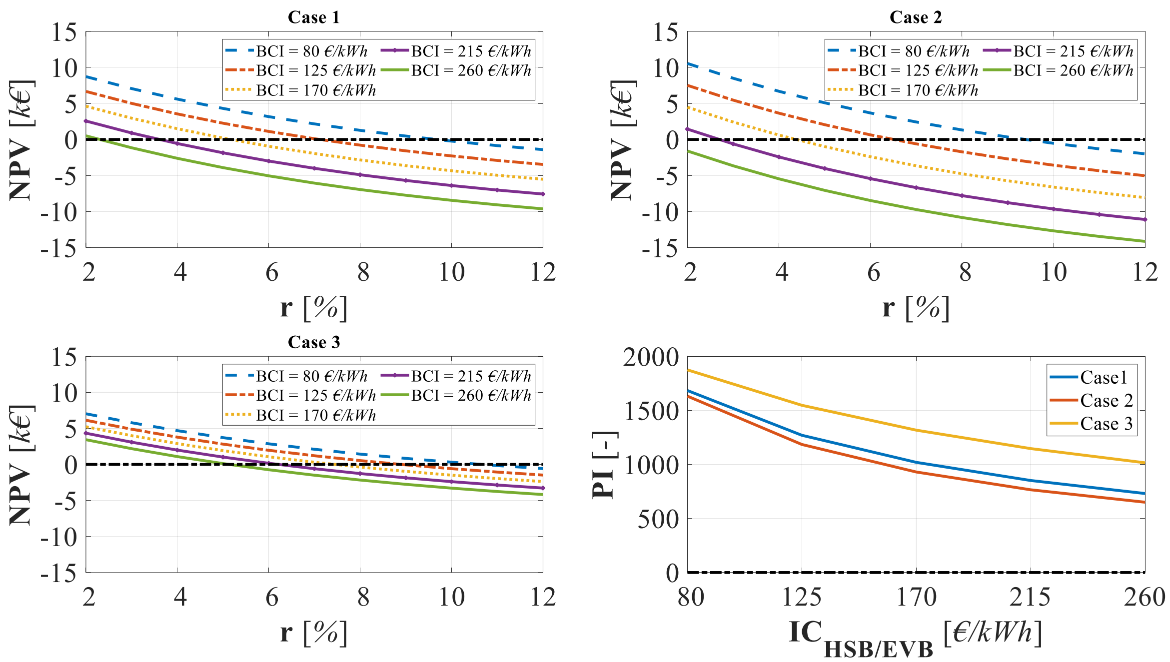

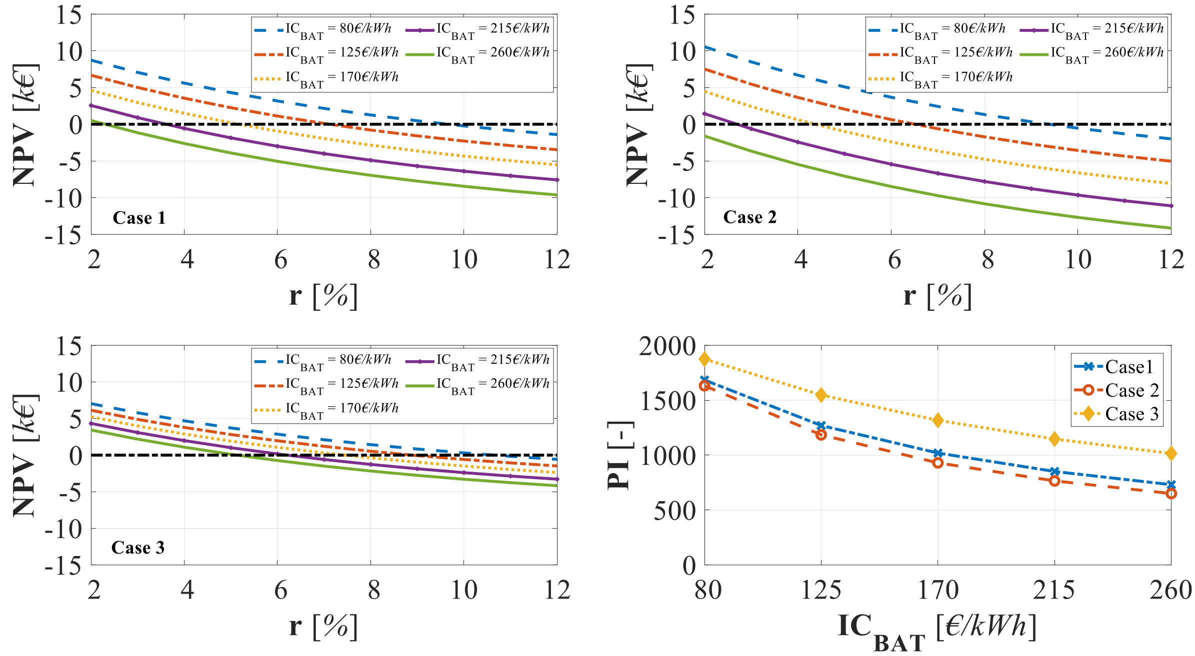

Fig. 7.30. Economic sensitivity analysis: NPV vs. IRR and PI as a function of the battery capital investment (BCI, target price 80 €/kWh).

Finally, it is worth noting that the economic analysis is carried out by assuming the Italian rules regarding the electricity exchange with the national grid. The Italian regulation does not support the positive balance between electricity exported to and delivered from the Grid, being low the economic compensation of electricity exported to the Grid. As the electricity price highly affects the refund from the exported energy and the viability of the system, different national regulations and electricity prices might lead to much encouraging economic results. In addition, with the penetration of renewable energies, energy prices are expected to be revisited in order to encourage the transition toward sustainable energy systems. Finally, a further optimization of the system could also enhance the energy and economic performance of the proposed V2B² concept. Such analysis, necessary to assess the optimal energy management system strategy will be developed as further investigation, with the aim to find out the optimal design and operating parameters which simultaneously minimize the energy and economic cost function.

7.6. Conclusions

Novel energy management schemes for grid-connected buildings and electric vehicles are presented with the aim to promote the net or nearly zero energy building goal at micro-grid scale level. This novel energy efficiency paradigm, in which electric vehicles are considered as key components for improving the buildings energy performance, is evaluated by means of a suitable dynamic simulator for energy and economic analyses. This scope is reached by the development of a new in-house simulation model, implemented in a computer code written in MatLab. By such tool the role of electric vehicles as energy vector among multiple buildings, integrating PV panels and electrical storages, is investigated.

In order to show the potentiality of the presented concept and of the related simulation model, three different scenarios, obtained by modelling the building integration of photovoltaic panels and the management of energy storages (including a suitable batteries swap option) are modelled and simulated. The obtained results are compared to those of a reference conventional system. Specifically, the simulated buildings are a single-family house and an office space, considered as the classic basic cluster of buildings linked to human activities. An electric vehicle, used for house-to-office trips, completes the considered examined system. Simulation results show that the electric vehicle can effectively benefit the novel concept of bidirectional Building To Vehicle To Building (V2B^2) system operation, where renewable energy transfer among buildings, energy storages, electric vehicle and grid use are optimized. Note that, in the proposed concept, the key factor is the use of electric vehicles as energy vectors. By such vehicles, working in synergy with the national power grid, the utilization of on-site energy generation devices at system level is enhanced. The annual electricity exported/imported to/from the grid can be optimized with a consequent improvement of the energy matching indexes, which show an encouraging performance of the investigated systems. Specifically, the proposed V2B^2 system, reached interesting results from the energy point of view (energy savings ranges between 45 to 77%). Regarding the economic convenience, the proposed scheme is highly influenced by initial costs and national electricity prices, showing that suitable energy policies and suitable capital costs reductions are still necessary to promote the diffusion of such kind of systems.

Future analyses, including sensitivity and parametric investigations, will be carried out by means of the developed model, also aiming to investigate the potentiality of the V2B^2 strategy at larger micro-grid levels and by utilising innovative electric vehicles.

CHAPTER 8

8. Conclusions

In this thesis, the energy performance assessment of innovative solar technologies and energy storage systems is conducted by means of suitably developed dynamic simulation models. Different approaches, depending on the investigated technology, were adopted:

- 1D models are developed for analysing stand-alone systems. These models are based on Hottel-Whillier-Bliss equations suitably modified for assessing the features of the analysed collectors. Specifically, for the vacuum solar thermal collector, the novelty is to couple a 1D mathematical model to a suitable optimization tool. Furthermore, regarding the hybrid photovoltaic/thermal prototype, special attention is paid for modelling the PV panel as an absorber plate. In fact, Hottel-Whillier-Bliss equations are conceived for assessing solar thermal collectors. Thus, with the aim of analysing the hybrid PV/T system performance, the PV panel was schematized as a metal sheet absorber plate.
- 2D models are developed and used for assessing the thermal behaviour of specific technologies integrated into the building envelope. Specifically, a two-dimensional approach is needed for assessing the spatial temperature distribution along the south façade of a high-rise building in which photovoltaics/thermal panels are integrated into the building envelope, and passive and active effects on the energy and thermal performance must be assessed.
- 3D model for assessing the energy performance of the novel high-vacuum flat-plate solar thermal collector designed by TVP solar company. The model is based on transient finite heat transfer thermal network. This approach is required for calculating the spatial temperature

field through different elements. In addition, an RC thermal model is developed with the aim of assessing the thermal capacity and the capability of storing hot water into the high-vacuum solar thermal collector.

For all the developed numerical models, experimental tests were conducted for various operating parameters (e.g. mass flow rate, tilt angle, weather conditions etc.) with the aim of experimentally validate them. Results on experimental validation are described in detail and the reliability of the developed models is established though the mean errors and mean percentage errors values. In addition, the effectiveness of the modelled devices and prototypes, in terms of energy, economic and environmental performance, has been analysed through suitable case studies. These analyses are conceived for showing how the proposed methodologies allow estimating the design and the feasibility of the proposed systems. The main findings of the thesis are summarised as follow:

- Referring to flat plate solar thermal collector, the main effects parameters are found out and ranked by means of Sobol parameter. Specifically, two different objective function were investigated (i.e. thermal efficiency and outlet fluid temperature). In case of thermal efficiency maximization, the first four parameters in the ranking are: 1) plate absorbance, 2) glass cover emissivity, 3) glass extinction coefficient, 4) gas used. In case of outlet fluid temperature, the first four parameters in the ranking are: 1) mass flow rate, 2) plate absorbance, 3) plate emissivity, 4) glass extinction coefficient two optimize solar thermal collector are detected and define through the characteristic curves.
- Interesting criteria and guidelines involving a combined system consisting of the PV/T prototype coupled with an air-to-air heat pump for space heating is also assessed. Specifically, by means of the developed tool, new performance maps are provided and interesting results in term of energy savings are achievable.
- Active and passive effects of building integration photovoltaic/thermal system into the south façade of a high-rise building were analysed. A special focus on the heating and cooling loads as well as thermal comfort was paid. In this framework, a novel parameter called "cooling inversion point" was defined. The proposed methodology can be useful for designers and practitioners in order to evaluate the magnitude of passive and active effects due to the building integration of air PV/T systems on the overall energy requirements and indoor thermal comfort, as a function of the system design and operating conditions;
- A novel energy management schemes for optimize the electricity exploitation from renewable energy devices is developed. The role of electric vehicles as energy vector among multiple

buildings, integrating PV panels and electrical storages, is investigated. Energy savings ranges between 45 to 77% are offered by the implementation of such management scheme.

References

[1] Kalogirou S. Solar Energy Engineering: Processes and Systems. 2013.

[2] IEA - International Energy Agency. Energy climate and change – World energy outlook special report. Special report on energy and climate change on iea.org/ publications website visited on February 2018.

[3] Cheng C, Ren C, Wang Z. The impact of renewable energy and innovation on carbon emission: An empirical analysis for OECD countries. Energy Procedia. 2019 158:3506-12.

[4] Athienitis AK, O'Brien W. Modeling, Design, and Optimization of Net-Zero Energy Buildings 2015.

[5] Soares N, Bastos J, Pereira L, Soares A, Amara A, Asadi E, et al. A review on current advances in the energy and environmental performance of buildings towards a more sustainable built environment. Renewable and Sustainable Energy Reviews. 2017 77:845-60.

[6] Sato D, Yamada N. Review of photovoltaic module cooling methods and performance evaluation of the radiative cooling method. Renewable and Sustainable Energy Reviews. 2019 104:151-66.

[7] Beikircher T, Möckl M, Osgyan P, Streib G. Advanced solar flat plate collectors with full area absorber, front side film and rear side vacuum super insulation. Solar Energy Materials and Solar Cells. 2015 141:398-406.

[8] Sakhaei S, Valipour M. Performance enhancement analysis of The flat plate collectors: A comprehensive review. Renewable and Sustainable Energy Reviews. 2019;102:186-204.

[9] Hassanzadeh A, Jiang L, Winston R. Coupled optical-thermal modeling, design and experimental testing of a novel medium-temperature solar thermal collector with pentagon absorber. Solar Energy. 2018 173:1248-61.

[10] Bakari R, Minja R, Njau K. Effect of Glass Thickness on Performance of Flat Plate Solar Collectors for Fruits Drying. 2014.

[11] Subedi I, Silverman T, Deceglie M, Podraza N. Emissivity of solar cell cover glass calculated from infrared reflectance measurements. Solar Energy Materials and Solar Cells. 2019 190:98-102.

[12] Giovannetti F, Föste S, Ehrmann N, Rockendorf G. High transmittance, low emissivity glass covers for flat plate collectors: Applications and performance. Solar Energy. 2014 104:52-9.

[13] Boudaden J, Oelhafen P, Schüler A, Roecker C, Scartezzini JL. Multilayered Al2O3/SiO2 and TiO2/SiO2 coatings for glazed colored solar thermal collectors. Solar Energy Materials and Solar Cells. 2005 89:209-18.

[14] Kalogirou S, Tripanagnostopoulos Y, Souliotis M. Performance of solar systems employing collectors with colored absorber. Energy and Buildings. 2005 37:824-35.

[15] García A, Solano JP, Vicente PG, Viedma A. Flow pattern assessment in tubes with wire coil inserts in laminar and transition regimes. International Journal of Heat and Fluid Flow. 2007 28:516-25.

[16] Jaisankar S, Radhakrishnan TK, Sheeba KN. Experimental studies on heat transfer and friction factor characteristics of forced circulation solar water heater system fitted with helical twisted tapes. Solar Energy. 2009 83:1943-52.

[17] Pandey KM, Chaurasiya R. A review on analysis and development of solar flat plate collector. Renewable and Sustainable Energy Reviews. 2017 67:641-50.

[18] Souliotis M, Papaefthimiou S, Caouris YG, Zacharopoulos A, Quinlan P, Smyth M. Integrated collector storage solar water heater under partial vacuum. Energy. 2017 139:991-1002.

[19] Moss R, Shire S, Henshall P, Arya F, Eames P, Hyde T. Performance of evacuated flat plate solar thermal collectors. Thermal Science and Engineering Progress. 2018;8:296-306.

[20] Moss RW, Henshall P, Arya F, Shire GSF, Eames PC, Hyde T. Simulator testing of evacuated flat plate solar collectors for industrial heat and building integration. Solar Energy. 2018;164:109-18.

[21] Juanicó LE. Modified vacuum tubes for overheating limitation of solar collectors: A dynamical modeling approach. Solar Energy. 2018 171:804-10.

[22] Saleh AM. Modeling of flat-plate solar collector operation in transient states. Master thesis of Sci in Engg Purdue University, Fort Wayne, Indiana. 2012.

[23] Zhou F, Ji J, Yuan W, Zhao X, Huang S. Study on the PCM flat-plate solar collector system with antifreeze characteristics. International Journal of Heat and Mass Transfer. 2019 129:357-66.

[24] Dara JE, Ikebudu KO, Ubani NO, Chinwuko CE, Ubachukwu OA. Evaluation of a passive flat-plate solar collector. International Journal of Advancements in Research & Technology. 2013;2.

[25] Wolf M. Performance analyses of combined heating and photovoltaic power systems for residences. Energy Conversion. 1976 16:79-90.

[26] Kasaeian A, Nouri G, Ranjbaran P, Wen D. Solar collectors and photovoltaics as combined heat and power systems: A critical review. Energy Conversion and Management. 2018 156:688-705.

[27] Abdelrazik AS, Al-Sulaiman FA, Saidur R, Ben-Mansour R. A review on recent development for the design and packaging of hybrid photovoltaic/thermal (PV/T) solar systems. Renewable and Sustainable Energy Reviews. 2018 95:110-29.

[28] Al-Waeli AHA, Sopian K, Kazem HA, Chaichan MT. Photovoltaic/Thermal (PV/T) systems: Status and future prospects. Renewable and Sustainable Energy Reviews. 2017 77:109-30.

[29] Babu C, Ponnambalam P. The role of thermoelectric generators in the hybrid PV/T systems: A review. Energy Conversion and Management. 2017 151:368-85.

[30] Slimani MEA, Amirat M, Kurucz I, Bahria S, Hamidat A, Chaouch WB. A detailed thermal-electrical model of three photovoltaic/thermal (PV/T) hybrid air collectors and photovoltaic (PV) module: Comparative study under Algiers climatic conditions. Energy Conversion and Management. 2017;133:458-76.

[31] Kabir E, Kumar P, Kumar S, Adelodun AA, Kim K-H. Solar energy: Potential and future prospects. Renewable and Sustainable Energy Reviews. 2018 82:894-900.

[32] Tonui JK, Tripanagnostopoulos Y. Air-cooled PV/T solar collectors with low cost performance improvements. Solar Energy. 2007 81:498-511.

[33] Jin GL, Ibrahim A, Chean YK, Daghigh R, Ruslan H, Mat S, et al. Evaluation of Single-Pass Photovoltaic-Thermal Air Collector with Rectangle Tunnel Absorber. American Journal of Applied Sciences. 2009 277-82.

[34] Franklin JC, Chandrasekar M. Performance enhancement of a single pass solar photovoltaic thermal system using staves in the trailing portion of the air channel. Renewable Energy. 2019 135:248-58.

[35] Fan W, Kokogiannakis G, Ma Z. A multi-objective design optimisation strategy for hybrid photovoltaic thermal collector (PVT)-solar air heater (SAH) systems with fins. Solar Energy. 2018 163:315-28.

[36] Ali AHH, Ahmed M, Abdel-Gaied SM. Investigation of heat transfer and fluid flow in transitional regime inside a channel with staggered plates heated by radiation for PV/T system. Energy. 2013 59:255-64.

[37] Hussain F, Othman MYH, Yatim B, Ruslan H, Sopian K, Anuar Z, et al. An improved design of photovoltaic/thermal solar collector. Solar Energy. 2015 122:885-91.

[38] Yuan W, Ji J, Li Z, Zhou F, Ren X, Zhao X, et al. Comparison study of the performance of two kinds of photovoltaic/thermal(PV/T) systems and a PV module at high ambient temperature. Energy. 2018 148:1153-61.

[39] Wu S, Chen C, Xiao L. Heat transfer characteristics and performance evaluation of water-cooled PV/T system with cooling channel above PV panel. Renewable Energy. 2018 125:936-46.

[40] Chauhan A, Tyagi VV, Anand S. Futuristic approach for thermal management in solar PV/thermal systems with possible applications. Energy Conversion and Management. 2018 163:314-54.

[41] Yang X, Sun L, Yuan Y, Zhao X, Cao X. Experimental investigation on performance comparison of PV/T-PCM system and PV/T system. Renewable Energy. 2018 119:152-9.

[42] Al-Shamani AN, Alghoul MA, Elbreki AM, Ammar AA, Abed AM, Sopian K. Mathematical and experimental evaluation of thermal and electrical efficiency of PV/T collector using different water based nano-fluids. Energy. 2018 145:770-92.

[43] Nazri NS, Fudholi A, Bakhtyar B, Yen CH, Ibrahim A, Ruslan MH, et al. Energy economic analysis of photovoltaic–thermal-thermoelectric (PVT-TE) air collectors. Renewable and Sustainable Energy Reviews. 2018 92:187-97.

[44] Tripanagnostopoulos Y, Nousia T, Souliotis M, Yianoulis P. Hybrid photovoltaic/thermal solar systems. Solar Energy. 2002 72:217-34.

[45] Florschuetz LW. Extension of the Hottel-Whillier model to the analysis of combined photovoltaic/thermal flat plate collectors. Solar Energy. 1979 22:361-6.

[46] Das D, Kalita P, Roy O. Flat plate hybrid photovoltaic- thermal (PV/T) system: A review on design and development. Renewable and Sustainable Energy Reviews. 2018 84:111-30.

[47] Herrando M, Ramos A, Freeman J, Zabalza I, Markides CN. Technoeconomic modelling and optimisation of solar combined heat and power systems based on flat-box PVT collectors for domestic applications. Energy Conversion and Management. 2018 175:67-85.

[48] Tripanagnostopoulos Y. Photovoltaic/Thermal Solar Collectors. In: Sayigh A, editor. Comprehensive Renewable Energy. Oxford: Elsevier; 2012. p. 255-300.

[49] Bigorajski J, Chwieduk D. Analysis of a micro photovoltaic/thermal – PV/T system operation in moderate climate. Renewable Energy. 2018.

[50] T.T. Chow GNT, C. Menezo. Hybrid solar: A review on photovoltaic and thermal power integration. International Journal of Photoenergy. 2012

[51] Rejeb O, Dhaou H, Jemni A. A numerical investigation of a photovoltaic thermal (PV/T) collector. Renewable Energy. 2015 77:43-50.

[52] Kuo CJ, Liu J, Umar ML, Lan W, Huang C, Syu S. The photovoltaic-thermal system parameter optimization design and practical verification. Energy Conversion and Management. 2019 180:358-71.

[53] Thinsurat K, Bao H, Ma Z, Roskilly AP. Performance study of solar photovoltaic-thermal collector for domestic hot water use and thermochemical sorption seasonal storage. Energy Conversion and Management. 2019 180:1068-84.

[54] Fuentes M, Vivar M, de la Casa J, Aguilera J. An experimental comparison between commercial hybrid PV-T and simple PV systems intended for BIPV. Renewable and Sustainable Energy Reviews. 2018 93:110-20.

[55] Michalena E, Tripanagnostopoulos Y. Contribution of the solar energy in the sustainable tourism development of the Mediterranean islands. Renewable Energy. 2010 35:667-73.

[56] Anderson TN, Duke M, Morrison GL, Carson JK. Performance of a building integrated photovoltaic/thermal (BIPVT) solar collector. Solar Energy. 2009 83:445-55.

[57] Yang T, Athienitis AK. A study of design options for a building integrated photovoltaic/thermal (BIPV/T) system with glazed air collector and multiple inlets. Solar Energy. 2014 104:82-92.

[58] Athienitis AK, Barone G, Buonomano A, Palombo A. Assessing active and passive effects of façade building integrated photovoltaics/thermal systems: Dynamic modelling and simulation. Applied Energy. 2018 209:355-82.

[59] Tomar V, Tiwari GN, Bhatti TS. Performance of different photovoltaic-thermal (PVT) configurations integrated on prototype test cells: An experimental approach. Energy Conversion and Management. 2017 154:394-419.

[60] Sultan SM, Ervina Efzan MN. Review on recent Photovoltaic/Thermal (PV/T) technology advances and applications. Solar Energy. 2018 173:939-54.

[61] Zhang Q, Yang Z, Li N, Feng R, Shi P. A novel solar photovoltaic/thermal assisted gas engine driven energy storage heat pump system (SESGEHPs) and its performance analysis. Energy Conversion and Management. 2019 184:301-14.
[62] Wang N, Phelan PE, Harris C, Langevin J, Nelson B, Sawyer K. Past visions, current trends, and future context: A review of building energy, carbon, and sustainability. Renewable and Sustainable Energy Reviews. 2018 82:976-93.
[63] Wang N, Phelan PE, Gonzalez J, Harris C, Henze GP, Hutchinson R, et al. Ten questions concerning future buildings beyond zero energy and carbon neutrality. Building and Environment. 2017 119:169-82.
[64] Petrichenko K, Aden N, Tsakiris A. Tools for Energy Efficiency in Buildings. A guide for policy-makers and experts. In: UNEP BEA, etc., editor.2016
[65] Becchio C, Corgnati SP, Delmastro C, Fabi V, Lombardi P. The role of nearly-zero energy buildings in the transition towards Post-Carbon Cities. Sustainable Cities and Society. 2016 27:324-37.
[66] D'Agostino D, Cuniberti B, Bertoldi P. Energy consumption and efficiency technology measures in European non-residential buildings. Energy and Buildings. 2017 153:72-86.
[67] Ferreira M, Almeida M, Rodrigues A. Cost-optimal energy efficiency levels are the first step in achieving cost effective renovation in residential buildings with a nearly-zero energy target. Energy and Buildings. 2016 133:724-37.
[68] Negendahl K. Building performance simulation in the early design stage: An introduction to integrated dynamic models. Automation in Construction. 2015 54:39-53.
[69] Szalay Z, Zöld A. Definition of nearly zero-energy building requirements based on a large building sample. Energy Policy. 2014 74:510-21.
[70] Nembrini J, Samberger S, Labelle G. Parametric scripting for early design performance simulation. Energy and Buildings. 2014 68, Part C:786-98.
[71] Todorović MS. BPS, energy efficiency and renewable energy sources for buildings greening and zero energy cities planning: Harmony and ethics of sustainability. Energy and Buildings. 2012 48:180-9.
[72] European Parliament. Directive 2010/31/EU of the European Parliament and of the Council on the energy performance of buildings (recast). In: Parliament E, editor.19 May 2010.
[73] Diakaki C, Grigoroudis E, Kolokotsa D. Towards a multi-objective optimization approach for improving energy efficiency in buildings. Energy and Buildings. 2008 40:1747-54.
[74] Crawley DB, Hand JW, Kummert M, Griffith BT. Contrasting the capabilities of building energy performance simulation programs. Part Special: Building Performance Simulation. 2008 43:661-73.
[75] IBPSA-USA. Building Energy Software Tools. In: Energy UDo, editor.2018.
[76] Attia S, Hensen JLM, Beltrán L, De Herde A. Selection criteria for building performance simulation tools: contrasting architects' and engineers' needs. Journal of Building Performance Simulation. 2012 5:155-69.
[77] Connolly D, Lund H, Mathiesen BV, Leahy M. A review of computer tools for analysing the integration of renewable energy into various energy systems. Applied Energy. 2010 87:1059-82.
[78] Mahmud K, Amin U, Hossain MJ, Ravishankar J. Computational tools for design, analysis, and management of residential energy systems. Applied Energy. 2018 221:535-56.
[79] Allegrini J, Orehounig K, Mavromatidis G, Ruesch F, Dorer V, Evins R. A review of modelling approaches and tools for the simulation of district-scale energy systems. Renewable and Sustainable Energy Reviews. 2015 52:1391-404.
[80] Castaldo VL, Pisello AL. Uses of dynamic simulation to predict thermal-energy performance of buildings and districts: a review. Wiley Interdisciplinary Reviews: Energy and Environment. 2018 7:e269.

[81] Attia S, Hamdy M, O'Brien W, Carlucci S. Assessing gaps and needs for integrating building performance optimization tools in net zero energy buildings design. Energy and Buildings. 2013 60:110-24.
[82] Wang H, Zhai Z. Advances in building simulation and computational techniques: A review between 1987 and 2014. Energy and Buildings. 2016 128:319-35.
[83] Fumo N. A review on the basics of building energy estimation. Renewable and Sustainable Energy Reviews. 2014 31:53-60.
[84] Bigot D, Miranville F, Fakra AH, Boyer H. A nodal thermal model for photovoltaic systems: Impact on building temperature fields and elements of validation for tropical and humid climatic conditions. Energy and Buildings. 2009 41:1117-26.
[85] Bigot D, Miranville F, Boyer H, Bojic M, Guichard S, Jean A. Model optimization and validation with experimental data using the case study of a building equipped with photovoltaic panel on roof: Coupling of the building thermal simulation code ISOLAB with the generic optimization program GenOpt. Energy and Buildings. 2013 58:333-47.
[86] Guichard S, Miranville F, Bigot D, Boyer H. A thermal model for phase change materials in a building roof for a tropical and humid climate: Model description and elements of validation. Energy and Buildings. 2014 70:71-80.
[87] Lee ES, Geisler-Moroder D, Ward G. Modeling the direct sun component in buildings using matrix algebraic approaches: Methods and validation. Solar Energy. 2018 160:380-95.
[88] Shen P, Braham W, Yi Y. Development of a lightweight building simulation tool using simplified zone thermal coupling for fast parametric study. Applied Energy. 2018 223:188-214.
[89] Clarke JA, Hensen JLM. Integrated building performance simulation: Progress, prospects and requirements. Building and Environment. 2015 91:294-306.
[90] Attia S, Gratia E, De Herde A, Hensen JLM. Simulation-based decision support tool for early stages of zero-energy building design. Energy and Buildings. 2012 49:2-15.
[91] Fonseca I Casas P, Fonseca I Casas A, Garrido-Soriano N, Casanovas J. Formal simulation model to optimize building sustainability. Advances in Engineering Software. 2014 69:62-74.
[92] Ioannidis Z, Buonomano A, Athienitis AK, Stathopoulos T. Modeling of double skin façades integrating photovoltaic panels and automated roller shades: Analysis of the thermal and electrical performance. Energy and Buildings. 2017 154:618-32.
[93] Capizzi G, Sciuto GL, Cammarata G, Cammarata M. Thermal transients simulations of a building by a dynamic model based on thermal-electrical analogy: Evaluation and implementation issue. Applied Energy. 2017 199:323-34.
[94] Figueiredo A, Kämpf J, Vicente R, Oliveira R, Silva T. Comparison between monitored and simulated data using evolutionary algorithms: Reducing the performance gap in dynamic building simulation. Journal of Building Engineering. 2018 17:96-106.
[95] Van der Veken J., Saelens D., Verbeeck G., Hens H. Comparison of steady state and dynamic building energy simulation programs. Proceedings of the international Buildings IX ASHRAE conference on the performance of exterior envelopes of whole buildings. 2004
[96] Melo AP, Cóstola D, Lamberts R, Hensen JLM. Assessing the accuracy of a simplified building energy simulation model using BESTEST: The case study of Brazilian regulation. Energy and Buildings. 2012 45:219-28.
[97] Mantesi E, Hopfe CJ, Cook MJ, Glass J, Strachan P. The modelling gap: Quantifying the discrepancy in the representation of thermal mass in building simulation. Building and Environment. 2018 131:74-98.
[98] IEA SHC. Testing and Validation of Building Energy Simulation Tools. Comparative Test Case Specification. Annex 43/SHC Task 34. Department of Civil Engineering, Aalborg University, Denmark2003-2007.

[99] Coakley D, Raftery P, Keane M. A review of methods to match building energy simulation models to measured data. Renewable and Sustainable Energy Reviews. 2014 37:123-41.

[100] Ryan MR, Sanquist TF. Validation of building energy modeling tools under idealized and realist conditions. Energy and Buildings. 2012 47:375-82.

[101] Judkoffm R, Wortmanm D, O'Doherty B, Burch J. A methodology for validating building energy analysis simulations, SERI/TR-254-1508. Solar Energy Research Institute (now National Renewable Energy Laboratory). Golden, CO, 1983.

[102] Neymark J, Judkoff R, Knabe G, Le H-T, Durig M, Glass A, et al. Applying the building energy simulation test (BESTEST) diagnostic method to verification of space conditioning equipment models used in whole-building energy simulation programs. Energy and Buildings. 2002 34 917-31.

[103] Ren Z, Chen D, James M. Evaluation of a whole-house energy simulation tool against measured data. Energy and Buildings. 2018 171:116-30.

[104] Ben-Nakhi AE, Aasem EO. Development and integration of a user friendly validation module within whole building dynamic simulation. Energy Conversion and Management. 2003 44:53-64.

[105] Lomas KJ, Eppel H, Martin CJ, Bloomfield DP. Empirical validation of building energy simulation programs. Energy and Buildings. 1997 26:253-75.

[106] Nageler P, Schweiger G, Pichler M, Brandl D, Mach T, Heimrath R, et al. Validation of dynamic building energy simulation tools based on a real test-box with thermally activated building systems (TABS). Energy and Buildings. 2018 168:42-55.

[107] Zhu Q, Li A, Xie J, Li W, Xu X. Experimental validation of a semi-dynamic simplified model of active pipe-embedded building envelope. International Journal of Thermal Sciences. 2016 108:70-80.

[108] Romaní J, Cabeza LF, de Gracia A. Development and experimental validation of a transient 2D numeric model for radiant walls. Renewable Energy. 2018 115:859-70.

[109] Loutzenhiser PG, Manz H, Moosberger S, Maxwell GM. An empirical validation of window solar gain models and the associated interactions. International Journal of Thermal Sciences. 2009 48:85-95.

[110] Malet-Damour B, Guichard S, Bigot D, Boyer H. Study of tubular daylight guide systems in buildings: Experimentation, modelling and validation. Energy and Buildings. 2016 129:308-21.

[111] Alaidroos A, Krarti M. Experimental validation of a numerical model for ventilated wall cavity with spray evaporative cooling systems for hot and dry climates. Energy and Buildings. 2016 131:207-22.

[112] Zingre KT, Yang E-H, Wan MP. Dynamic thermal performance of inclined double-skin roof: Modeling and experimental investigation. Energy. 2017 133:900-12.

[113] Blanco JM, Arriaga P, Rojí E, Cuadrado J. Investigating the thermal behavior of double-skin perforated sheet façades: Part A: Model characterization and validation procedure. Building and Environment. 2014 82:50-62.

[114] Anđelković AS, Mujan I, Dakić S. Experimental validation of a EnergyPlus model: Application of a multi-storey naturally ventilated double skin façade. Energy and Buildings. 2016 118:27-36.

[115] Sandels C, Brodén D, Widén J, Nordström L, Andersson E. Modeling office building consumer load with a combined physical and behavioral approach: Simulation and validation. Applied Energy. 2016 162:472-85.

[116] Attia S. State of the Art of Existing Early Design Simulation Tools for Net Zero Energy Buildings: A Comparison of Ten Tools. Université catholique de Louvain, Louvain La Neuve, Belgium; 2011

[117] Lirola JM, Castañeda E, Lauret B, Khayet M. A review on experimental research using scale models for buildings: Application and methodologies. Energy and Buildings. 2017 142:72-110.

[118] Cattarin G, Pagliano L, Causone F, Kindinis A. Empirical and comparative validation of an original model to simulate the thermal behaviour of outdoor test cells. Energy and Buildings. 2018 158:1711-23.
[119] Strachan P, Svehla K, Heusler I, Kersken M. Whole model empirical validation on a full-scale building. Journal of Building Performance Simulation. 2016 9:331-50.
[120] CEN European Committee for Standardizations. EN 15265:2007 - Thermal Performance of buildings – Calculation of Energy Use for Space Heating and Cooling – General Criteria and Validation Procedures. Brussels, 2007.
[121] ASHRAE. Standard 90.1-2004: Energy Standard for Building Except Low-rise Residential Buildings. 2004
[122] Al-Homoud MS. Computer-aided building energy analysis techniques. Building and Environment. 2001 36:421-33.
[123] Judkoff R, Neymark J. International Energy Agency Building Energy Simulation Test (BESTEST) and Diagnostic Method. NREL/TP-472-6231. Golden, Colorado 2005
[124] ASHRAE. Standard Method of Test for the Evaluation of Building Energy Analysis Computer Programs. 2014.
[125] Chow TT. A review on photovoltaic/thermal hybrid solar technology. Applied Energy. 2010 87:365-79.
[126] Tyagi VV, Kaushik SC, Tyagi SK. Advancement in solar photovoltaic/thermal (PV/T) hybrid collector technology. Renewable and Sustainable Energy Reviews. 2012 16:1383-98.
[127] Tripathy M, Sadhu PK, Panda SK. A critical review on building integrated photovoltaic products and their applications. Renewable and Sustainable Energy Reviews. 2016 61:451-65.
[128] Tripanagnostopoulos Y. Aspects and improvements of hybrid photovoltaic/thermal solar energy systems. Solar Energy. 2007 81:1117-31.
[129] Sathe TM, Dhoble AS. A review on recent advancements in photovoltaic thermal techniques. Renewable and Sustainable Energy Reviews. 2017 76:645-72.
[130] Biyik E, Araz M, Hepbasli A, Shahrestani M, Yao R, Shao L, et al. A key review of building integrated photovoltaic (BIPV) systems. Engineering Science and Technology, an International Journal. 2017 20:833-58.
[131] Baljit SSS, Chan H-Y, Sopian K. Review of building integrated applications of photovoltaic and solar thermal systems. Journal of Cleaner Production. 2016 137:677-89.
[132] Yang T, Athienitis AK. A review of research and developments of building-integrated photovoltaic/thermal (BIPV/T) systems. Renewable and Sustainable Energy Reviews. 2016 66:886-912.
[133] Tonui JK, Tripanagnostopoulos Y. Improved PV/T solar collectors with heat extraction by forced or natural air circulation. Renewable Energy. 2007 32:623-37.
[134] Kumar R, Rosen MA. Performance evaluation of a double pass PV/T solar air heater with and without fins. Applied Thermal Engineering. 2011 31:1402-10.
[135] Susanti L, Homma H, Matsumoto H, Suzuki Y, Shimizu M. A laboratory experiment on natural ventilation through a roof cavity for reduction of solar heat gain. Energy and Buildings. 2008 40:2196-206.
[136] Candanedo LM, Athienitis AK, Park KW. Convective Heat Transfer Coefficients in a Building-Integrated Photovoltaic/Thermal System. Journal of Solar Energy Engineering. 2011 133:021002--14.
[137] Pantic S, Candanedo L, Athienitis AK. Modeling of energy performance of a house with three configurations of building-integrated photovoltaic/thermal systems. Energy and Buildings. 2010 42:1779-89.
[138] Agrawal B, Tiwari GN. Optimizing the energy and exergy of building integrated photovoltaic thermal (BIPVT) systems under cold climatic conditions. Applied Energy. 2010 87:417-26.

[139] Rajoria CS, Agrawal S, Chandra S, Tiwari GN, Chauhan DS. A Novel investigation of building integrated photovoltaic thermal (BIPVT) system: A comparative study. Solar Energy. 2016 131:107-18.

[140] Kim J-H, Kim J-T. A Simulation Study of Air-Type Building-Integrated Photovoltaic-Thermal System. Energy Procedia. 2012 30:1016-24.

[141] Kamthania D, Nayak S, Tiwari GN. Performance evaluation of a hybrid photovoltaic thermal double pass facade for space heating. Energy and Buildings. 2011 43:2274-81.

[142] Farshchimonfared M, Bilbao JI, Sproul AB. Channel depth, air mass flow rate and air distribution duct diameter optimization of photovoltaic thermal (PV/T) air collectors linked to residential buildings. Renewable Energy. 2015 76:27-35.

[143] Nagano K, Mochida T, Shimakura K, Murashita K, Takeda S. Development of thermal-photovoltaic hybrid exterior wallboards incorporating PV cells in and their winter performances. Solar Energy Materials and Solar Cells. 2003 77:265-82.

[144] Assoa YB, Ménézo C. Dynamic study of a new concept of photovoltaic–thermal hybrid collector. Solar Energy. 2014 107:637-52.

[145] Dehra H. An investigation on energy performance assessment of a photovoltaic solar wall under buoyancy-induced and fan-assisted ventilation system. Applied Energy. 2017 191:55-74.

[146] Athienitis AK, Bambara J, O'Neill B, Faille J. A prototype photovoltaic/thermal system integrated with transpired collector. Solar Energy. 2011 85:139-53.

[147] Yang T, Athienitis AK. Experimental investigation of a two-inlet air-based building integrated photovoltaic/thermal (BIPV/T) system. Applied Energy. 2015 159:70-9.

[148] Bigaila E, Rounis E, Luk P, Athienitis AK. A Study of a BIPV/T Collector Prototype for Building Façade Applications. Energy Procedia. 2015 78:1931-6.

[149] Rounis ED, Athienitis AK, Stathopoulos T. Multiple-inlet Building Integrated Photovoltaic/Thermal system modelling under varying wind and temperature conditions. Solar Energy. 2016 139:157-70.

[150] Mirzaei PA, Carmeliet J. Influence of the underneath cavity on buoyant-forced cooling of the integrated photovoltaic panels in building roof: a thermography study. Progress in Photovoltaics: Research and Applications. 2015 23:19-29.

[151] Sohel MI, Ma Z, Cooper P, Adams J, Scott R. A dynamic model for air-based photovoltaic thermal systems working under real operating conditions. Applied Energy. 2014 132:216-25.

[152] Zogou O, Stapountzis H. Flow and heat transfer inside a PV/T collector for building application. Applied Energy. 2012 91:103-15.

[153] Wang Y, Tian W, Ren J, Zhu L, Wang Q. Influence of a building's integrated-photovoltaics on heating and cooling loads. Applied Energy. 2006 83:989-1003.

[154] Lamnatou C, Mondol JD, Chemisana D, Maurer C. Modelling and simulation of Building-Integrated solar thermal systems: Behaviour of the coupled building/system configuration. Renewable and Sustainable Energy Reviews. 2015 48:178-91.

[155] Delisle V, Kummert M. Cost-benefit analysis of integrating BIPV-T air systems into energy-efficient homes. Solar Energy. 2016;136:385-400.

[156] Rasoul Asaee S, Nikoofard S, Ismet Ugursal V, Beausoleil-Morrison I. Techno-economic Assessment of Photovoltaic (PV) and Building Integrated Photovoltaic/Thermal (BIPV/T) System Retrofits in the Canadian Housing Stock. Energy and Buildings. 2017

[157] Saadon S, Gaillard L, Giroux-Julien S, Ménézo C. Simulation study of a naturally-ventilated building integrated photovoltaic/thermal (BIPV/T) envelope. Renewable Energy. 2016 87:517-31.

[158] Zogou O, Stapountzis H. Energy analysis of an improved concept of integrated PV panels in an office building in central Greece. Applied Energy. 2011 88:853-66.

[159] Nemati O, Candanedo Ibarra LM, Fung AS. Review of computer models of air-based, curtainwall-integrated PV/T collectors. Renewable and Sustainable Energy Reviews. 2016 63:102-17.

[160] Tiwari GN, Saini H, Tiwari A, Deo A, Gupta N, Saini PS. Periodic theory of building integrated photovoltaic thermal (BIPVT) system. Solar Energy. 2016 125:373-80.

[161] Paris B, Eynard J, Grieu S, Talbert T, Polit M. Heating control schemes for energy management in buildings. Energy and Buildings. 2010 42 1908–17.

[162] The European Parliament and the Council. Directive 2012/27/EU on energy efficiency, amending Directives 2009/125/EC and 2010/30/EU and repealing Directives 2004/8/EC and 2006/32/EC. Official Journal of the European Union, Brussels, 25 October 2012. 2012.

[163] D'Agostino D. Assessment of the progress towards the establishment of definitions of Nearly Zero Energy Buildings (nZEBs) in European Member States. Journal of Building Engineering. 2015 1:20-32.

[164] Guillén-Lambea S, Rodríguez-Soria B, Marín JM. Review of European ventilation strategies to meet the cooling and heating demands of nearly zero energy buildings (nZEB)/Passivhaus. Comparison with the USA. Renewable and Sustainable Energy Reviews. 2016 62:561-74.

[165] Kolokotsa D, Rovas D, Kosmatopoulos E, Kalaitzakis K. A roadmap towards intelligent net zero- and positive-energy buildings. Solar Energy. 2011 85:3067-84.

[166] Buonomano A, De Luca G, Montanaro U, Palombo A. Innovative technologies for NZEBs: An energy and economic analysis tool and a case study of a non-residential building for the Mediterranean climate. Energy and Buildings. 2016 121:318-43.

[167] Wang Z, Zhao J, Li M. Analysis and optimization of carbon trading mechanism for renewable energy application in buildings. Renewable and Sustainable Energy Reviews. 2017 73:435-51.

[168] Torcellini P, Pless S, Leach M. A pathway for net-zero energy buildings: Creating a case for zero cost increase. Building Research and Information. 2014 43:25-33.

[169] Sartori I, Napolitano A, Voss K. Net zero energy buildings: A consistent definition framework. Energy and Buildings. 2012 48:220-32.

[170] Cooper M. Renewable and distributed resources in a post-Paris low carbon future: The key role and political economy of sustainable electricity. Energy Research & Social Science. 2016 19:66-93.

[171] Yeatts DE, Auden D, Cooksey C, Chen C-F. A systematic review of strategies for overcoming the barriers to energy-efficient technologies in buildings. Energy Research & Social Science. 2017

[172] Li DHW, Yang L, Lam JC. Zero energy buildings and sustainable development implications – A review. Energy. 2013 54:1-10.

[173] Marszal AJ, Heiselberg P, Bourrelle JS, Musall E, Voss K, Sartori I, et al. Zero Energy Building – A review of definitions and calculation methodologies. Energy and Buildings. 2011 43:971-9.

[174] Sharifi A, Murayama A. A critical review of seven selected neighborhood sustainability assessment tools. Environmental Impact Assessment Review. 2013 38:73-87.

[175] Attia S. Chapter 11 - NZEB Case Studies and Learned Lessons. Net Zero Energy Buildings (NZEB): Butterworth-Heinemann; 2018 p. 303-41.

[176] Marique A-F, Dujardin S, Teller J, Reiter S. School commuting: the relationship between energy consumption and urban form. Journal of Transport Geography. 2013 26:1-11.

[177] Mohammadi N, Taylor JE. Urban infrastructure-mobility energy flux. Energy. 2017 140:716-28.

[178] Marique A-F, Reiter S. A simplified framework to assess the feasibility of zero-energy at the neighbourhood/community scale. Energy and Buildings. 2014 82:114-22.

[179] Marique A-F, de Meester T, De Herde A, Reiter S. An online interactive tool to assess energy consumption in residential buildings and for daily mobility. Energy and Buildings. 2014 78:50-8.

[180] Dujardin S, Marique AF, Teller J. Spatial planning as a driver of change in mobility and residential energy consumption. Energy and Buildings. 2014 68:779-85.
[181] Mohammadi N, Taylor JE. Urban energy flux: Spatiotemporal fluctuations of building energy consumption and human mobility-driven prediction. Applied Energy. 2017;195:810-8.
[182] Yong JY, Ramachandaramurthy VK, Tan KM, Mithulananthan N. A review on the state-of-the-art technologies of electric vehicle, its impacts and prospects. Renewable and Sustainable Energy Reviews. 2015 49:365-85.
[183] Faria R, Moura P, Delgado J, de Almeida AT. A sustainability assessment of electric vehicles as a personal mobility system. Energy Conversion and Management. 2012 61:19-30.
[184] Langbroek JHM, Franklin JP, Susilo YO. When do you charge your electric vehicle? A stated adaptation approach. Energy Policy. 2017 108:565-73.
[185] Onn CC, Chai C, Abd Rashid AF, Karim MR, Yusoff S. Vehicle electrification in a developing country: Status and issue, from a well-to-wheel perspective. Transportation Research Part D: Transport and Environment. 2017 50:192-201.
[186] Amini MH, Moghaddam MP, Karabasoglu O. Simultaneous allocation of electric vehicles' parking lots and distributed renewable resources in smart power distribution networks. Sustainable Cities and Society. 2017 28:332-42.
[187] Mahmud K, Town GE, Morsalin S, Hossain MJ. Integration of electric vehicles and management in the internet of energy. Renewable and Sustainable Energy Reviews. 2018 82:4179-203.
[188] Hu J, Morais H, Sousa T, Lind M. Electric vehicle fleet management in smart grids: A review of services, optimization and control aspects. Renewable and Sustainable Energy Reviews. 2016 56:1207-26.
[189] Yang Z, Li K, Foley A. Computational scheduling methods for integrating plug-in electric vehicles with power systems: A review. Renewable and Sustainable Energy Reviews. 2015 51:396-416.
[190] Azadfar E, Sreeram V, Harries D. The investigation of the major factors influencing plug-in electric vehicle driving patterns and charging behaviour. Renewable and Sustainable Energy Reviews. 2015 42:1065-76.
[191] Tascikaraoglu A. Evaluation of spatio-temporal forecasting methods in various smart city applications. Renewable and Sustainable Energy Reviews. 2018 82:424-35.
[192] García-Villalobos J, Zamora I, San Martín JI, Asensio FJ, Aperribay V. Plug-in electric vehicles in electric distribution networks: A review of smart charging approaches. Renewable and Sustainable Energy Reviews. 2014 38:717-31.
[193] Kyriakopoulos GL, Arabatzis G. Electrical energy storage systems in electricity generation: Energy policies, innovative technologies, and regulatory regimes. Renewable and Sustainable Energy Reviews. 2016 56:1044-67.
[194] Daina N, Sivakumar A, Polak JW. Modelling electric vehicles use: a survey on the methods. Renewable and Sustainable Energy Reviews. 2017 68:447-60.
[195] Alirezaei M, Noori M, Tatari O. Getting to net zero energy building: Investigating the role of vehicle to home technology. Energy and Buildings. 2016 130:465-76.
[196] Doroudchi E, Alanne K, Okur Ö, Kyyrä J, Lehtonen M. Approaching net zero energy housing through integrated EV. Sustainable Cities and Society. 2018 38:534-42.
[197] Liu C, Chau KT, Wu D, Gao S. Opportunities and Challenges of Vehicle-to-Home, Vehicle-to-Vehicle, and Vehicle-to-Grid Technologies. Proceedings of the IEEE. 2013 101:2409-27.
[198] Kempton W, Tomić J. Vehicle-to-grid power implementation: From stabilizing the grid to supporting large-scale renewable energy. Journal of Power Sources. 2005 144:280-94.
[199] Haines G., McGordon A., Jennings P. The simulation of vehicle-to-homesystems–using electric vehicle battery storage to smooth domestic electricitydemand,. EVER Monaco2009

[200] Cvetkovic I, Thacker T, Dong D, Francis G, Podosinov V, Boroyevich D, et al. Future home uninterruptible renewable energy system with vehicle-to-grid technology. 2009 IEEE Energy Conversion Congress and Exposition2009 p. 2675-81.

[201] Noori M, Zhao Y, Onat NC, Gardner S, Tatari O. Light-duty electric vehicles to improve the integrity of the electricity grid through Vehicle-to-Grid technology: Analysis of regional net revenue and emissions savings. Applied Energy. 2016 168:146-58.

[202] Doroudchi E, Lehtonen M, Kyyrä J. Demand Response Control of a Townhouse Thermal Storage by Greedy Variable Neighborhood Algorithm. 2016. 2016 11.

[203] Darcovich K, Recoskie S, Ribberink H, Pincet F, Foissac A. Effect on battery life of vehicle-to-home electric power provision under Canadian residential electrical demand. Applied Thermal Engineering. 2017 114:1515-22.

[204] Erdinc O. Economic impacts of small-scale own generating and storage units, and electric vehicles under different demand response strategies for smart households. Applied Energy. 2014 126:142-50.

[205] Wang D, Coignard J, Zeng T, Zhang C, Saxena S. Quantifying electric vehicle battery degradation from driving vs. vehicle-to-grid services. Journal of Power Sources. 2016 332:193-203.

[206] Wu Q, Nielsen A, Østergaard J, Cha S. Modeling of Electric Vehicles (EVs) for EV Grid Integration Study2010

[207] Kuang Y, Hu M, Dai R, Yang D. A Collaborative Decision Model for Electric Vehicle to Building Integration. Energy Procedia. 2017 105:2077-82.

[208] Marmaras C, Xydas E, Cipcigan L. Simulation of electric vehicle driver behaviour in road transport and electric power networks. Transportation Research Part C: Emerging Technologies. 2017 80:239-56.

[209] Angelis FD, Boaro M, Fuselli D, Squartini S, Piazza F, Wei Q. Optimal Home Energy Management Under Dynamic Electrical and Thermal Constraints. IEEE Transactions on Industrial Informatics. 2013 9:1518-27.

[210] Salpakari J, Rasku T, Lindgren J, Lund PD. Flexibility of electric vehicles and space heating in net zero energy houses: an optimal control model with thermal dynamics and battery degradation. Applied Energy. 2017 190:800-12.

[211] Kelly N, Samuel A, Hand J. Testing integrated electric vehicle charging and domestic heating strategies for future UK housing. Energy and Buildings. 2015 105:377-92.

[212] Carlisle N., Van Geet O., Pless S. Definition of a "Zero Net Energy" Community. In: National Renewable Energy Laboratory G, Colorado, editor. Technical Report NREL/TP-7A2-460652009

[213] Saltelli A. Sensitivity analysis in practice. Hoboken, NJ: Wiley. 2004

[214] Smith C, Weiss T. Design Application of the Hottel-Whillier-Bliss Equation. 1977

[215] Swinbank WC. Long-wave radiation from clear skies. 1964

[216] Matuska T, Metzger J, Zmrhal V. Design tool KOLEKTOR 2.2 for virtual prototyping of solar flat-plate collectors. 2008

[217] Mitchell JW. Heat transfer from spheres and other animal forms. Biophysical journal. 1976 16:561-9.

[218] Pepper, Hollands. Summary of benchmark numerical studies for 3-D natural convection in an air-filled enclosure. Numerical Heat Transfer, Part A: Applications. 2002 1–11.

[219] Solar energy - Solar thermal collectors - Test methods (ISO 9806:2017). 2017.

[220] Saltelli A, Aleksankina K, Becker W, Fennell P, Ferretti F, Holst N, et al. Why so many published sensitivity analyses are false: A systematic review of sensitivity analysis practices. Environmental Modelling & Software. 2019 114:29-39.

[221] Helvaci HU, Khan ZA. Mathematical modelling and simulation of multiphase flow in a flat plate solar energy collector. Energy Conversion and Management. 2015 106:139-50.

[222] Tiwari GN, Meraj M, Khan ME, Mishra RK, Garg V. Improved Hottel-Whillier-Bliss equation for N-photovoltaic thermal-compound parabolic concentrator (N-PVT-CPC) collector. Solar Energy. 2018 166:203-12.
[223] Sakellariou E, Axaopoulos P. An experimentally validated, transient model for sheet and tube PVT collector. Solar Energy. 2018 174:709-18.
[224] Jaisankar S, Radhakrishnan TK, Sheeba KN. Studies on heat transfer and friction factor characteristics of thermosyphon solar water heating system with helical twisted tapes. Energy. 2009 34:1054-64.
[225] Qiu G, Wei X, Xu Z, Cai W. A novel integrated heating system of solar energy and air source heat pumps and its optimal working condition range in cold regions. Energy Conversion and Management. 2018 174:922-31.
[226] Kim T, Choi B-I, Han Y-S, Do KH. A comparative investigation of solar-assisted heat pumps with solar thermal collectors for a hot water supply system. Energy Conversion and Management. 2018 172:472-84.
[227] Santoli L, Mancini F. Prestazioni energetiche degli edifici: le norme UNI TS 11300-3/42011
[228] International Organization for Standardization. 13790:2008 - Energy performance of buildings -- Calculation of energy use for space heating and cooling. 2008
[229] Handbook SE. www.solarelectricityhandbook.com/solar-irradiance.html. 2019.
[230] Danandeh MA, Mousavi G SM. Solar irradiance estimation models and optimum tilt angle approaches: A comparative study. Renewable and Sustainable Energy Reviews. 2018 92:319-30.
[231] Buonomano A, Palombo A. Building energy performance analysis by an in-house developed dynamic simulation code: An investigation for different case studies. Applied Energy. 2014 113:788-807.
[232] Buonomano A. Code-to-Code Validation and Application of a Dynamic Simulation Tool for the Building Energy Performance Analysis. Energies. 2016 9.
[233] Corgnati SP, Fabrizio E, Raimondo D, Filippi M. Categories of indoor environmental quality and building energy demand for heating and cooling. Building Simulation. 2011 4:97-105.
[234] Jradi M, Arendt K, Sangogboye FC, Mattera CG, Markoska E, Kjærgaard MB, et al. ObepME: An online building energy performance monitoring and evaluation tool to reduce energy performance gaps. Energy and Buildings. 2018 166:196-209.
[235] Jaffal I, Inard C. A metamathical model for building energy performance. Energy and Buildings. 2017 151:501-10.
[236] Andersen RK, Fabi V, Corgnati SP. Predicted and actual indoor environmental quality: Verification of occupants' behaviour models in residential buildings. Energy and Buildings. 2016 127:105-15.
[237] Čekon M, Čurpek J. A transparent insulation façade enhanced with a selective absorber: A cooling energy load and validated building energy performance prediction model. Energy and Buildings. 2019 183:266-82.
[238] Buonomano A, Montanaro U, Palombo A, Santini S. Dynamic building energy performance analysis: A new adaptive control strategy for stringent thermohygrometric indoor air requirements. Applied Energy. 2016 163:361-86.
[239] Buonomano A, Montanaro U, Palombo A, Santini S. Adaptive Control for Building Thermo-hygrometric Analysis: A Novel Dynamic Simulation Code for Indoor Spaces with Multi-enclosed Thermal Zones. Energy Procedia. 2015 78:2190-5.
[240] Buonomano A, Calise F, Palombo A. Solar heating and cooling systems by CPVT and ET solar collectors: A novel transient simulation model. Applied Energy. 2013 103:588-606.
[241] Buonomano A, Montanaro U, Palombo A, Santini S. Temperature and humidity adaptive control in multi-enclosed thermal zones under unexpected external disturbances. Energy and Buildings. 2017 135:263-85.

[242] Buonomano A, Calise F, Palombo A. Solar heating and cooling systems by absorption and adsorption chillers driven by stationary and concentrating photovoltaic/thermal solar collectors: Modelling and simulation. Renewable and Sustainable Energy Reviews. 2018 82:1874-908.
[243] Inard C, Bouia H, Dalicieux P. Prediction of air temperature distribution in buildings with a zonal model. Energy and Buildings. 1996 24:125-32.
[244] Li X, Wen J. Review of building energy modeling for control and operation. Renewable and Sustainable Energy Reviews. 2014 37:517-37.
[245] Ahmad T, Chen H, Guo Y, Wang J. A comprehensive overview on the data driven and large scale based approaches for forecasting of building energy demand: A review. Energy and Buildings. 2018 165:301-20.
[246] Xu X, Wang S. A simplified dynamic model for existing buildings using CTF and thermal network models. International Journal of Thermal Sciences. 2008 47:1249-62.
[247] Lombard C, Mathews EH. A two-port envelope model for building heat transfer. Building and Environment. 1998 34:19-30.
[248] Yang S, Pilet TJ, Ordonez JC. Volume element model for 3D dynamic building thermal modeling and simulation. Energy. 2018 148:642-61.
[249] Kontoleon KJ. Dynamic thermal circuit modelling with distribution of internal solar radiation on varying façade orientations. Energy and Buildings. 2012 47:139-50.
[250] Ramallo-González AP, Eames ME, Coley DA. Lumped parameter models for building thermal modelling: An analytic approach to simplifying complex multi-layered constructions. Energy and Buildings. 2013 60 174-84.
[251] Joudi A, Svedung H, Rönnelid M. Energy efficient surfaces on building sandwich panels - A dynamic simulation model. Energy and Buildings. 2011 43 2462-7.
[252] Harish VSKV, Kumar A. A review on modeling and simulation of building energy systems. Renewable and Sustainable Energy Reviews. 2016 56:1272-92.
[253] Maile T., Fischer M., Haymaker J., Bazjanac V. Formalizing Approximations, Assumptions, and Simplifications to Document Limitations in Building Energy Performance Simulation. CIFE Working Paper - Stanford University. 2010
[254] Boyer H, Chabriat JP, Grondin-Perez B, Tourrand C, Brau J. Thermal building simulation and computer generation of nodal models. Building and Environment. 1996 31:207-14.
[255] Martin K, Erkoreka A, Flores I, Odriozola M, Sala JM. Problems in the calculation of thermal bridges in dynamic conditions. Energy and Buildings. 2011 43 529-35.
[256] Tsilingiris PT. Parametric space distribution effects of wall heat capacity and thermal resistance on the dynamic thermal behavior of walls and structures. Energy and Buildings. 2006 38:1200-11.
[257] Mathworks. MatLab.
[258] Barone G, Buonomano A, Forzano C, Palombo A. WLHP Systems in Commercial Buildings: A Case Study Analysis Based on a Dynamic Simulation Approach. American Journal of Engineering and Applied Sciences. 2016 9:659-68.
[259] Kreider JF, Rabl A. Heating and cooling of buildings. New York (NY): McGraw-Hill. 2009
[260] Bergman TL, Lavine AS, Incropera FP, D.P. D. Fundamentals of Heat and Mass Transfer. 7th ed. John Wiley & Sons, New Jersey, USA. 2011.
[261] Gebhart B. A new method for calculating radiant exchanges. ASHRAE Transactions. 1959 92 95-104.
[262] Mottard J-M, Fissore A. Thermal simulation of an attached sunspace and its experimental validation. Solar Energy. 2007 81:305-15.

[263] Roeleveld D, Hailu G, Fung AS, Naylor D, Yang T, Athienitis AK. Validation of Computational Fluid Dynamics (CFD) Model of a Building Integrated Photovoltaic/Thermal (BIPV/T) System. Energy Procedia. 2015 78:1901-6.

[264] Shah RK, London AL. Laminar flow forced convection heat transfer and flow friction in straight and curved ducts. A summary of analytical solutions. Stanford Univ CA Dept of mechanical engineering. 1971

[265] Yang L, Yan H, Lam JC. Thermal comfort and building energy consumption implications – A review. Applied Energy. 2014 115:164-73.

[266] Roeleveld D., Kumar R., Naylor D., Fung A.S. A CFD study of natural convection inside a BIPV/T system. IBPSA eSim2016. 2016

[267] Damiano A, Gatto G, Marongiu I, Porru M, Serpi A. Real-Time Control Strategy of Energy Storage Systems for Renewable Energy Sources Exploitation. IEEE Transactions on Sustainable Energy. 2014 5:567-76.

[268] Buonomano A, Calise F, Palombo A. Buildings dynamic simulation: Water loop heat pump systems analysis for European climates. Applied Energy. 2012 91:222-34.

[269] Buonomano A, Calise F, Dentice d'Accadia M, Vanoli L. A novel solar trigeneration system based on concentrating photovoltaic/thermal collectors. Part 1: Design and simulation model. Energy. 2013 61:59-71.

[270] Buonomano A, Palombo A. Nzebs design and simulation: a new tool for dynamic energy performance analyses. Proceedings of the 27th International Conference on Efficiency, Cost, Optimization, Simulation and Environmental Impact of Energy Systems, ECOS 20142014

[271] Buonomano A, Montanaro U, Palombo A, Santini S. Temperature and humidity adaptive control in multi-enclosed thermal zones under unexpected external disturbances. Energy and Buildings. 2017;135:263-85.

[272] Delisle V, Kummert M. A novel approach to compare building-integrated photovoltaics/thermal air collectors to side-by-side PV modules and solar thermal collectors. Solar Energy. 2014 100:50-65.

[273] Jones AD, Underwood CP. A thermal model for photovoltaic systems. Solar Energy. 2001 70:349-59.

[274] Skoplaki E, Palyvos JA. On the temperature dependence of photovoltaic module electrical performance: A review of efficiency/power correlations. Solar Energy. 2009 83:614-24.

[275] Hoang P, Bourdin V, Liu Q, Caruso G, Archambault V. Coupling optical and thermal models to accurately predict PV panel electricity production. Solar Energy Materials and Solar Cells. 2014 125:325-38.

[276] De Soto W, Klein SA, Beckman WA. Improvement and validation of a model for photovoltaic array performance. Solar Energy. 2006 80:78-88.

[277] Mahmoudzadeh Andwari A, Pesiridis A, Rajoo S, Martinez-Botas R, Esfahanian V. A review of Battery Electric Vehicle technology and readiness levels. Renewable and Sustainable Energy Reviews. 2017 78:414-30.

[278] Tremblay O, Dessaint L-A. Experimental Validation of a Battery Dynamic Model for EV Applications. World Electric Vehicle Journal. 2009 Vol. 3

[279] van Haaren R. Assessment of Electric Cars‟ Range Requirements and Usage Patterns based on Driving Behavior recorded in the National Household Travel Survey of 2009. In: v1.1 ECRRaUP, editor.2011.

[280] Ruiz V, Pfrang A, Kriston A, Omar N, Van den Bossche P, Boon-Brett L. A review of international abuse testing standards and regulations for lithium ion batteries in electric and hybrid electric vehicles. Renewable and Sustainable Energy Reviews. 2018 81:1427-52.

[281] Majed C, Karaki SH, Jabr R, Panik F. Near Optimal Control of Fuel Cell Hybrid Electric Vehicles in Real-Time. SAE Technical Papers. 2016 2016-April.

[282] TeslaMotors. Tesla Roadster Features and Specifications. . 2017.
[283] Pasaoglu G, Fiorello D, Martino A, Zani L, Zubaryeva A, Thiel C. Travel patterns and the potential use of electric cars – Results from a direct survey in six European countries. Technological Forecasting and Social Change. 2014 87:51-9.
[284] Buonomano A, Calise F, Palombo A, Vicidomini M. Adsorption chiller operation by recovering low-temperature heat from building integrated photovoltaic thermal collectors: Modelling and simulation. Energy Conversion and Management. 2017 149:1019-36.

Publications from this study

Journal Publications

- **Published**

Athienitis AK, **Barone G**, Buonomano A, Palombo A. (2018). Assessing active and passive effects of façade building integrated photovoltaics/thermal systems: Dynamic modelling and simulation. *Applied Energy*.

Barone G, Buonomano A, Calise F, Palombo A. (2018). Energy recovery by the natural gas decompression: modelling and simulation. *Thermal Science*.

Barone G, Buonomano A, Calise F, Forzano C, Palombo A. (2019). Building to vehicle to building concept toward a novel zero energy paradigm: Modelling and case studies. *Renewable and Sustainable Energy Reviews*.

Agathokleous R, **Barone G**, Buonomano A, Forzano C, Kalogirou SA, Palombo A. (2019). Building façade integrated solar thermal collectors for air heating: experimentation, modelling and applications. *Applied Energy*.

Kalogirou SA, Agathokleous R, **Barone G**, Buonomano A, Forzano C, Palombo A. (2019). Development and validation of a new TRNSYS Type for thermosiphon flat-plate solar thermal collectors: energy and economic optimization for hot water production in different climates. *Renewable Energy*.

Barone G, Buonomano A, Forzano C, Palombo A, Panagopoulos O. (2019). Photovoltaic thermal collectors: Experimental analysis and simulation model of an innovative low-cost water-based prototype. *Energy*.

Barone G, Buonomano A, Forzano C, Palombo A, Panagopoulos O. (2019). Experimentation, modelling and applications of a novel low-cost air-based photovoltaic thermal collector prototype. *Energy Conversion and Management*.

Barone G, Buonomano A, Calise F, Forzano C, Palombo A. (2019). Energy recovery through natural gas turboexpander and solar collectors: modelling and thermoeconomic optimization. *Energy*.

Barone G, Buonomano A, Forzano C, Palombo A. (2019). Dynamic energy performance simulation of buildings: experimental validation of an in-house tool with a real test room. *Energies*.

- **Pending**

Barone G, Buonomano A, Forzano C, Palombo A, (2020). A novel dynamic simulation model for the thermo-economic analysis and optimisation of district heating systems. *Energy Conversion and Management*.

Barone G, Buonomano A, Forzano C, Palombo A, (2020). Sustainable energy design of cruise ships through dynamic simulations: multi-objective optimization for waste heat recovery. *Energy Conversion and Management*.

Barone G, Buonomano A, Forzano C, Palombo A, (2020). Enhancing trains envelope - HVAC systems: a new dynamic simulation approach for energy, economic, environmental impact and thermal comfort analyses. *Energy*.

Barone G, Buonomano A, Forzano C, Palombo A, (2020). Passive and active performance assessment of building integrated hybrid solar photovoltaic/thermal collector prototypes: energy, comfort and economic analyses. *Energy*.

Smyth M, **Barone G**, Buonomano A, Forzano C, Giuzio GF, Palombo A, Mondol J, Muhumuza J, Pugsley A, Zacharopoulos A. (2019). Modelling and experimental evaluation of an innovative Integrated Collector Storage Solar Water Heating (ICSSWH) prototype. *Applied Energy.*

- **Conference Proceedings**

Athienitis AK, **Barone G**, Buonomano A, Palombo A. (2017). Building Integrated Photovoltaics/Thermal (BIPV/T) system: a new dynamic simulation model and a case study. *Proceedings of 3rd Building Simulation Applications Conference BSA 2017, Bozen-Bolzano (South Tyrol, Italy)*.

Barone G, Buonomano A, Calise F, Palombo A. (2017). Energy recovery by the natural gas decompression: modelling and simulation. *Proceedings of 12th SDEWES, Dubrovnik (Croatia).*

Barone G, Buonomano A, Calise F, Palombo A. (2017). Modelling and simulation of Net Zero Energy Buildings by renewable energy and distributed electric generation". *Proceedings of 12th SDEWES, Dubrovnik (Croatia).*

Barone G, Buonomano A, Forzano C, Palombo A, Panagopoulos O. (2018). Air-based photovoltaic thermal collectors: theoretical and experimental analysis of a novel low-cost prototype. *Proceedings of 13th SDEWES, Palermo (Italy).*

Baggio P, **Barone G**, Buonomano A, Forzano C, Palombo A, Panagopoulos O. (2018). Low-Cost water-based photovoltaic thermal collectors: experimental investigation and simulation model. *Proceedings of 13th SDEWES, Palermo (Italy).*

Kalogirou SA, Agathokleous R, **Barone G**, Buonomano A, Forzano C, Palombo. O. (2018). A new TRNSYS type for thermosiphonic flat-plate solar thermal collectors: validation and optimization procedure. *Proceedings of 13th SDEWES, Palermo (Italy).*

Barone G, Buonomano A, Forzano C, Palombo. A. (2018). Experimental validation of a dynamic building energy simulation tool and case study analysis on low-emissivity and cool coatings. *Proceedings of 13th SDEWES, Palermo (Italy).*

Barone G, Buonomano A, Forzano C, Palombo A. (2019). Building integrated photovoltaic thermal collectors: modelling and experimental investigation of two novel cost-effective prototypes. *Proceedings of 4rd Building Simulation Applications Conference BSA 2019, Bozen-Bolzano (South Tyrol, Italy).*

Barone G, Buonomano A, Forzano C, Palombo A. (2019). Building To Vehicle To Building concept for electricity grid flexibility: simulation, case study and parametric analysis. *Proceedings of Intelligent Building Operations Workshop Boulder (Colorado, US).*

Barone G, Buonomano A, Forzano C, Palombo A. (2019). Building To Vehicle To Building approach for the NZEB target at a micro-grid level: a comprehensive sensitivity and parametric post-optimality analysis. *Proceedings of IAQVEC, Bari (Italy).*

Barone G, Buonomano A, Forzano C, Mondol J, Palombo A, Pugsley A, Smyth M, Zacharopoulos A. (2019). A novel Integrated Collector Storage Solar Water Heating (ICSSWH) prototype: experimental investigation and simulation model. *Proceedings of 14th SDEWES, Dubrovnik (Croatia).*

Barone G, Buonomano A, Forzano C, Palombo A, Vicidomini M. (2019). Heat recovery from liquefied natural gas engines onboard modern cruise ships: dynamic modelling and system thermoeconomic optimization. *Proceedings of 14th SDEWES, Dubrovnik (Croatia).*

Barone G, Buonomano A, Forzano C, Palombo A, Verrelli M. (2019). District heating: a dynamic simulation approach for energy and economic analyses. *Proceedings of 14th SDEWES, Dubrovnik (Croatia).*

Barone G, Buonomano A, Forzano C, Palombo A. (2019). HVAC systems for trains, metro and tramways: dynamic simulation modelling for an energy efficient design and case study. *Proceedings of 14th SDEWES, Dubrovnik (Croatia).*

Barone G, Buonomano A, Forzano C, Palombo A. Modelling and simulation of a Building To Vehicle To Building system layout: a case study and parametric analysis. *Proceedings of 14th SDEWES, Dubrovnik (Croatia).*

Chrysanthou R, Agathokleous, Barone G, Buonomano A, Forzano C, Kalogirou SA, Palombo A. (2019). Design and simulation of a vacuum solar thermal flat-plate collector prototype *Proceedings of 14th SDEWES, Dubrovnik (Croatia).*

Book chapter

Barone G, Buonomano A, Palombo, (2018) Nearly-Zero Energy Buildings in Mediterranean climates, REHVA Federation of European Heating, Ventilation and Air Condition Associations

Barone G, Buonomano A, Forzano C, Palombo, (2019) Chapter 6 – Solar thermal collectors, Solar Hydrogen Production, Elseevier